UNIVERSITÀ DEGLI STUDI DI CATANIA

Ph.D. in Materials Science and Nanotechnology XXXIII Cycle

Ph.D. Thesis

Multiferroic BiFeO₃ films and nanostructures for hybrid energy harvesters

E N H A N C E

Ph.D. Student: *QUENTIN GERARD RENE MICARD*

Advisors: Coordinator:
Prof. Graziella Malandrino   *Prof. Giuseppe Compagnini*
Prof. Guglielmo Guido Condorelli

2018-2021

Vuoi sapiri qual è lu megghiu jocu?

Fà beni e parra pocu!

Acknowledgement

I want to thank Professor Graziella Malandrino and Professor Guglielmo Guido Condorelli for allowing me to work with them during those three intense years, for their constant availability and, for their continuous scientific, technological, and personal advices. The trust and the liberty they gave me in my work have been fundamental for the thesis development.

I am grateful to Bio-nanotech Research and Innovation Tower (BRIT) laboratory of University of Catania for the Rigaku SmartLab diffractometer facility.

I want to thank AIXTRON and Professor Michael Heuken, who hosted my colleagues and me for gaving us insights into the MOCVD processes' industrial development. Thank you also to Faraz Habib for the time and the understanding he gave me on my reactor.

I would like to thanks my colleague from Graziella's group: Gabriel Rodriguez Barrientos, Nishant Peddagopu, also involved in the ENHANCE Project, and Francesca Lo Presti. All the shared moments inside and outside the lab have been a great part of my life in Catania. A special thanks to Dr. Anna Lucia Pellegrino, who took the time to train, support me and clear my doubts on all matters of experimental work. I want to highlight the important work of the master students who have followed and helped me in several aspects of this thesis work: Marco Patané, Vanessa Cutraro, and Federica Pizzorni.

I want to thank Professor Paul Muralt, who followed me during my secondment period in EPFL. He helped me to understand more about the theoretical and functional aspect of ferroelectric materials and he has been the source of many advices.

In UFC/Femto-ST, I would like to acknowledge the strong and constant support of Professor Samuel Margueron who introduced me and guided me in the Raman spectroscopy analysis. I also thank Giacomo Clementi who, like my other colleagues from ENHANCE, followed me during those last years; by his extreme dedication to his work, he pushed me to give my best in my research. I thank Merieme Ouhabaz, our project manager, for her work in the project and her continuous help with device microfabrication.

To my dear friends, near and far: Vanessa Jungbluth, Théo Calvayrac, Benjamin Trapletti, Nampoina Rakotonavalona, Omar Ould Abdesselam, Lucas Millanvois, and many more. Thank you for accompanying me through all the highs and lows of the thesis work. Thank you for the calls, the visits, the travels, and the small words.

I am thanking my family: my grandmothers, my parents Yves and Isabelle and my sisters Mathilde and Marie. Even far from them, their constant support and encouragements have been fundamental.

Finally, I need to thank Giada Giuffrida, who cleared my doubts, walked by my side, and made those years brighter.

Table of contents

Introduction

The reduction of car's CO_2 emission and energy use in a smart way are today the biggest challenges car industry must surpass. One simple approach is to reduce car weight and to optimize its energy consumption. Today's cars are composed of complex networks of wires, making them ultra-monitored and always more connected, but it has a dramatic impact on vehicles' mass. Thus, simplifying these networks is one big step toward reducing cars' weight without impacting their efficiency. This aim can be achieved by the integration of maintenance-free sensors operating wirelessly and powered by their environment. To answer this challenge, the MSCA-ITN ENHANCE project, a multidisciplinary research consortium, aims to develop a hybrid energy harvesting system capable of powering wireless sensors for the car of tomorrow.

Due to their ability to exploit different types of wasted energy present in a car, as sunlight, motor vibrations, and heat, hybrid energy harvesters' development presents a high interest. $Pb(Zr_xTi_{1-x})O_3$ (PZT) is commonly used for this kind of application, especially for vibrational harvesters. It has been combined with a large spectrum material to optimize its properties for many applications. The major drawback of PZT is its environmental impact, but it can be replaced by lead-free perovskite based structures such as $BiFeO_3$ (BFO), $LiNbO_3$ (LNO), and $(K,Na)NbO_3$ (KNN). For this purpose, the optimization of their synthesis and properties are of special interest.

$BiFeO_3$ is a multiferroic material, meaning that at least two of the three ferroic orders: ferroelectricity, ferromagnetism or antiferromagnetism and ferroelasticity coexist. Among multiferroics, perovskite $BiFeO_3$ and its derived systems are interesting because they maintain their properties in extreme temperature environments due to their Curie (T_C = 1103 K) and Neel temperatures (T_N=643 K) well above room temperature. Photoelectric, pyroelectric, and piezoelectric properties are the most studied and appealing characteristics, making BFO an important material for energy harvesting applications.

Different deposition techniques have been used to obtain thin films of BFO and its derived systems. The main deposition techniques which have been applied to the production of BFO films are: chemical solution deposition (CSD), pulsed laser deposition (PLD), sputtering, sol-gel and Metal-Organic Chemical Vapor Deposition (MOCVD). So far, compared to other methods, MOCVD has been relatively unexplored and never used to develop $BiFeO_3$ deposition on silicon to fit the standard of the MEMs industry.

In this context, the research activity of the present thesis has been focused on the deposition of thin-films of pure and doped $BiFeO_3$ systems using a Metal-Organic Chemical Vapor Deposition (MOCVD) approach. MOCVD deposition technique offers a large number of advantages compared to other thin-films production methods. Many MOCVD precursors are available; thus, when working on material optimization, many $BiFeO_3$ systems can be quickly obtained and tested by a simple tuning of precursors ratio. This flexibility is also found in the great variety of used substrates. MOCVD is also very appealing in terms of film morphological consistency, chemical homogeneity, and density. As pulsed laser deposition (PLD), the proper combination of precursors, deposition conditions and substrates can lead to thin-films epitaxial growth. However, unlike PLD, MOCVD offers the possibility to deposit homogeneous samples on large area substrates and, because of its important presence in the industry, scale-up of new processes is easier.

The versatility conceded by the deposition of thin film by MOCVD permitted the deposition of a large quantity of simple and complex $BiFeO_3$ systems. As material chemical composition has a critical influence on its properties, precursors' thermal behavior has been checked by thermogravimetric analysis (TGA) for complex doped systems. The understanding of the films' chemical compositions and homogeneity has been obtained by energy-dispersive X-ray analyses (EDX) and X-ray ray photoelectron spectroscopy (XPS). The polycrystalline or epitaxial nature of the films has been controlled by X-ray diffraction (XRD) and by transmission electron microscopy (TEM) in the case of intricate nanostructures. Morphological study of the materials has been done by field emission scanning electron microscopy (FE-SEM) and atomic force microscopy (AFM). Coupled to the AFM, piezoresponse force microscopy (PFM) and piezoresponse force spectroscopy (PFS) have permitted the imaging of ferroelectric domains and the confirmation of the films' piezoelectric properties.

The carried work aims to bring a methodology for the synthesis of $BiFeO_3$ systems thin films that is compatible with conventional industrial processes. Along with studying of the deposition protocols within the University of Catania, national and international collaborations have been crucial for the in-depth analysis of thin films structures and functional properties.

This work is articulated around the following points:

- Selection of commercially available precursors for $BiFeO_3$ deposition by MOCVDfor $BiFeO_3$ on commercially available silicon substrates.
- Investigation of $LaNiO_3$ deposition as buffer layer by MOCVD on $SrTiO_3$ and Si.
- Investigation on the impact of rare earth and transition metals doping on $BiFeO_3$ films properties: optical bandgap, ferroelectricity, piezoelectricity, pyroelectricity, photoelectricity and magnetoelectricity.
- Deposition of singly and bi-doped $BiFeO_3$ films and nanocomposites with control of their structural, morphological, and chemical integrity.
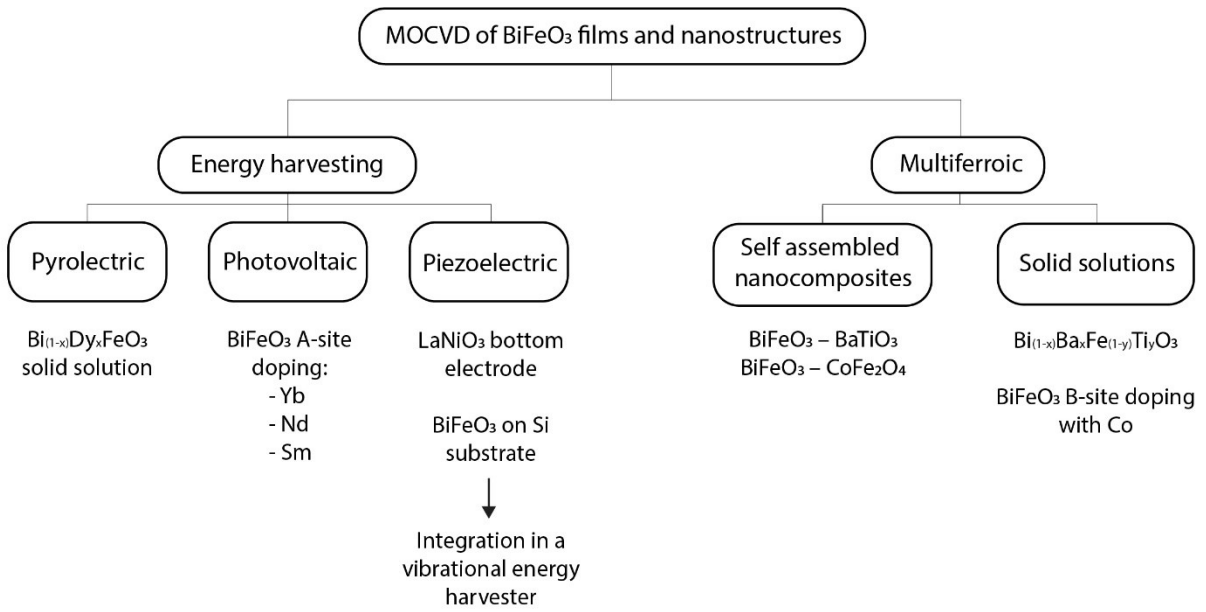
The thesis is organized as in the following. The first chapter reports the $BiFeO_3$ films grown by MOCVD on IrO_2/Si substrates, in which the conductive IrO_2 layer functions as a bottom electrode and a buffer layer. This part of the work focuses on optimizing the MOCVD route for the deposition of homogeneous $BiFeO_3$ thin films on Si (001) that were buffered with an IrO2 layer. The method is compatible with conventional industrial processes to create a functional hybrid energy harvester. Special attention has been given to the impact of the different deposition parameters on the films' quality. Moreover, preliminary work for the deposition of $LaNiO_3$ buffer layer has been done. The use of Si-based substrates presents a major advantage for reducing the production cost of the BFO compared to the widely spread single-crystals substrates.

The second chapter is devoted to the depositions of $BiFeO_3$ films on $SrTiO_3$ single crystal and its conductive variant $Nb:SrTiO_3$. These substrates are attractive to grow quickly epitaxial thin films of $BiFeO_3$ systems and so being able to obtain high repeatability when investigating materials properties. $BiFeO_3$ doping is the most common and simple way to tune its properties. $BiFeO_3$ A-site doping with rare earth elements has been intensively studied for all the deposition techniques mentioned above. Many elements have been used to substitute Bi^{3+} ions in BFO perovskite structures incorporated following a multitude of deposition methods. This work focused on dopant from the lanthanide series with: Neodymium (Nd), Samarium (Sm), Dysprosium (Dy) and Ytterbium (Yb). Along with depositions tuning and film morphological and chemical characterization, the functional properties have been investigated.

The A-site of the $BiFeO_3$ perovskite structure can be substituted, but B-site doping with transition metal is also a common procedure for modifying $BiFeO_3$ properties. Combining $BiFeO_3$ with $BaTiO_3$ in ceramics mixed systems or layered structures improves the properties of BFO, playing a crucial role in reducing the conductivity of the mixture and decreasing the leakage current, potentially allowing for a better multiferroic material. In particular, due to their strongly enhanced dielectric and energy storage properties, the BFO–BTO solid solution films represent promising candidates for energy storage applications. In the third chapter, an in depth study is reported on the impact of precursors ratio used during the deposition by MOCVD and how it allows the self-growth of a $Bi_{(1-x)}Ba_xFe_{(1-y)}Ti_yO_3$ solution or a $Bi_{(1-x)}Ba_xFeO_3/Bi_{(1-x)}Ba_xFe_{(1-y)}Ti_yO_3$ nanocomposite films.

Finally, one last modification of the BFO systems is addressed using Co as a doping element. The Co-doping is appealing because it has for objective the deposition of a self-assembled magnetoelectric thin film. In the case of doping leading to a solid solution, Co is substituting the B site of the perovskite and has an important influence on BFO magnetic properties. Then, if careful attention is given to the deposition conditions, BFO-CFO nanocomposite thin-film can be deposited through a single step MOCVD process. The nanocomposite is composed of a BFO matrix with embedded CFO nanorods; in this configuration, coupling between BFO ferroelectric properties and CFO magnetic properties is expected.

Thesis roadmap

```
                    ┌─────────────────────────────────────────┐
                    │  MOCVD of BiFeO₃ films and nanostructures │
                    └─────────────────────────────────────────┘
```

$MOCVD\ of\ BiFeO_3\ films\ and\ nanostructures$

Energy harvesting

Multiferroic

Pyrolectric | **Photovoltaic** | **Piezoelectric** | **Self assembled nanocomposites** | **Solid solutions**

$Bi_{(1-x)}Dy_xFeO_3$ solid solution

$BiFeO_3$ A-site doping:
- Yb
- Nd
- Sm

$LaNiO_3$ bottom electrode

$BiFeO_3$ on Si substrate

↓

Integration in a vibrational energy harvester

$BiFeO_3 - BaTiO_3$
$BiFeO_3 - CoFe_2O_4$

$Bi_{(1-x)}Ba_xFe_{(1-y)}Ti_yO_3$

$BiFeO_3$ B-site doping with Co

1. State of the art

The name perovskite refers to the class of compounds which share the same crystal structure as $CaTiO_3$ which was discovered on the Ural Mountains by Gustav Rose and named after the Russian mineralogist Lev Perovski. The perovskite crystal structure was first described by V.M. Goldschmidt in 1926 [1] in his work on tolerance factors, that represent a milestone in exploring the perovskite family of materials.

1.1. The perovskite structure

1.1.1. The ideal perovskite

In his ideal form, a perovskite possesses a cubic ABO_3 structure (space group P_{m3m}) (Figure 1), with A and B being the larger and the smaller cations, respectively. If the cubic structure is centred with the A cations, A resides in the dodecahedral sites coordinated by twelve oxygen anions and the BO_6 octahedra occupying the cube corners.
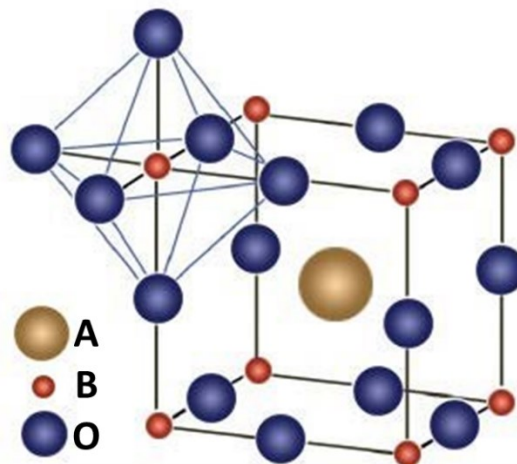
Figure 1 ABO$_3$ ideal cubic perovskite structure centered around the A-site. [2]

Most perovskites do not have this ideal cubic structure at room temperature. Instead, they often present distortions relative to the theoretical ideal cubic structure. The "tolerance factor" introduced in Goldschmidt's work is an indicator of the perovskite structure stability. The tolerance factor can be calculated using the Equation 1.

$$t = \frac{R_A + R_O}{\sqrt{2} * (R_B + R_O)} \quad Equation. 1$$

In Equation 1, R_A, R_B, and R_O are the ionic radii of A, B and O^{2-}. Different charges combination between the two cations are possible: A^{3+} and B^{3+} or A^{1+} and B^{5+} or A^{2+} and B^{4+}. To follow Goldschmidt's method, it is important to use the ionic radii values for the six-coordinated ions

defined by Shannon [3], even if A ion is 12-coordinated, since Goldschmidt description considers the ionic radii in a six-coordination environment [1]. For t=1, the tolerance factor suggests the formation of an ideal perovskite structure. A deviation of the tolerance factor indicates possible structural distortion. In the case of a tolerance factor inferior to 1 caused by a too-small A ion, the BO_6 octahedra can tilt to occupy the space, causing a lattice distortion. The ideal cubic structure can form for 0.89 < t < 1 and, the perovskite structure is stable but distorted for 0.8< t < 0.89. A hexagonal structure can be one of the variants of the distorted perovskite ideal configuration, usually it is observed for t>1 but the tolerance factor gives only a general indication of the studied structure, which in this case makes hexagonal structure also visible for t<1 [4].

Changes in the ideal composition ABO_3 have a significant impact in the distortions observed in most perovskites' structures. The adaptable nature of perovskites is mostly due to the various possible substitutions at the A and B sites. Insertion of dopant elements can help to modify and adapt the material properties for a specific use, depending on their nature and their concentration.

1.1.2.   BiFeO₃ structure and properties

Bismuth ferrite, $BiFeO_3$, (space group R3c) can be described based on a hexagonal unit cell: a_{hex}=5.57Å, c_{hex}=13.86 Å and, V_{hex}=378.80 Å^3. Its structure can also be seen as a rhombohedral cell: a_{rh}=5.63 Å, α_{rh}= 59.34° and, V_{rh}= 124.6 Å^3. The hexagonal cell contains six perovskite $BiFeO_3$ unit cells and, the rhombohedral cell contains two of the perovskite-like structure of $BiFeO_3$ [5,6]. Compared to the ideal perovskite structure, $BiFeO_3$ perovskite-like unit cell is a rhombohedral distorted cell (pseudocubic) with a_{pc}=3.956 Å, α_{pc}=89.45° (Figure 2) [7]. $BiFeO_3$, tolerance factor t is 0.88 with Bi^{3+} $r_{6\text{-coord}}$ = 1.03 Å, Fe^{3+} $r_{6\text{-coord}}$ = 0.55 Å and O^{2-} $r_{6\text{-coord}}$ = 1.4 Å [3].
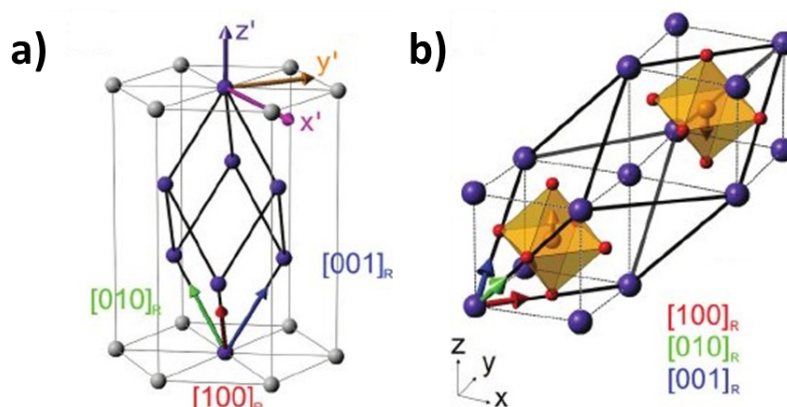

Figure 2 BiFeO₃ a) hexagonal unit cell with the rhombohedral cell and b) 2 pseudo-cubic cell included in the rhombohedral one. [8]

The unit vectors of the rhombohedral and hexagonal cells are related to the perovskite one by the transformation matrix Equation 2,3,4 and 5 [5,9,10].

$$\begin{pmatrix} a \\ b \\ c \end{pmatrix}_{rh} = \begin{vmatrix} 0 & 1 & 1 \\ 1 & 0 & 1 \\ 1 & 1 & 0 \end{vmatrix} \times \begin{pmatrix} A \\ B \\ C \end{pmatrix}_{pc} \qquad Equation.\,2$$

$$\begin{pmatrix} a \\ b \\ c \end{pmatrix}_{hex} = \begin{vmatrix} -1 & 1 & 0 \\ 0 & -1 & 1 \\ 2 & 2 & 2 \end{vmatrix} \times \begin{pmatrix} A \\ B \\ C \end{pmatrix}_{pc} \qquad Equation.\,3$$

$$\begin{pmatrix} a \\ b \\ c \end{pmatrix}_{hex} = \begin{pmatrix} 1 & -1 & 0 \\ 0 & 1 & -1 \\ 1 & 1 & 1 \end{pmatrix} \times \begin{pmatrix} A \\ B \\ C \end{pmatrix}_{rh} \qquad Equation.\,4$$

$$\begin{pmatrix} a \\ b \\ c \end{pmatrix}_{rh} = \frac{1}{3} \begin{pmatrix} 2 & 1 & 1 \\ -1 & 1 & 1 \\ -1 & -2 & 1 \end{pmatrix} \times \begin{pmatrix} A \\ B \\ C \end{pmatrix}_{hex} \qquad Equation.\,5$$

In $BiFeO_3$, the ferroelectric properties, and so the internal polarization, comes mostly from the lone pair (s^2 orbital) of Bi^{3+} ions, so the A-site. Internal $BiFeO_3$ polarization is oriented in the $[001]_{hex}$ || $[111]_{rh}$ || $[111]_{pc}$ direction. Bismuth ferrite also displays antiferromagnetic properties. Its magnetic properties depend on the element occupying the perovskite B-site, in this case, Fe^{3+} ions [11].

Because it is ferroelectric, $BiFeO_3$ exhibits a wide range of other functional properties, that find special interest in energy harvesting applications. As it is reported in Figure 3. it is not only ferroelectric but also piezoelectric and pyroelectric. Moreover, compared to other perovskites its small bandgap, ranging from 2.3 to 2.8 eV, makes it a good candidate for solar harvesting applications [11].

The theoretical potential of $BiFeO_3$ is huge, but one of the most important challenges with $BiFeO_3$ is its enormous leakage current. Mainly the consequences of an important concentration of oxygen vacancies and the presence of mixed Fe valences, $BiFeO_3$ in its pure form shows a too high conductivity to be used directly for an out of the lab application. Further optimizations of the material are required to reduce its leakage [12].

1.2.   Available forms of BiFeO$_3$

1.2.1.   Single crystal of BiFeO$_3$

Today, no BiFeO$_3$ single crystals are commercially available. Experimental works report the growth of BiFeO$_3$ single crystals from millimeter to centimeter size. Crystals are grown by melting Bi$_2$O$_3$ and Fe$_2$O$_3$, with, B$_2$O$_3$ added and acting as a flux thus reducing the mixture liquidus [13] [14]. An in-depth knowledge of Bi$_2$O$_3$–Fe$_2$O$_3$ phase diagram [15] lead to improved quality BFO single crystals. Using the flux method, X-ray analyses have reported that growth direction is along the polar axis [111]$_{Rh}$ of the structure [16]. Laser-diode heating floating-zone (LDFZ) is the method used to grow what are, so far, the largest BiFeO3 single crystals with a diameter of 4mm and a length up to 50 mm [17]. The advantage of this technique is the possibility to reshape the single crystal to adapt it to the study of specific properties [18]. Finally, the fluoride ion-assisted hydrothermal method can be used to grow various sizes of BFO single crystals, according to the processing conditions. The produced nanoplates lateral size range from 6.5 to 14.4 μm wide with a thickness that can be tailored from 80 nm to 1.14 μm [19].

1.2.2.   Thin films of BiFeO$_3$

1.2.2.1.   Single crystal substrates

Epitaxial growth of BiFeO$_3$ has only been achieved by using single-crystal substrates, preferentially SrTiO$_3$ (with sometimes SrRuO$_3$ bottom electrode) and doped (Nb, La) conductive SrTiO$_3$. Through MOCVD, PLD or MBE BFO orientation matches the one of SrTiO$_3$ (commercially available: (100)$_{pc}$, (110)$_{pc}$ and (111)$_{pc}$) [20-22].

1.2.2.2.   Metallic substrates

BiFeO$_3$ films directly deposited on metallic substrates have not been intensively investigated. Nevertheless, few attempts are reported: BiFeO$_3$ deposited by PLD on flexible magnetic Ni tapes with a preferential orientation (110)$_{pc}$ [23] and screen printed of polycrystalline BiFeO$_3$ (Poly-BFO) on noble metal foils (Ag, Au and Pt) [24].

1.2.2.3.   On silicon

Direct deposition of BFO on Si is not common; the use of a buffer layer/bottom electrode is the preferred structure. Nevertheless, spray pyrolysis on (100) Si has given (001) oriented BFO (001)$_{pc}$ [25] and poly-BFO has been obtained by laser-MBE [26].

1.2.2.4.   Use of buffer layer

1.2.2.4.1.   *SrRuO$_3$*

Due to their structures, some single-crystal substrates are materials of choice to deposit BFO thin films. SrTiO$_3$, SrTiO$_3$:Nb, [27] MgO, LaAlO$_3$ and YSZ [28] all have been used

directly or in combination with bottom electrodes. MOCVD [27], spin-coating [29], sputtering [30], or PLD [31] have been explored for deposition of BFO films, their final orientations depending on the substrate ones.

Combined with single crystal or Si substrates, SrRuO$_3$ (SRO) is one of the most used bottom electrodes for deposition of BFO doped and un-doped systems [32]. Independently of the deposition technique: spin coating [29], sputtering [30], or by pulsed laser deposition [31], (001)$_{pc}$ and (111)$_{pc}$ oriented BFO films have been obtained. BFO film orientation depends on the bottom electrode orientation, which is itself determined by substrate orientation [33-36].

1.2.2.4.2. LaNiO$_3$

LaNiO$_3$ is another conductive perovskite that displays promising results as a bottom electrode for high-quality BFO films. The studies show that both LaNiO$_3$ and BiFeO$_3$ are prepared by sol-gel process on Si based substrates. The systems are polycrystalline but can present preferred orientation (001)$_{pc}$ and (110)$_{pc}$ [37-39].

1.2.2.4.3. Platinum

On Si substrate, platinum bottom electrodes have been used in the following structures: Si/SiO$_2$/TiO2/Pt and Si/SiO$_2$/Ti/Pt. Polycrystalline tetragonal, P$_{4mm}$ BFO has been deposited on those substrates by sol-gel and PLD [40-42]. Poly-BFO with preferential (001)$_{pc}$ orientation has been obtained on Pt (111) with a chemical solution route [43].

1.2.2.4.4. Conductive oxide

After metallic electrodes and conductive perovskites, conductive oxides can also be used as bottom electrodes. The sol-gel method on FTO or ITO coated glass or quartz is well developed and can be used for poly-BFO deposition [44]. Those structures are of great interest for photovoltaic devices [45,46]. If deposition at high temperature is required, as in the MOCVD process, IrO$_2$ can be used as bottom electrode and buffer layer for the growth of poly-BFO on Si [47].

1.3. Tuning of the material in thin films

1.3.1. Strained and stressed films

Applying strain on film to tune BFO thin film properties has been studied several times. Different compressive strains can be applied to the film by varying the thickness of a strain tuning layer or the BFO itself [48,49]. Another similar approach consists to take advantage of lattice mismatch between BFO and its substrate ((001)- oriented LaAlO$_3$, SrTiO$_3$, MgO and buffered Si substrates to influence materials bandgap and ferroelectric properties [30]. Finally, self-assembled nano composites, such as BiFeO$_3$-CoFe$_2$O$_4$ can also achieve strain engineering. Constraints between the two materials enable a magneto-structural coupling between antiferromagnetic BFO and ferrimagnetic CFO [50].

1.3.2. Doping

Single or co-doping at the A / B sites are the most established methods to tune BFO films or ceramics properties. [51] BFO doping with rare-earth elements [52] or transition metals [53] has been used to tune multiferroic, ferroelectric, dielectric, magnetic and photovoltaic properties. [54-56] Highly doped systems also present some potentials in properties enhancement. The superior concentration of doping elements implies that, as demonstrated for $BiFeO_3$-$BaTiO_3$, homogeneous solid solution cannot always be achieved, and the material may present multiple phases [57]. Modification induced in doped systems is not only functional but also structural. In the case of fibers doping, increase of the specific surface area, pore size and reduce grains size are reported [58].

Due to its simplicity, doping is the favorite technique to tune BFO properties. However, modifications of process conditions during material deposition can also have a significant impact on final properties. For example, processing atmosphere and gas ratio used in the ceramic or film production can influence the microstructure, quantity of impurities and the bulk photovoltaic properties [33,54].

We saw that the use of self-assembled nanocomposites or highly doped BFO matrix are of special interest. Superlattice structures have been investigated as another way to combine materials properties and to take benefit of their interactions, in our case, between BFO and other functional materials. Most of the studied systems are $BiFeO_3$-$BaTiO_3$ systems stacked to create and enhance the magnetoelectric coupling control [59-61]. Tunability of ferroelectricity and ferromagnetism have also been investigated in other multilayers such as $BiFeO_3$-$BiMnO_3$ [62], $BiFeO_3$ -Fe_3O_4 [63] and $BiFeO_3$ - $La_{2/3}Sr_{1/3}MnO_3$ [64].

1.3.3. Post process treatment

After optimizing the process conditions, strain, dopants, and structure, some last steps can still improve $BiFeO_3$ properties. The poling procedure consists of the application of an electric field on BFO films or ceramics to control the polarization state in the material. Global polarization, polarization relaxation, polarization fatigue, all can have an influence on conduction currents in the material. The linear dependence of the current on the polarization was clearly be observed [65]. Knowing this, poling can improve photovoltaic efficiency in pure $BiFeO_3$ [66] or multi-doped BFO systems [67] and, so, bring adapted solutions for either energy harvesting or sensor applications [68]. Similarly, the application of magnetic field can be used to tune photoelectrochemical behaviors [33].

1.4. Temperature dependance of the material properties

For BiFeO$_3$ films, very few studies have been done. In the temperature range from -193 to 27°C, dependence between temperature and permittivity is visible as ε_r increases while sample temperature rises [69]. On the other hand, from 0 to 400°C, material permittivity shows great stability [70].

For doped and undoped BiFeO$_3$ [71], BiFeO$_3$–BaTiO$_3$ [72,73] or related ceramics systems [74,75], the dielectric behavior was investigated over a wide range of temperature, starting at room temperature, and going at least to 350°C. As the temperature rises, permittivity increases as well as the dielectric loss, which follows linearly the temperature gain. Ceramics' Curie temperature can be tuned by doping or changing ceramic stoichiometry [74,75].

In BiFeO$_3$–BaTiO$_3$ ceramics, the temperature dependence of piezoelectric coefficient is reported [76]. The coefficient d$_{33}$ increases first and then decreases in the temperature range. The piezoelectric temperature enhancement is partly related to the augmentation of the dielectric constant and its quick deterioration at high temperature comes from thermal depolarization. A study on Ca-doped BiFeO$_3$–BaTiO$_3$ ceramics has reported a similar behavior for the electromechanical coupling [77]. BiFeO$_3$–PbTiO$_3$ ceramic shows an increase of conductivity up to 350°C, but it presents variations of the permittivity and dielectric loss like lead-free systems [78].

Some modified BFO ceramics show that doping or combination with lead-free materials provide a high thermal stability [79]. As an example, LiNbO$_3$ doping gives permittivity stability in the 200°C-500°C temperature range [80]. Mg-doped BiFeO$_3$–BaTiO$_3$ ceramics present a constant d$_{33}$ coefficient up to 400°C [81].

1.5. Challenges and drawback of the material

Studies of BFO films have established the deposition, tuning, and working mechanisms of the material. However, several challenges are still present. The first one concerns the film deposition method, with the majority of the films deposited through pulsed laser deposition, sol-gel or sputtering, the MOCVD, the technique of choice for film quality and upscale perspective, is still not enough spread. Moreover, if not deposited on single crystal substrate, BFO films are polycrystalline with in general no preferential orientation. Working on oriented samples on low cost substrate still need to be pushed forward. Finally, despite its huge interest for energy harvesting, very few devices have been designed and tested [82] [83]. Thanks to the various strategies explored, we have a broad understanding of the material possibilities and huge flexibility to adapt the material to the working environment of energy harvesting device [84].

References

[1] V. M. Goldschimdt, Geochemische Verteilungsgesetze der Elemente, Akad. Oslo. J. Mat. Natur. 2 (1926) 7.

[2] F.G. Santomauro, J. Grilj, L. Mewes, G. Nedelcu, S. Yakunin, T. Rossi, G. Capano, A. Al Haddad, J. Budarz, D. Kinschel, D.S. Ferreira, G. Rossi, M. Gutierrez, T. Daniel Grolimund, V. Samson, M. Nachtegaal, G. Smolentsev, M.V. Kovalenko, M. Chergui, Localized holes and delocalized electrons in photoexcited inorganic perovskites: Watching each atomic actor by picosecond X-ray absorption spectroscopy, Struct. Dyn. (2017) 044002; doi: 10.1063/1.4971999

[3] R. D. Shannon, Revised effective ionic radii and systematic studies of interatomic distances in halides and chalcogenides, ActaCrystallogr. 32 (1976) 751.

[4] U. Müller, Inorganic Structural Chemistry, Wiley & Sons Ltd. (1993).

[5] J. M. Moreau, C. Michel R. Gerson, W.J. James, Ferroelectric $BiFeO_3$ X-Ray and Neutron Diffraction Study, J. Phys. Chem. Solids 32 (1971) 1315-1320.

[6] J. D. Bucci, B. K. Robertson, W. J. James, The Precision Determination of the Lattice Parameters and the Coefficients of Thermal Expansion of $BiFeO_3$, Appl. Cryst. 5 (1972) 187.

[7] F. Kubel, H. Schmid, Structure of a Ferroelectric and Ferroelastic Monodomain Crystal of the Perovskite $BiFeO_3$, Acta Cryst. B46 (1990) 698-702.

[8] K. I. Doig, F. Aguesse, A. K. Axelsson, N. M. Alford, S. Nawaz, V. R. Palkar, S. P. P. Jones, R. D. Johnson, R. A. Synowicki, J. Lloyd-Hughes, Coherent magnon and acoustic phonon dynamics in tetragonal and rare-earth-doped $BiFeO_3$ multiferroic thin films, Phys. Rev. B 88 (2013) 094425.

[9] C. Michel, Structures and relationships of some Perovskite-type compounds, Doctoral dissertation (1970) 2281.

[10] G. Burns, A. M. Glazer, Space groups for solid state scientists, J. Appl. Cryst. 12 (1979) 42

[11] G. Catalan, J.F. Scott, Physics and Applications of Bismuth Ferrite, Adv. Mater. 21 (2009) 2463–2485.

[12] G.A. Smolenskiĭ, I.E. Chupis, Ferroelectromagnets, Soviet Physics Uspekhi 25 (1982) 475.

[13] F. Kubel, H. Schmid, Growth, twinning and etch figures of ferroelectric/ ferroelastic dendritic $BiFeO_3$ single domain crystalsKubel, J. Cryst. Growth 129 (1993) 515—524.

[14] X. Martí, P. Ferrer, J. Herrero-Albillos, J. Narvaez, V. Holy, N. Barrett, M. Alexe, G. Catalan, M. Physical, SKIN LAYER OF $BiFeO_3$ single crystal, Phys. Rev. Lett. 106 (2010) 236101.

[15] J. Lu, L.J. Qiao, P.Z. Fu, Y.C. Wu, Phase equilibrium of Bi_2O_3–Fe_2O_3 pseudo-binary system and growth of BiFeO3, J. Cryst. Growth 318 (2011) 936–941.

[16] R. Haumont, R. Saint-Martin, C. By, Centimeter-size $BiFeO_3$ single crystals grown by flux method, Phase Transitions 9 (2008) 81.

[17] T. Ito, T. Ushiyama,Y. Yanagisawa, R. Kumai, Y. Tomioka, Growth of Highly Insulating Bulk Single Crystals of Multiferroic $BiFeO_3$ and Their Inherent Internal Strains in the Domain-Switching Process, Cryst. Growth Des. 11 (2011) 5139–5143.

[18] M. Białek,T. Ito, H. Rønnow, J.-Ph. Ansermet, Terahertz-optical properties of a bismuth ferrite single crystal, Physical Review B 99 (2019) 064429.

[19] X. Yang, R. Zeng, Z. Ren, Y. Wu, X. Chen, M. Li, J. Chen, R. Zhao, D. Zhou, Z. Liao, H. Tian, Y. Lu, X. Li, J. Li, G. Han, Single-crystal $BiFeO_3$ Nanoplates with Robust Antiferromagnetism, ACS Appl. Mater. Interfaces 10 (2018) 6 5785–5792.

[20] T. Yag, C. Wang, X. Zhang, Y. Feng, H. Guo, K. Jin, X. Gao, Z. Li, X. Li, Surface double-layer structure in (110) oriented BiFeO3 thin film, Appl. Phys. Lett. 105 (2014) 202901.

[21] R. Nechache, C. Harnagea, L. Gunawan, L.-P. Carignan, C. Maunders, D. Ménard, G.A. Botton, A. Pignolet, Growth, Structure and Properties of $BiFeO_3$-$BiCrO_3$ Films, IEEE T. Ultrason. Ferr. 54 (2007) 12.

[22] K. Sone, H. Naganuma, T. Miyazaki, T. Nakajima, S. Okamura, Jpn. Crystal Structures and Electrical Properties of Epitaxial $BiFeO_3$ Thin Films with (001), (110), and (111) Orientations Jpn. J. Appl. Phys. 49 (2010) 09MB03

[23] L. Yan, M. Zhuo, Z. Wang, J. Yao, N. Haberkorn, S. Zhang, L. Civale, J. Li, D. Viehland, Q. X. Jia, Appl. Phy. Lett. 101. (2012) 012908

[24] E. Khomyakova, J. Pavlic, M. Makarovic, H. Ursic, J. Walker, V.Ya. Shur, T. Rojac, B. Malic, A. Bencan, Screen-printed BiFeO3 thick films on noble metal foils, Ferroelectrics 496 (2016) 193-203.

[25] V. Annapu Reddy, N.P. Pathak, R. Nath, Enhanced magnetoelectric coupling in transition-metal-doped $BiFeO_3$ thin films Solid State Communications 171 (2013) 40–45.

[26] X. Yao, C. Wanga, S. Tiana, Y. Zhou, X. Lia, C. Ge, E. Guo, M. He, X. Bai, P. Gao, G. Yang, K. Jin, Growth and physical properties of $BiFeO_3$ thin films directly on Si substrate, J. Cryst. Growth 522 (2019) 110–116.

[27] M.R. Catalano, G. Spedalotto, G.G. Condorelli, G. Malandrino, MOCVD Growth of Perovskite Multiferroic $BiFeO_3$ Films: The Effect of Doping at the A and/or B Sites on the Structural, Morphological and Ferroelectric Properties, Adv. Mater. Interfaces (2017), 1601025.

[28] D. Scillato, N. Licciardello, M.R. Catalano, G.G. Condorelli, R. Lo Nigro, G. Malandrino, $BiFeO_3$ Films Doped in the A or B Sites: Effects on the Structural and Morphological Properties, J. Nanosci. Nanotechnol 11 (2011) 9 8221-8225.

[29] C.H. Chen, J.L. Her, T.M. Pan, Structural and electrical properties of the sol-gel derived multiferroic $BiFeO_3$ monolayer and $NiTiO_3$–$BiFeO_3$ bilayer thin films, Ceram. Int. 46 (2020) 9 13219-13224.

[30] H. Wang, F. Khatkhatay, J. Jian, J. Huang, M. Fan, H. Wang, Strain Tuning of Ferroelectric and Optical Properties of Rhombohedral-like $BiFeO_3$ thin films on $SrRuO_3$-buffered Substrates, Mater. Res. Bull. 110 (2018) 120-125.

[31] M. Campanini, E. Gradauskaite, M. Trassin, D. Yi, P. Yu, R. Ramesh, R. Ernia, M.D. Rossell, Imaging and quantification of charged domain walls in $BiFeO_3$, Nanoscale 12 (2020) 9186-9193.

[32] X. Chen, G. Wu, H. Zhang, N. Qin, T. Wang, F. Wang, W. Shi, D. Bao, Nonvolatile bipolar resistance switching effects in multiferroic $BiFeO_3$ thin films on $LaNiO_3$-electrodized Si substrates, Appl. Phys. A (2010) 100: 987–990.

[33] H. Zhu, X. Sun, L. Kang, M. Hong, M. Liu, Z.Yu, J. Ouyang, Charge transport behaviors in epitaxial $BiFeO_3$ thick films sputtered with different Ar/O2 flow ratios, Scr. Mater 115 (2016) 62–65.

[34] J. Wu, J. Wang, BiFeO3 thin films of (111)-orientation deposited on SrRuO$_3$ buffered Pt/TiO2/SiO$_2$/Si(1 0 0) substrates, Acta Mater 58 (2010) 1688–1697.

[35] Y. Liu, Y. Qi, P. Zhou, C. Guan, H. Chen1, J. Wang, Z. Ma, Tianjin Zhang, Mechanisms of resistive switching in BiFeO$_3$ thin films modulated by bottom electrode, J. Phys. D: Appl. Phys. (2017)

[36] S. Xu, Y. Zhang, H. Zhen Guo, W. Geng, Z. Bai, An-Quan Jiang, Improved Polarization Retention of BiFeO3 Thin Films Using GdScO$_3$ (110) Substrates, Chin. Phys. Lett. 34 (2017) 2 027701.

[37] W. Zhang, H. Wu, X. Zhang, H. Zhu, F. Hu, Growth of (001) preferentially oriented BiFeO$_3$ films on Si substrate by sol-gel method, Mater. Res. Express 2019.

[38] X. Wang, H. Liu, B. Yanc, Enhanced ferroelectric properties of Ce-substituted BiFeO$_3$ thin films on LaNiO3/Si substrates prepared by sol–gel process, J. Eur. Ceram. Soc. 29 (2009) 1183–1187.

[39] X. Chen, G. Wu, H. Zhang, N. Qin, T. Wang, F. Wang, W. Shi, D. Bao, Nonvolatile bipolar resistance switching effects in multiferroic BiFeO$_3$ thin films on LaNiO3-electrodized Si substrates, Appl. Phys. A (2010) 100: 987–990.

[40] R. Anlin Goldaa, A. Marikanib, E. John Alexc, Enhancement of dielectric, ferromagnetic and electrochemical properties of BiFeO$_3$ nanostructured films through rare earth metal doping, Ceram. Inter. 46 (2020) 1962–1973.

[41] K. Y. Yun, D. Ricinschi, T. Kanashima, M. Noda, M. Okuyama, Giant Ferroelectric Polarization Beyond 150μC/cm2 in BiFeO$_3$ Thin Film, JJAP 43 (2004) 647-648.

[42] S. Xiao, H. Sun, X. Liu, H. Sui, Investigations on photovoltaic performance of sol–gel derived BiFeO3-based heterostructures via compositional modification, Mater. Lett 260 (2019) 126964.

[43] S. Yakovlev, J. Zekonyte, C.H. Solterbeck, M. Es-Souni ,Interfacial effects on the electrical properties of multiferroic BiFeO$_3$/Pt/Si thin film heterostructures, Thin Solid Films 493 (2005) 24–29.

[44] C. Kumari, I. Varun, S.P. Tiwari, A. Dixit, Robust non-volatile bipolar resistive switching in sol-gel derived BiFeO3 thin films, Superlattices and Microstruct. 120 (2018) 67-74.

[45] Z. Lu, X. Yang, C. Jin, P. Li, . Wan, J. Liu, Nonvolatile Electric-Optical Memory Controlled by Conductive Filaments in Ti-Doped BiFeO$_3$, Adv. Electron. Mater. 4 (2018) 1700551.

[46] J. Liua, H. Deng, H. Cao, X. Zhai, J. Tao, L. Sun, P. Yang, J. Chu, Influence of rare-earth elements doping on structure and optical properties of BiFeO3thin films fabricated by pulsed laser deposition, Appl. Surf. Sci. 307 (2014) 543–547.

[47] Q. Micard, G.G. Condorelli, G. Malandrino, Piezoelectric BiFeO3 Thin Films: Optimization of MOCVD Process on Si, Nanomaterials 10 (2020) 630.

[48] C. J. M. Daumont, S. Farokhipoor, A. Ferri, J. C. Wojdeł, J. Íñiguez, B. J. Kooi, B. Noheda, Tuning the atomic and domain structure of epitaxial films of multiferroic BiFeO$_3$, Phys. Rev. B 81 (2010) 144115.

[49] M.M. Saj Mohan, S. Bandyopadhyay, T. Jogi, S. Bhattacharya, R. Ramadurai, Realization of rhombohedral, mixed, and tetragonal like phases of BiFeO$_3$ and ferroelectric domain engineering using a strain tuning layer on LaAlO3(001) substrate, J. Appl. Phys. 125 (2019) 012501.

[50] T. Amrillah, S.K. Vandrangi, Y. Bitla, T.H. Do, S.C. Liao, C.Y. Tsai, Y.Y. Chin, Y.T. Liu, M.L. Lin, Q. He, H.J. Lin, H.Y. Lee, C.H. Lai, E. Arenholz, J.Y. Juang, Y.H. Chu, Tuning the magnetic properties of self-assembled $BiFeO_3$–$CoFe_2O_4$ heteroepitaxy by magnetostructural coupling, Nanoscale 16 (2016).

[51] M.R. Catalano, G. Spedalotto, G. G. Condorelli, G. Malandrino Catalano, MOCVD Growth of Perovskite Multiferroic $BiFeO_3$ Films: The Effect of Doping at the A and/or B Sites on the Structural, Morphological and Ferroelectric Properties, Adv. Mater. Interfaces 4 (2017) 1601025.

[52] D. Kan, L.P. lova, V. Anbusathaiah, C.J. Cheng, S. Fujino, V. Nagarajan, K.M. Rabe, I. Takeuchi, Universal Behavior and Electric-Field-Induced Structural Transition in Rare-Earth-Substituted BiFeO3, Adv. Funct. Mater. 20 (2010) 1108–1115.

[53] A. Radojković, D.L. Golić, J. Ćirković, Z.M. Stanojević, D. Pajić, F. Torić, A. Dapčević, P. Vulić, Z. Branković, G. Branković, Tuning of $BiFeO_3$ multiferroic properties by light doping with Nb, _Ceram. Inter. 44 (2018) 14.

[54] C.S. Tu, P.Y. Chen, C.S. Chen, C.Y. Lina, V.H. Schmidt, Tailoring microstructure and photovoltaic effect in multiferroic Nd substituted $BiFeO_3$ ceramics by processing atmosphere modification, J. Eur. Ceram. Soc. 38 (2018) 4 1389-1398.

[55] X. Yuan, L. Shi, J. Zhao, S. Zhou, J. Guo, S. Pan, X. Miao, L. Wu, Tuning Ferroelectric, Dielectric, and Magnetic Properties of $BiFeO_3$ Ceramics by Ca and Pb Co-Doping, Phys. Status Solidi B (2018)1800499.

[56] Y. Zhang, H. Zheng, X. Wang, H. Li, Y. Wu, Y. Zhang, H. Su, G. Yuan, Enhanced photovoltaic properties of gradient calcium-doped $BiFeO_3$ films, Ceram. Inter. 46 (2020) 8 A.

[57] T. Zheng, J. Wu, Perovskite $BiFeO_3$–$BaTiO_3$ Ferroelectrics: Engineering Properties by Domain Evolution and Thermal Depolarization Modification, Adv. Electron. Mater. (2020) 2000079.

[58] Y. Tie, S.Y. Ma, S.T. Pei, Q.X. Zhang, K.M. Zhu, R. Zhang, X.H. Xu, T. Han, W.W. Liu, Pr doped $BiFeO_3$ hollow nanofibers via electrospinning method as a formaldehyde sensor, Sens. Actuators: B Chem. 308 (2020) 127689.

[59] S. Hohenberger, J.K. Jochum, M.J. Van Bael, K. Temst, C. Patzig, T. Höche, M. Grundmann, M. Lorenz, Enhanced Magnetoelectric Coupling in BaTiO3-BiFeO3 Multilayers, Materials 13 (2020) 197.

[60] M. Lorenz, D. Hirsch, C. Patzig, T. Höche, S. Hohenberger, H. Hochmuth, V. Lazenka, K. Temst, M. Grundmann, Correlation of Interface Impurities and Chemical Gradients with High Magnetoelectric Coupling Strength in Multiferroic $BiFeO_3$–$BaTiO_3$, Superlattices Appl. Correlation of Interface Impurities and Chemical Gradients with High Magnetoelectric Coupling Strength in Multiferroic BiFeO3−BaTiO3, ACS Appl. Mater. Interfaces 9 (2017) 18956–18965.

[61] M. Lorenz, G. Wagner, V. Lazenka, P. Schwinkendorf, H. Modarresi, M.J. Van Bael, A. Vantomme, K. Temst, O. Oeckler, M. Grundmann, Correlation of magnetoelectric coupling in multiferroic BaTiO3-$BiFeO_3$ superlattices with oxygen vacancies and antiphase octahedral rotations, Appl. Phys. Lett. 106 (2015) 012905.

[62] C. Jin, W. Geng, L. Wang, W. Han, D. Zheng, S. Hu, M. Ye, Z. Xu, Y. Ji, J. Zhao, Z. Chen, G. Wang, Y. Tang, Y. Zhu, X. Mac, L. Chen, Tuning Ferroelectricity and Ferromagnetism in $BiFeO_3$/$BiMnO_3$ Superlattices, Nanoscale 17 (2020).

[63] H. Yang, C. Jin, W. B. Mi, H. L. Bai, G.F. Chen, Electronic and magnetic structure of $Fe_3O_4/BiFeO_3$ multiferroic superlattices: First principles calculations, J. Appl. Phys. 112 (2012) 063925.

[64] N. Feng, W. Mi, X. Wang, Y. Cheng, U. Schwingenschlögl, Superior Properties of Energetically Stable $La_{2/3}Sr_{1/3}MnO_3$/Tetragonal $BiFeO_3$ Multiferroic Superlattices, ACS Appl. Mater. Interfaces 7 (2015) 19.

[65] Y. Yao, B. Zhang, L. Chen, Y. Yang, Z. Wang, H.N. Alshareef, X.X. Zhang, Polarization-tuned diode behaviour in multiferroic $BiFeO_3$ thin films, J. Phys. D: Appl. Phys. 46 (2013) 055304.

[66] R.K. Katiyara, P. Misraa, G. Morella, R.S. Katiyara, Effect of Poling on Photovoltaic Properties in Highly Oriented $BiFeO_3$ Thin Films, Integrated Ferroelectrics: An International Journal 157 (2014) 168-173.

[67] P.P. Biswas, Ch. Thirmal, S. Pal, M. Miryala, M. Murakami, P. Murugavel, The composition and poling-dependent photovoltaic studies in ferroelectric $(Bi_{1-x}Sr_x)(Fe_{1-x}Ti_x)O_3$ thin films, J. Mater. Sci.: Mater. Electron 31 (2020) 1515–1523.

[68] P.P. Biswas, S. Pal, V. Subramanian, P. Murugavel, Polarization driven self-biased and enhanced UV−visible photodetector characteristics of ferroelectric thin film, J. Phys. D: Appl. Phys. (2020) 53 275302.

[69] F. Shao, J.K. Chen, K.H. Chew, G.L. Zhao, Z.Y. Ren, P.F. Liu, Q. Liu, J. Teng, X.G. Xu, J. Miao, Y. Jiang, Activation energy mediated band structure in strained multiferroic $BiFeO_3$ thin films, Ceram. Int. 46 (2020) 6838–6846.

[70] V.R. Palkar, J.John, R. Pinto, Observation of saturated polarization and dielectric anomaly in magnetoelectric thin films, Appl. Phys. Lett. 80 (2002) 1628.

[71] S. Das, R.C. Sahoo, T.K. Nath, Investigation of room temperature multiferroic properties in sol-gel derived gadolinium, cobalt doped BiFeO3 nanoceramics, J. Appl. Phys. 127 (2020) 054101.

[72] H. Yang, C. Zhoub, X. Liu, Q. Zhoub, G. Chenb, W. Li, H.W Yang, Piezoelectric properties and temperature stabilities of Mn- and Cu-modified BiFeO3–BaTiO3 high temperature ceramics, J. Eur. Ceram. Soc. 33 (2013) 1177–1183.

[73] S.O. Leontsev, R.E. Eitel, Dielectric and Piezoelectric Properties in Mn-Modified (1-x) $BiFeO_3$–$xBaTiO_3$ Ceramics, J. Am. Ceram. Soc. 92 (2009) 2957–296.

[74] R. Zuo, C. Ye, X. Fang, Na0.5K0.5NbO3–BiFeO3 lead-free piezoelectric ceramics, J. Phys. Chem. Solids 69 (2008) 230–235.

[75] F. Kanga, L. Zhanga, B. Huangb, P. Maoa, Z. Wanga, Q. Suna, J. Wanga, D. Huc, Enhanced electromechanical properties of SrTiO3-BiFeO3-BaTiO3 ceramics via relaxor behavior and phase boundary design, J. Eur. Ceram. Soc. 40 (2020) 1198–1204.

[76] T. Zheng, J. Wu, Perovskite BiFeO3–BaTiO3 Ferroelectrics: Engineering Properties by Domain Evolution and Thermal Depolarization Modification, Adv. Electron. Mater. (2020) 2000079.

[77] J. Wang, C. Zhou, Q. Li, L. Yang, J. Xu, G. Chen, C. Yuan, G. Rao, Simultaneously enhanced piezoelectric properties and depolarization temperature in calcium doped $BiFeO_3$-BaTiO3 ceramics, J. Alloys Compd. 748 (2018) 758-765.

[78] K. Auromun, S. Hajra, R.N.P. Choudhary , B. Behera, Structural, dielectric and electrical characteristics of yttrium modified 0.7BiFeO$_3$-0.3PbTiO$_3$, Solid State Sci. 101 (2020) 106139.

[79] F. Akram, J. Kim, S.A. Khan, A. Zeb, H.G. Yeo, Y.S. Sung , T.K. Song, M.H. Kim, S. Lee, Less temperature-dependent high dielectric and energy-storage properties of eco-friendly BiFeO3eBaTiO3-based ceramics , J. Alloys Compd. 818 (2020) 152878

[80] R.A. Malika, A. Zaman, A. Hussain, A. Maqboold, T.K. Songa, W.J. Kime, Y.S. Sungf, M.Ho. Kima, Temperature invariant high dielectric properties over the range 200 °C–500 °C in BiFeO$_3$ based ceramics, J. Eur. Ceram. Soc. (2018) 2259–2263.

[81] C. Zhou, A. Feteira, X. Shan, H. Yang, Q. Zhou, J. Cheng, W. Li, H Wang, Remarkably high-temperature stable piezoelectric properties of Bi(Mg$_{0.5}$Ti$_{0.5}$)O$_3$ modified BiFeO$_3$–BaTiO$_3$, ceramics, Appl. Phys. Lett. 101 (2012) 032901.

[82] T. Yoshimura, S. Murakami, K. Wakazono, K. Kariya, N. Fujimura, Piezoelectric Vibrational Energy Harvester Using Lead-Free Ferroelectric BiFeO$_3$ Films, Appl. Phys. Express 6 (2013) 051501.

[83] M. Aramaki, T. Yoshimura, S. Murakami, K. Satoh, N. Fujimura, Demonstration of High-performance Piezoelectric MEMS Vibration Energy Harvester using BiFeO$_3$ Film with Improved Electromechanical Coupling Factor, Sens. Actuator A Phys. 291 (2019) 167-173.

[84] N. Wang, X. Luo, L. Han, Z. Zhang, R. Zhang, H. Olin, Y. Yang, Structure, Performance, and Application of BiFeO$_3$, Nano-Micro Lett. (2020) 12:81.

2. BiFeO₃ thin film on Silicon substrate

2.1. MOCVD of BiFeO₃ on IrO₂/Si

2.1.1. Introduction

Multiferroics are materials in which at least two of the three ferroic orders, ferroelectricity, ferromagnetism or antiferromagnetism, and ferroelasticity coexist. Among multiferroics, perovskite bismuth ferrite (BiFeO₃) and its derived systems are of special interest for keeping their properties in extreme temperature environments because of their Curie (T_C = 1103 K) and Neel temperatures (T_N = 643 K) well above room temperature [1,2]. In addition to ferroelectric and antiferromagnetic properties, BiFeO₃ nanostructures, combined with graphene, show appealing photocatalytic activity [3,4]. Photoelectric, pyroelectric, and piezoelectric properties are the most studied and appealing characteristics, which make BiFeO₃ an important material for energy harvesting applications [5]. The possibility of combining the above-mentioned properties in a single device, a hybrid energy harvester, makes BiFeO₃ one of the most promising materials for the next generation of lead-free harvesters. For piezoelectric harvester, $Pb(Zr_xTi_{1-x})O_3$ (PZT) has been commonly used [6,7], but the rising of environmental issues and questions on process sustainability has brought the light on lead-free perovskite-like systems , such as BiFeO₃, LiNbO₃ [8,9], and (K,Na)NbO₃ [10], because of their encouraging capabilities for hybrid energy harvesting [11–13].

Different deposition techniques have been used to obtain thin films of BiFeO₃, and their derived systems [14–16]. Most of the synthetic routes continue to rely on expensive single crystal substrates, such as SrTiO₃, SrTiO₃:Nb, and LaAlO₃ [17,18], but recently flexible or even bendable substrates are investigated [19].

The main deposition techniques that have been applied to the production of BiFeO₃ films are: chemical solution deposition [20,21], pulsed laser deposition (PLD) [22,23], sputtering [24], sol-gel [15,16], and Metal Organic Chemical Vapor Deposition (MOCVD) [25–28]. So far, only sol-gel and sputtering have been applied to deposit BiFeO₃ film used in a piezoelectric harvester [28,29], due to their simplicity and low operating temperature, which enable the use of a wide variety of substrates. The latest results for photovoltaic oriented devices have been obtained by PLD deposited films [23]. However, these techniques may have some drawbacks due to the substrate dimensions and difficulty in process scalability. MOCVD is a very appealing technique in terms of homogeneous and conformal deposition on large area substrates and easy possibility of scaling up, thus appointing itself as one of the best industrially applicable process.

This study aims to optimize a method for the fabrication of highly homogeneous BiFeO₃ (from now on BFO) thin films on Si (001) that were buffered with an IrO₂ layer, compatible with conventional industrial processes in order to create a functional hybrid energy harvester.

Moreover, special attention has been given to the impact of the different deposition parameters on the quality of the films that were grown on Si. Si-based substrates present many advantages, the first one is the important cost reduction when compared to the widely spread single crystals. Subsequently, when considering that Micro Electro-Mechanical systems (MEMs) microfabrication on Si implies well known protocols and techniques, keeping Si as base material for future functional structures is a key factor in lowering the cost and avoid the time-consuming process development for single crystals.

X-ray diffraction (XRD) has been used for structural characterization, field-emission scanning electron microscopy (FE-SEM) and energy dispersive X-ray analysis (EDX) have been used for the morphological and chemical analysis, respectively. Finally, local piezoresponse force spectroscopy (PFS) [30] and the domain mapping with piezoresponse force microscopy (PFM) have confirmed the piezoelectric/ferroelectric properties of the samples.

2.1.2.   Materials and methods

2.1.2.1.   Thin film Deposition

Bi(phenyl)$_3$ and Fe(tmhd)$_3$ (phenyl = $-C_6H_5$, H-tmhd = 2,2,6,6-tetramethyl-3,5-heptandione), were mixed and used as a multicomponent precursor mixture. Bi(phenyl)$_3$ and Fe(tmhd)$_3$ were purchased from Strem Chemicals Inc. (France) and used without any further purification. Thin film depositions were performed in a customized, horizontal, hot wall MOCVD reactor with a 20° inclined sample holder. The bi-metallic mixture was placed in an alumina boat and heated at 120 °C. Argon and oxygen were used, respectively, as carrier and reactant gasses, by varying their flow from 150 sccm to 900 sccm (standard cubic centimeter per minute) for both species. The depositions were carried out in the temperature range 600–800 °C for 60 min. BFO films were deposited on a 10 mm × 10 mm Si (001) substrate coated with a 200 nm film of IrO$_2$ acting, at the same time, as bottom electrode for piezoelectric characterization and as buffer layer between BFO and Si.

2.1.2.2.   Thin film Characterization

Analyses of crystalline phases were done through X-ray diffraction (XRD) measurements. θ–2θ XRD patterns were recorded in grazing incidence mode (0.8°) using a Smartlab diffractometer (Rigaku, Japan), which was equipped with a rotating anode of Cu Kα radiation operating at 45 kV and 200 mA. The morphologies were examined through field emission gun scanning electron microscopy (FE-SEM), using a SUPRA VP 55 microscope (ZEISS, Germany). The films were analyzed by energy dispersive X-ray (EDX) analysis using an INCA-Oxford windowless detector (Oxford Instruments, UK) with an electron beam energy of 15 keV. Film roughness and ferroelectric properties were measured on an Atomic Force Microscopy NT-MDT solver PRO with a conductive gold coated silicon cantilever, CSG10/Au, purchased from NT-MDT (NT-MDT, Russia). The BFO samples were grounded to the IrO$_2$ bottom electrode and a good contact was obtained with silver paint.

2.1.3.   Results and Discussion

2.1.3.1.   Metal Organic Chemical Vapor Deposition (MOCVD) Grown BiFeO₃ Films on IrO₂/Si Substrate

Starting deposition experiments, as presently reported, are based on earlier works performed on single crystals SrTiO₃ [26]. Good results were obtained in the temperature range 750–800 °C, with the best film quality and piezoelectric performance being obtained for the films that were deposited at 800 °C on SrTiO₃. Thus, preliminary depositions have been carried out at 750 °C and 800 °C with Ar and O₂ gas flows of 150 sccm for both species. Nevertheless, films that are deposited at 800 °C are not homogeneous and show delamination due to the effect of the high temperature on the IrO₂ bottom layer, which causes its corrugation. Films deposited at 750 °C on a 10 × 10 mm² IrO₂/Si substrate, while using a susceptor with an inclination of 20°, show good properties in term of homogeneity and adhesion. The susceptor inclination has no effect on adherence, but it might have some effect on the homogeneity of the film. The sample structure has been checked using XRD and patterns have been recorded in the range 20–60° (Figure 1a) and are in agreement with the ICDD data (Card No 20-0169) based on the rhombohedal structure, space group R3c, of the BFO phase.
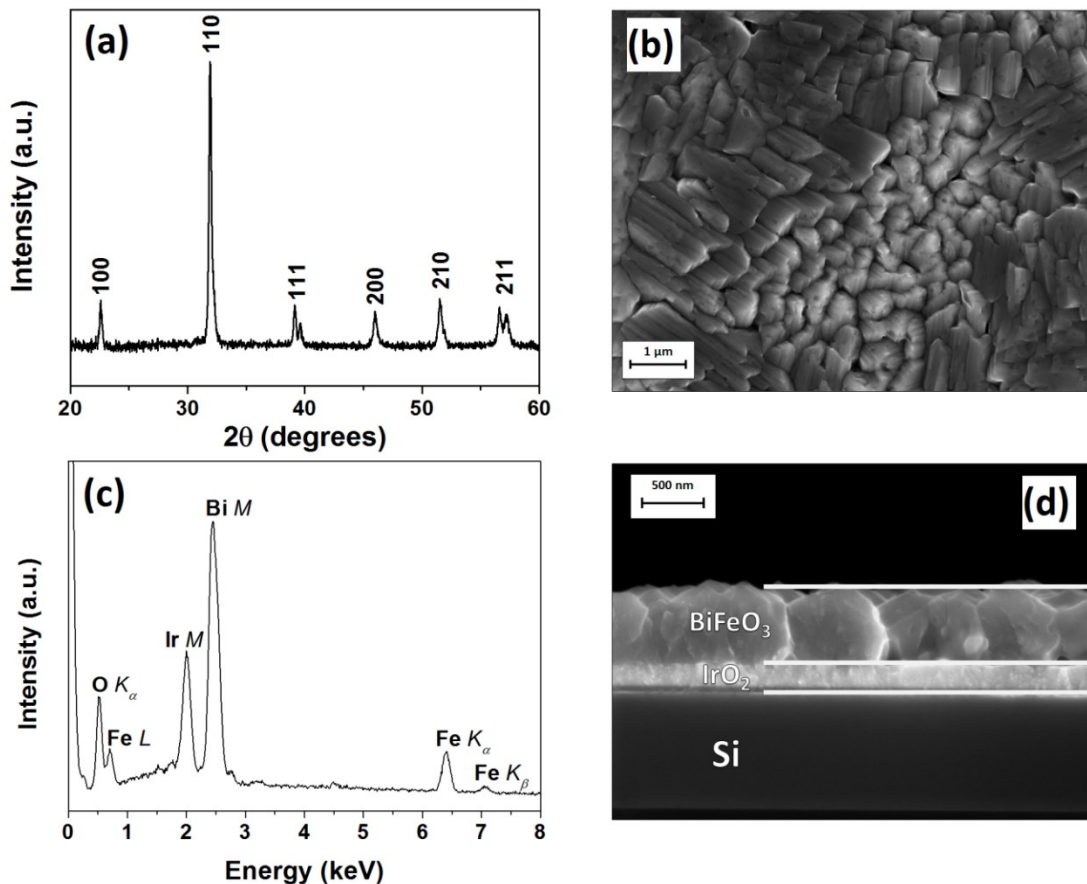

Figure 1 (a) X-ray diffraction (XRD) pattern, (b) field-emission scanning electron microscopy (FE-SEM) top view image, (c) energy dispersive X-ray analysis (EDX) analysis, and (d) FE-SEM cross section image of the BiFeO₃ thin film deposited on IrO₂/Si substrate

The main diffraction peaks are observed at 2θ = 22.60°, 31.90°, and 39.15°, which are associated, respectively, with the 100, 110, and 111 reflections of the BFO phase, considering a pseudocubic structure. $BiFeO_3$ might be considered pseudocubic, having the rhombohedral structure cell parameters of a_{rh} = 3.965 Å and α_{rh} = 89.4° [2]. Thus, the deposited thin films are polycrystalline and comparison of the peak intensities with the database values indicates a slight preferential orientation along the <110> direction.

FE-SEM has been used to monitor film morphology and, when coupled with energy dispersive X-ray analysis (EDX), to check chemical homogeneity and assess the elemental quantification in the films. The BFO films show a very uniform and dense morphology with massive and well coalesced grains. They adopt elongated shapes with two different preferential orientations (Figure 1b). EDX analysis shows chemical composition homogeneity on large sample areas. The sample average composition indicates a Bi:Fe ratio equal to 1 (Figure 1c). Film thickness has been also checked by several cross sections and shows an average value of 600 nm (Figure 1d). The IrO_2 layer of 200 nm is clearly identifiable between the MOCVD grown BFO film and Si substrate (Figure 1d).

2.1.3.2. Impact of Gas Flows on $BiFeO_3$ Film Growth

Basic deposition parameters produced good quality films in terms of structure and composition. Nevertheless, the impact of the gas flows (either carrier or reactant) on the film morphology and quality is one of the major steps to develop a fully optimized process. Starting from the initial parameters, deposition temperature = 750 °C, Flow(Ar) = 150 sccm, Flow(O_2) = 150 sccm, and duration 1h, the effect of the gas flow variation has been investigated by changing one gas flow (Ar or O_2) and maintaining constant all of the other parameters to understand the impact of each one of them on the final product. In Figure 2, the results of BFO films deposited with diverse Ar or O_2 flows are summarized based on the FE-SEM comparative images.
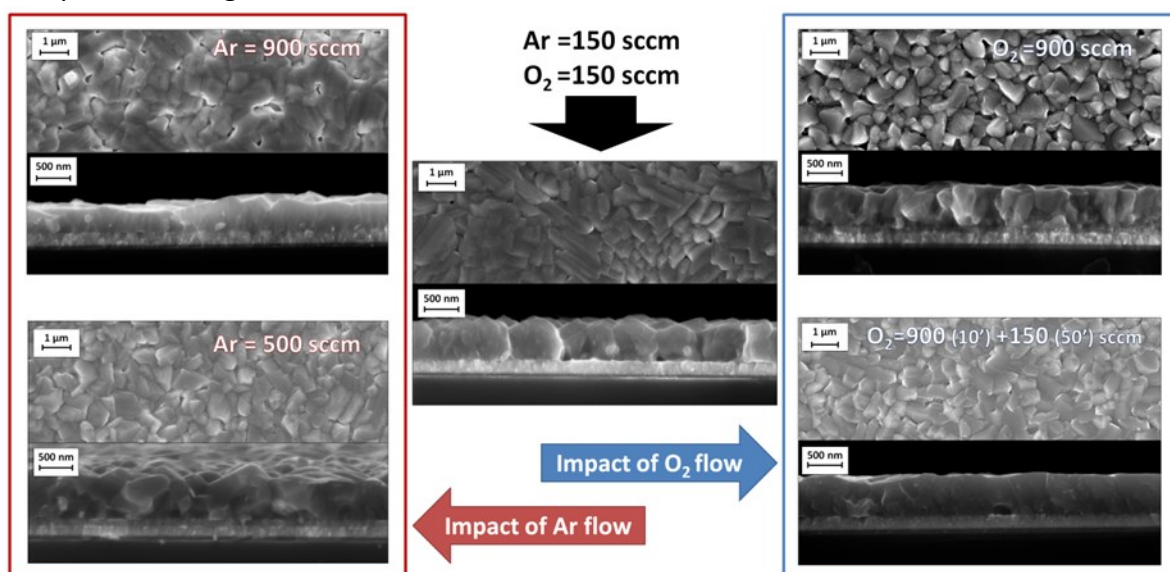

Figure 2. Comparison of $BiFeO_3$ (BFO) thin films deposited under different conditions. BFO reference sample is in the center, on the left the impact of the argon flow and on the right the impact of the oxygen flow on BFO are presented.

The morphologies of films deposited with 500 sccm or 900 sccm Ar flows, keeping all the other parameters constant, are reported on the left side of Figure 2. The FE-SEM plan-view images show homogeneous samples with grains of 700–800 nm. The cross-section images show that the deposition at 500 sccm does not present major changes in terms of density and thickness with respect to the 150 sccm Ar deposited film. On the other hand, at 900 sccm, the cross section of the film indicates an important increase of film density, but the main drawback is that the film growth rate is significantly decreased when compared to our reference experimental conditions. The average growth rates drop from 9 nm/min to 4 nm/min. This variation might be related to a dilution effect, since the carrier flow increase determines the precursor dilution. The coupled influence of the carrier flow increase and precursor dilution is responsible for the lower growth rate and, consequently, for the formation of thinner but denser films at the highest carrier flow (900 sccm).

When considering previous results with argon, a significant flow of oxygen, 900 sccm, has firstly been tested. BFO growth rate is not limited by the high O_2 flow and, at the same time, film top-view and cross section show a denser film composed of grains of about 800–850 nm (Figure 2, right side). According to these first observations, and to the promising impact that the high oxygen flow has on the film quality, a deposition experiment has been tailored while using a first step of 10 min. with Flow (O_2) = 900 sccm followed by a second one of 50 min. with Flow (O_2) = 150 sccm. The first step enables the creation of a seed layer with smaller nucleation sites, the second allows for these nuclei to grow, giving rise to coalesced grains forming a dense and homogeneous film. FE-SEM analysis (Figure 2, right side) confirms this observation, the grain size is smaller, and cross section shows an important diminution of the roughness and extremely dense BFO film. As expected, the growth rate is unchanged when compared to the reference sample. Thus, a visible improvement of the film quality is observed by simply varying the oxygen flow during the deposition of the film and, at the same time, the process remains straightforward without adding extra steps.

2.1.3.3. Impact of the Temperature on BiFeO$_3$ Film

Attempts to tune the sample orientation by changing deposition temperature have been done in the 600–800 °C temperature range with an Ar flow of 150 sccm and an O_2 flow of 900 sccm for 10 min. and 150 sccm for 50 min. Depositions that were performed at 600 °C lead to a deterioration of film quality and homogeneity. FE-SEM image shows flat iron rich islands on the BFO film surface. Moreover, material quality and density are also heavily impacted by the low temperature process, coalescence is incomplete, and cracks are visible. At 800 °C, the IrO_2 layer is no longer stable and it starts to interact with the film. The buffer layer corrugates in several points, forming bumps on the surface and leading to the delamination of the $Si/IrO_2/BFO$ structure. Defects that are caused by extreme conditions make the samples realized outside of the temperature range 650–750 °C, difficult to be analyzed and compared to previous results. Within this ideal 100 °C deposition range, XRD patterns, as reported in Figure 3a–c, indicate that polycrystalline single phase BFO films are deposited.

When comparing the various sample patterns, it has been observed that a preferential orientation competition takes place between the (100) and (110) planes, but no complete orientation is observed, whatever the deposition parameters. The cross-section images (Figure 3d–f) of the films deposited in this temperature range show similar thicknesses, thus pointing to similar growth rates. Specifically, growth rates have been evaluated every 50 °C between 600 °C and 750 °C, yielding growth rates of 7, 10, 11, and 10 nm/min., respectively, for 600, 650, 700, and 750 °C.
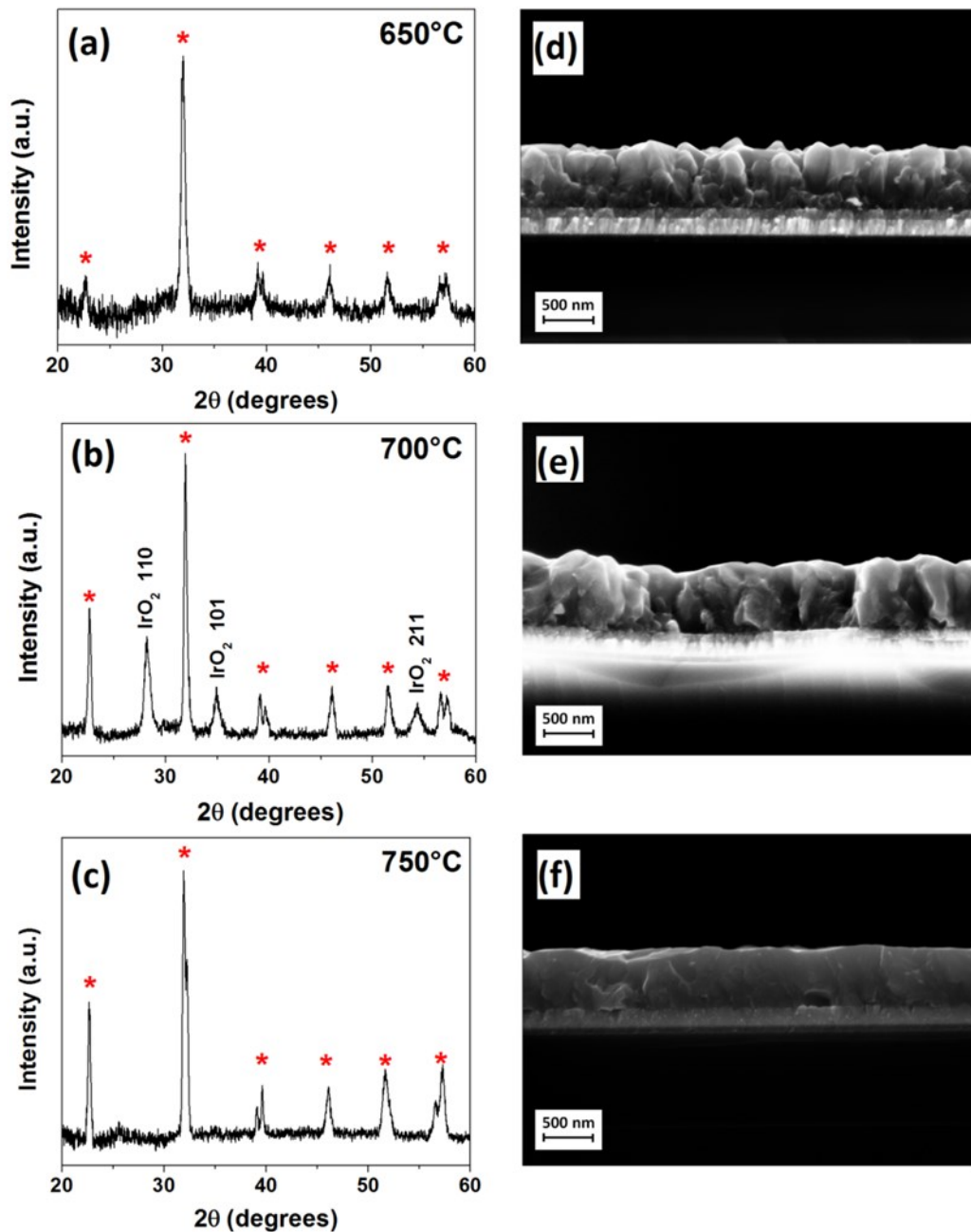

Figure 3. XRD diffraction patterns and FE-SEM cross section images of BFO thin films deposited at (a,d) 650 °C, (b,e) 700 °C, and (c,f) 750 °C.

This independence between film thickness and substrate temperature in the 600–750 °C range seems to point to a mass transport regime. Figure 4 represents the plot of the ln growth rate vs. 1000/T. The apparent activation energy of 22 kJ/mol, as derived from the Arrhenius plot, clearly indicates that, in the used deposition temperature range, BFO film growth occurs in the mass transport-limited regime.
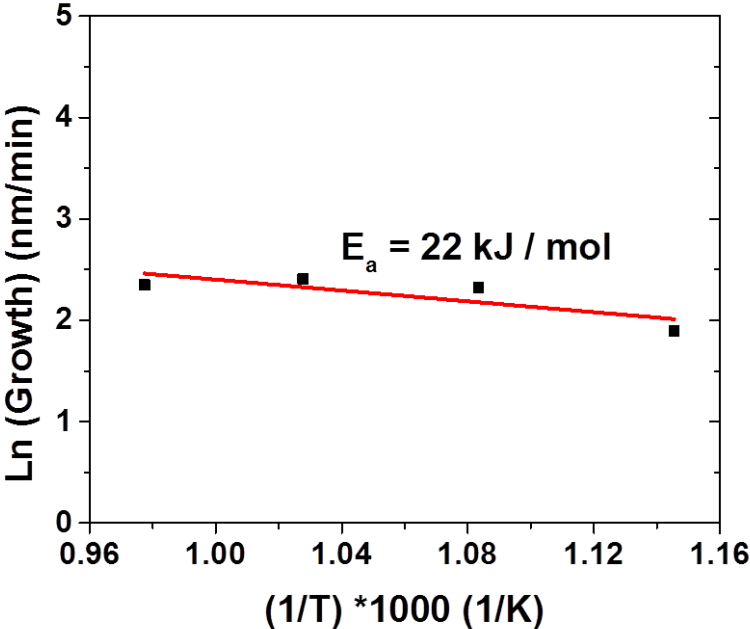
Figure 4. Arrhenius plot of the ln growth rate vs. 1000/T for the BiFeO$_3$ MOCVD process starting from the Bi(phenyl)$_3$ and Fe(tmhd)$_3$ precursors.

2.1.3.4. Functional Properties

BFO thin film topography on the IrO$_2$ buffer layer has been recorded by a classical contact mode vertical atomic force microscopy (AFM) scan (Figure 5a). The 5 µm × 5 µm investigated area exhibits the same morphology as the one that was observed by FE-SEM (Figure 1) with a root mean square (RMS) roughness of 28.6 nm.

Figure 5. (a) Atomic force microscopy (AFM) scan of a 5 µm × 5 µm area and (b) butterfly loop (the "black" curve corresponds to the −9V to +9V scan and "red" curve corresponds to the +9V to −9V) of the "as deposited" BFO thin film on Si obtained by PFS.

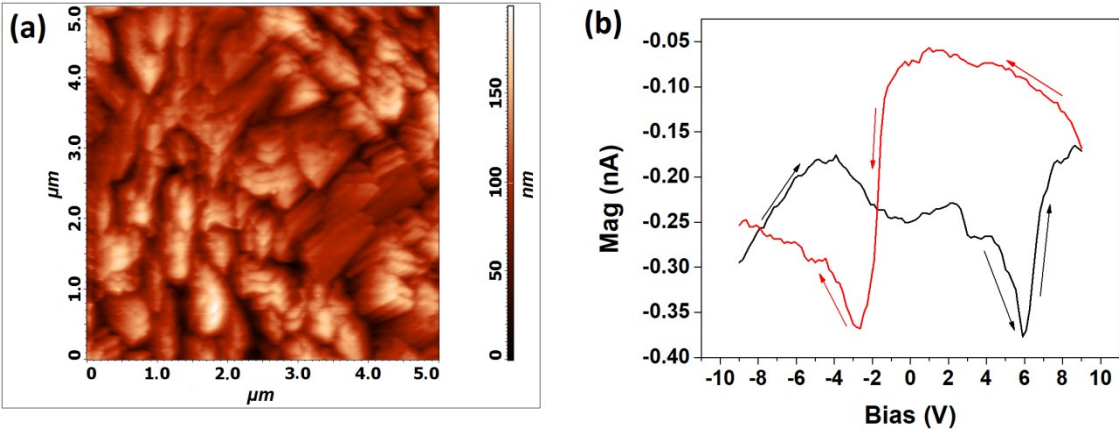The piezoelectric property of the deposited film on the IrO_2/Si substrate has been investigated through piezoresponse force spectroscopy (PFS). Piezoresponse (in terms of the amplitude of the out of plane displacement, Mag), as a function of the alternating voltage, showed the typical butterfly loop [30,31] for an applied bias from −9 V to 9 V between microscope cantilever tip and BFO bottom electrode IrO_2 (Figure 5b), indicating the piezoelectric behavior of the film.

In Figure 5b the unit for the Mag is nA, because the instrument measures the vertical displacement from the photocurrent of the laser beam reflected by the displaced tip. In particular, the tip displacement is proportional to the difference between the photocurrent incident on different photodiode sections. Figure 5b shows a hysteresis loop, since, after applying a −9V bias and then reducing the bias until 0V (black curve), the piezoresponce is different from that observed when applying a +9V bias and then reducing it to 0V (red curve).

Following this first observation, a study of ferroelectric domain switching [32] has been carried out on a 2.5 μm × 2.5 μm area. Figure 6a reports the AFM topography of the scanned area. At first, a PFM image of the ferroelectric domain of the "as-deposited" BFO film was obtained in terms of phase difference between the vertical piezoresponse signal and an applied alternating voltage, before the application of any bias voltage (Figure 6b). Subsequently, to observe the switching of the domains, a bias voltage of −9V was applied to the entire area through the scanning tip and map of the ferroelectric domains was recorded with a 0 V bias voltage (Figure 6c). Subsequently, a similar PFM image was obtained at 0V (Figure 6d), after the application of a +9V bias. The polycrystalline nature of the film might limit phase scan interpretation and, indeed, the measured signal is the average of all the ferroelectric domains that were placed between the cantilever tip and the bottom electrode. Very few differences between domain phases of the "as prepared" BFO film and the film after application of the −9 V bias are visible (Figure 6c). On the other hand, the impact of the application of +9 V bias on the film polarization was much more important (Figure 6d), indicating the switching of several ferroelectric domains. As an example, the material has a visible response after bias voltage application because of domains switching when comparing the circled zones on Figure 6b–d.
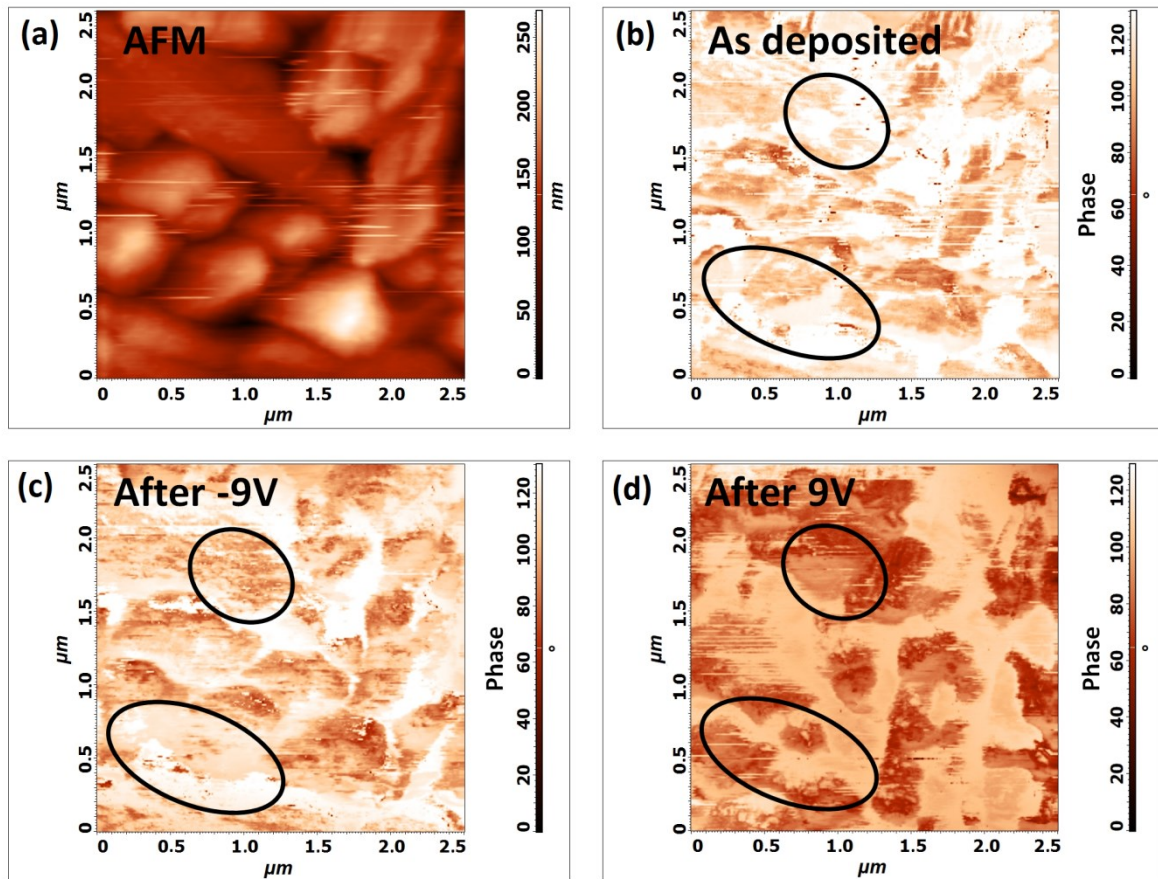
Figure 6. Ferroelectric domains switching: (a) AFM image of the scanned 2.5 μm × 2.5 μm area and (b) phase scan of the "as deposited" BFO film; (c) phase scan of the BFO film after the application of a −9 V bias; and (d) phase scan of the BFO film after the application of a 9 V bias.

PFS and PFM confirmed the piezoelectric properties of the as deposited BFO film. Furthermore, even if sample polycrystallinity might limit ferroelectric mapping, domains switching can be observed by reducing the working area, thus confirming the functional properties of the BFO thin film on Si.

2.1.4.   Conclusion

In conclusion, BFO films have been successfully deposited by MOCVD on silicon substrate, with an IrO_2 bottom electrode, acting as a buffer layer since it can stand high temperatures. The morphology, density, thickness, and Bi:Fe ratio in the films are homogenous on the whole sample surface of 10 mm × 10 mm. The BFO thin films show different growth orientations, but no specific relationship has been found between orientation and experimental conditions. Various experiments indicate that the optimal deposition temperature range is between 650 °C and 750 °C with a fixed argon flow of 150 sccm and the use of high oxygen flow, 900 sccm for 10 min., in order to induce the formation of numerous BFO nucleation sites, and 150 sccm for 50 min. to trigger the growth of a denser film with smaller grains when compared to the other investigated conditions.

Thus, the BFO films can be successfully deposited on Si at a lower temperature and in a more cost-effective process, with respect to the previously reported methodologies. Moreover, the present approach offers the major advantage to be easily scalable and the use of IrO_2, as a conductive oxide, gives the opportunity for future characterizations and device microfabrications. Finally, it can be pointed out that the material quality and production cost of lead-free perovskites, as BFO, are key points for the scaling-up development of a new generation of hybrid energy harvesting devices. The MOCVD approach, as presently reported, answers to both demands and it is compatible with the current technologies.

2.2. MOCVD of LaNiO$_3$ bottom electrodes

Interest for the technology transfer of MOCVD BFO growth process from academic research to industry is extremely high. An MOCVD process for the deposition of polycrystalline perovskite BFO films has been successfully developed and optimized to some extent. Films complexity and polycrystalline nature can be the source defects in the material and may finally impact device efficiency. Working on the nature of a more suited bottom electrode, which may also act as a buffer layer, is a direct way to improve film general quality. For the deposition of BFO thin film, LaNiO$_3$ (LNO) is a candidate of choice to act as a buffer layer. Using LNO as bottom electrode in the fabrication of ferroelectric device is very attractive due to its conductive property, of special interest for functional characterization. In addition, LNO has a perovskite structure, and thus it shows a good lattice match with respect to BFO [33][34]. In particular, LNO displays a trigonal structure which can be seen as a hexagonal cell of parameters: a=5.457 Å, c =13.146 Å and γ=120°, or can be described as a rhombohedral cell with parameters of a=3.8375 Å and α=90.64°. Rhombohedral LaNiO$_3$ can be approximated as a pseudo-cubic system: a=3.859 [35][36][37]. LNO cell parameter corresponds well to many other perovskite materials such as SrTiO$_3$ (STO), LaAlO$_3$ (LAO), BaTiO$_3$ (BTO), Pb(Zr,Ti)O$_3$ (PZT) and of course BFO. LNO epitaxial growth on oriented cubic or pseudo cubic single crystal substrates is well established [38][39][40]. Stabilizing the LNO phase on single crystal is a first step but investigating its stability on Si is of higher interest due to the incomparable opportunity this system would offer for process scale-up.

Compared to other nickelates, the biggest interest of LNO is due to its unique property, as a perovskite, to present a metallic conductivity in a wide temperature range, from 1 to 1000 K, with no metal to insulator transition (MIT). The other nickelates obtained with lanthanide elements possessed a MIT temperature which increases as the lanthanide (Ln^{3+}) dimension decreases [41][42].

Several examples already report deposition of LNO by MOCVD using similar precursors combination:

- La(tmhd)$_3$, Ni(tmhd)$_2$ [43-45]
- La(tmhd)$_3$, Ni(acim)$_2$ or Ni(tmhd)$_2$ [46]

Arrhenius plots of the film growth rate function of the temperature and function of the deposition regime have been reported for atmospheric pressure CVD and pulsed injection CVD. Also, it is worth noting that the relation between La:Ni ratio in the film and in the precursors mixture is strongly influenced by the deposition technique [45]. Optimization of the deposition process is also challenging because of the many factors which can disturb the formation of the desired phase.

The existence of many phases $La_{n+1}Ni_nO_{3n+1}$ and the decrease of their stability in the following order: La_2NiO_4 (n=1) > $La_3Ni_2O_7$ (n=2) > $La_4Ni_3O_{10}$ (n=3) > $LaNiO_3$ (n=∞) is a major obstacle for the growth of the desired phase. Phase with n≥ 4 are unstable [42] [47].

2.2.1.   Methods

In this research activity, the study, has been devoted to the deposition of LNO and its use as a buffer layer for the growth of BFO on Si (001) and $SrTiO_3$ (100) substrates.

A simple synthetic MOCVD approach has been adopted, the versatility of the method facilitated the work on multiple precursor systems to define the most promising precursor mixture. Depositions have been carried out in the same MOCVD hot wall reactor used for the deposition of BFO thin film systems. Substrates were heated up to 750°C and maintained on a 20° susceptor to optimize gas flow on the substrate. Argon and oxygen have been used, respectively, as carrier and reactant, with a similar flow rate of 150mL/min. MOCVD workflow consisted in a single step deposition using 3 different precursors mixture:

- La(hfa)$_3$·diglyme (hfa= 1,1,1,5,5,5-exafluoro-2,4-pentanedione; diglyme = bis(2-methoxyethyl) ether and Ni(acac)$_2$ (acac= acetylacetonate), vaporized at 120°C
- La(hfa)$_3$ ·diglyme and Ni(hfa)$_2$·diglyme, vaporized at 115°C
- La(hfa)$_3$·diglyme and Ni(tta)$_2$·TMEDA (tta= 4,4,4-Trifluoro-1-(2-thienyl)-1,3-butanedione) (TMEDA= N,N,N',N'-tetramethylethylenediaminee), vaporized at 130°C

The individual thermal behavior of the single precursors was investigated by thermogravimetric analysis (TGA), samples weight was 5-10 mg, and the analyses were made under nitrogen. In order to compensate the high fluorine content in the precursors, O$_2$ gas flow have been saturated with water, (through a bubbler), to make it reacting with the fluorine, to be eliminated as HF gas. Films have been deposited at 750°C and their morphologies have been studied by FE-SEM and their chemical composition controlled by EDX. Finally, films' deposited phases have been checked by XRD.

2.2.2. Thermal properties of the precursors and MOCVD growth

The thermal behavior of the individual precursors has been investigated through TG analysis at atmospheric pressure and under a flow of nitrogen. All studied precursors showed a TGA with a single step indicating an evaporation of the precursor without decompositions. The TG curves of the La(hfa)$_3$·diglyme, Ni(hfa)$_2$·Diglyme and Ni(tta)$_2$ ·TMEDA have very low residues, between 0% to 2% of the initial weight. Ni(hfa)$_2$·Diglyme and Ni(tta)$_2$ ·TMEDA are showing vaporization in a temperature range significantly lower or higher, respectively, of the La(hfa)$_3$·diglyme one. Despite having an important 20% of residue, Ni(acac)$_2$ has a suited thermal behavior, with a complete vaporization in the 250-275°C temperature range, similar to La(hfa)$_3$·diglyme behaviour (Figure 7).

Knowing the precursor general thermal behavior, the mixtures containing Ni(acac)$_2$ and Ni(hfa)$_2$·diglyme have been heated up to 120°C and 115°C respectively in the reactor sublimation zone and the mixture Ni(tta)$_2$·TMEDA have been used at 130°C.
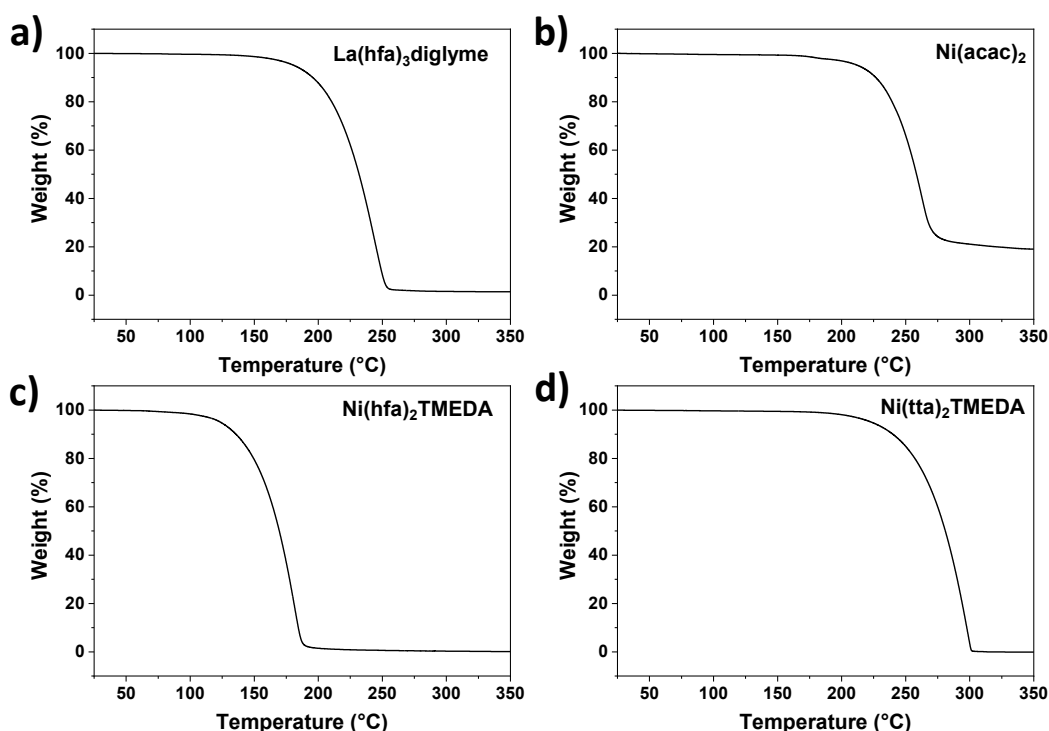

Figure 7. TGA curves of the used precursors a) La(hfa)$_3$·diglyme, b) Ni(acac)$_2$, c) Ni(hfa)$_2$ ·diglyme and d) Ni(tta)$_2$·TMEDA

2.2.3. Morphological and structural characterization

Sample morphology have been observed through FE-SEM and reported in Figure 8. Depositions performed on silicon show dense polycrystalline films for all the precursors mixture, with the best density obtained using Ni(acac)$_2$ showing well coalesced grains (Figure 8 a and c). Ni(tta)$_2$·TMEDA seems to give films with higher roughness with some visible round agglomerations of grains (Figure 8b). On STO, general films homogeneity improves, with the formation of cubic grains using Ni(acac)$_2$ and Ni(hfa)$_2$·diglyme (Figure 8d and f). As it is expected using a single crystal substrate, films obtained using Ni(tta)$_2$·TMEDA present a smoother surface even though being clearly polycrystalline (Figure 8e).
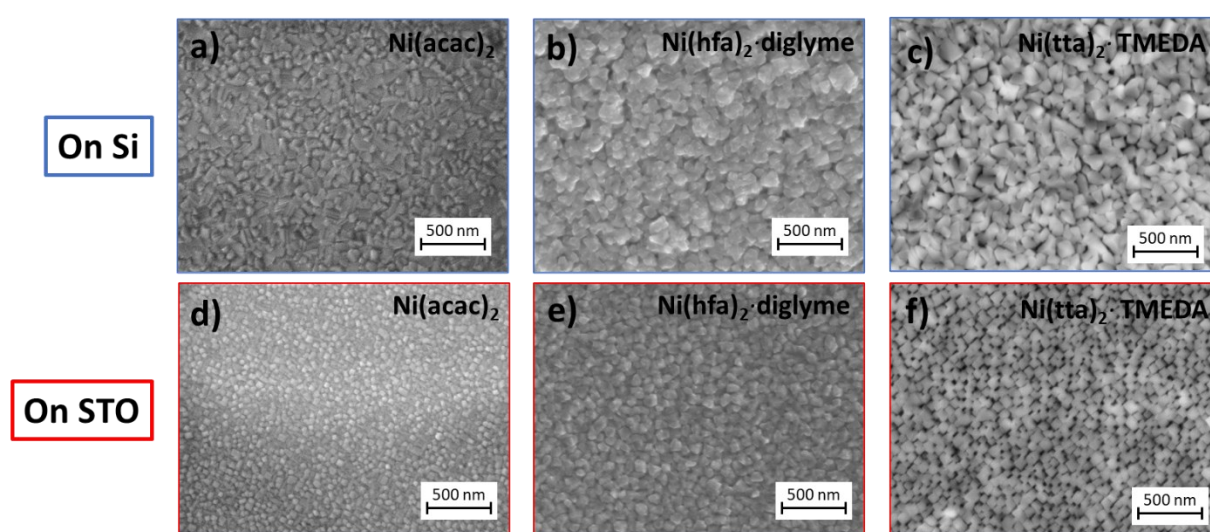
Figure 8. FE-SEM images of the thin films deposited on Si (001) with La(hfa)$_3$·diglyme and, a) Ni(acac)$_2$ or b) Ni(hfa)$_2$·diglyme or c) Ni(tta)$_2$·TMEDA and deposited on STO (001) with with La(hfa)$_3$·diglyme and, d) Ni(acac)$_2$ or e) Ni(hfa)$_2$·diglyme or f) Ni(tta)$_2$·TMEDA

Modifications in La:Ni ratio in the initial precursors' mixture do not have a noticeable impact on the film morphology. EDX analysis shows that the La:Ni precursor ratio directly influence the La:Ni films ratio but important variations in the films ratio have been noted for identic process parameters and for all the used precursors. Finally, important fluorine amount is present in the film indicating the formation of at least one fluoride phase. The attempts made to reduce fluoride phases content by post process annealing at 700°C under 150ml/min oxygen flow saturated in water did not have noticeable impact on film chemical composition.

XRD study of the deposited films with the different precursors mix shows that Si and STO substrates influence only the preferential orientation of the different film phases, but not their nature. For each precursor mixture, it has been decided to report the pattern which give the best understanding of the deposited phases (Figure 9).

Following the EDX analysis, all the precursors mix lead to the deposition of a significant amount of the LaOF despite the use of a water bubbler. The most promising films have been

obtained using Ni(acac)$_2$. In this case the most stable La-Ni-O phase, the La$_2$NiO$_4$ forms as a major component and only minor LaOF and NiO parasitic phases are present (Figure 9a). Regardless of the initial precursors ratio or process conditions, mixtures containing
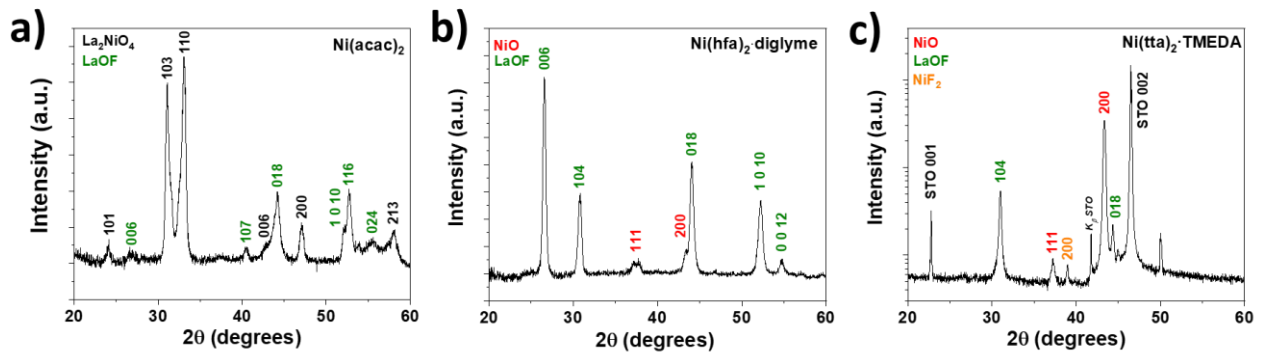
Figure 9. XRD pattern recorded in grazing incidence (0.8°) of the thin films deposited on Si (001) with La(hfa)$_3$·diglyme and, a) Ni(acac)2 or b) Ni(hfa)$_2$·diglyme. XRD pattern recorded in Bragg-Brentano configuration of films deposited on SrTiO3 (001) with La(hfa)$_3$·diglyme and c) Ni(tta)$_2$·TMEDA

Ni(hfa)$_2$·diglyme or Ni(tta)$_2$·TMEDA led only to the formation of LaOF, NiO and NiF$_2$ phases (Figure 9b and c).

2.2.4.   Conclusion

This preliminary study for LaNiO$_3$ deposition by MOCVD process highlighted the difficulty to stabilize a pure LaNiO$_3$ phase. The major critical point encountered is the presence of LaOF phase in the samples, indicating its significant stability compared to the others. Attempts to reduce its formation did not show a significant effect. Compared to the other mixtures, the precursors mix of La(hfa)$_3$·diglyme and Ni(acac)$_2$ showed the most promising results in term of phase formation with the stabilization of La$_2$NiO$_4$.

Obtaining a LaNiO$_3$ phase is a great challenge, one of the reasons is the stability of the Ni^{3+} ion which decrease at high temperatures and in environment with low oxygen partial pressure. The most stable Ni^{2+} oxidation state directly impacts the deposition of NiO and the La$_{n+1}$Ni$_n$O$_{3n+1}$ stoichiometry, favoring formation of the La$_2$NiO$_4$ phase [48].

More recent studies have shown that the partial substitution of the Ni by other transition elements as Fe or Mn can have a positive effect on stabilization of the LaNiO$_3$ phase [49] [50].

Future optimization route of this process should focus on several points:

- Reduction of the LaOF phase
- Tuning of the process parameters for the La(hfa)$_3$·diglyme and Ni(acac)$_2$ mixture
  - Lower deposition temperature
  - Richer oxygen environment
  - Other precursor ratios
- Doping LaNiO$_3$ B-site with transition metals

2.3.   Microfabrication on BiFeO₃ cantilevers

During the secondment periods done in Prof. Paul Muralt's Lab at EPFL and in Prof. Ausrine Bartasyte's Lab at UFC/Femto-ST, simple microfabrication of cantilevers of BiFeO₃(poly)/IrO₂/Si has been attempted. To understand the critical points for the fabrication of vibrational harvester's particular attention has to be placed both on the films' growth and on the preparation of the cantilevers.

2.3.1.   Work realized in EPFL

Au top electrodes with a Cr layer to improve the adhesion have been deposited by sputtering through a hard mask. The electrodes design has been done to respect the standard setup used at the EPFL (*Ecole Polytechnique Fédérale de Lausanne*). Deposited electrodes may be used to perform classic Polarization-Voltage and Capacitance-Voltage loop and, by clamping the sample at one extremity, to apply an AC voltage to measure its displacement and so to obtain the direct $e_{31,f}$ piezoelectric coefficient of the studied cantilever (Figure 10a and b) [51].
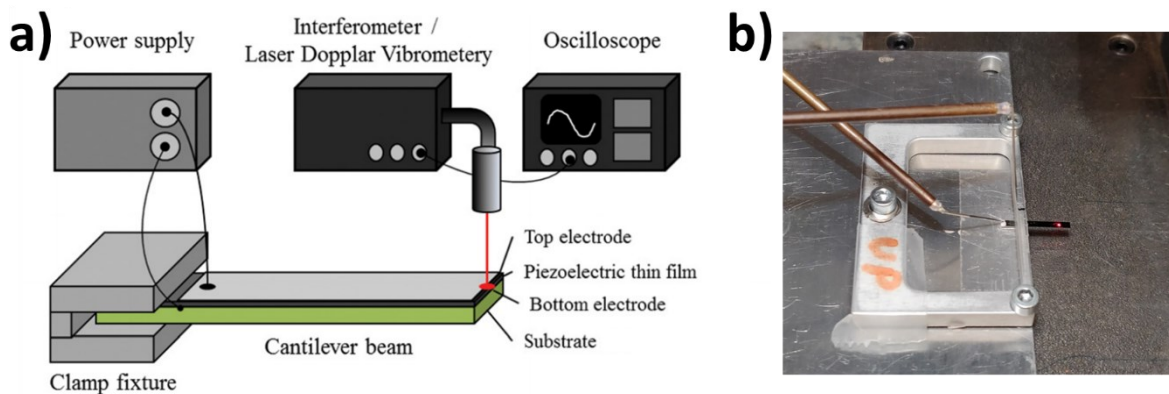
Figure 10. a) Scheme to measure the e_{31f} piezoelectric coefficient [52] b) BFO/IrO₂/Si samples campled in the EPFL Set-up

The first group of samples, deposited at the University of Catania, was made to study the impact of process conditions on film piezoelectric behavior. All samples have been deposited for one hour but at different Ar and O₂ flows. Impact on the growth rate, film density, and quality have been investigated in the previous part (Chapter 1.3). The electrode pattern reported in Figure 11a. was deposited as 200 nm thick Cr/Au gold film on the sample surface. Then, the samples have been glued by UV tape (Figure 11b), and after their alignment in the machine, the cantilevers have been separated by the dicing of the substrate so they can be clamped for individual piezoelectric measurements. After being exposed to UV, UV tape allows an easy beam separation (Figure 11c). The last step consisted of reaching the IrO₂ bottom electrode, the film surface was gently scratched with a diamond tip and silver paste is added to ensure good contact. (Figure 11d). Initial sample sizes were 2 cm x 1.2cm and the final samples are 1.5 mm x 9 mm.
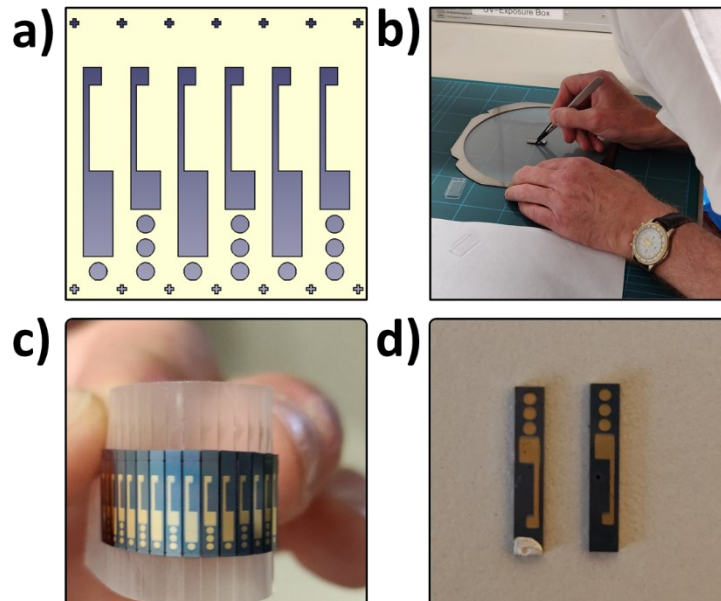
Figure 11. Preparation steps of the BFO/IrO₂/Si beams with a) electrodes design, b) samples position on UV tape for dicing, c) diced cantilever and d) samples freed from the UV tape.

The sample preparation steps have been carried out with care. However, short circuits in the cantilevers have been quickly noted, leading to a complete failure of the prepared cantilever, independently of the process condition used for BFO film deposition.

FE-SEM sample investigation gave some hints on the critical problems we have encountered when using the films for microfabrication. As seen before, the deposited films are pure polycrystalline BFO, but a close investigation of the surface revealed the presence of 100-200 nm wide pinholes (Figure 12a). Cross-sections (Figure 12b) showed a significant film thickness variation on large samples with, in some cases, a film thickness close to the one of the top electrodes. The coupling of those two major defects favored the contact between the top and the bottom electrode. The presence of a short circuit in a device hampers its functional characterization.
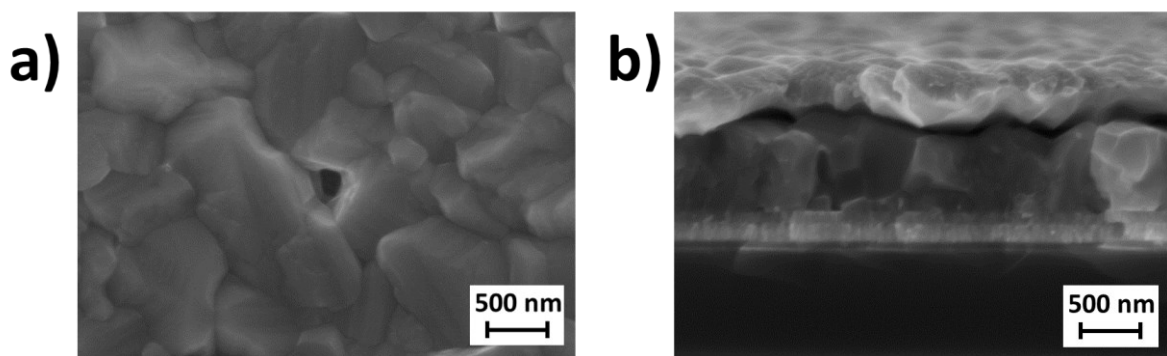
Figure 12. FE-SEM image of a BFO/IrO₂/Si sample, which shows potential causes of short circuit: a) pinhole visible in the plan view and b) cross section of the Au/Cr/BFO/IrO₂/Si stack.

2.3.2. Work realized in UFC/Femto-ST

Considering the first feedback of the microfabrication steps, new attempts to improve the process and to reduce the causes of failure have been made—the first modification concerned deposition duration, which have been increased to obtain thicker films. It is worth noting that for a longer deposition time, at 750°C, the substrate thermal stability is even more critical. The following substrates IrO_2/Si, IrO_2/SiO_2/Si and IrO_2/TiN/Si, present good thermal stability. On the other hand, on IrO_2/Pt/Si and IrO_2/Ir/Si substrates, the Pt or Ir metallic layer films show a tendency to agglomerate when left at high temperature for more than one hour. This does not impact the nature of the deposited BFO films, but it compromises its structural integrity, leading to important cracks and delamination (Figure 13a).
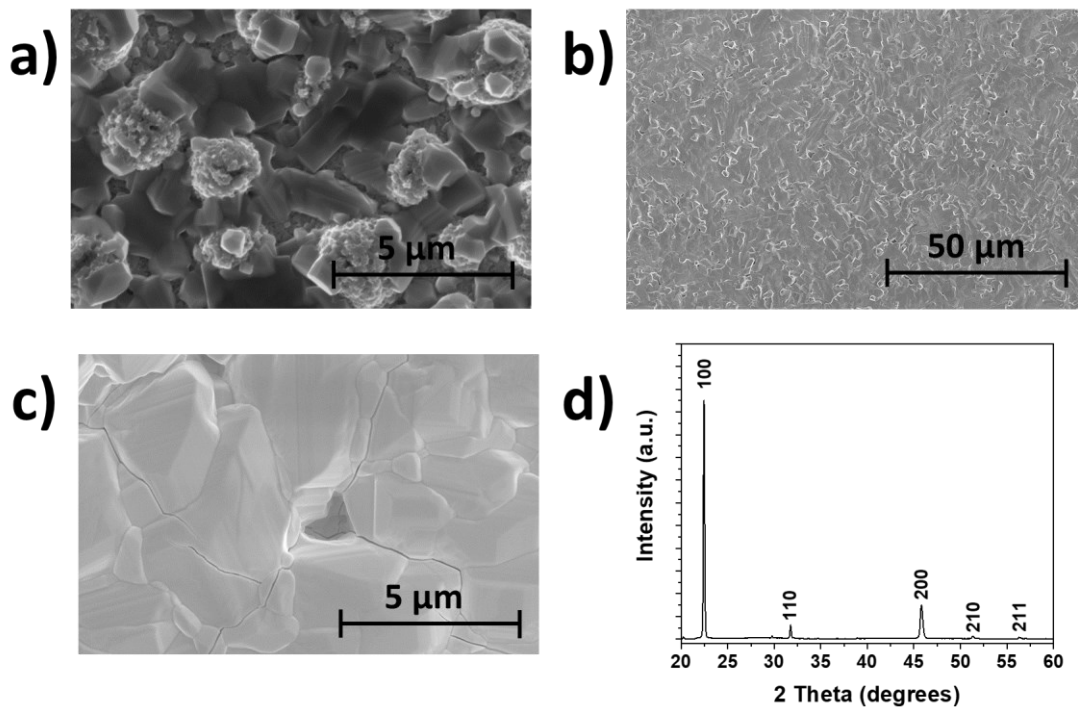
Figure 13. FE-SEM images of a) BFO deposited on an unstable substrate; b) low magnification of a new sample prepared for microfabrication; c) closer investigation for defects with no sign of contacts to the bottom electrode and d) XRD pattern of the new textured BFO film.

As seen during the first trials, one of the problems for microfabrication is the thickness difference on large samples with at some point uncovered bottom electrode. Considering the substrate position in the reactor, the further the sample is from the precursor sublimation zone, the thinner the deposited film will be. As a final attempt, to improve the thickness homogeneity of the samples (2 cm x 1.5 cm), films have been deposited in a two-step process, each step consisting of a 2-hour deposition, with a rotation of 180° between the 2 steps. The deposited films show a high density, large grain sizes and a significant increase in film thickness between 900 nm and 1.2 µm. Small superficial cracks are still visible, but a closer FE-SEM investigation does not indicate that the few visible defects are directly linked to the bottom

electrode (Figure 13b and c). BFO films deposited on IrO$_2$/Si substrate with the previously reported route are polycrystalline and up to 500 nm thick films, no preferential orientation is clearly visible. However, with the two-step thicker films have been obtained and preferential orientation growth along the [001]$_{pc}$ is clearly visible, as shown in Figure 13d.

Cr/Au electrodes have been sputtered on the film, the part where the electrode was not necessary for the beam clamping, were protected by high-temperature tape. Sample edges have been cut and cantilevers freed by dicing of the silicon substrates. Prior to dicing, samples have been coated in resin to help to maintain sample structural integrity during the cutting process (Figure 14.b).
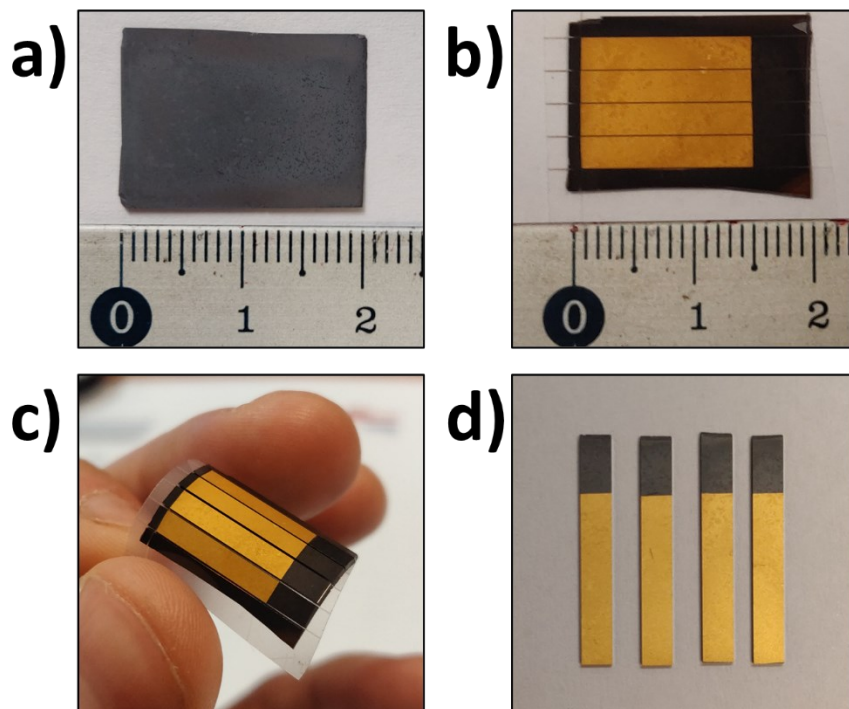
Figure 14. Preparation steps of the new BFO cantilever on Si samples: a) 2 cm x 1.5 cm as deposited samples; b) Cr/Au top electode sputtering and resin coating (redish coloration), c) and d) liberation of the BFO cantilever

Unfortunately, despite all the extra care devoted to the film deposition and the cantilever preparation, the Au/BFO/IrO$_2$ structure does not behave like a metal/insulator/metal structure, but more like a small resistor. Conductivity measurements indicate a film resistivity of 40 Ω. Such a small value can be explained in different ways: direct short circuit caused by contact between the bottom and the top electrode or important leakage material. BiFeO$_3$ films are known for their important leakage current that can cause device failure [53]. Oxygen vacancies in the material can be the main cause of high leakage currents. Some post-process procedures have been investigated to reduce them [54]. The most common one is rapid thermal annealing (RTA) under air or oxygen atmosphere.

One sample has been processed under air and the other under oxygen atmosphere as those two conditions seem to offer the best results in reducing sample conductivity [55] [56]. Before sputtering top electrodes, samples have been heated at 700°C for one minute and the first part of the cool-down process has been carefully controlled to avoid too much thermal stress in the sample and film delamination (Figure 15).
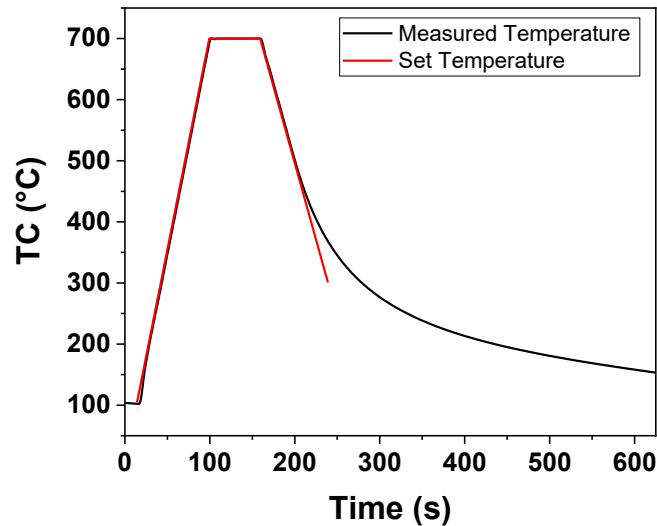
Figure 15. Temperature profile followed for the RTA of the BFO on Si samples under atmosphere or oxygen. Black curve reports the temperature measured by the thermocouple while red one is the value set in the software.

Less leakage current is expected and so a reduced conductivity. However, both RTA treatments did not have a noticeable effect on the conductivity of the samples compared to the untreated one. This important conductivity makes ferroelectric, piezoelectric and characterization for vibrational energy harvester impossible.

Future improvements of the process are needed to reach a functional BFO vibrational energy harvester. Film general quality can always be pushed forward and the tendency to have $[001]_{pc}$ growth orientation for BFO on IrO_2 is a promising route for the development of highly textured BFO film on Si-based substrates. Finally, as leakage current is always a source of failure in BFO films, working with doped BFO films to reduce leakage impact would be interesting. In addition, even if the reduction of oxygen vacancies by post-process RTA did not show significant results, performing deposition in a richer oxygen environment may contribute to reducing at least partially the quantity of oxygen vacancies.

References

[1] Choi, T.; Lee, S.; Choi, Y.J.; Kiryukhin, V.; Cheong, S.-W. Switchable ferroelectric diode and photovoltaic effect in $BiFeO_3$. *Science* **2009**, *324*, 63-66. doi:10.1126/science.1168636.

[2] Catalan, G.; Scott, J.F. Physics and Applications of Bismuth Ferrite. *Adv. Mater.* **2009**, *21*, 2463-2485. doi:10.1002/adma.200802849.

[3] Irfan, S.; Liang, G.; Li, F.; Chen, Y.; Rizwan, S.; Jin, J.; Zheng, Z.; Ping, F., Effect of graphene oxide nano-sheets on structural, morphological and photocatalytic activity of $BiFeO_3$-based nanostructures, *Nanomaterials* **2019**, *9*, 1337/1-1337/15. DOI:10.3390/nano9091337.

[4] Li, J.; Wang, Y.; Ling, H.; Qiu, Y.; Lou, J.; Hou, X.; Bag, S. P.; Wang, J.; Wu, H.; Chai, G., Significant enhancement of the visible light photocatalytic properties in 3D $BiFeO_3$/graphene composites, *Nanomaterials* **2019**, *9*, 65/1-65/12. DOI:10.3390/nano9010065.

[5] Queraltó, A.; Frohnhoven, R.; Mathur, S.; Gómez, A. Intrinsic piezoelectric characterization of $BiFeO_3$ nanofibers and itsimplications for energy harvesting, *Appl. Surf. Sci.* **2020**, *509*, 144760/1-144760/8. doi:10.1016/j.apsusc.2019.144760.

[6] Hwang, G.T.; Annapureddy, V.; Han, J.H.; Joe, D.J.; Baek, C.; Park, D.Y.; Kim, D.H.; Park, J.H.; Jeong, C.K.; Park, K-I.; Choi, J.J; Kim, D.K.; Ryu, J.; Lee, K.J. Self-Powered Wireless Sensor Node Enabled by an Aerosol-Deposited PZT Flexible Energy Harvester. *Adv. Energy Mater.* **2016**, *6*, 1600237/1-1600237/9. doi:10.1002/aenm.201600237.

[7] Muralt, P.; Polcawich, R. G.; Trolier-McKinstry, S. Piezoelectric thin films for sensors, actuators, and energy harvesting *MRS Bulletin* **2009**, *34*, 658-664. doi.org/10.1557/mrs2009.177.

[8] Bartasyte, A.; Margueron, S.; Baron, T.; Oliveri, S.; Boulet, P. Toward High-Quality Epitaxial $LiNbO_3$ and $LiTaO_3$ Thin Films for Acoustic and Optical Applications. *Adv. Mater. Interfaces* **2017**, *4*, 1600998/1-1600998/36. doi:10.1002/admi.201600998.

[9] Almirall, A.; Oliveri, S.; Daniau, W.; Margueron, S.; Baron, T.; Boulet, P.; Ballandras, S.; Chamaly S.; Bartasyte, A. High-frequency surface acoustic wave devices based on epitaxial Z-$LiNbO_3$ layers on sapphire. *Appl. Phys. Lett.* **2019**, *114*, 162905/1-162905/5. doi:10.1063/1.5086757.

[10] Tkach, A.; Santos, A.; Zlotnik, S.; Serrazina, R.; Okhay, O.; Bdikin, I.; Costa, M.E.; Vilarinho, P.M. Effect of Solution Conditions on the Properties of Sol–Gel Derived Potassium Sodium Niobate Thin Films on Platinized Sapphire Substrates. *Nanomaterials* **2019**, *9*, 1600/1-1600/14. doi.org/10.3390/nano9111600.

[11] Vats, G.; Chauhan, A.;Vaish, R. Thermal Energy Harvesting Using Bulk Lead-Free Ferroelectric Ceramics. *Int. J. Appl. Ceram. Technol.* **2015**, *12*, E49-E54. doi:10.1111/ijac.12214.

[12] Kumar, A.; Sharma, A.; Kumar, R.; Vaish, R.; Chauhan, V.S. Finite element analysis of vibration energy harvesting using lead-free piezoelectric materials: A comparative study. *J. Asian Ceram. Soc.* **2014**, *2:2*, 139-143. doi:10.1016/j.jascer.2014.02.001.

[13] Vidal, J.V.; Turutin, A.V.; Kubasov, I.V.; Kislyuk, A.M.; Malinkovich, M.D.; Parkhomenko, Y.N.; Kobeleva, S.P.; Pakhomov, O.V.; Sobolev, N.A.; Kholkin, A.L. Low-Frequency Vibration Energy Harvesting With Bidomain $LiNbO_3$ Single Crystals. *IEEE T Ultrason. Ferr.*, **2019**, *66*, 1480-1487. doi:10.1109/TUFFC.2019.2908396

[14] Zhang, Y.; Wang, Y.; Qi, J.; Tian, Y.; Sun, M.; Zhang, J.; Hu, T.; Wei, M.; Liu, Y.; Yang, J. Enhanced Magnetic Properties of $BiFeO_3$ Thin Films by Doping: Analysis of Structure and Morphology. *Nanomaterials* **2018**, *8*, 711/1-711/13. doi:10.3390/nano8090711.

[15] Hou, P.; Liu, B.; Guo, Z.; Zhou, P.; Wang, B.; Zhao L. Effect of Ho doping on the crystal structure, surface morphology and magnetic property of $BiFeO_3$ thin films prepared via the sol-gel technology. *J. Alloys Comp.* **2019**, *775*, 59-62. doi:10.1016/j.jallcom.2018.10.112.

[16] Sheoran, N.; Kumar, A.; Kumar, V.; Banerjee A. Structural, Optical, and Multiferroic Properties of Yttrium (Y^{3+})-Substituted $BiFeO_3$ Nanostructures. *J. Supercond. Nov. Magn.* **2020**. doi:10.1007/s10948-019-05411-2.

[17] Scillato, D; Licciardello, N.; , Catalano, M. R.; Condorelli, G.G., Lo Nigro, R.; Malandrino, G. $BiFeO_3$ Films Doped in the A or B Sites: Effects on the Structural and Morphological Properties *J. Nanosci. Nanotechnol.* **2011**, 11, 8221-8225. doi:10.1166/jnn.2011.5048.

[18] Zhang, Q.; Huang, H.H.; Sando, D.; Summers, M.; Munroe, P.; Standard, O.; Valanoor, N. Mixed-phase bismuth ferrite thin films by chemical solution deposition. *J. Mater. Chem. C* **2018**, *6*, 2882-2888. doi:10.1039/C7TC05841A.

[19] Qian, J.; Wang, Y.; Liu, R.; Xie, X.; Yan, X.; Leng, J.; Yang C. Bendable $Bi(Fe_{0.95}Mn_{0.05})O_3$ ferroelectric film directly on aluminum substrate, *J. Alloys Comp.* **2020**, *827*, 154381/1-154381/6. doi:10.1016/j.jallcom.2020.154381.

[20] Xu, H.-M.; Wang, H.; Shi, J.; Lin, Y.; Nan, C. Photoelectrochemical Performance Observed in Mn-Doped $BiFeO_3$ Heterostructured Thin Films. *Nanomaterials* **2016**, *6*, 215/1-215/9. doi:10.3390/nano9111600.

[21] Xuemei, C.; Guangda, H.; Jing, Y.; Xi, W.; Changhong, Y.; Weibing, W. Enhanced multiferroic properties of (1 1 0)-oriented $BiFeO_3$ film deposited on $Bi_{3.5}Nd_{0.5}Ti_3O_{12}$-buffered indium tin oxide/Si substrate. *J. Physics D: Appl. Phys.* **2008**, *41*, 225402/1- 225402/5. doi:10.1088/0022-3727/41/22/225402.

[22] Tian, G.; Ojha, S.; Ning, S.; Gao, X.; Ross, C.A. Structure, Ferroelectricity, and Magnetism in Self-Assembled $BiFeO_3$–$CoFe_2O_4$ Nanocomposites on (110)-$LaAlO_3$ Substrates. *Adv. Electron. Mater.* **2019**, *5*, 1900012/1- 1900012/8. doi:10.1002/aelm.201900012.

[23] Zhou, Y.; Wang, C.; Tian, S.; Yao, X.; Ge, C.; Guo, E.J.; He, M.; Yang, G.; Jin, K. Switchable ferroelectric diode and photovoltaic effects in polycrystalline $BiFeO_3$ thin films grown on transparent substrates. *Thin Solid Films* **2020**, *698*, 137851/1-137851/6. doi:10.1016/j.tsf.2020.137851.

[24] Zhu, H.; Zhao, Y.; Wang, Y. Orientation dependent leakage current behaviors and ferroelectric polarizations of off-axis sputtered $BiFeO_3$ thin films. *J. Alloys Comp.* **2019**, *803*, 942-949. doi:10.1016/j.jallcom.2019.06.343.

[25] Catalano, M. R.; Spedalotto, G.; Condorelli, G. G.; Malandrino G. MOCVD Growth of Perovskite Multiferroic $BiFeO_3$ Films: The Effect of Doping at the A and/or B Sites on the Structural, Morphological and Ferroelectric Properties. *Adv. Mater Interfaces* **2017**, 1601025/1-1601025/7. doi:10.1002/admi.201601025.

[26] Condorelli, G. G.; Catalano, M. R.; Smecca, E.; Lo Nigro, R.; Malandrino, G. Piezoelectric domains in $BiFeO_3$ films grown via MOCVD: Structure/property relationship, *Surf. Coat. Technol.* **2013**, *230*, 168-173. doi:10.1016/j.surfcoat.2013.06.081

[27] Deepak, N.; Carolan, P.; Keeney, L.; Zhang, P. F.; Pemble, M. E.; Whatmore, R. W. Bismuth Self-Limiting Growth of Ultrathin $BiFeO_3$ Films, *Chem. Mater*. **2015**, *27*, 6508-6515.doi:10.1021/acs.chemmater.5b03034

[28] T. Yoshimura, ; Murakami, S.; Wakazono, K.; Kariya, K.; Fujimura, N. Piezoelectric Vibrational Energy Harvester Using Lead-Free Ferroelectric $BiFeO_3$ Films. *Appl. Phys. Express* **2013**, *6*, 051501. doi:10.7567/APEX.6.051501.

[29] Aramaki M.; Yoshimura, T.; Murakami, S.; Satoh, K.; Fujimura N. Demonstration of high-performance piezoelectric MEMS vibration energy harvester using $BiFeO_3$ film with improved electromechanical coupling factor. *Sensors Actuat. A-Phys.* **2019**, *291*, 167–173. doi:10.1016/j.sna.2019.03.050.

[30] Wu, S.; Zhang, J.; Liu, X.; Lv, S.; Gao, R.; Cai, W.; Wang, F.; Fu, C. Micro-Area Ferroelectric, Piezoelectric and Conductive Properties of Single $BiFeO_3$ Nanowire by Scanning Probe Microscopy. *Nanomaterials* **2019**, *9*, 190/1-190/9. doi:10.3390/nano9020190.

[31] C. Tudisco, C.; Pellegrino, A.L.; Malandrino, G.; Condorelli, G. G. Surface anchoring of bi-functional organic linkers on piezoelectric $BiFeO_3$ films and particles: Comparison between carboxylic and phosphonic tethering groups, *Surf. Coat. Technol*. **2018**, *343*, 75–82. doi.org/10.1016/j.surfcoat.2017.11.014.

[32] Iwanowska, M.; Stolichnov, I.; Colla, E.; Tagantsev, A.; Muralt, P.; Setter, N. Polarization Reversal in BiFeO3 Capacitors: Complex Behavior Revealed by PFM, *Ferroelectrics* **2011**, *421*, 54. doi: 10.1080/00150193.2011.594326

[33] H. Han, J. Zhong, S. Kotru, P. Padmini, X. Y. Song, and R. K. Pandey. Improved ferroelectric property of $LaNiO_3/Pb(Zr_{0.2}Ti_{0.8})O_3/LaNiO_3$ capacitors prepared by chemical solution deposition on platinized silicon. Appl. Phys. Lett. (2006)

[34] Xin Li, Jiwei Zhai, and Haydn Chen. $(Pb,La)(Zr,Sn,Ti)O_3$ antiferroelectric thin films grown on $LaNiO_3$-buffered and Pt-buffered silicon substrates by sol-gel processing. J. Appl. Phys. (2005)

[35] H. Guo, Z. W. Li, L. Zhao, Z. Hu, C. F. Chang, C. Y. Kuo, W. Schmidt, A. Piovano, T. W. Pi, O. Sobolev, D. I. Khomskii, L. H. Tjeng, and A. C. Komarek. Antiferromagnetic correlations in the metallic strongly correlated transition metal oxide $LaNiO_3$. Nat. Commun. (2018)

[36] J. L. García-Muñoz, J. Rodríguez-Carvajal, P. Lacorre, and J. B. Torrance. Neutrondiffraction study of $RNiO_3$ (R=La,Pr,Nd,Sm): Electronically induced structural changes across the metal-insulator transition. Phys. Rev. B (1992)

[37] Junjie Zhang, Hong Zheng, Yang Ren, and J. F. Mitchell. High-Pressure Floating-Zone Growth of Perovskite Nickelate $LaNiO_3$ Single Crystals. Cryst. Growth Des. (2017)

[38] K. Tsubouchi, I. Ohkubo, H. Kumigashira, Y. Matsumoto, T. Ohnishi, M. Lippmaa, H. Koinuma, M. Oshima, Epitaxial growth and surface metallic nature of $LaNiO_3$ thin films, App. Phy. Lett. 92 (2008) 262109

[39] N. Wakiya, T. Azuma, K. Shinozaki, N. Mizutani, Low-temperature epitaxial growth of conductive LaNiO thin films by RF magnetron sputtering, Thin Solid Films 410 (2002) 114–120

[40] T. Yu, Y.F. Chen, Z.G. Liu, X.Y. Chen, L. Sun, N.B. Ming, L.J. Shi, Epitaxial growth of conductive $LaNi0_3$ thin films by pulsed laser ablation, Materials Letters 26 (1996) 73-76

[41] J. Chen, H. Hu, J. Wang, T. Yajima, B. Ge, X. Ke, H. Dong, Y. Jiang, N. Chen, Overcoming synthetic metastabilities and revealing metal-to-insulator transition & thermistor bi-functionalities for d-band correlation perovskite nickelates, Mater. Horiz 4 (2019)

[42] D.H. Kuo, C.Y. Chou, Y.K. Kuo, Phase Stabilization of a LaNiO3 Perovskite and the Electric Resistivity of its A/B-Site Substituted, Ni-Deficient $La(Ni_{0.6}Fe_{0.3})O_3$ Modifiers Int. J. Appl. Ceram. Technol. 7 [2] (2010) 217–225

[43] M.Burriel, G. Garcia, M.D. Rossell, A. Figueras, G. Van Tendeloo, J. Santiso, Enhanced High-Temperature Electronic Transport Properties in Nanostructured Epitaxial Thin Films of the $La_{n+1}NinO_{3n+1}$ Ruddlesden-Popper Series (n = 1, 2, 3, inf), Chem. Mater. 19 (2007)

[44] N. Chaban, M. Weber, S. Pignard, and J. Kreisel. Phonon Raman scattering of perovskite $LaNiO_3$ thin films, Appl. Phys. Lett. 97 (2010)

[45] S. Kuprenaite, V. Astié, S. Margueron, C. Millon, J.M. Decams, Z. Saltyte, P. Boulet, V.Plausinaitiene, A. Abrutis, A. Bartasyte, Relationship Processing–Composition–Structure– Resistivity of $LaNiO_3$ Thin Films Grown by Chemical Vapor Deposition Methods, Coatings 9 (2019) 35

[46] O.Yu Gorbenko, A.A. Bosak, Growth of $LaNiO_3$ thin films on MgO by flash MOCVD, J. Cryst. Growth, 186 (1998)

[47] M. Zinkevich and F. Aldinger, 'Thermodynamic Analysis of the Ternary La– Ni–O System, J. Alloy Compd., 375 (2004) 147–161

[48] J. S. Choi, M. Sheeraz, J.S. Bae, J. H. Lee, J. Lee, J. Lee, S. Lee, H. Jeen, Y. S.Oh, C. W. Ahn, T. H. Kim, Effect of Ceramic-Target Crystallinity on Metal-to-Insulator Transition of Epitaxial Rare-Earth Nickelate Films Grown by Pulsed Laser Deposition, ACS Appl. Electron. Mater. 1 (2019) 1952–1958

[49] Y. Luo, X. Wang, Q. Qian, Q. Chen, Studies on B sites in Fe-doped $LaNiO_3$ perovskite for SCR of NOx with H_2, Int. J. Hydrog. Energy 39 (2014) 28 15836-15843

[50] E. P. Komarala, I. Komissarov, B. A. Rosen, Effect of Fe and Mn Substitution in LaNiO$_3$ on Exsolution, Activity, and Stability for Methane Dry Reforming, Catalysts 10 (2020) 2

[51] A. Mazzalai, D. Balma, N. Chidambaram, R. Matloub, P. Muralt, Characterization and Fatigue of the Converse Piezoelectric Effect in PZT Films for MEMS Applications, J. Microelectromech. Syst. 24 (2015) 4.

[52] D.M. Chun, M. Sato, I. Kanno, Precise measurement of the transverse piezoelectric coefficient for thin films on anisotropic substrate, J. Appl. Phys 113 (2013) 044111.

[53] G. Catalan, J.F. Scott, Physics and Applications of Bismuth Ferrite, Adv. Mater. 21 (2009) 2463–2485.

[54] M.D. Casper, M.D. Losego, J.P. Maria, Optimizing phase and microstructure of chemical solution-deposited bismuth ferrite (BiFeO$_3$) thin films to reduce DC leakage, J Mater Sci 48 (2013) 1578–1584.

[55] L. Haimin, Q. Chunli, Z. Jianguo, H. Mingzhe, Y. Qingsong, Effect of Different Annealing Atmosphere on Ferroelectric Properties of 0.7BiFeO$_3$-0.3PbTiO$_3$ Thin Films, Rare Metal Materials and Engineering 45 2016 1449-1454.

[56] V.R. Singh, A. Dixit, S. Garg, D.C Agrawal, Effect of heat treatment on the structure and properties of chemical solution processed multiferroic BiFeO$_3$ thin films, Appl. Phys. A 90 (2008) 197–202.

3. Lanthanide doping at A-site of BiFeO₃ films: optimization of the synthetic procedure and functional properties

3.1.   Pyroelectric Dy-doped BiFeO₃

Multiferroics are multifunctional oxides with fundamental physical properties that are very promising for potential applications in several fields: transducers, energy harvesting, sensors, spintronics [1]. $BiFeO_3$ (BFO) and its related systems, with their high ferroelectric and magnetic transition temperatures (T_C = 1103 K and T_N = 643 K) [2], are of special interest, as they maintain their ferroelectric, piezoelectric and pyroelectric properties even in an extreme temperature environment.

The development of BFO based energy harvesters has been mostly investigated for exploiting their photoelectric and piezoelectric properties [3,4]. Instead, power generation employing the pyroelectric effect has been more rarely studied, and, in particular, previous works based on BFO thin films are limited to pure BFO, La-doped BFO, or $BFO/Pb(Zr_xTi_{1-x})O_3$ bi-layers [5]. Pyroelectricity originates from a change of an internal polarization of the material, particularly of the spontaneous ferroelectric polarization, upon a temperature change [6]. Pyroelectricity is thus of special interest for thermal energy harvesting, meaning the transformation of heat fluctuations into electricity. It is of interest in systems with temperature variations with time, and it differs from the thermoelectric effect needing a thermal gradient, and thus a spatial temperature difference [7,8]. As leading materials for energy harvesting, $Pb(Zr_xTi_{1-x})O_3$ (PZT) and $(1-x)[Pb(Mg_{1/3}Nb_{2/3})O_3]-x[PbTiO_3]$ (PMN-PT) have been widely incorporated and combined with lead-free materials to tune their piezoelectric and pyroelectric properties [9-13], but today the use of lead-based materials raises environmental issues, which are always at the center of our attention. The answer is the development and integration of lead-free perovskite-like materials, such as $BiFeO_3$, $LiNbO_3$ [14-16], or $(K,Na)NbO_3$ [17], in energy harvesters [18-20]. The possibility of combining at least two of the previous properties in a single device, a hybrid energy harvester, makes BFO one of the most promising materials for the next generation of energy harvesters and, recently, some BFO-based energy harvesting devices have already been studied [21-24]. In general, the pyroelectric properties of ceramics and single crystals have been intensively studied compared to thin films. Films present several advantages: with their smaller heat capacity, they are subjected to a larger temperature change upon a given heat input and are suitable for integration into microsystems [25]. Fine-tuned depositions can give high-quality materials and some deposition techniques offer good process scalability [7, 26]. Among the above mentioned lead-free materials, BFO presents an intrinsic polarization of 60 $\mu C/cm^2$ and 100 $\mu C/cm^2$ along the $[001]_{pc}$ and $[111]_{pc}$ directions,

respectively [1, 27], (pc stands for the pseudocubic unit cell), which makes it a perfect candidate to investigate its pyroelectric response.

Moreover, pyroelectricity is strongly influenced by material preparation conditions, and a fine-tuning of BFO thin film properties can be achieved in many ways. Numerous approaches have been reported: strained films [28, 29], modified synthesis parameters [30, 31], synthesis of BFO nanocomposites [32,33], but, by far, the easiest and most used approach is the ionic substitution, which is achieved by doping BFO films with transition metals and/or rare-earth elements [34-37]. Doing so, BFO structure and properties can be widely modified, adapting and designing the material to different situations/use/working conditions, and recent works have been focused on BFO A-site doping. BFO systems have been deposited on various substrates using pulsed laser deposition (PLD) [38,39], metal-organic chemical vapor deposition (MOCVD) [40-43], sputtering [44], sol-gel [45, 46] and chemical solution deposition [38, 47].

In this study, we report on the giant pyroelectric properties of pure BFO and Dy-doped BFO (BDFO) films deposited, through a simple, easily scalable MOCVD approach, on Nb-doped SrTiO$_3$ (STO:Nb) (001) single crystal substrates. Bi(phenyl)$_3$, Fe(tmhd)$_3$ and Dy(hfa)$_3$diglyme (phenyl= -C$_6$H$_5$; H-tmhd=2,2,6,6-tetramethyl-3,5-heptandione; H-hfa= 1,1,1,5,5,5-hexafluoro-2,4-pentanedione; diglyme= bis(2-methoxyethyl) ether) are used as precursors, mixed in a tri-component source. The high-quality epitaxial growth of BDFO on STO:Nb is confirmed through X-ray diffraction (XRD) and Raman spectroscopy, while field emission scanning electron microscopy (FE-SEM) allowed to assess the flat, homogeneous surfaces of deposited films. The effect of Dy-doping, whose amount has been evaluated by means of X-ray photoelectron spectroscopy (XPS) and energy dispersive X-ray analysis (EDX), on ferroelectric, dielectric and pyroelectric properties of BDFO thin films has been investigated. Materials bandgap have been evaluated by UV-Vis spectroscopy and Atomic force microspy (AFM) coupled with piezoresponse force microscopy (PFM) have been used to investigate the samples piezoelectric response. Permittivity and loss tangent have been determined using impedance–capacitance–resistance (LCR) measurements. The correlation between Dy-doping and the pyroelectric response of BDFO thin films has been established by applying an oscillating temperature ramp on the samples. A clear-cut trend has been observed with the best dielectric and pyroelectric properties found for an intermediate Dy doping.

3.1.1.   Experimental details

Films depositions were carried out in a customized, horizontal, hot-wall MOCVD reactor. Bi(phenyl)$_3$ and Fe(tmhd)$_3$ precursors were purchased from Strem Chemicals Inc. and used without further purification, while the Dy(hfa)$_3$•diglyme was synthesized in our lab following the protocol reported in ref. [48]. A tri-metallic mixture of the mentioned precursors was placed in an alumina boat and heated at 120 °C. Oxygen and argon were used, respectively, as reactant and carrier gases; their flows were kept constant for the whole

deposition at 150 sccm (standard cubic centimeter per minute) for both species. The depositions were carried out in the temperature range 750 °C to 800 °C for 60 min. BFO films were deposited on a 5 mm x 10 mm STO:Nb (100) substrate acting at the same time as the bottom electrode for ferroelectric and functional characterization [40].

XRD patterns were recorded using a Rigaku Smartlab diffractometer, equipped with a rotating anode of Cu K_α radiation operating at 45 kV and 200 mA. Bragg-Brentano patterns were acquired with a resolution step of 0.02°. Film surface morphology was examined by field emission scanning electron microscopy (FE-SEM) using a ZEISS VP 55 microscope. Films atomic composition was analyzed by energy dispersive X-ray analysis (EDX), using an INCA Oxford windowless detector with an electron beam energy of 15 keV and a resolution of 127 eV for the Mn K_α. X-ray photoelectron spectra (XPS) were measured at 45° takeoff angle, relative to the surface plane, with a PHI 5600 Multi Technique System (base pressure of the main chamber 3 x 10^{-10} Torr). The spectra were excited with the Al-Kα radiation. XPS peak intensities were obtained after a Shirley background removal. Spectra calibration was achieved by fixing the "adventitious" C 1s peak at 285.0 eV.

Before any functional characterization, 150 nm thick Cr/Au top electrodes (3.84 mm^2) were sputtered on the samples through a hard mask. Dielectric properties were investigated through capacitance and loss measurements with an impedance–capacitance–resistance (LCR) meter (Model HP 4284A, Hewlett–Packard, Tokyo, Japan) at 500 mV at room temperature. Several points were taken at three frequencies: 100 Hz, 1 kHz, and 10 kHz. Films PE negative half loops have been measured at a constant frequency of 5 kHz to limit the impact of leakage currents [49]. Measurement are the results of 20 average loops under an applied field from -200 to 0 kV/cm. BDFO pyroelectric coefficients were measured following a classic dynamic method. An oscillating triangular signal has been used to control a Peltier element for applying temperature changes on the samples. Simultaneously to the temperature oscillation, the current between the film top and bottom electrode was registered [50]. Measurements were performed at room temperature at 10 mHz with a variation of 4 °C (RT ± 2 °C). The slow heating rate of 0.08 °C/s, coupled with the small substrate thickness, 0.5 mm, enables a good and homogeneous thermal transfer across the whole sample.

Raman spectra were collected using Jobin-Yvon/Horiba LabRAM and Renishaw Raman RM-1000 spectrometers. Raman spectroscopy measurements have been performed in a backscattering geometry with a 100x magnification objective (1µm focusing spot) at room temperature. *We used a 514.5-nm line of an Ar$^+$ ion,* and its power was maintained at 0.8 to avoid heating the sample. Incident laser and scattering light have been polarized parallel (HH) or perpendicular to each other (HV).

UV-Vis spectrometer was used to collect the absorption spectra of the deposited films on transparent STO (100) single crystal substrate. Then bandgap was calculated by using Tauc's plot equation.

3.1.2.   Precursors thermal behavior

A straightforward MOCVD route, using a multicomponent precursor mixture, has been applied for the fabrication of pure and doped $BiFeO_3$ films, using the $Bi(phenyl)_3$ and $Fe(tmhd)_3$, as Bi and Fe sources, and the $Dy(hfa)_3\bullet diglyme$ to dope $BiFeO_3$ films at the A-site with Dy^{3+}. Three different Dy doping amounts in the precursor mixture have been evaluated by using Dy/(Dy+Bi) molar ratios of 8%, 11% and 15%, giving rise to films with the following compositions (vide infra): $Bi_{0.94}Dy_{0.06}FeO_3$ (from now on BDFO- 6%), $Bi_{0.92}Dy_{0.08}FeO_3$ (BDFO-8%) and $Bi_{0.89}Dy_{0.11}FeO_3$ (BDFO-11%).

The thermal behaviors of the multicomponent source containing $Bi(phenyl)_3$, $Fe(tmhd)_3$, and $Dy(hfa)_3\bullet diglyme$ have been investigated by thermogravimetric (TG) measurements at atmospheric pressure under nitrogen flow. A precedent study has shown that $Bi(phenyl)_3$/ $Fe(tmhd)_3$ mixture in the 1:0.66 ratio has excellent thermal behavior with a final residue of 5% [40]. To focus the thermal study of the three metallic precursor mixture, the higher content Dy mixture in a ratio Bi:Fe:Dy of 1: 0.66: 0.18 has been chosen as case study.

TG dynamic analysis shows a single step indicating that the mixture *evaporates* without decomposition in the temperature range of 140–270 °C (Figure 1a). Compared to the bicomponent mixture used for pure BFO deposition, we noted a slight residue increase of 12% of the initial mass.

Then, mixture mass transport properties behavior has been investigated by isothermal gravimetric analysis. Samples were brought to temperature, through a 5°C/min heating ramp, and maintained at 110°C, 120°C, 130°C, and 140°C for 3 hours (Figure 1b). Isothermal curves indicate a linear behavior for the 110°C-130°C temperature range, thus confirming that the mixture seems to perform as an ideal single-source mixture. From 140°C, deviation starts to be visible, indicating a preferential use of the precursor mixture up to 130°C. This has been assessed through a designed experiment: the mixture sample has been maintained for 3 hours at 130°C and then subjected to a heating ramp. The mixture source behavior is unchanged, thus displaying important thermal stability at 130°C (Figure 1c)

Mixture vaporization rate (mg/min) has been calculated from previous isothermal curves. The apparent vaporization energy has been derived, and it is equal to 24 ± 0.91 kJ/mol (Figure 1d).
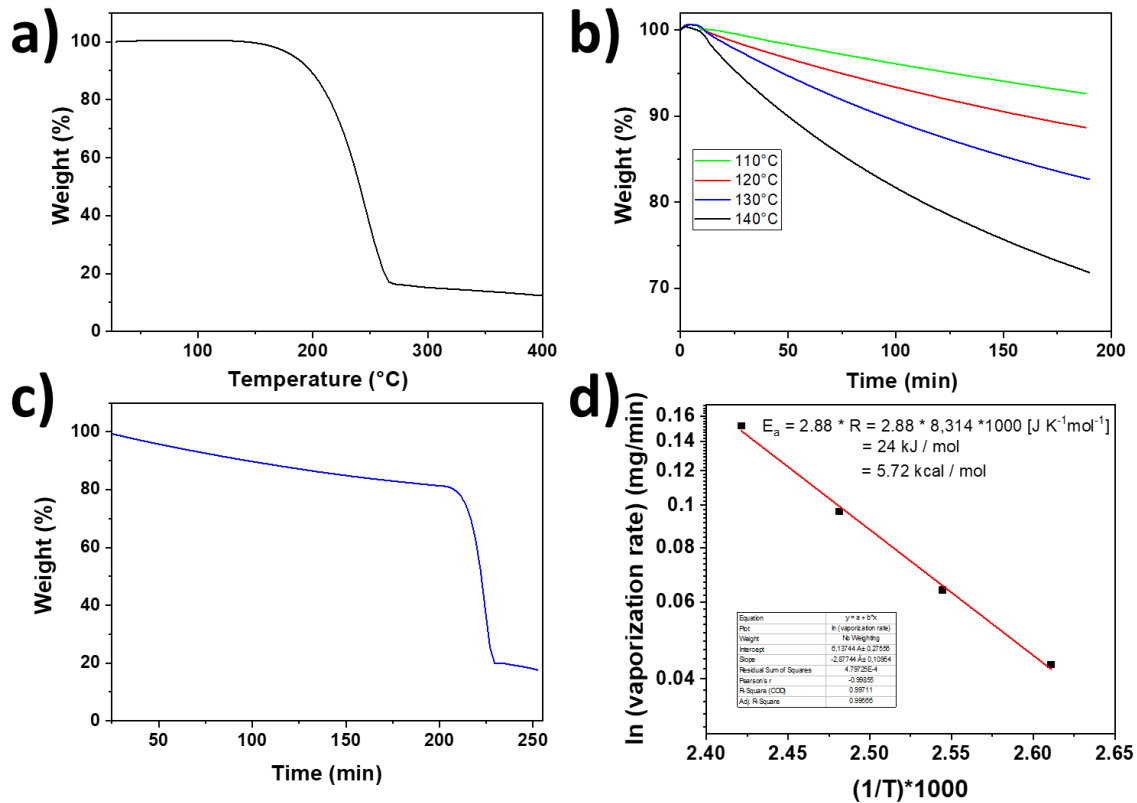
Figure 1. a) TGA analysis of the precursor mixture, b) Isothermal behavior of the precursor mixture at various temperatures, c) TGA of the precursors mixture after 3h isotermal at 130°C and d) Arrehnius plot of the precursor mixture vaporization rate.

3.1.3. Structural Characterization

X-ray diffraction. BDFO structural characteristics have been investigated by XRD, the planes and their reflections are reported considering a pseudocubic structure. In fact, the parent BFO has a rhombohedral structure with a_{rh} = 3.965 Å and α_{rh} = 89.41° but, given the angle of almost 90°, it is usually referred as pseudocubic. Thus, a lattice mismatch of 1.53% at room temperature is expected for the epitaxial $(001)_{pc}$ BFO films on the $SrTiO_3$ substrate having a perovskite cubic structure with an a-axis parameter a_S = 3.905 Å. The θ-2θ XRD patterns of BFO and BDFO are reported in Figure 2a. For all samples, pure and Dy-doped BFO, the diffraction patterns show exclusively reflections associated with BFO-like phase and STO:Nb 001 and 002 reflections, thus indicating that highly oriented films are grown without forming any parasitic phases.

A closer look at the second-order reflections, Figure 2b, reveals structural changes caused by the dopants. Firstly, the increase of the Dy content causes a broadening of the BDFO 002 reflection. In addition, a shift of the 002 reflections toward higher angles and, consequently, the decrease of the out-of-plane lattice parameter are observed, as the average A-site ionic radius is reduced when the smaller Dy^{3+} *($r_{12\text{-}coord}$ = 1.24 Å)* replaces Bi^{3+} *($r_{12\text{-}coord}$ = 1.36 Å)* [51,52].

The films out-of-plane alignment has been confirmed by recording the rocking curves of the 002 reflections of the four studied films. The second order reflections are at the following positions: 45.75°, 45.73°and 45.93°, 45.97° for the BFO, BDFO-6%, BDFO-8% and BDFO-11%, respectively. The rocking curves and the full width half maximum (FWHM) values of each system have been reported in Figure 2c. Pure BFO and BDFO-6% films show a similar mosaicity, with a FWHM of 0.27° and 0.24°, respectively. At higher doping, the shift of the 002 reflection and its broadening, visible in the θ-2θ patterns, are reflected on the rocking curves FWHM values of 0.78° and 1.04° for the BDFO-8% and BDFO-11%, respectively. It is worth noting that even if the increasing doping indicates a higher misalignment of film grains, all the films are of high quality in terms of pure phase and high out-of-plane orientation.
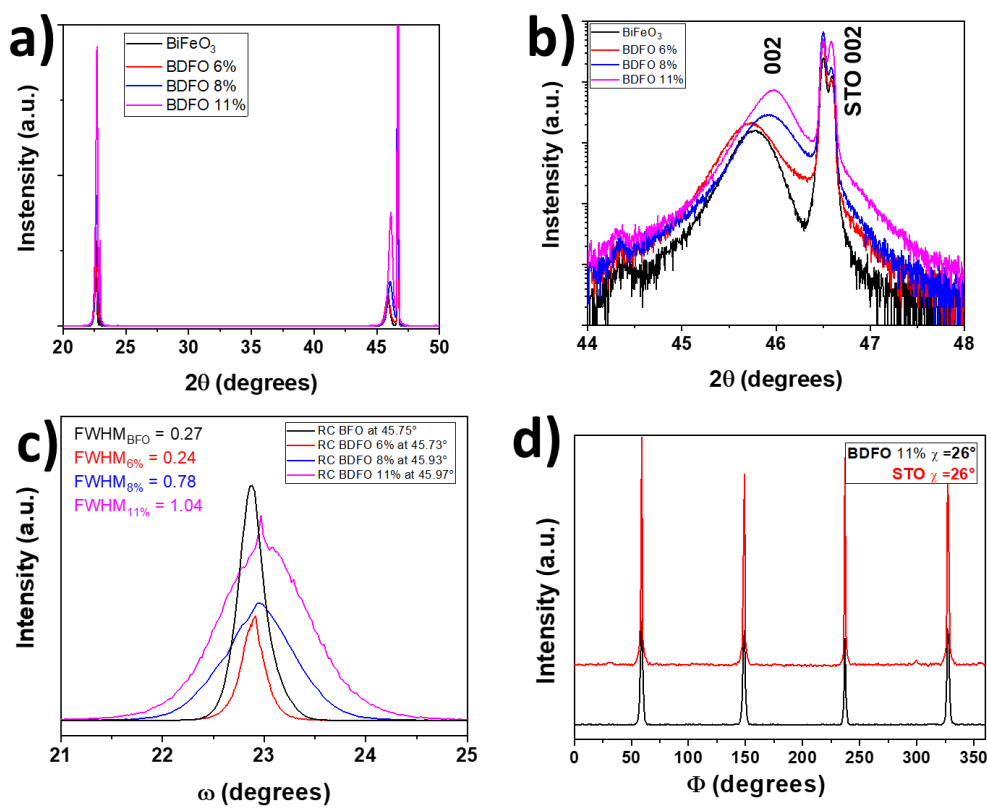
Figure 2. XRD patterns of the doped and undoped BFO films: a) ϑ-2ϑ patterns and b) enlarged 2ϑ region in the 44°-48°; c) rocking curves of the BFO and BDFO films around their 002 reflections; d) φ scan of 210 reflections of the BDFO 11% film and the STO:Nb substrate.

Considering the remarkable out-of-plane alignment, in-plane alignment has been investigated by recording Φ-scans of the BDFO films. A similar study has already been performed on BFO deposited on STO (001) [40], demonstrating its epitaxial growth on STO single crystal. Following a similar approach, Φ-scan patterns of the highest doping content film, the BDFO-11% and the STO:Nb substrate have been recorded at χ=26° to observe both BDFO ($2\theta = 51.52°$) and STO:Nb 210 ($2\theta = 52.33°$) reflections (Figure 2d). The presence of four peaks every

90° of Φ indicates that the film is in-plane aligned. The correspondence of the (210) BDFO poles with the STO:Nb (210) poles demonstrates that BDFO films are epitaxially grown cube-on-cube on STO:Nb single crystal substrate.
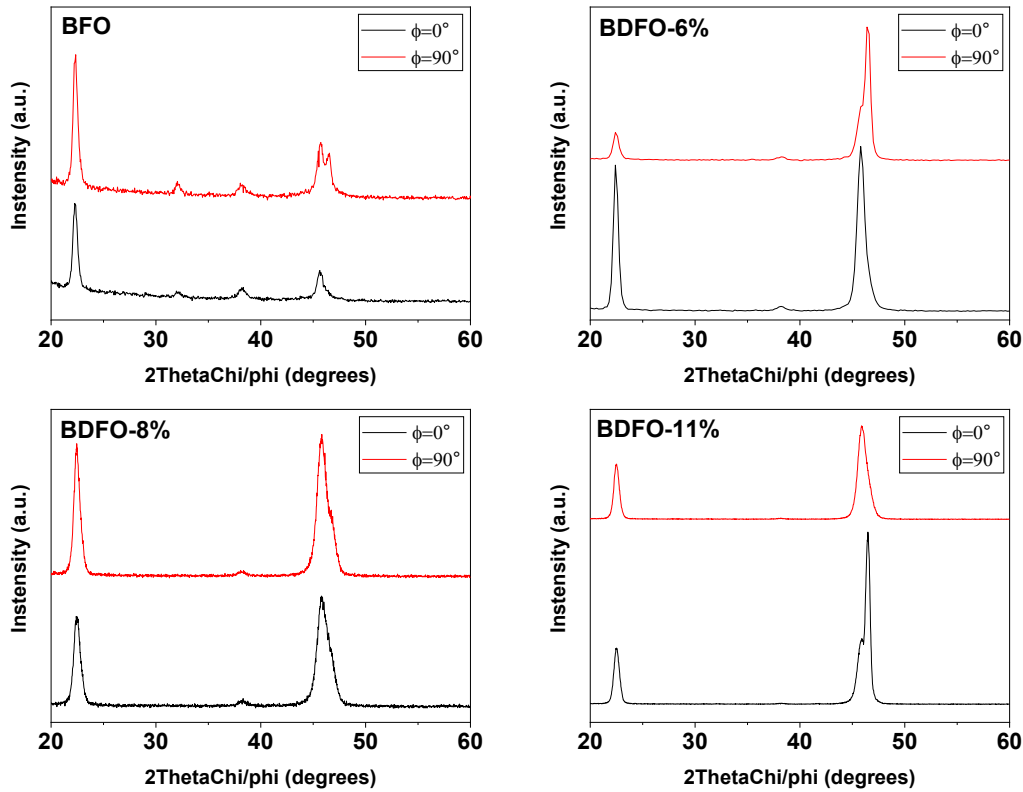
Figure 3. In-plane XRD patterns (ω=0.5°) realised at Φ= 0° 8 (black) and 90° (red) for a) undoped BFO, b) BDFO-6%, c) BDFO-8% and d) BDFO-11%.

All BFO and BDFO thin films in-plane diffraction patterns have been recorded with $2\theta\chi$ /ϕ scans starting from 20° to 60°, so both the first order and second-order reflection of the 00l diffraction peak can be observed (Figure 3). During the measurements for both ϕ=0° and 90°, the diffractometer axis ω has been maintained at an angle of 0.5° to limit diffraction from the STO substrate. Rotating the samples along ϕ allows the observation of the reflection of the (h00)$_{pc}$ and (0k0)$_{pc}$. Diffraction patterns have been aligned on the Au 111 diffraction peak ($2\theta\chi$ /ϕ=38.185°), due to the top electrode, and on STO 002 ($2\theta\chi$ /ϕ=46.485°). The pure BFO thin film sample reveals a small component of the 110 reflections at $2\theta\chi$ /ϕ =32.048° (Figure 3a). All the Dy-doped systems show a good in-plane orientation. For all films, cubic lattice parameters have been calculated thanks to the out-of-plane and in-plane diffraction patterns (Table 1).

	Calculated lattice parameter in Å from		
	Out-of-plane	In-plane Φ=0°	In-plane Φ=90°
BFO	3,960	3,982	3,958
BDFO-6%	3,962	3,964	3,964
BDFO-8%	3,948	3,966	3,961
BDFO-11%	3,946	3,944	3,945

The calculated parameters do not permit us to clearly understand if a structural change happens in the film with the Dy-doping concentration increase. However, because of the doping, a clear out-of-plane and in-plane contraction of the lattice is visible, reducing the lattice mismatch between the film and the STO substrate to 1%. Diffraction peaks of the film 120 and the substrate 210 reflection peaks have been done between 2θ= 50° to 54° with χ=26° (Figure 4). Pure BFO peaks splitting in the 120 and -120 reflections assess the rhombohedral nature of the film. For Dy-doped systems a shift toward higher angles is observed. The extremely broad nature of their peaks suggests the presence of a peak splitting like what have been observed for BFO. Literature reports a phase transition from rhombohedral tot orthorhombic structure in the case of BFO Dy-doping, with a morphotropic phase boundary around a Dy content of 8% [53]. Fully orthorhombic BDFO have been observed for Dy-doping of 15%, indicating a slow transition from the rhombohedral to the orthorhombic phase [54,55]. Present XRD study reports the structural transition between pure rhombohedral BFO film and distorted rhombohedral BDFO-6%, 8% and 11% systems.
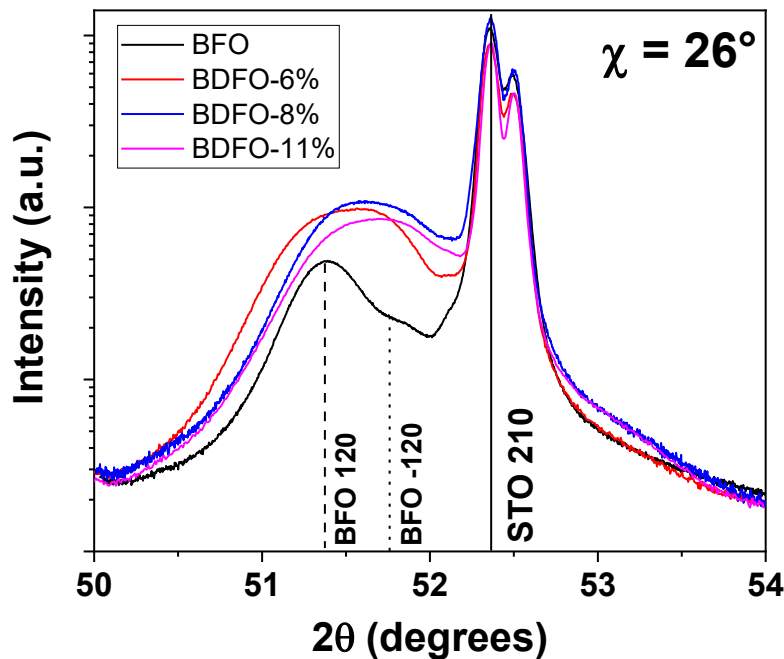

Figure 4. XRD patterns of the BFO and BDFO thin films acquired in Bragg-Brentano mode (ϑ-2ϑ) for χ=26°.

Raman spectroscopy. BFO rhombohedral unit cell (space group R3c) is composed of 10 atoms which implies30 (3N) vibration model and 27 (3N-3, 3 is the number of acoustic vibration mode) optical mode: $\Gamma_{opt,R3c}$ = 4A1 + 5A2 + 9E. The modes A1 and E (2 time degenerated) are Raman and IR active and the A2 modes are silent. [56-59].

BiFeO$_3$ Raman tensor [60]:

$$A_1(z) = \begin{pmatrix} a & & \\ & a & \\ & & b \end{pmatrix}, \quad E(x) = \begin{pmatrix} & c & d \\ c & & \\ d & & \end{pmatrix}, \quad E(y) = \begin{pmatrix} c & & \\ & -c & d \\ & d & \end{pmatrix}$$

BiFeO$_3$ is an optically uniaxial crystal, which means that the refractive index of one crystal axis (the optical axis) is different from the refractive index of the two other axes. This specific axis is called the optical axis and is parallel to the ferroelectric polarization [0001]$_{hex}$ || [111]$_{pc}$ for the BiFeO$_3$. The angle θ between the BFO optical axis and the phonon propagation vector directly influences the phonon wavenumber [61]. Pure E(TO) and A1(LO) modes are visible for θ=0° and E(LO) and A1(TO) modes for θ= 90°. In those configurations, Raman spectroscopy can detect 13 modes.

In the present study, epitaxial BiFeO$_3$ (001)$_{pc}$ and BDFO (001)$_{pc}$ films have been deposited on Nb:SrTiO$_3$ (100). The scattering surface being different from (111)$_{pc}$, it is expected to observe ordinary E(TO) phonons and phonons with mixed symmetry LO-TO and mixed A1-E character dependent on the θ angle between [111]$_{pc}$ and the laser direction [62,63]. In this case, θ ≈ 54.7 ° and 22 modes can theoretically be observed [64,65].

Raman spectroscopy from (001)$_{pc}$ BFO scattering surface (after a rotation of θ ≈ 54.7 °) has the following Raman tensors [66]:

$$A_1(z') = \begin{pmatrix} a' & & \\ & b' & c' \\ & c' & d' \end{pmatrix}, \quad E(x') = \begin{pmatrix} & e' & f' \\ e' & & \\ f' & & \end{pmatrix}, \quad E(y') = \begin{pmatrix} g' & & \\ & h' & i' \\ & i' & j' \end{pmatrix}$$

In a backscattered geometry configuration for a (001)$_{pc}$ oriented BFO we have the following selection rule (Table 2):

Table. 2 Raman modes selection rules for BFO (001) in backscattered configuration.

	A$_1$(LO+TO)	A$_1$(TO)	E(LO+TO)	E(TO)
-Z(XX)Z	X		X	
-Z(XY)Z or -Z(YX)Z				X
-Z(YY)Z	X		X	

Recent work on BFO single crystal by *Himcinschi et al.* [65] reported that in-plane rotation (Φ azimuthal angle) of the sample impacts the Raman intensities but does not lead to phonon frequency dispersion as the θ angle does. Between single crystal and BFO thin film, it must be noted that epitaxial growth of BFO might induce strain on the film because of the film/substrate lattice mismatch [67]. A mismatch of 1.53% is expected when BFO is deposited on STO, which is relatively small and should not induce an important change in the material symmetry.

Several examples of $(001)_{pc}$ single crystal or thin-film are reported in the literature, but in the past θ = 54.7° angle has been neglected and so been the sources to controversial attribution of the vibration modes. Based on *Hlinka et al.* [62], *Talkenbergerst et al.* [64] proposed a new interpretation of the previous works, considering the mixed mode natures. We updated their work (Table 3) with new results obtained on BFO single crystal along the $[001]_{pc}$ [65] and with the present data of epitaxial BFO $(001)_{pc}$/ Nb:STO (100).
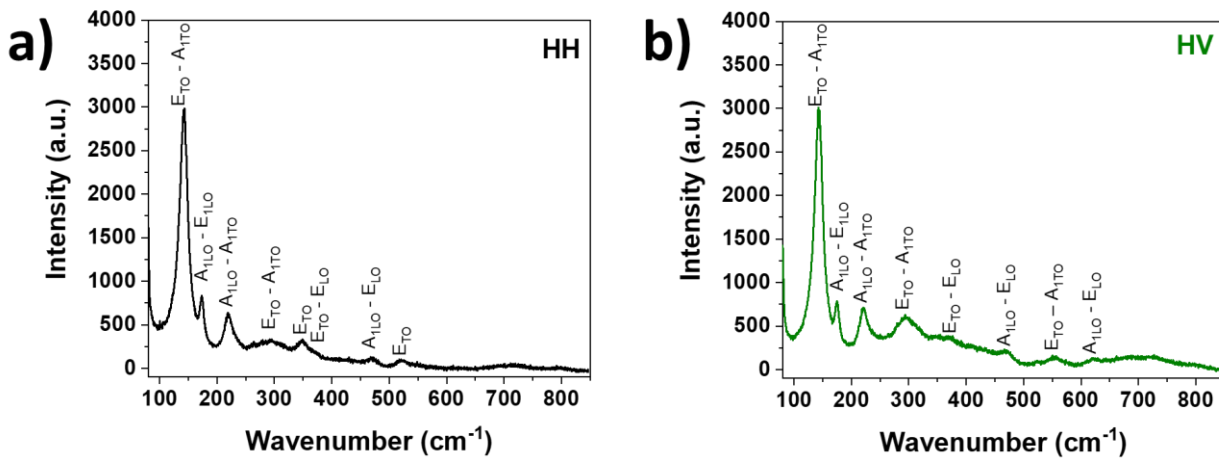
Figure 5. Raman spectra of pure BFO $(001)_{pc}$ thin film on STO:Nb (100) collected in a) HH and b) HV configurations.

Typical BFO Raman spectra collected in (HH) and (HV) configuration are reported in Figure 5. BDFO Raman spectra (HH) have been compared to the BFO one in Figure 6a. Under the same measurement conditions, a diminution of the Raman intensity signal is observed, and is caused by the change of BDFO band gap value with respect to BFO (from 2.68 eV to 2.25 eV, see Figure.8). Thus, the excitation laser is being absorbed by the BDFO, leading to a diminution of the signal. Wavenumber shift and variation of peak width for the $E_{TO}(2)$-A1$_{TO}(1)$, A1$_{LO}(1)$-$E_{LO}(2)$, and A1$_{LO}(2)$-A1$_{TO}(2)$ modes for all the samples are reported in Figure 6b,c,d. Apparent shifts toward higher wavenumbers are observable for all 3 modes. Moreover, peak width is also subjected to noticeable changes confirming the structural modification caused by the Dy doping.

Figure 6. a) Raman spectra of BFO ond BDFO thin films (001)$_{pc}$ on STO:Nb (001) collected in HH configuration. Peak position and with of the a) E$_{TO}$(2)-A1$_{TO}$(1), b) A1$_{LO}$(1)-E$_{LO}$(2) and c) A1$_{LO}$(2)-A1$_{TO}$(2) modes.

Table. 3 Comparison between present work and previously calculated or measured Raman modes for BFO $(001)_{pc}$.

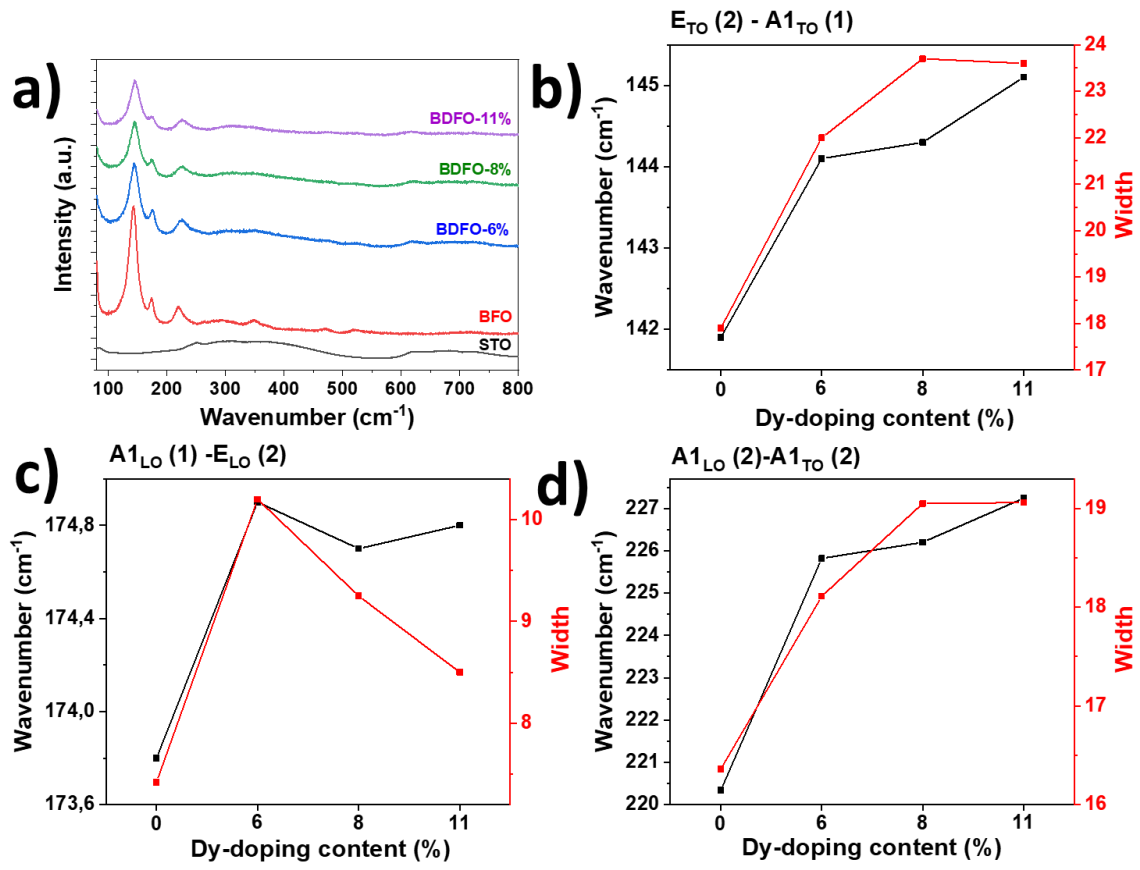| Phonon mode	Extraordinary Phonon mode	[64] Calc. [7] at θ=54.7° T = 5K	[63] Single crystal $(001)_{pc}$ T=4K	[69] Single domain crystal $(001)_{pc}$ T=81K	[68] Film $(001)_{pc}$ RT	[70] $(001)_{pc}$ RT	[64] Film $(001)_{pc}$ RT	[65] single crystal $(001)_{pc}$ RT	This work HH $(001)_{pc}$ RT	This work HV $(001)_{pc}$ RT
				57						
(1)	$E_{TO}(1)$	74	77	74.2	-	-	-	-	-	-
	1 $E_{TO}(1)$-$E_{LO}(1)$	79.5	-	79.6	-	-	-	-	-	-
	-						105			
(2)	$E_{TO}(2)$	132	136	127	-	-	118	-	-	-
	2 $E_{TO}(2)$-$A1_{TO}(1)$	143.9	147	145	136	140	135	138	142.1	143.2
	3 $A1_{LO}(1)$-$E_{LO}(2)$	176.1	176	168	168	173	172	172	173.7	175.2
				175.9						
	4 $A1_{LO}(2)$-$A1_{TO}(2)$	224.2	227	212	212	220	218	220	220.2	222
				224.2						
(3)	$E_{TO}(3)$	240	-	-	-	-	-	237	-	-
	5 $E_{TO}(3)$-$E_{LO}(3)$	241.7	-	-	-	-	-	-	-	-
(4)	$E_{TO}(4)$	265	265	265.4	-	265	266	-	-	-
	6 $E_{TO}(4)$-$E_{LO}(4)$	275.6	279	277.7	275	279	277	-	-	-
(5)	$E_{TO}(5)$	278	-	-	-	-	-	-	-	-
	7 $E_{TO}(5)$-$A1_{TO}(3)$	294.5	-	295.2	-	288	-	288	291.3	295
	8 $E_{TO}(6)$-$E_{LO}(5)$	349.0	351	350.4	335	350	350	-	-	-
(6)	$E_{TO}(6)$	351	-	-	-	-	-	347	348.8	-
	9 $E_{TO}(7)$-$E_{LO}(6)$	370.6	375	371.5	363	371	365	370	369.1	366.8
(7)	$E_{TO}(7)$	374	-	-	-	-	-	-	-	-
	10 $E_{TO}(8)$-$E_{LO}(7)$	434.5	437	-	425	-	-	432	-	-
(8)	$E_{TO}(8)$	441	-	-	-	-	-	-	-	-
	11 $A1_{LO}(3)$-$E_{LO}(8)$	473.7	473	473.0	456	-	465	470	469.2	469.8
			490							
(9)	$E_{TO}(9)$	523	525	523.1	-	520	517	520	520.68	-
	12 $E_{TO}(9)$-$A1_{TO}(4)$	551.9	-	553	549	550	548	545	-	553.3
	13 $A1_{LO}(4)$-$E_{LO}(9)$	606.3	-	-	597	-	-	620	-	620.9

3.1.4. Compositional and morphological investigation

Compositional analysis. This work principal aim is to define a relation between the dopant concentration and multifunctional properties. XPS and EDX analyses have been used to assess the presence of Dy in the film and to determine the solid solution average composition. The Dy doping is assessed by the presence of the $3d_{5/2}$ peak at 1297.8 eV. Due to the low kinetic energy of the $3d_{5/2}$ derived photoelectrons (188.8 eV) and, in turn, to their low mean free path [71], Dy detection is strongly affected by the presence of surface overlayers and, therefore, a preliminary 10 min sputtering is needed to clearly detect the Dy $3d_{5/2}$ band. Note that the Dy 4d peak at about 153 eV cannot be detected because of its overlapping with the much more intense Bi 4f signals. Thus, quantitative XPS analysis of Dy is hampered due to the combination of the low mean free path of Dy $3d_{5/2}$ photoelectrons and to the effects of the sputtering process [72, 73], which can induce changes on the surface composition.

EDX spectra also confirm the presence of Dy dopant in the thin film. Two Dy peaks can be observed: M line at 1.29 keV and L_{α} line at 6.49 keV. The proximity between Dy L_{α} and Fe K_{α} (6.39 keV) lines makes precise Dy quantification challenging, but an accurate approach to EDX Dy and Fe quantification makes possible to estimate film composition. Since the EDX software does not allow the use of the Dy M lines for Dy quantification, Dy L_{α} and Fe K_{α} lines have to be used for elements quantification. To overcome this problem, an undoped BFO film has been used as a reference to get a conversion coefficient between the Fe K_{α} and the Fe L line intensity. Then, for Dy-doped films, the study of the ratio between the Fe K_{α} line and the Fe L line, compared to the reference value obtained for pure BFO sample, allowed us to separate the contribution of the Dy L peak in the quantification of Fe in the films. Table 4 reports the nominal precursor mixture composition, deposited films stoichiometry and overall (Bi+Dy) / Fe ratio in the films.

Table. 4 Relationship between precursor nominal composition and film stoichiometry based on EDX evaluation.

Precursor composition	Film stoichiometry	
	Dy / (Dy + Bi)	(Bi + Dy) / Fe
$BiFeO_3$	0%	0.95
$Bi_{(1-x)}Dy_xFeO_3$ (x = 0.08)	6%	0.96
$Bi_{(1-x)}Dy_xFeO_3$ (x = 0.11)	8%	0.91
$Bi_{(1-x)}Dy_xFeO_3$ (x = 0.15)	11%	0.95

This approach enables to estimate the increase of doping element in the film: interesting is the linear trend between the mixture nominal element composition and the final film composition, which allows, in a flexible and simple way, to predict and finely tune film properties.

Morphological characterization. BFO and BDFO film samples, deposited on STO:Nb (5 mm x 10 mm), present mirror-like surface quality. FE-SEM micrographs of the studied films, obtained through detection of secondary electrons, are reported in Figure 7. The morphology of pure BFO film is very uniform (Figure 7a) and presents well-coalesced, large, squared grains of about 500 nm in average. Dy-doped BFO films, with increasing Dy doping from 6% to 11%, are reported in Figure 7b, c, d, respectively, and show an even smoother morphology with a flat surface formed by fully coalesced regular grains; thus, the increase of doping content seems to improve film morphology.

Finally, sample thickness has been checked through FE-SEM cross-sections. The thicknesses of both BFO and BDFO samples are in the range of 450-500 nm, indicating a similar growth rate of 8 nm.min^{-1} for a 1-hour MOCVD process [35].
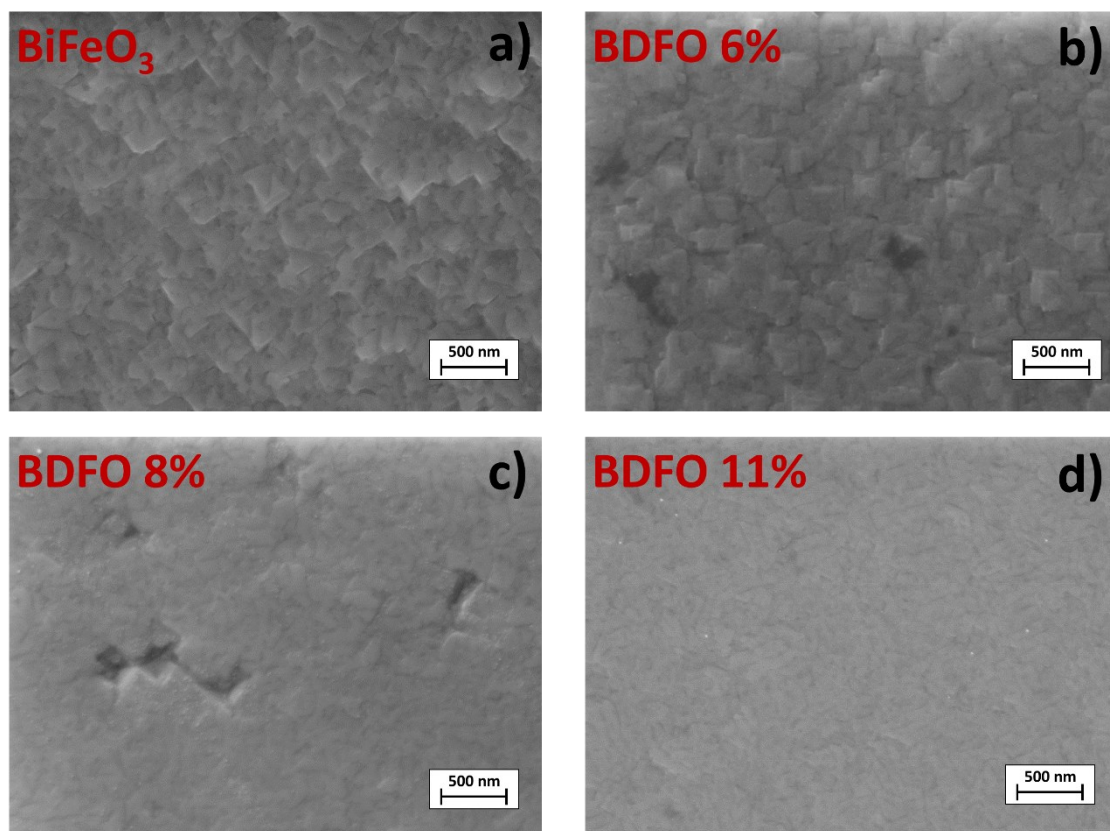
Figure 7. Secondary electron FE-SEM plan view images of a) BiFeO$_3$, b) BDFO 6%, c) BDFO 8%, and d) BDFO 11%.

3.1.5.   Functional characterizations

Bandgap. The optical absorption of the MOCVD deposited BFO, and BDFO films was measured in a UV-Vis spectrometer, then the optical bandgap value was obtained using Tauc's equation [74, 75]. Films have been deposited on a transparent substrate of SrTiO$_3$ (100).

Film bandgap was extrapolated from the plot of $(\alpha * h * \nu)^{1/n}$ vs $(h * \nu)$, with (n =1/2 because of BFO direct bandgap) with α, h and ν being the film absorption coefficient, the Planck's

constant and the photon frequency, respectively [75]. For $(\alpha*h*v)^2 = 0$, the linear region's fitted curve gives a film bandgap of 2.68 eV, which indicates a maximum absorption for a wavelength of 460 nm (Figure 8). Reported optical band gap values for pure rhombohedral BFO film range from 2.01 eV to 2.82 eV, the variation being caused by deposition method and used substrate [76].
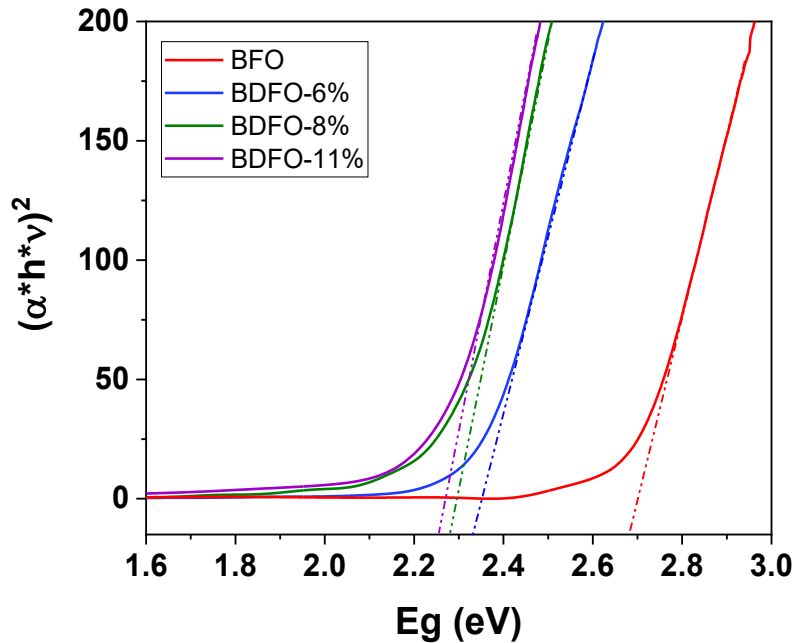
Figure 8. Tauc's plots of the undoped and Dy-doped BFO thin films calculated from UV-Vis absorption spectra.

The same approach has then been applied to Dy-doped BFO thin films, also deposited on transparent STO. Tauc's plots of all the studied samples are reported in Figure 8, where the influence of Dy doping on the material bandgap can be observed. First, Dy-doping of 6% has a strong impact on material bandgap, inducing an important reduction of its value up to 2.33 eV. Dy-dopings of 8% and 11% also have a noticeable influence on the bandgap, bringing it to 2.28 eV and 2.25 eV, respectively. As the Dy percentage increases, the dopant impact on the bandgap value seems to be reduced and tends to a limit (Table. 5).

Table. 5 Summary table of the bandgap energy value for the different Dy-doped BFO films.

$BiFeO_3$	2.68 eV
BDFO-6%	2.33 eV
BDFO-8%	2.28 eV
BDFO-11%	2.25 eV

Piezoresponse force microscopy. Piezoelectric and ferroelectric properties of the BDFO films have been investigated through piezoresponse spectroscopy (PFS) and piezoresponse force microscopy (PFM). Previous studies have already reported PFM and PFS investigation of BFO thin films on Nb:STO 001 [40] and have described good and stable piezoelectric and ferroelectric properties with a 2V coercive voltage. We decided to focus on the new BDFO

systems (6%, 8%, and 11%) to explore the Dy-doping effect on piezoelectric and ferroelectric properties.

Single-point PFS have been measured by applying a ±9V round trip on the sample between the cantilever tip and the sample conductive substrate (Figure 9). Measured piezoresponse amplitude (Mag) is a function of the applied oscillating voltage (V_{ac}) for a defined bias voltage, from -9V to 9V.

Figure 9 shows typical butterfly loops, characteristic of the film piezoelectric behavior, obtained for BDFO-6% and BDFO-8%. Local ferroelectric switchings (Phase) are reported for the same samples and correspond to the phase difference between V_{ac} and the induced vertical piezoresponse signal from the sample at different bias voltage. The coercive voltage value of 2V found for BDFO-6% is similar to the previous measured value of pure BFO [35]. However, BDFO-8% coercive voltage benefits of a significant increase to the value of 3V.
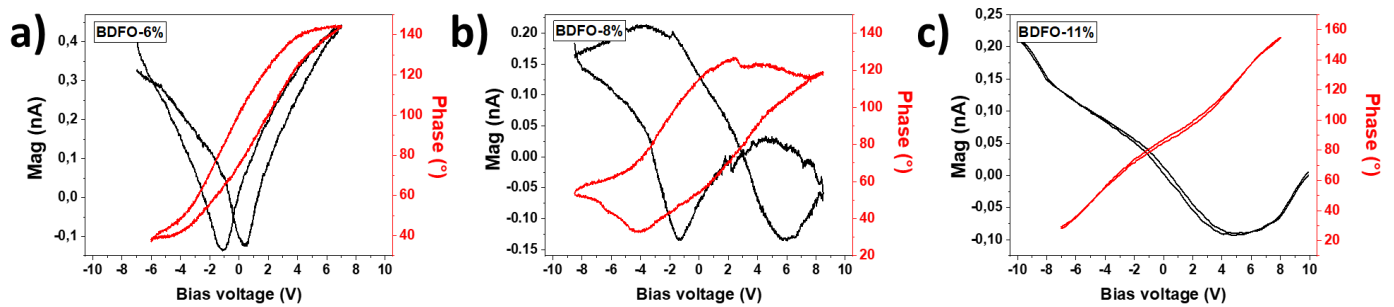
Figure 9. PFS spectroscopy of the BDFO thin film a) BDFO-6%, b) BDFO-8% and c) BDFO-11%. Films piezoelectric response (Mag) is reported as black curves and phase switching as red curves.

Local measurements showed promising piezoelectric and ferroelectric answer for BDFO-6% and BDFO-8%. To go further in this investigation, we decided to perform a writing experiment to map samples ferroelectric domain. On the other hand, BDFO-11% did not show a significative response, so no writing experiment was attempted.

Atomic force microscopy (AFM) topography scans of the studied 4µm x 4µm samples are reported (Figure 10). Simultaneously, phase maps of the ferroelectric domains of the "as-deposited" films were recorded by using a V_{ac}=0.9 V at a 0 V bias voltage (Figure 10 b and d). A 7 V bias was then applied to the films from the PFM tip on a smaller 1µm x 1µm area. After the writing, the new phase image of the larger 4µm x 4µm area has been recorded at 0 V bias voltage to observe the switching of ferroelectric domains. The areas exposed to the 7 V bias show a significant phase switch (Figure 10 c and e) compared to the initial phase scan, thus confirming the ferroelectric nature of BDFO 6% and 8%.

BDFO-6%

BDFO-8%

Figure 10. BDFO-6% a) AFM topography scan b) PFM phases scan before applying +7V bias voltage c) PFM phases scan after applying +7V bias voltage. BDFO-8% c) AFM topography scan d) PFM phases scan before applying +7V bias voltage e) PFM phases scan after applying +7V bias voltage.

Polarization. The polarization-electric field (P-E) negative unipolar loops have been measured between -200 and 0 kV/cm at 5 kHz to limit leak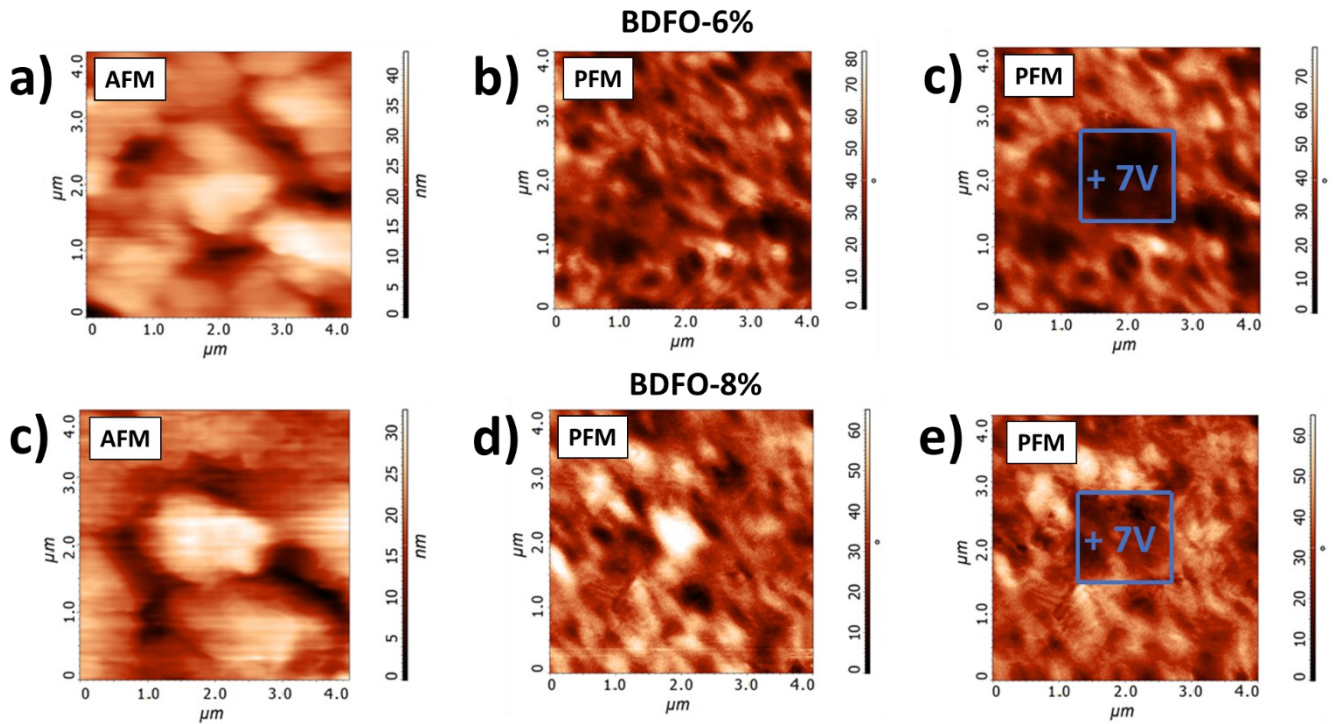age current impact on the measurements (the sample had a more important leakage under positive polarity) [49]. The Figure 11 reports P-E unipolar loops of 500 nm-thick BFO, BDFO-6%, BDFO-8% and BDFO-11% thin films at room temperature. Unipolar loops do not allow the material ferroelectric switch, thus film polarization cannot be measured and compared. However, impact of film ferroelectric properties can be easily observed, as the asymmetric shape of the reported P-E unipolar loops is the direct consequence of material ferroelectric behavior. All thin film ferroelectric half loops show a rounded tip and an increasing charge with decreasing electric field amplitude, which is common for BiFeO$_3$ systems [73]. This difference with the classical shape of ferroelectric hysteresis loops indicates the presence of important leakage currents in the samples. As the thin film Dy-doping increases from 6% to 8%, the impact of a ferroelectric behavior is more and more visible. For a Dy doping amount superior to 8%, a significant reduction of the BDFO properties has been observed. A similar behavior has been previously reported and attributed to a phase transition from a ferroelectric to a paraelectric phase due to the rare-earth doping amount [1, 11, 34]. Thus, larger ferroelectric contributions are visible for the Dy-doped BFO films, compared to the undoped BFO one, which indicates the strong influence of Dy-doping on material properties.
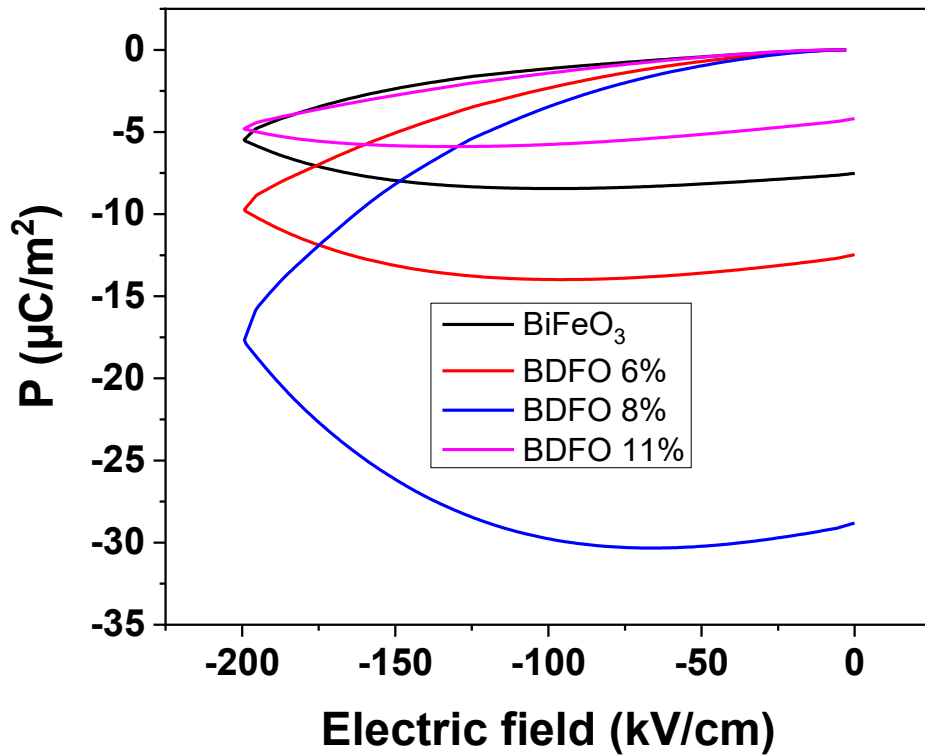
Figure 11. P-E negative unipolar loops of doped and undoped BFO films, measured between -200 and 0 kV/cm at 5 kHz.

Permittivity. Sample relative permittivity (ε_r) and dielectric loss [tan(δ)] at three different frequencies (100 Hz, 1 kHz and 10 kHz) are reported in Figure 12a. Sample permittivity values have been calculated from the capacitance measured in parallel plate configuration: (Au/Cr)/BDFO/STO:Nb. Compared to previous studies, pure $BiFeO_3$ films possess a similar relative permittivity value of $\varepsilon_{r\ BFO}$= 130 at 1 kHz, in the literature reported values oscillate around ε_r = 100, depending on the synthetic method and the measurement frequency [26,77]. The major aspect of this test is to evidentiate the impact of Dy-doping on the film permittivity. The first two levels of doping (6% and 8%) provoke an important and significant increase of the film permittivity, the highest value of $\varepsilon_{r\ BDFO}$=250 at 1 kHz is obtained for a Dy doping content of 8%. Above this concentration, similarly to the trend observed during the polarization study of BDFO films, a deterioration of the film permittivity has been detected with a ε_r decrease from 250 to 170 between BDFO-8% and BDFO 11%. Dy-doping also affects dielectric losses of the films at 100 Hz (Figure 12b). At this frequency, the tan(δ) of BFO is 4.7, while for the BDFO samples lower losses are observed, of about 0.4 for the 6% and 11% samples and 1.9 for the 8% one.

Figure 12. a) Relative permittivity (ε_r) and b) dielectric loss [tan(δ)] of doped and undoped BFO films, measured at 100 Hz, 1 kHz, 10 kHz.

Pyroelectric properties. The oscillating temperature method was applied for the pyroelectric measurements. While the average temperature was achieved using heating elements, the temperature oscillation was 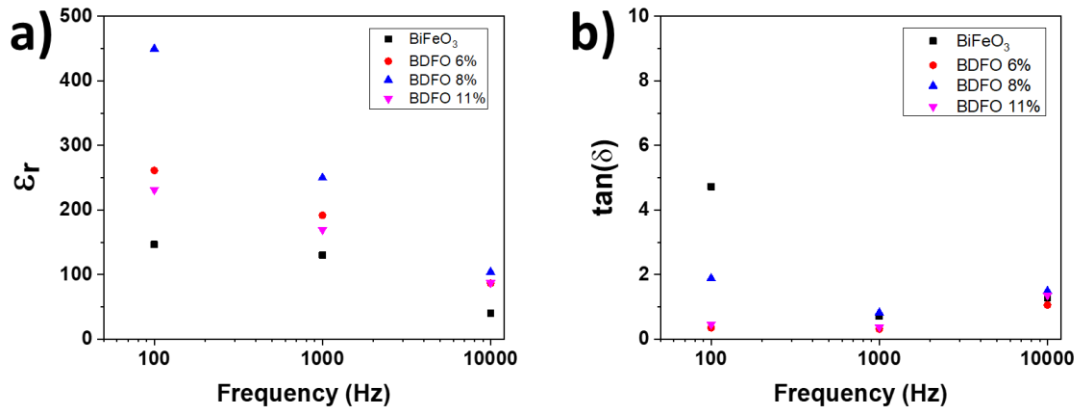realized with Peltier cooling elements in the substrate chuck. A critical parameter is the homogeneous temperature distribution within the sample. Thus, before starting any measurement, to ensure a homogeneous temperature of the whole sample, temperature equilibrium between the Peltier and the samples had to be achieved [78]. All the four systems, pure and Dy-doped BFO films, have been carefully put into thermal equilibrium and precycled to avoid thermally stimulated currents before their pyroelectric properties were investigated. Samples have been tested "as-deposited", no poling has been performed.

Pyroelectric responses of BFO, BDFO 6%, BDFO 8% and BDFO 11% samples are reported in Figure 13a, b, c and d, respectively. Pyroelectric current (in blue) is easily identified because it reverses its sign when the applied temperature ramp (triangular temperature waveforms in black) is reversed. The pyroelectric coefficients were calculated using equation 1:

$$p_i = \frac{i_p}{\frac{dT}{dt} \times A} \qquad . (1)$$

where p_i, i_p, A and dT/dt are the pyroelectric coefficient, pyroelectric current, area of the electrode and heating rate of the sample, respectively [60]. Because of the leakage in the samples, pyroelectric current does not always reach saturation. In addition, the domains do not adapt immediately to the change of temperature, because of domain wall traps and build-up of film stress (elastic energy). This creep is well seen at the end of the temperature ramp. In contrast, when the temperature goes back to its average value, there is an easy back-switching and a reduction of elastic energy. The polarization reacts immediately, as seen at the beginning of the temperature ramp, in the case of samples reported in Figure 13a, b, and

d. A similar behavior is observed for the BDFO 8% sample (Figure 13c), but in addition the back-switching seems to be very quick, leading to a kind of overshoot.
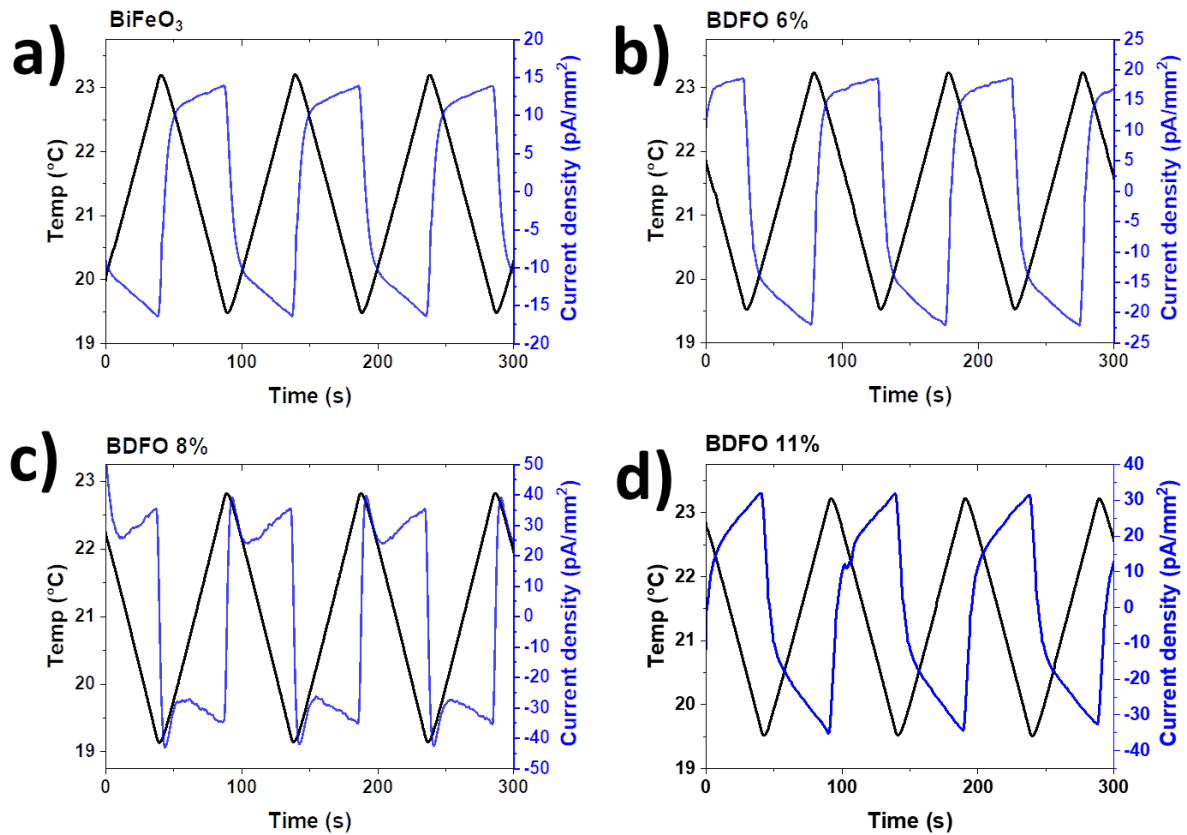
Figure 13. Pyroelectric responses of a) BiFeO₃, b) BDFO 6%, c) BDFO 8%, d) BDFO 11% to a triangular temperature waveform ΔT=4 °C at RT.

Even though samples have a very leaky behavior, excellent pyroelectric coefficients have been measured and this indicates a possibility that films are likely self-poled. For each film, the pyroelectric coefficient value has been reported along with the relative permittivity and the figure of merit for pyroelectric energy harvesting application (F_E) in the Table 6. F_E is calculated with Equation 2, where ε_0 and ε_r are vacuum permittivity and material relative permittivity, respectively [79]. Figure of merit values are of great interest to simplify the comparison of materials for a given application. Whatever the electronics for harvesting the pyroelectric energy, the delivered current is governed by the pyroelectric coefficient of the material, and the voltage by the charge on the capacitor (also proportional to p_i) divided by the capacitance, which is proportional to the dielectric constant ($\varepsilon_0\varepsilon_r$), yielding the material's figure of merit for pyroelectric energy harvesting as given in Equation 2.

$$F_E = \frac{p_i^2}{\varepsilon_0 \times \varepsilon_r} \quad . (2)$$

Pyroelectric response is closely linked to the material polarization and the ferroelectric transition temperature, and typically it increases along with dP/dT [80]. Because PE loops have shown an increase of the film ferroelectric component till a nominal Dy doping of 8%, a similar behavior of the pyroelectric coefficient is expected, followed by a deterioration of pyroelectric properties for a higher doping ratio. If interest in BFO ceramic pyroelectric properties is well established, results regarding thin film characterization are still limited. Previous studies report pyroelectric values up to 90 μC/(m² K) for undoped BFO ceramics, 91 μC/(m² K) for BFO/PZT thin films, 137 μC/(m² K) for $Bi_{(1-x)}Sm_xFeO_3$ ceramics and 145.5 μC/(m² K) for $Bi_{(1-x)}Gd_xFeO_3$ ceramics [5, 12, 26]. The undoped BFO thin film deposited in this work displays a pyroelectric coefficient of **188 μC**/(m² K), a value higher than any previously reported coefficient for BFO, regardless of the chosen synthetic route. This important increase of the pyroelectric coefficients can be mainly explained by the epitaxial nature of the grown films [81]. Moreover, the dense and homogeneous nature of the film, made possible by the MOCVD protocol used for the sample preparation, also have a significant impact on film pyroelectric coefficients [7]. As expected, Dy-doping has a strong impact on film pyroelectric behavior, which follows a similar trend to that observed in the P-E measurements. For a Dy doping of 8% a maximum value of p_i = **426** μC/(m² K) is found, which is more than twice the value of the pure BFO film.

Efficiency for energy harvesting is easily compared thanks to the F_E which depends not only on sample pyroelectric response but is also influenced by permittivity. Ideally, improvement of pyroelectric generator comes with increasing pyroelectric coefficient and reducing the permittivity. Presently reported undoped BFO films already show similar F_E than PZT and PMN-25PT assessing the importance of good quality lead-free material [85, 86]. Then, even though a certain increase of the film permittivity is observed till a Dy-doping of 8%, the huge pyroelectric response gives rise to a F_E as high as 82 J/(m³K²) for the BDFO-8%, suggesting outstanding properties compared to previous BFO systems and equivalent to single crystal $LiTaO_3$ [7].

Table. 6 Comparison of presently obtained pyroelectric coefficient, permittivity and FE for the BFO and Dy-doped BFO films with respect to available literature values for BFO, LiTaO₃, LiNbO₃, PZT and PMN-25PT systems.

System	Synthesis method	Shape	T measurement (°C)	p_i [μC/(m²*K)]	ε_r	F_E [J/(m³K²)]	Ref
$BiFeO_3$	MOCVD	Thin film	RT	188	130 (at 1 kHz)	30.71	This Work
BDFO-6%	MOCVD	Thin film	RT	256	190 (at 1 kHz)	38.96	This Work
BDFO-8%	MOCVD	Thin film	RT	426	250 (at 1 kHz)	81.98	This Work
BDFO-11%	MOCVD	Thin film	RT	288	170 (at 1 kHz)	55.1	This Work
$BiFeO_3$	PLD	Thin film	RT	40	~100 (at 10 kHz)	1.81	[11]
$Bi_{1-x}La_xFeO_3$	PLD	Thin film	RT	85	~240 (at 10 kHz)	3.4	[11]
BFO/PZT (70/30)	sol-gel	Thin film	RT	91	288 (at 1 kHz)	3.25	[5]
BFO/PZT (30/70)	sol-gel	Thin film	RT	5.1	244 (at 1 kHz)	0.02	[5]
$BiFeO_3$	chemical solution	Thin film	RT	15	76 (at 1kHz)	0.33	[82]
$BiFeO_3$	solid-state-reaction	Ceramic	RT	71	~100 (100 kHz)	5.69	[83]
$BiFeO_3$	solid-state-reaction	Ceramic	25	90	-	-	[84]
$Bi_{1-x}Nd_xFeO_3$ (x=0 – 0.15)	solid-state-reaction	Ceramic	RT	30 - 50	100 to 140 (at 1kHz)	1 - 2	[77]
$Bi_{1-x}Sm_xFeO_3$ (x = 0.01– 0.08)	solid-state-reaction	Ceramic	RT	137	120- 140 (100 kHz)	15.1 - 17.66	[12]
$BiFeO_3$	solid-state-reaction	Ceramic	RT	90	103 (1 MHz)	8.88	[26]
$Bi_{1-x}Eu_xFeO_3$ (x=0.05)	solid-state-reaction	Ceramic	RT	133.2	145 (1 MHz)	13,82	[26]
$Bi_{1-x}Gd_xFeO_3$ (x=0.05)	solid-state-reaction	Ceramic	RT	145.5	141 (1 MHz)	16.96	[26]
$Bi_{1-x}Tb_xFeO_3$ (x=0.05)	solid-state-reaction	Ceramic	RT	88	122 (1 MHz)	7.17	[26]
$Bi_{1-x}Dy_xFeO_3$ (x=0.05)	solid-state-reaction	Ceramic	RT	98	128 (1 MHz)	8.47	[26]
Other lead-free systems							
LiTaO₃		single crystal		190	47	87	[7]
LiNbO₃		single crystal		96	31	34	[80]
Other lead-based systems							
PZT (Toshiba)		ceramic	RT	350	471	29	[85]
PMN- 25 PT		ceramic	RT	602	1648	25	[86]

3.2. Nd and Yb doping for photovoltaic

Perovskite solar cells have grown in interest over the past years, the combination of their growing power conversion efficiency and their ferroelectrics properties makes them of particular interest. However, despite the promising results they have been obtained in lead-based perovskites, the environmental problems related to the production and the stability of such material arise.

In these circumstances, photovoltaic, ferroelectric, lead-free perovskites or related structures, such as $BiFeO_3$, $LiNbO_3$, and $(K,Na)NbO_3$, are of high interest. In conventional PV-devices, the photoexcited electrons and holes are separated by a built-in electric field at the p-n junction and have a photovoltage limited by their bandgap. Different working mechanisms can be described in ferroelectric materials. The electron/hole separation comes from the built-in electric field induced by the remnant polarization of the material (Figure 14), and the bandgap of the ferroelectric material does not limit the V_{oc}. Moreover, because the remnant polarization is not limited to a reduced region, like the p-n junction, but is present throughout the bulk of the ferroelectric material, it helps separate electron-hole pairs, which is no more limited to the depletion zone. [87,88]
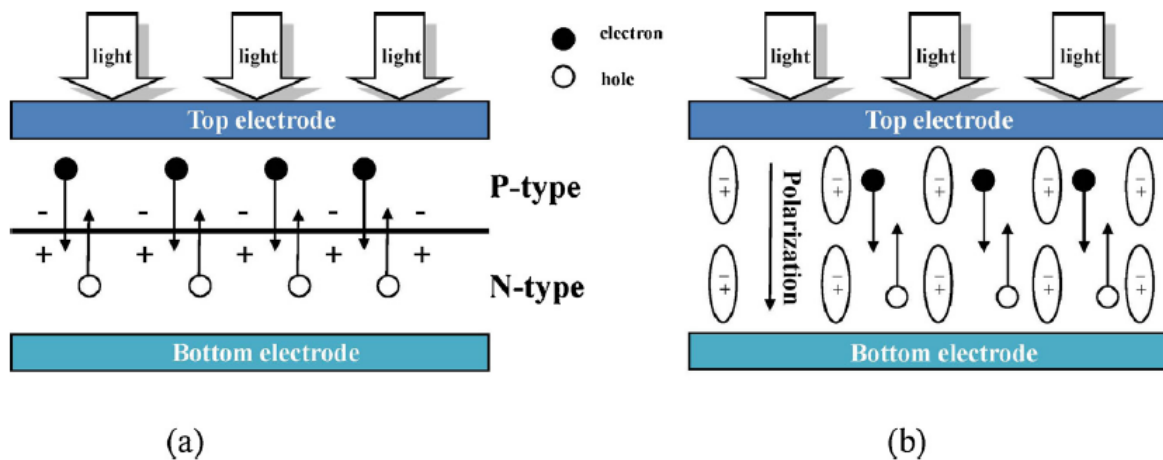
Figure 14. Schematic illustration of the working principle of (a) p-n junction photovoltaic devices and (b) ferroelectric photovoltaic devices [87].

Despite all the efforts made during the last years, ferroelectric PV with lead-free perovskite is still an academic research topic, and the latest BFO PV-devices are made by sol-gel or PLD, which are not suited to an industrial scale-up. BFO deposition by MOCVD is a solution that can be adapted to actual production constraints, maintain high film quality, and reduce production cost [39,89].

Another fundamental aspect is the tuning of BFO properties, from light absorption to carrier lifetime, many routes have been tried working on film thickness, film orientation, nature of the electrodes [90]. Every aspect of device preparation influences the final efficiency. Nevertheless, bismuth ferrite doping with lanthanides or transition metal is the most used approach to modify and significantly improve film properties as the bandgap, V_{oc}, and J_{sc}, which are looked at to compare different processes, impact the film properties. [91]

To use lead-free perovskites as PV transducers and for easy sample characterization, device critical aspects are the thin-film exposition to the light source and the harvesting of the generated photocurrent. Thanks to their simplicity, simple parallel plate electrode structures are widely used and are often combined with transparent electrodes. In our case, 3 sample structures can be considered. Among the 3 configurations proposed (Figure 15), A / B and C, all can be analyzed and theoretically be integrated as a PV transducer (in A and B illumination comes from the top, in C from the bottom).
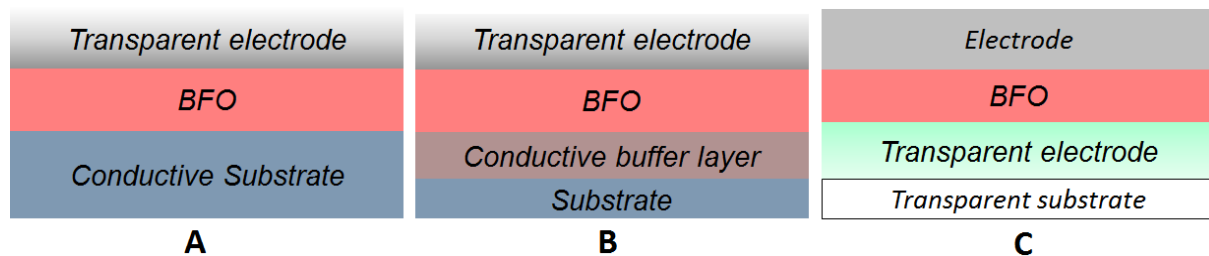
Figure 15. Investigated photovoltaic structure for the characterization and the integration of lead-free perovskite thin films.

- **Configuration A** in the case of BFO is the easiest to realize using $Nb:SrTiO_3$ conductive single crystal substrates. $Nb:SrTiO_3$ is useful for thin-film preparation and properties investigation. However, substrate cost, reduced size, and limited microfabrication capability make it a poor candidate for large scale PV transducers.

- **Configuration B** is the configuration where Si is the main substrate combined to a conductive layer on the top of which perovskite can be deposited. We have the following structure $BFO/IrO_2/Si$, IrO_2 acting as the bottom electrode and buffer layer for bismuth ferrite. As for configuration A, the last step is the deposition of a transparent top electrode.

- **Configuration C** is by far the most used structure for the study of BFO in PV-devices with a functional film deposited directly on a glass substrate coated with a transparent electrode (ITO or FTO). In the previous studies on PV-BFO, sol-gel, PLD, and sputtering are the three techniques used for thin film deposition. They offer a deposition temperature much lower than the 750/800 °C substrate temperature, required for MOCVD so that glass can be used as a transparent substrate. For high deposition temperatures, above 500°C, commercial products such as quartz coated with ITO are

available. Few references regarding FTO/Quartz can be found, but they are all prepared "in-lab," and so far, only FTO/Glass can be bought. Top electrodes nature can be as varied as the metal sources available.

Investigation of the lanthanides doping influence on the photoelectric properties of the material is one of the aspects of this work. To do so, pure BFO, BFO Nd-doped and Yb-doped thin-films have been deposited on (1cm x 1cm) STO (100) samples (configuration A). The use of single crystal substrate allows to focus only on the doping impact without worrying about film general quality or orientation. For each doping element, four doping level were deposited. The prepared samples have been sent to Dr. David Munoz-Rojas and Abderrahime Sekkat in Laboratoire des Matériaux et du Génie Physique (LMGP) for ongoing photovoltaic characterizations. A summary table of previous works on photovoltaic properties for previous BiFeO$_3$ based systems is reported in Appendix 2.

3.2.1.   Nd-doping

A simple single-step MOCVD approach has been used for the deposition of Nd-doped BFO films on STO:Nb (100). The multicomponent precursor mixture is composed of a Bi(phenyl)$_3$ and Fe(tmhd)$_3$ (*1:0.66*) ratio in which Nd(hfa)$_3$diglyme is added. In this way, the dopant amount in the film can be easily modified by a simple change of the Nd(hfa)$_3$diglyme quantity in the vaporized precursor mixture (at 120°C). Deposition temperature was maintained at 750°C for one hour, under an argon and oxygen gas flow of 150ml/min. Argon and oxygen are respectively carrier and reactant gas.

The oriented growth of BFO-Nd on STO:Nb is confirmed through X-ray diffraction (XRD), while field emission scanning electron microscopy (FE-SEM) allowed to assess the flat, homogeneous surfaces of deposited films. Nd-doping amount has been measured by energy dispersive X-ray analysis (EDX) and the doping impact on bandgap controlled by UV-Vis spectroscopy. Finally, preliminary photovoltaic measurements have been done. Samples are referred by the Nd-doping percentage measured in the film.

Morphological characterization of the films has been done using FE-SEM. Micrographs are reported in Figure.16. Deposited thin-films morphologies are very similar between each other with flat and homogeneous surface across the films. Only BFO-Nd 7% seems to have a slightly less coalesced feature than the other films (Figure 16a). At higher doping concentration, 14.5% superficial cubic-like grains are visible, which may be associated with Bi$_2$O$_3$ phase (Figure 16c).
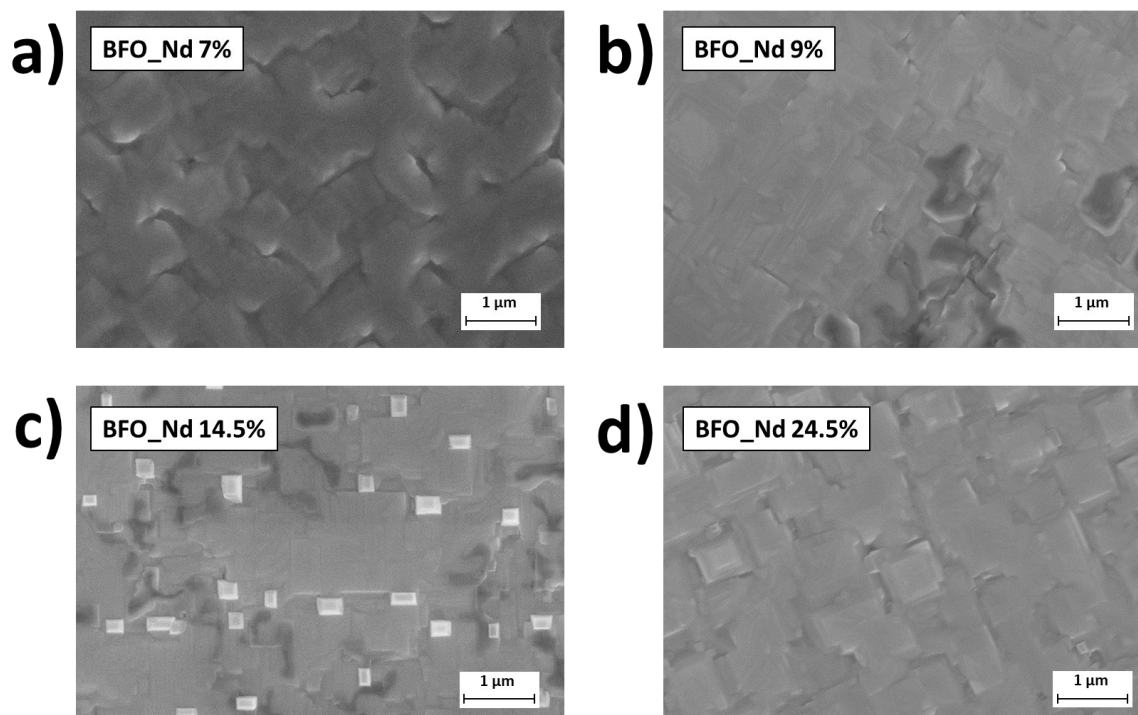
Figure 16. *Secondary electron FE-SEM plan view images of a) BFO-Nd 7%, b) BFO-Nd 9%, c) BFO-Nd 14.5%, and d) BFO-Nd 24.5%.*

Coupled with FE-SEM, EDX analysis confirmed the presence of Nd-dopant in the reported films. On EDX spectra the presence of Nd dopant is permitted by the identification of the L line at 5.228 keV. While Dy quantification might have been limited by peaks overlap, quantification of Nd does not suffer from the same limitation. In Table 7 the nominal precursor compositions have been reported and the percentage of Nd-doping and the (Bi+Nd) / Fe ratio in the films.

Table. 7 *Relationship between precursor nominal composition and film stoichiometry based on EDX evaluation.*

Precursor composition	Film stoichiometry	
	Nd/ (Nd + Bi)	(Bi + Nd) / Fe
$Bi_{(1-x)}Nd_xFeO_3$ (x = 0.088)	7%	0.96
$Bi_{(1-x)}Nd_xFeO_3$ (x = 0.118)	9%	0.92
$Bi_{(1-x)} Nd_xFeO_3$ (x = 0.177)	14.5%	0.96
$Bi_{(1-x)} Nd_xFeO_3$ (x = 0.235)	24.5%	0.91

X-ray diffraction analysis. Extended x-ray scans (from 20° to 80°) have been done to identify the deposited phase. The substrate STO 002 reflection peak was used as a reference to evaluate the doping impact on the deposited films. Only for BFO-Nd 14.5% low signal of Bi2O3 parasitic phase was measured, which correspond well to the previous morphological investigation. A zoomed part of the diffraction patterns (from 44.5° to 47°) around substrate

and film second order reflections is reported (Figure 17). BFO 002 theoretical diffraction peak is indicated. Second-order reflection of BFO-Nd 7%, 9%, 14.5% and 24.5% are respectively at 45.34°, 45.25°, 45.71°, and 45.77°. As Nd-doping concentration increases average size of the A-site decrease because of the substitution of Bi3+ by Nd3+, which has a smaller ionic radius (Bi^{3+} r$_{12\text{-coord}}$ = 1.36 Å and Nd^{3+} r$_{12\text{-coord}}$ = 1.31 Å) [51]. The reduction of the cell parameter causes the shift toward higher angles. However, for the lower doping content (7% and 9%) a shift toward lower angle angles is visible. A possible explanation of the general peak shift may be attributed to some internal strain, but this feature requires further investigation to fully explain the mechanism behind this phenomenon.
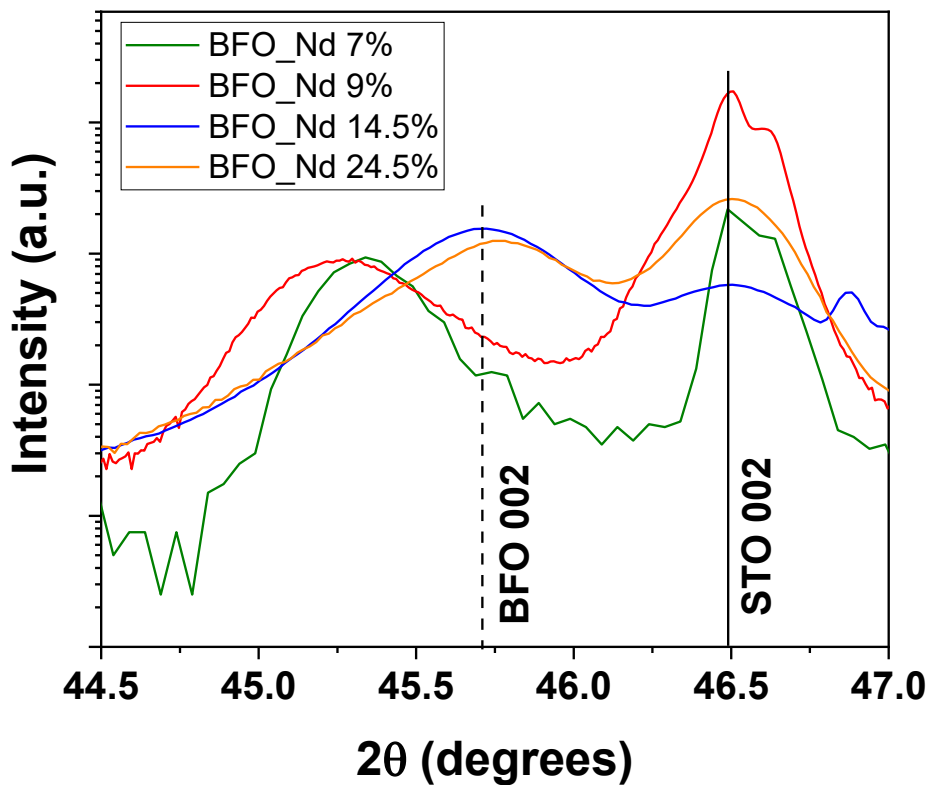
Figure 17. XRD ϑ-2ϑ patterns of the second-order reflection Nd-doped BFO films.

Optical bandgaps of the reported systems deposited on transparent undoped STO (100) substrate have been calculated using a UV-Vis spectrometer. From the measured optical absorption, the bandgap value was obtained using Tauc's equation, the film bandgaps were extrapolated from the plot of $(\alpha * h * v)^2$ vs $(h * v)$, see Chapter 3.1.5 [74,75].
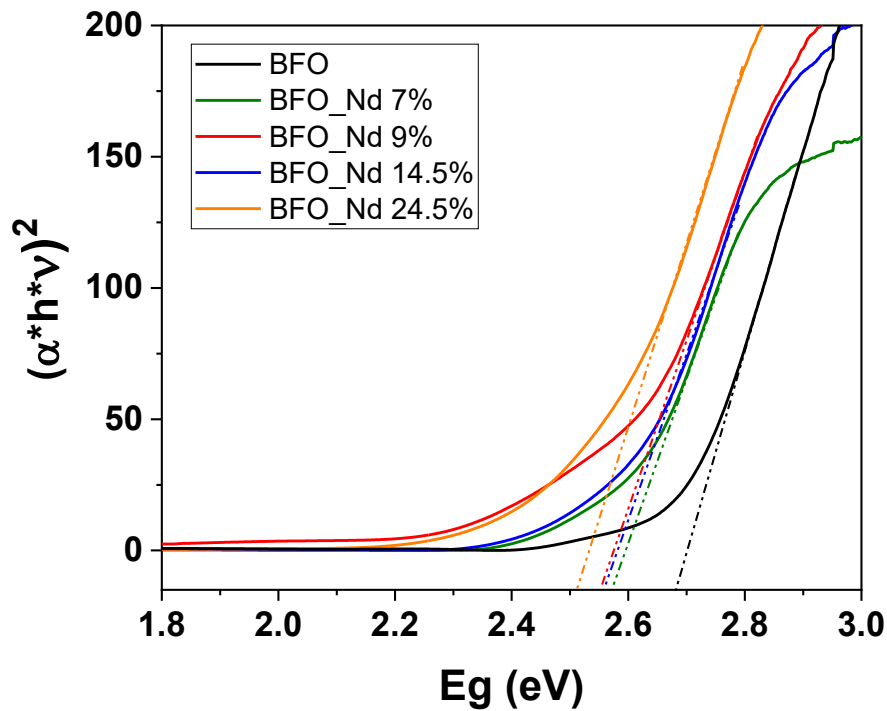
Figure 18. Tauc's plots of the undoped and Nd-doped BFO thin films calculated from UV-Vis absorption spectra.

Nd-doped BFO thin-film Tauc's plots have been compared to the one of pure BFO thin film to examine Nd-doping's influence on the material bandgap (Figure 18). As observed for Dy-doping, the first Nd-doping of 7% has a noticeable impact on the material bandgap, inducing a diminution of its value up to 2.57 eV. However, for Nd-doping of 9% and 14.5%, material bandgap modification is limited with identic values of 2.56 eV. Then, for the highest doping amount of 24.5%, a small decrease of the bandgap to 2.52 eV is noted (Table 8).

Table. 8 Summary table of the bandgap energy value for the different Nd-doped BFO films.

BFO-Nd 7%	2.57 eV
BFO-Nd 9%	2.56 eV
BFO-Nd 14.5%	2.56 eV
BFO-Nd 24.5%	2.52 eV

Figure 20 shows the semi-log plot of current versus voltage (I-V) for the pure and Nd-doped BFO thin films. For the measurement, STO:Nb was used as the bottom electrode, and an indium/aluminum top electrode was deposited on the film (*Configuration A*), a scheme of the studied structure is reported in Figure 19.
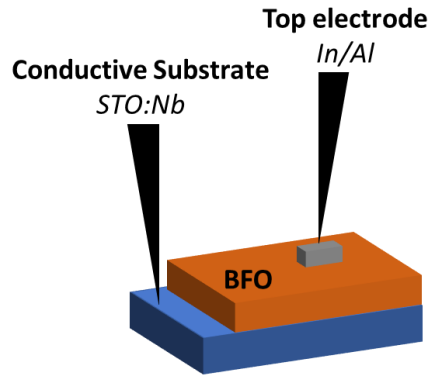
Figure 19. Schematic view of the investigated structure for (I-V) measurements in dark or under light.

BFO films and BFO-Nd 7% show good answers with a noticeable increase in the measured current between the dark or under light configuration. However, with the increase of Nd-doping, a decrease in terms of current output was measured. Moreover, Nd-doping also significantly impacts the leakage current reduction with a value of 1.14×10^{-7} A and 1.09×10^{-8} A for BFO and BFO-Nd 7% at -2V, respectively (Figure 20b). A close-up comparison of the BFO and BFO-Nd 7% I-V curve for the samples kept in the dark and under illumination is reported. Under dark conditions, pure BFO film shows a diodelike rectifying I-V behavior (Figure 20c). Under light, BFO displays, analogously to BFO-Nd 7%, (in the dark and under light) a good rectifying behavior (Figure 20c and d). As observed before, a substantial photoinduced current is measured in the two systems.
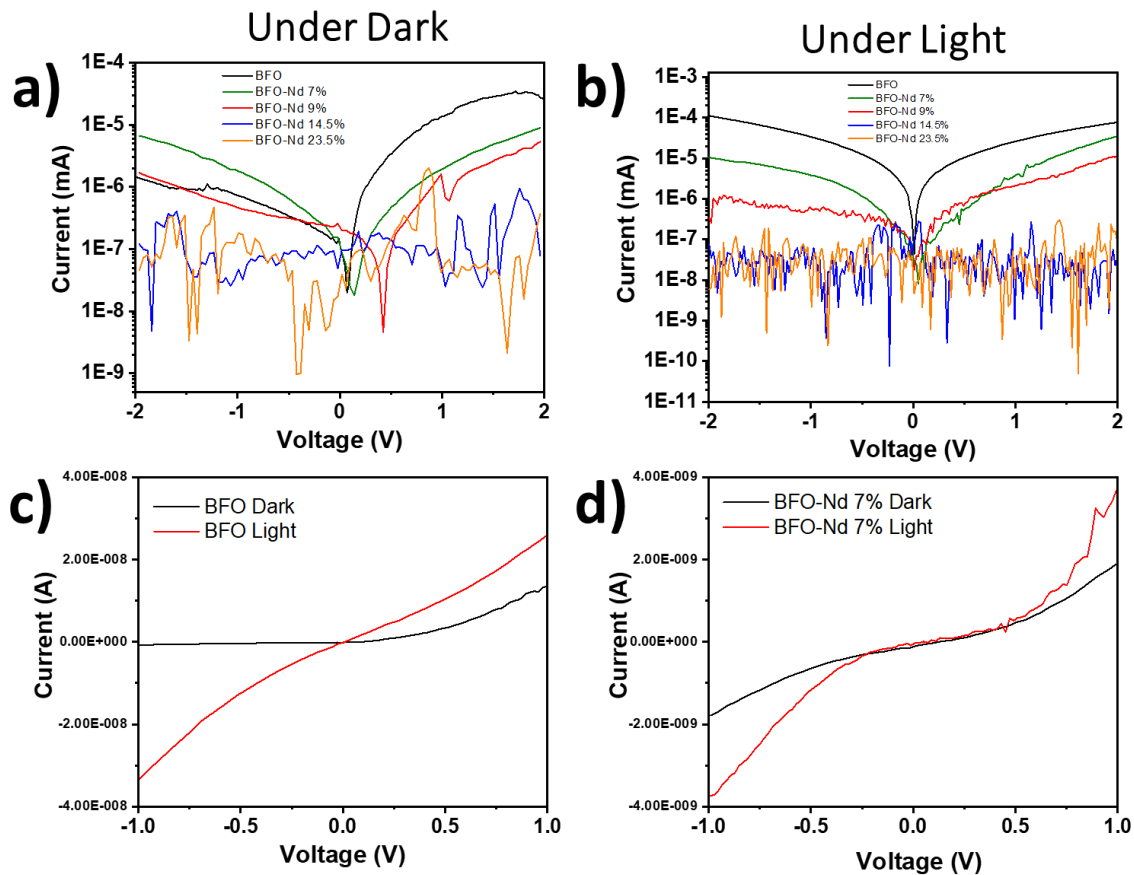
Figure 20. Semi-log plot (I-V) curves of the undoped and Nd-doped BFO thin films a) in dark or b) under light and comparison of (I-V) curves in dark/under-light of c) undoped BFO film and d) BFO-Nd 7% film.

75

3.2.2.   Yb-doping

MOCVD hot-wall reactor with one sublimation zone has been used to investigate the MOCVD process. The single-source precursor mixtures, of 250 mg, were composed of: Bi(phenyl)$_3$ and Fe(tmhd)$_3$ in a (*1:0.66*) ratio. Various amounts of Yb(hfa)$_3$diglyme were incorporated in the initial Bi:Fe mixture to achieve ytterbium doping. During the one-hour depositions, the substrate temperature was maintained at 750°C and the precursor mixture vaporized at 120°C. A constant flow of argon (150 mL/min) and oxygen (150mL/min) have been used as a carrier and reactant gas, respectively.

Films morphologies have been observed by field emission scanning electron microscopy (FE-SEM), and the film elemental compositions have been studied by energy dispersive X-ray analysis (EDX). Film structure and growth quality has been controlled by X-ray diffraction analysis (XRD). Finally, the Yb-doped films optical band gap has been calculated using UV-Vis spectroscopy, and the relation between dopant concentration and material bandgaps assessed. Samples are indexed by the Yb-doping percentage measured in the film.
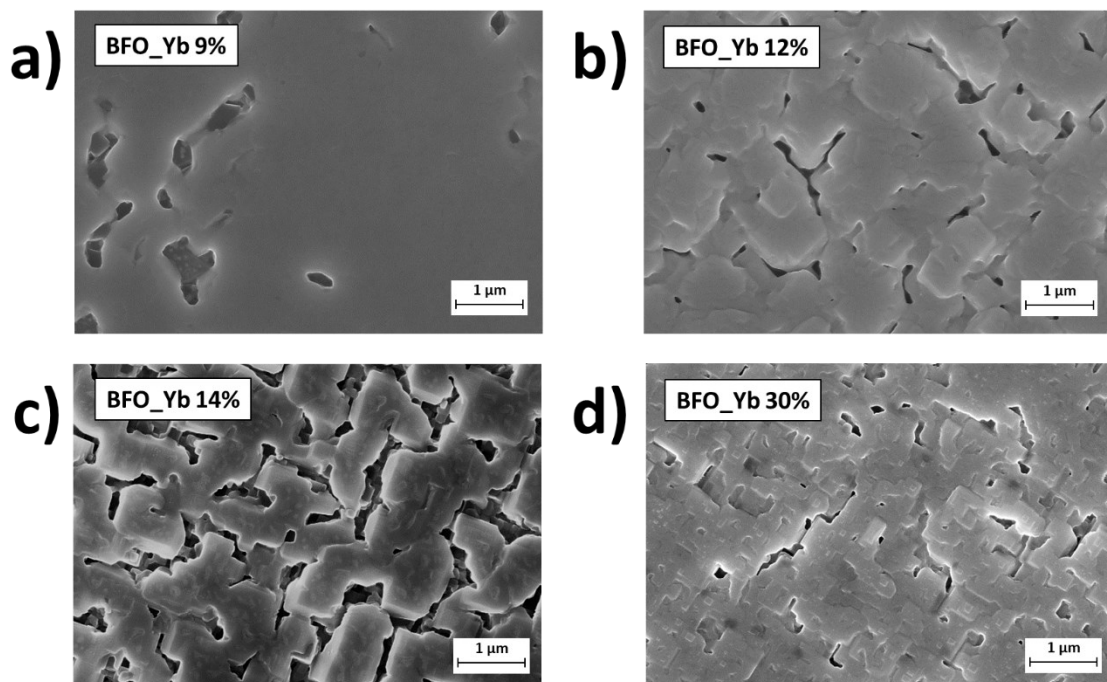
Figure 21. Secondary electron FE-SEM plan view images of a) BFO-Yb 9%, b) BFO-Yb 12%, c) BFO-Yb 14%, and d) BFO-Yb 30%.

Morphological characterization. Micrographs obtained by FE-SEM are reported in Figure 21. The morphology of BFO-Yb 9% is the more uniform and smoother observed between the deposited samples, even if complete coalescence is not achieved at some point of the film (Figure 21a). At higher doping concentration, 12% and 14% similar morphologies are visible with large 500 nm squared grains but, the coalescence is still not complete (Figure 21b and c).

For the BFO-Yb 30%, grains are still visible, but the surface quality is higher than the one obtained for the previous 12% and 14% doping.

The presence of Yb dopant in the film was confirmed using EDX. Two Sm peaks can be observed: M line at 1.29 keV and L_α line at 6.49 keV. No peak overlap is noticed, and precise quantification of the dopant has been possible. In Table 9 the nominal precursor compositions have been reported and correlated to the percentage of Yb-doping and to the (Bi+Yb) / Fe ratio in the films.

Table. 9 Relationship between precursor nominal composition and film stoichiometry based on EDX evaluation.

Precursor composition	Film stoichiometry	
	Yb/ (Yb + Bi)	(Bi + Yb) / Fe
$Bi_{(1-x)}Yb_xFeO_3$ (x = 0.088)	9%	1.06
$Bi_{(1-x)}Yb_xFeO_3$ (x = 0.118)	12%	0.98
$Bi_{(1-x)}Yb_xFeO_3$ (x = 0.177)	14%	1.08
$Bi_{(1-x)}Yb_xFeO_3$ (x = 0.235)	30%	0.93
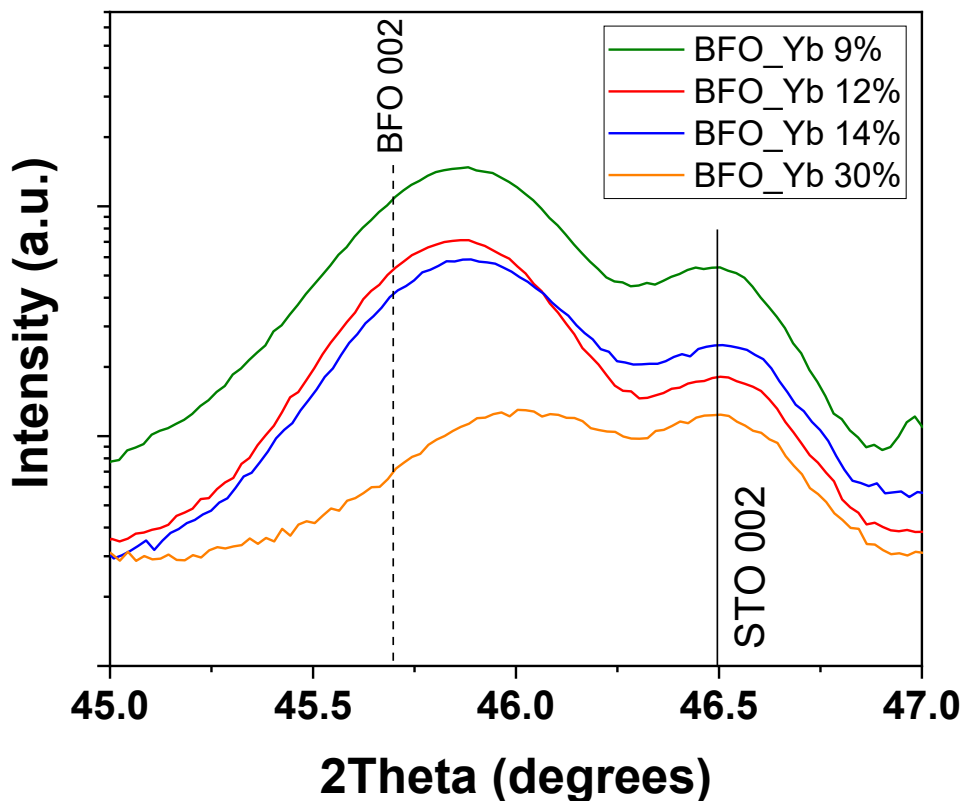
Figure 22. XRD ϑ-2ϑ patterns of the second-order reflection Yb-doped BFO films.

X-ray diffraction. Large XRD scans have revealed no secondary phases, with only visible the reflection peaks of the film and the substrates (00l) planes. In Figure 22. are reported the second-order reflection of the films and substrate at 45.86°, 45.86°, 45.87°, 46° for the BFO-Yb 9%, BFO-Yb 12%, BFO-Yb 14%, and BFO-Yb 30% respectively. The increase of Yb doping is visible because it induces a shift of the peaks toward higher angles, as the average A-site ionic radius is reduced when the smaller Yb^{3+} ($r_{12\text{-coord}}$ = 1.20 Å) substitute Bi^{3+} ($r_{12\text{-coord}}$ = 1.36 Å). [51] A broadening of the 002 reflection peak is also visible and increases with the quantity of Yb-doping.

Optical bandgap. A UV-Vis spectrometer has been used to measure the optical absorption of the BFO-Yb films deposited on undoped STO (100), a transparent substrate. From the optical absorption, the bandgap value was obtained using Tauc's equation [74,75]. The film bandgaps were extrapolated from the plot of $(\alpha*h*v)^2$ vs $(h*v)$, see Chapter 3.1.5.
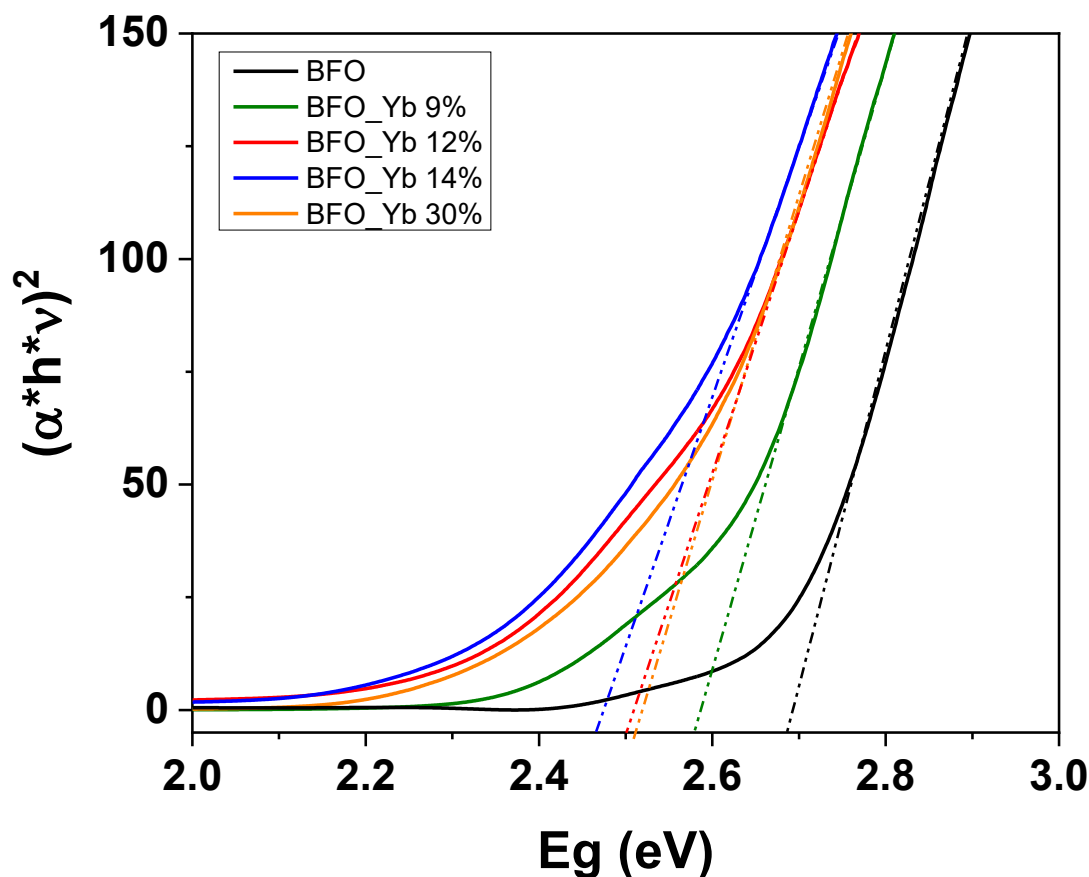
Figure 23. Tauc's plots of the undoped and Yb-doped BFO thin films calculated from UV-Vis absorption spectra.

BFO-Yb thin-film Tauc's plots have been compared to the one of pure BFO thin film (Figure 23). The influence of Yb doping on the material bandgap can be observed. As observed for Dy-doping, the first Yb-doping of 9% has a strong impact on the material bandgap, inducing an important reduction of its value up to 2.58 eV. Then, Yb-doping of 12% and 14% impact is also important with an optical bandgap value of 2.50 eV and 2.46 eV, respectively. Finally, for the highest doping amount of 30%, an increase of the bandgap to 2.51 eV is measured, indicating a limit in the bandgap tuning with Yb (Table 10).

Table. 10 Summary table of the bandgap energy value for the different Yb-doped BFO films.

BFO-Yb 9%	2.58 eV
BFO-Yb 12%	2.50 eV
BFO-Yb 14%	2.46 eV
BFO-Yb 30%	2.51 eV

3.3.   Sm-doping

An MOCVD approach similar to the one used for the previously presented systems has been applied. Depositions have been realized in a MOCVD hot-wall reactor with one sublimation zone for the vaporization of the precursor mixtures (250 mg). The mixtures consist of Bi(phenyl)$_3$ and Fe(tmhd)$_3$ in a (*1:0.66*) ratio in which an increased amount of Sm(hfa)$_3$diglyme is added to reach the desired concentrations in the film. Depositions have been carried out at 750°C and the precursor mixture vaporized at 120°C. A constant flow of argon (900 mL/min) and oxygen (150mL/min) have been used as carrier and reactant gas, respectively. Four different Sm-doping ratios have been achieved, and deposited films are reported with respect to their Sm-doping amount.

The produced samples have been sent to Ramesh's Lab at Berkley University for in-depth ferroelectric and piezoelectric characterizations. As requested to facilitate those measurements, film thickness has been reduced by a smaller deposition duration (15 minutes) and an increase of argon flow compared to previous experiments (from 150mL/min to 900 mL/min).

Film microstructures have been investigated through field emission scanning electron microscopy (FE-SEM) and their chemical quantification by energy dispersive X-ray analysis (EDX). Finally, identification of the deposited phases and control of the film out-of-plane orientations were studied by X-ray diffraction analysis (XRD). Ferroelectric and piezoelectric characterizations are still ongoing. A summary table of previous works on piezoelectric characterization of BiFeO$_3$ based systems is reported in Appendix 1.
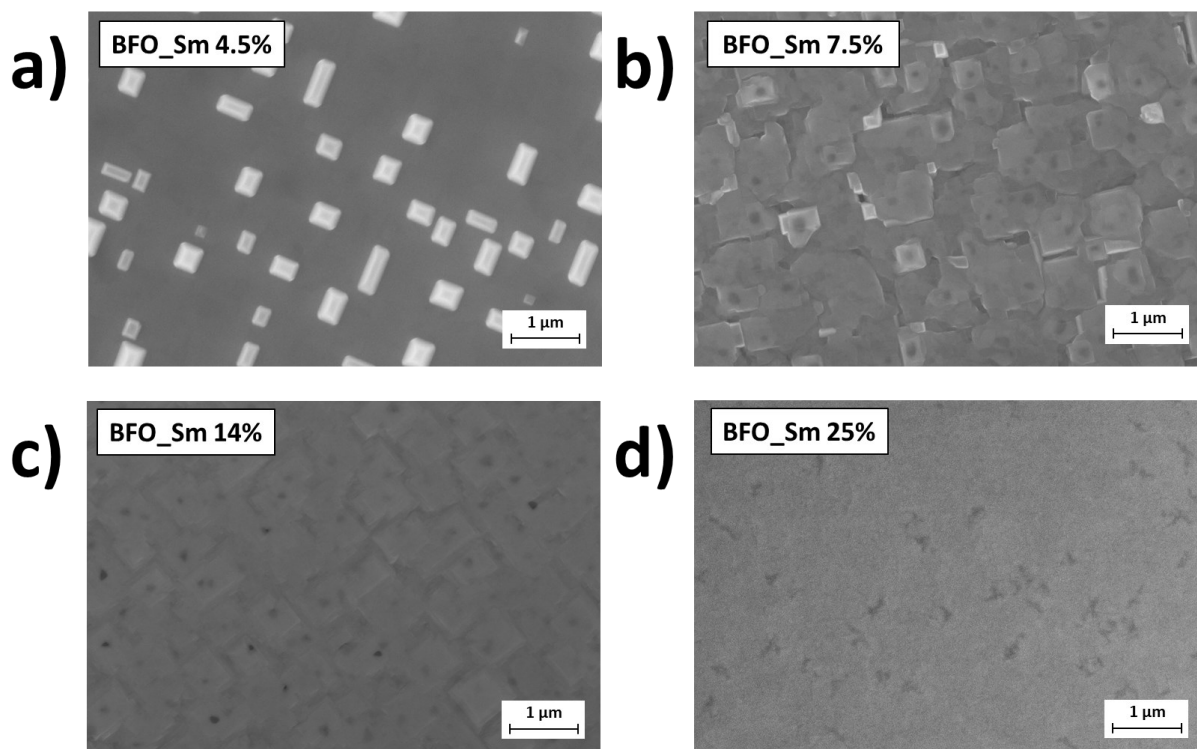
Figure 24. Secondary electron FE-SEM plan view images of a) BFO-Sm 4.5%, b) BFO-Sm 7.5%, c) BFO-Sm 14%, and d) BFO-Sm 25%

As it has been done for the other BFO based samples, FE-SEM observations have been used to observe the film morphologies for the different obtained Sm-doping concentrations. General film morphologies are very smooth and regular; only for BFO-Sm 4.5%, cubic shaped grains are noticed, typical of a Bi_2O_3 superficial parasitic phase. For BFO-Sm 7.5% and 14% microstructure is well defined with large square grains of about 1 μm. BFO-Sm 25% sample shows a homogeneous surface with few un-coalesced spots (darker on the images, see Figure 24.d). FE-SEM cross-section shows the impact of the high Ar flow rate and the reduced deposition time. The measured thickness of the as-deposited samples ranges between 120 to 150 nm (Figure 25.a). Coupled with the FE-SEM investigation, the film component atomic percentages have been assessed by EDX. Samarium percentages in the films with respect to bismuth ((Sm)/(Sm+Bi)) are already reported in the sample names; four concentrations have been achieved 4.5%, 7.5%, 14%, and 25%. Even for low doping concentration, a precise samarium quantification is possible because Sm L and M lines (5.633 keV and 1.078 keV, respectively) do not overlap with other element lines (Figure 25.b). Doping concentration does not significantly impact either film morphologies or thickness.
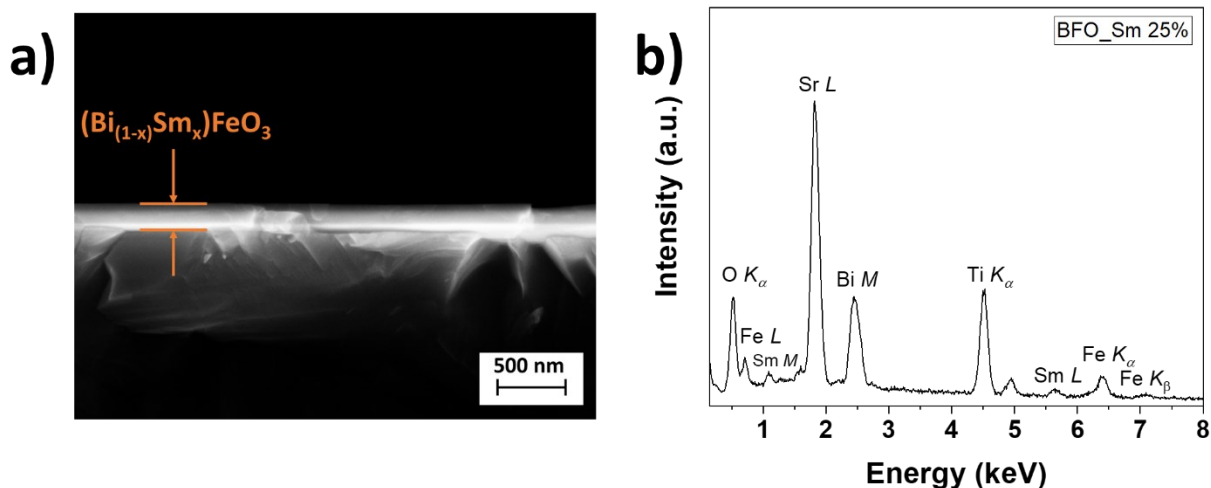
Figure 25. a) FE-SEM cross- section image of the deposited Sm-doped BFO thin films and b) EDX spectra of BFO-Sm 30%.
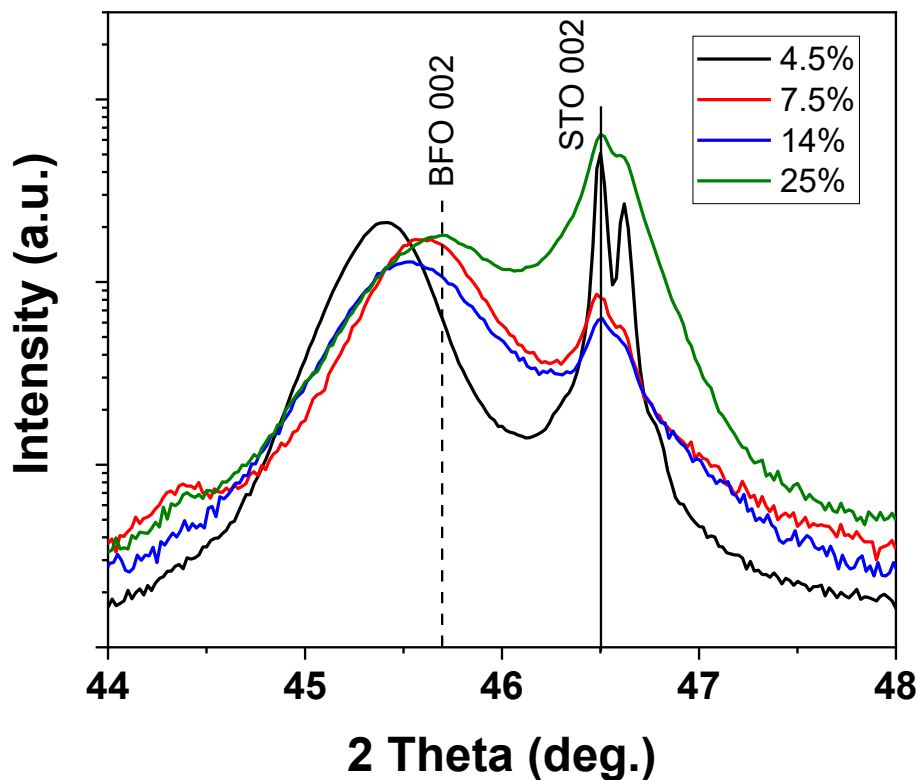
Figure 26.. XRD ϑ-2ϑ patterns of the second-order reflection Sm-doped BFO films.

X-ray diffraction analysis. Large x-ray scans (from 20° to 80°) have been done on the reported samples to confirm the deposited phases. All films show great out-of-plane alignment in the [001] direction. To compare films, diffraction patterns have been centered around the STO 002 diffraction peak at 2θ=46.485°. Only for BFO-Sm 4.5% small amount of Bi_2O_3 is visible, and no other phases have been observed. In Figure 26. a close-up between 44° and 48° shows the second-order reflection of the films and substrate (00l) plane. BFO 002 theoretical diffraction peak position is indicated at 2θ=45.69°. The 002 diffractions peaks of BFO-Sm 4.5%, 7.5%, 14%,

and 25% are respectively at 45.41°, 45.53°, 45.60°, and 45.69°. The reduction of the cell parameter causes the shift toward higher angles because of the substitution of Bi^{3+} by Sm^{3+}, which has a smaller ionic radius (Bi^{3+} $r_{12\text{-coord}}$ = 1.36 Å and Sm^{3+} $r_{12\text{-coord}}$ = 1.28 Å) [51]. An increase in the peak width is also visible as the Sm concentration rises. However, especially for lower doping concentration, a substantial shift toward lower angles is noted. Wang et al. [29] have reported a similar behavior for BFO thin films grown on STO with increased film strain while its thickness decreases. As the deposited films are 120-150 nm, a similar phenomenon is observed.

3.4. Conclusions

The main aim of the present study is to determine if dense films of undoped and Dy-doped $BiFeO_3$, as deposited on STO:Nb (100) through a simple, industrially appealing MOCVD route, may be integrated as lead-free pyroelectric energy harvester. Thus, ferroelectric, dielectric and pyroelectric properties of $Bi_{1-x}Dy_xFeO_3$ (x = 0, 0.06, 0.08 and 0.11) thin films have been investigated. An extraordinary high pyroelectric coefficient of 188 µC/(m² K) has been found for the undoped BFO film, an indication of the possible self-poling and the high quality, of the epitaxial films grown by MOCVD. Dy^{3+} substitution has been shown to lead to a large increase of pyroelectric properties with respect to the undoped system. A giant value of the pyroelectric coefficient of 426 µC/(m² K) has been achieved for the 8% Dy^{3+} doping. Above this concentration, pyroelectric properties start to degrade. The presently found pyroelectric coefficients are significantly higher than those reported in the literature and the figure of merit values for energy harvesting are impressively promising. In fact, the obtained F_E value of 82 J/(m³ K²) for the BDFO-8% sample, is a striking improvement with respect to the previously highest reported value of F_E = 17 J/(m³ K²) for a $Bi_{1-x}Sm_xFeO_3$ ceramic sample.

Other lanthanide dopings have been carried out in this part. Neodymium and ytterbium have been investigated for the tuning of $BiFeO_3$ photovoltaic properties. Pure $BiFeO_3$ and solid solutions of $Bi_{1-x}Nd_xFeO_3$ (x = 0.07, 0.09, 0.145 and 0.245) and, $Bi_{1-x}Yb_xFeO_3$ (x = 0.09, 0.12, 0.14 and 0.30) have been prepared by MOCVD on 1 cm x 1cm STO:Nb (100) conductive substrate. Prepared samples have been sent to Dr. David Munoz-Rojas and Abderrahime Sekkat at LMGP to investigate their photovoltaic properties. Preliminary results show the moderate influence of Nd-doping on $BiFeO_3$ properties even though it helps reducing leakage current. According to the bandgap measurements, Yb-doping seems to have a more defined impact on the film photovoltaic response.

The last type of the lanthanide used to substitute Bi^{3+} ions in the $BiFeO_3$ perovskite structure was samarium. Interest in this doping was brought to us by Prof. Ramamoorthy Ramesh (University of California, Berkeley). An MOCVD approach, similar to those previously described, has been used to prepare thinner 100-150 nm films of pure $BiFeO_3$ and $Bi_{1-x}Sm_xFeO_3$ (x = 0.09, 0.12, 0.14 and 0.30) solid solutions. Classical morphological and

structural characterization has been reported. Ferroelectric and piezoelectric characterizations are still ongoing.

The very appealing and excellent properties reported in this study indicate that the presently described, straightforward and facile MOCVD synthetic route produces high quality epitaxial BFO and Ln-doped BFO thin films, which may be envisaged as lead-free materials of choice for energy harvesting.

References

[1] G. Catalan, J.F. Scott, Physics and Applications of Bismuth Ferrite. Adv. Mater. 21 (2009) 2463–2485.

[2] T. Choi, S. Lee, Y.J. Choi, V. Kiryukhin, S.-W. Cheong, Switchable ferroelectric diode and photovoltaic effect in BiFeO$_3$. Science 324 (2009) 63–66.

[3] A. Queraltó, R. Frohnhoven, S. Mathur, A. Gómez, Intrinsic piezoelectric characterization of BiFeO$_3$ nanofibers and its implications for energy harvesting, Appl. Surf. Sci. 509 (2020) 144760/1–144760/8.

[4] J. Yun J, G. Tiantian, L.W. Zhong, Y. Ya, Configuration design of BiFeO$_3$ photovoltaic devices for self-powered electronic watch, Nano Energy 64 (2019) 103909/1-103909/9.

[5] J. Seo-Hyeon, L. Sung-Gap, L. Seung-Hwan, Structural and pyroelectric properties of sol–gel derived multiferroic BFO thin films Mater. Res. Bull. 47 (2012) 409–412.

[6] R. L. Lyer, C. B. Roundy, Pyroelectric coefficient direct measurement technique and application to a NSE response time detector, IEEE Trans. Sonics & Ultrasonics 19 (1972) 333-338.

[7] H. Hongyin, L. Xi, H. Emil, C. Chao, Z. Hao, L. Li, Advances in lead-free pyroelectric materials: a comprehensive review, J. Mater. Chem. C (2020) 8, 1494.

[8] Y. Yang, W. Guo, K. C. Pradel, G. Zhu, Y. Zhou, Y. Zhang, Y. Hu, L. Lin, Z. L. Wang, Pyroelectric nanogenerators for harvesting thermoelectric energy, Nano Lett. (2012) 12, 2833–2838.

[9] G.T Hwang, V. Annapureddy, J.H. Han, D.J. Joe, C. Baek, D.Y Park, D.H. Kim, J.H. Park, C.K. Jeong, K.-I. Park, C.K. Jeong Kwi-Il Park, J.J Choi, J.D. Kyung, K.J. Ryu, K.J. Let, Self-Powered Wireless Sensor Node Enabled by an Aerosol-Deposited PZT Flexible Energy Harvester, Adv. Energy Mater. (2016) 6, 1600237/1–1600237/9.

[10] P. Muralt, R.G. Polcawich, S. Trolier-McKinstry, Piezoelectric thin films for sensors, actuators, and energy harvesting, MRS Bulletin (2009) 34, 658–664.

[11] L. Zhang, Y.L. Huang, G. Velarde, A. Ghosh, S. Pandya, D. Garcia, R. Ramesh, L.W. Martin, Enhanced pyroelectric properties of Bi$_{1-x}$La$_x$FeO$_3$ thin films APL Mater. 7 (2019) 111111.

[12] Y.B. Yao, W.C. Liu, C.L. Mak, Pyroelectric properties and electrical conductivity in samarium doped BiFeO$_3$ ceramics, J. Alloys Comp. 527 (2012) 157– 162.

[13] Wei Zhang, Ming-Min Yang, Xiao Liang, Hai-Wu Zheng, Yu Wang, Wen-Xiu Gao, Guo-Liang Yuan, Wei-Feng Zhang, Xiao-Guang Li, Hao-Su Luo, Ren-Kui Zheng, Piezo strain-enhanced photovoltaic effects in BiFeO$_3$/La0.$_7$Sr$_{0.3}$MnO$_3$/PMN-PT heterostructures, Nano Energy 18 (2015) 315-324.

[14] G. Clementi, G. Lombardi, S. Margueron, M.A. Suarez, E. Lebrasseur, S. Ballandras, J. Imbaud, F. Lardet-Vieudrin, L. Gauthier-Manuel, B. Dulmet, M. Lallart, A. Bartasyte, LiNbO$_3$ films − A low-cost alternative lead-free piezoelectric material for vibrational energy harvesters, Mech. Syst. Signal Proc. 149 (2021) 107171.

[15] A. Almirall, S. Oliveri, W. Daniau, S. Margueron, T. Baron, P. Boulet, S. Ballandras, S. Chamaly, A. Bartasyte, A. High-frequency surface acoustic wave devices based on epitaxial Z-LiNbO$_3$ layers on sapphire. Appl. Phys. Lett. 114 (2019) 162905/1–162905/5.

[16] G. Clementi, S. Margueron, M.A. Suarez, T. Baron, B. Dulmet, A. Bartasyte, Piezoelectric and Pyroelectric Energy Harvesting from Lithium Niobate Films, J. Phys.: Conf. Ser. (2019) 1407 012039.

[17] A. Tkach, A. Santos, S. Zlotnik, R. Serrazina, O. Okhay, I. Bdikin, M.E. Costa, P.M. Vilarinho, Effect of Solution Conditions on the Properties of Sol–Gel Derived Potassium Sodium Niobate Thin Films on Platinized Sapphire Substrates, Nanomaterials 9 (2019), 1600.

[18] G. Vats, A. Chauhan, R. Vaish, Thermal Energy Harvesting Using Bulk Lead-Free Ferroelectric Ceramics, Int. J. Appl. Ceram. Technol. 12 (2015), E49–E54.

[19] A. Kumar, A. Sharma, R, Kumar, R. Vaish, V.S. Chauhan, Finite element analysis of vibration energy harvesting using lead-free piezoelectric materials: A comparative study, J. Asian Ceram. Soc. 2 (2014) 139–143.

[20] J.V Vidal, A.V. Turutin, I.V Kubasov, A.M. Kislyuk, M.D. Malinkovich, Y.N. Parkhomenko, S.P. Kobeleva, O.V. Pakhomov, N.A. Sobolev, A.L. Kholkin, Low-Frequency Vibration Energy Harvesting with Bidomain $LiNbO_3$ Single Crystals, IEEE T Ultrason. Ferr. 66 (2019) 1480–1487.

[21] T. Yoshimura, S. Murakami, K. Wakazono, K. Kariya, N. Fujimura, Piezoelectric Vibrational Energy Harvester Using Lead-Free Ferroelectric $BiFeO_3$ Films, Appl. Phys. Express 6 (2013) 051501.

[22] M. Aramaki, T. Yoshimura, S. Murakami, K. Satoh, N. Fujimura, Demonstration of high-performance piezoelectric MEMS vibration energy harvester using $BiFeO_3$ film with improved electromechanical coupling factor, Sens. Actuat. A-Phys. 291 (2019) 167–173.

[23] L. Haitao, C.S. Lin Koh, Y.H. Lee, Y. Zhang, G.C. Phan-Quang, C. Zhu, Z. Liu, Z. Chen, H.Y. Fan Sim, C.L. Lay, Q. An, X.Y. Ling, A wearable solar-thermal-pyroelectric harvester: Achieving high power output using modified rGO-PEI and polarized PVDF, Nano Energy 73 (2020) 104723.

[24] J. Ma, J. Ren, Y. Jia, Z. Wu, L. Chen, N.O. Haugen, H. Huang, Y. Lieu, High efficiency bi-harvesting light/vibration energy using piezoelectric zinc oxide nanorods for dye decomposition, Nano Energy 62 (2019) 376–383.

[25] Paul Muralt, Micromachined infrared detectors based on pyroelectric thin films, Rep. Prog. Phys. 64 (2001) 1339.

[26] Y. Yao, W. Liu, Y. Chan, C. Leung, C. Mak, B. Ploss, Studies of Rare-Earth-Doped $BiFeO_3$ Ceramics, Int. J. Appl. Ceram. Technol. 8 (2011) 5, 1246–1253.

[27] J. T. Heron, D. G. Schlom, R. Ramesh, Electric field control of magnetism using $BiFeO_3$-based heterostructures, Appl. Phy. Rev. 1 (2014) 021303.

[28] M. M. Saj Mohan, S. Bandyopadhyay, T. Jogi, S. Bhattacharya, R. Ramadurai, Realization of rhombohedral, mixed, and tetragonal like phases of $BiFeO_3$ and ferroelectric domain engineering using a strain tuning layer on $LaAlO_3$(001) substrate, J. Appl. Phys. 125 (2019) 012501/1-012501/11.

[29] J. Wang, J. B. Neaton, H. Zheng, V. Nagarajan, S. B. Ogale, B. Liu, D. Viehland, V. Vaithyanathan, D. G. Schlom, U. V. Waghmare, N. A. Spaldin, K. M. Rabe, M. Wuttig, R. Ramesh, Epitaxial $BiFeO_3$ Multiferroic Thin Film Heterostructures, Science 299 (2003) 1719-1722.

[30] H. Zhu, X. Sun, L. Kang, M. Hong, M. Liu, Z. Yu, J. Ouyang, Charge transport behaviors in epitaxial $BiFeO_3$ thick films sputtered with different Ar/O_2 flow ratios, Scripta Mater. 115 (2016) 62–65.

[31] C.S. Tu, P.Y. Chen, C.S. Chen, C.Y. Lin, V.H. Schmidt, Tailoring microstructure, and photovoltaic effect in multiferroic Nd substituted $BiFeO_3$ ceramics by processing atmosphere modification, J. Europ. Cer. Soc. 38 (2018) 1389-1398.

[32] S. Hohenberger, J.K. Jochum, M. J. Van Bael, K. Temst, C. Patzig, T. Höche, M. Grundmann, M. Lorenz, Enhanced Magnetoelectric Coupling in $BaTiO_3$-$BiFeO_3$ Multilayers—An Interface Effect, Materials 13 (2020) 197.

[33] C. Jin, W. Geng, L. Wang, W. Han, D. Zheng, S. Hu, M. ye, Z. Xu, Y. Ji, J. Zhao, Z. Chen, G. Wang, Y. Tang, Y. Zhu, X. Ma, L. Chen, Tuning Ferroelectricity and Ferromagnetism in $BiFeO_3$/$BiMnO_3$ Superlattices, Nanoscale 12 (2020) 9810-9816.

[34] C.H. Yang, D. Kan, I. Takeuchi, V. Nagarajan, J. Seidel, Doping $BiFeO_3$: approaches and enhanced functionality, Phys. Chem. Chem. Phys. 14 (2012), 15953–15962.

[35] M. R. Catalano, G. Spedalotto, G.G. Condorelli, G. Malandrino, MOCVD Growth of Perovskite Multiferroic $BiFeO_3$ Films: The Effect of Doping at the A and/or B Sites on the Structural, Morphological and Ferroelectric Properties, Adv. Mater. Interfaces 4 (2017) 1601025.

[36] A. Radojković, D.L. Golić, J. Ćirković, Z.M. Stanojević, D. Pajić, F. Torić, A. Dapčević, P. Vulić, Z. Branković, G. Branković, Tuning of $BiFeO_3$ multiferroic properties by light doping with Nb, Ceramics International (2018) 16739-16744.

[37] T. Zheng, J. Wu, Perovskite $BiFeO_3$–$BaTiO_3$ Ferroelectrics: Engineering Properties by Domain Evolution and Thermal Depolarization Modification, Adv. Electron. Mater. 6, 5 (2020) 2000079/1-2000079/10.

[38] G. Tian, S. Ojha, S. Ning, X. Gao, C.A. Ross, Structure, Ferroelectricity, and Magnetism in Self-Assembled $BiFeO_3$–$CoFe_2O_4$ Nanocomposites on (110)-$LaAlO_3$ Substrates, Adv. Electron. Mater. 5 (2019) 1900012/1–1900012/8.

[39] Y. Zhou, C. Wang, S. Tian, X. Yao, C. Ge, E.J. Guo, M. He, G. Yang, K. Jin, Switchable ferroelectric diode and photovoltaic effects in polycrystalline $BiFeO_3$ thin films grown on transparent substrates. Thin Solid Films 698 (2020) 137851/1–137851/6.

[40] G.G. Condorelli, M.R. Catalano, E. Smecca, R. Lo Nigro, G. Malandrino, Piezoelectric domains in $BiFeO_3$ films grown via MOCVD: Structure/property relationship, Surf. Coat. Technol. 230 (2013) 168–173.

[41] N. Deepak, P. Carolan, L. Keeney, P.F. Zhang, M.E. Pemble, R.W. Whatmore, Bismuth Self-Limiting Growth of Ultrathin $BiFeO_3$ Films. Chem. Mater. 27 (2015) 6508–6515.

[42] Q. Micard, A. L. Pellegrino, R. Lo Nigro, A. Bartasyte, G. G. Condorelli, G. Malandrino, Piezoelectric Ba and Ti co-doped $BiFeO_3$ textured films: selective growth of solid solutions or nanocomposites, J. Mater. Chem. C 8 (2020) 16168-16179.

[43] Q. Micard, G. G. Condorelli, G. Malandrino, Piezoelectric $BiFeO_3$ Thin Films: Optimization of MOCVD Process on Si. Nanomaterials 10 (2020) 630.

[44] H. Zhu, Y. Zhao, Y. Wang, Orientation dependent leakage current behaviors and ferroelectric polarizations of off-axis sputtered $BiFeO_3$ thin films, J. Alloys Comp. 803 (2019) 942–949.

[45] P. Hou, B. Liu, Z. Guo, P. Zhou, B. Wang, L. Zhao, Effect of Ho doping on the crystal structure, surface morphology and magnetic property of $BiFeO_3$ thin films prepared via the sol-gel technology. J. Alloys Comp. 775 (2019) 59–62.

[46] N. Sheoran, A. Kumar, V. Kumar, A. Banerjee, Structural, Optical, and Multiferroic Properties of Yttrium (Y^{3+})-Substituted $BiFeO_3$, Nanostructures. J. Supercond. Nov. Magn. 7 (2020) 2017-2029.

[47] C. Xuemei, H. Guangda, Y. Jing, W. Xi, Y. Changhong, W. Weibing, Enhanced multiferroic properties of (110)-oriented $BiFeO_3$ film deposited on $Bi_{3.5}Nd_{0.5}Ti_3O_{12}$-buffered indium tin oxide/Si substrate, J. Phys. D Appl. Phys. 41 (2008) 225402/1–225402/5.

[48] G. Malandrino, I. L. Fragala, Lanthanide "second-generation" precursors for MOCVD applications: Effects of the metal ionic radius and polyether length on coordination spheres and mass-transport properties, Coord. Chem. Rev. 250 (2006) 1605-1620.

[49] S. K. Singh, K. Maruyama, H. Ishiwara, Frequency-Dependent Polarization in $BiFeO_3$ Thin Films, Integrated Ferroelectrics 97 (2008) 83–89.

[50] M. Davis, D. Damjanovic, N. Setter, Pyroelectric properties of $(1–x)Pb(Mg_{1/3}Nb_{2/3})O_3$-$xPbTiO_3$ and $(1–x)Pb(Zn_{1/3}Nb_{2/3})O_3$-$xPbTiO_3$ single crystals measured using a dynamic method, J. Appl. Phys. 96 (2004) 2811-2815.

[51] Y. Q. Jia, Crystal Radii and Effective Ionic Radii of the Rare Earth Ions, J. Solid State Chem. 95 (1991) 184-187.

[52] T. Durga Rao, T. Karthik, S. Asthana, Investigation of structural, magnetic, and optical properties of rare earth substituted bismuth ferrite, J. Rare Earths 31 (2013) 370-375.

[53] C.H. Yang, D. Kan, I. Takeuchi, V. Nagarajand, J. Seidel, Doping $BiFeO_3$: approaches and enhanced functionality, Phys. Chem. Chem. Phys. 14 (2012) 15953–15962.

[54] V. A. Khomchenko, D. V. Karpinsky, A. L. Kholkin, N. A. Sobolev, G. N. Kakazei, J. P. Araujo, I. O. Troyanchuk, B.F.O. Costa, J. A. Paixão, Rhombohedral-to-orthorhombic transition and multiferroic properties of Dy substituted $BiFeO_3$, Journal of Applied Physics 108 (2003) 074109.

[55] M. Muneeswaran, N. V. Giridharan, Effect of Dy-substitution on the structural, vibrational, and multiferroic properties of $BiFeO_3$ nanoparticles, Journal of Applied Physics 115 (2014) 214109.

[56] D. Rout, K.S. Moon, and S.-J. L. Kang, Temperature dependent Raman Scattering Studies of Polycrystalline BiFeO3 Bulk Ceramics J. Raman Spectrosc. **40** (2009) 618-26

[57] M. K. Singh, S. Ryu, H. M. Jang, Polarized Raman scattering of multiferroic BiFeO3 thin films with pseudo-tetragonal symmetry, Phys. Rev. B **72** (2005) 132101

[58] M. N. Iliev, M. V. Abrashev, D. Mazumdar, V. Shelke, A. Gupta, Polarized Raman spectroscopy of nearly tetragonal BiFeO3 thin films, Phys. Rev. B 82 (2010) 014107

[59] G.L. Yuan, S.W. Or, H.L. W.Chan, Structural transformation and ferroelectric–paraelectric phase transition in Bi1–x Lax FeO3 (x = 0–0.25) multiferroic ceramics, J. Phys. D 40 (2007) 1196

[60] Claus, R., Merten, L. & Brandmüller, J. Light Scattering by Phonon-Polaritons, Springer, Berlin (1975).

[61] E. Borissenko, M. Goffinet, A. Bosak, P. Rovillain, M. Cazayous, D. Colson, P. Ghosez, M. Krisch, Lattice dynamics of multiferroic BiFeO3 studied by inelastic x-ray scattering, J. Phys. Condens. Matter 2013, 25, 102201

[62] J. Hlinka, J. Pokorny, S. Karimi, I. M. Reaney, Angular dispersion of oblique phonon modes in $BiFeO_3$ from micro-Raman scattering, Phy. Rev. B 23 (2011) 020101

[63] H. Fukumura, S. Matsui, H. Harima, T. Takahashi, T. Itoh, K. Kisoda, M. Tamada, Y. Noguchi, M. Miyayama, Observation of phonons in multiferroic $BiFeO_3$ single crystals by Raman scattering, J. Phys.: Condens. Matter 19 (2007) 365224

[64] A. Talkenberger, I. Vrejoiu, F. Johann, C. Röder, G. Irmer, D. Rafaja, G. Schreiber, J. Kortus, C. Himcinschi, Raman spectroscopic investigations of epitaxial $BiFeO_3$ thin films on rare earth scandate substrates, J. Raman Spectrosc. 46 (2015) 1245–1254

[65] C. Himcinschi, J. Rix, C. Röder, M. Rudolph, M. Yang , D. Rafaja, J. Kortus, M. Alexe, Ferroelastic domain identification in $BiFeO_3$ crystals using Raman spectroscopy, Scientific Report 9 (2019) 379

[66] M. I. Aroyo, J. M. Perez-Mato, D. Orobengoa, E. Tasci, G. de la Flor, A. Kirov, Crystallography online: Bilbao Crystallographic Server, Bulg. Chem. Commun. 43 (2011) 2 183-197 Scopus Web of Science

[67] K. Streiffer, C. B. Parker, A. E. Romanov, M. J. Lefevre, L. Zhao, J. S. Speck, W. Pompe, C. M. Foster, G. R. Bai, Domain patterns in epitaxial rhombohedral ferroelectric films. I. Geometry and experiments, J. Appl. Phys. (1998) 83 5.

[68] M. K. Singh, Hyun M. Jang, S. Ryu, M. Jo, Polarized Raman scattering of multiferroic $BiFeO_3$ epitaxial films with rhombohedral R3c symmetry, Applied Physics Letters 88 (2006) 042907

[69] R. Palai, H. Schmid, J. F. Scott, R. S. Katiyar, Raman spectroscopy of single-domain multiferroic $BiFeO_3$, Phys. Rev. B 81 (2010) 139903

[70] C. Beekman, A. A. Reijnders, Y. S. Oh, S.W. Cheong, K. S. Burch, Raman study of the phonon symmetries in $BiFeO_3$ single crystals, Phys. Rev. B 86 (2012) 020403

[71] M. P. Seah in "Practical Surfaces Analysis, vol. 1, " D. Briggs, M.P. Seah , (Eds.) WILEY-VCH, Weinheim, Germany, 1995, p 201.

[72] N. Q. Lam, Ion bombardment effects on the near-surface composition during sputter profiling, Surf. Interface Anal. 12 (1988) 65-77.

[73] W.R. Victor, M. Arumugam, T. Pandirengan, M. Durairaj, R.R. Varimalla, Multiferroic Consequence of Porous $(BiFeO_3)_x$–$(BiCrO_3)_{1-x}$ Composite Thin Films by Novel Sol–Gel Method, Acta Metall. Sin. 31 (2017) 299-307.

[74] J. Tauc, R. Grigorovic, A. Vancu, Optical Properties and Electronic Structure of Amorphous Germanium, Phys. Stat. Sol. 15 (1966) 627

[75] B.D. Viezbicke, S. Patel, B. E. Davis, D. P. Birnie, Evaluation of the Tauc Method for Optical Absorption Edge Determination: ZnO Thin Films as a Model System, Physica Status Solidi B 252 (2015) 1700-1710

[76] D. Sando, C. Carrétéro, M. N. Grisolia, A. Barthélémy, V. Nagarajan, M. Bibes, Revisiting the Optical Band Gap in Epitaxial BiFeO$_3$ Thin Films, Adv. Optical Mater. (2017) 1700836

[77] G. L. Yuan, S.W. Or, Enhanced piezoelectric and pyroelectric effects in single-phase multiferroic Bi$_{1-x}$Nd$_x$FeO$_3$ (x=0–0.15) ceramics, Appl. Phys. Lett. 88 (2006) 062905.

[78] M. Daglish, A dynamic method for determining the pyroelectric response of thin films, Integrated Ferroelectrics 22 (1998) 473–488.

[79] S. Jachalke, E. Mehner, H. Stöcker, J. Hanzig, M. Sonntag, T. Weigel, T. Leisegang, and D. C. Meyer, How to measure the pyroelectric coefficient? Appl. Phys. Rev. 4 (2017) 021303.

[80] C. R. Bowen, J. Taylor, E. Le Boulbar, D. Zabek, A. Chauhan, R. Vaish, Pyroelectric materials and devices for energy harvesting applications, Energy Environ. Sci. 7 (2014) 3836-3856.

[81] R. Moalla, B. Vilquin, G. Saint-Girons, G. Le Rhun, E. Defay, G. Sebald, N. Baboux, R. Bachelet, Huge gain in pyroelectric energy conversion through epitaxy for integrated self-powered nanodevices, Nano Energy 41 (2017) 43-48.

[82] Y.W. Li, J.L. Sun, J. Chen, X.J. Meng, J.H. Chu, Preparation and characterization of BiFeO$_3$ thin films grown on LaNiO$_3$-coated SrTiO$_3$ substrate by chemical solution deposition, J. Cryst. Growth 285 (2005) 595–599.

[83] Y. Yaoa, T. Tao, B. Liang, C.L. Mak, S.G. Lu, Pyroelectric properties, and AC impedance study of bismuth ferrite (BiFeO$_3$) ceramics, Ceram. Int. 45 (2019) 1308-1313.

[84] Y. Yao, B. Ploss, C.L. Mak, K.H. Wong, Pyroelectric properties of BiFeO$_3$ ceramics prepared by a modified solid-state-reaction method, Appl. Phys. A 99 (2009) 211–216.

[85] T. Takenaka, K. Sakata, Pyroelectric properties of Grain-Oriented Bismuth Layer-Structured Ferroelectric Ceramics, Jpn. J. Appl. Phys. 22 (1983) 53-56.

[86] J. Kim, S. Yamanaka, A. Nakajima, T. Katou, Y. Kim, T. Fukuda, K. Yoshii, Y. Nishihata, M. Baba, M. Takeda, N. Yamada, T. Nakayama, K. Niihara, H. Tanaka, Pyroelectric power generation with ferroelectrics (1-x)PMN-xPT, Ferroelectrics, 512 (2017) 92-99.

[87] G. Chen, J. Chen, W. Pei, Y. Lu, Q. Zhang, Q. Zhang, Y. He, Bismuth ferrite materials for solar cells: Current status and prospects, Materials Research Bulletin 110 (2019) 39–49.

[88] Y. Yuan, Z. Xiao, B. Yang, J. Huang, Arising applications of ferroelectric materials in photovoltaic devices, J. Mater. Chem. A, 2014, 2, 6027–6041.

[89] Wu, Y. Zhang, H. Su, G. Yuan, Enhanced photovoltaic properties of gradient calcium-doped BiFeO3 films, Ceramics International 46 (2020) 10083–10088.

[90] M. M. Seyfouri, D. Wang, Recent progress in bismuth ferrite-based thin films as a promising photovoltaic material, Critical Reviews in Solid State and Materials Sciences (2020) 1-26.Y. Zhang, H. Zheng, X. Wang, H. Li, Y.

[91] J. Liu, H. Deng, H. Cao, X. Zhai, J. Tao, L. Sun, P. Yang, J. Chu, Influence of rare-earth elements doping on structure and optical properties of BiFeO3 thin films fabricated by pulsed laser deposition, Applied Surface Science 307 (2014) 543–547.

4. Co-doping at A- and B-sites of BiFeO₃ films: selective growth of solid solutions or nanocomposites

4.1.   Introduction

In the last two decades, considerable attention has been focused not only to search new multiferroic materials, but also on the synthesis and characterization of mixed multifunctional materials in order to exploit novel systems with appealing functionalities. The multiferroic bismuth ferrite (BiFeO₃, BFO from now on) [1,2] has received considerable attention since it is probably the only material that is both magnetic and ferroelectric at room temperature. A lot of research has been devoted to the optimization of the BiFeO₃ as ceramics,[3] thin films [4] and nanostructures [4,5]. The interest for the BFO is also boosted by its being a lead-free perovskite since the rising of environmental issues and questions on process sustainability has put in evidence lead-free perovskite systems. The structure of perovskites can be described as a cubic compact packing of oxygen and A cations, where A cations substitute 1/4 of the oxygen atoms in the packing thus having a 12-fold coordination, and B cations, which occupies 1/4 of the octahedral sites. Thus, having the BFO phase the ABO₃ perovskite structure, there is a huge variety of doping possibilities by substitution at the 12-fold coordinated A-site or at the 6-fold coordinated octahedral B-site, or even substitution at both sites. Many studies have been reported on singly doped BiFeO₃ at the A-site with alkaline earth (Ca, Ba) [6,7] or the B-site with transition metals (Ti) [8], but the synthesis and characterization mainly regard ceramic materials. A few studies have been also reported on BiFeO₃ films singly doped with Ca, [9,10]   Ba, [11] La [12-14] or Ti [15] which apply mainly pulsed laser deposition (PLD) and solution routes as synthetic approaches.

In regard to co-doped BiFeO₃ as solid solutions, particular attention has been devoted to the preparation of mixed systems containing BiFeO₃ and BaTiO₃ (BFO-BTO), mainly as ceramic mixed systems, [16-25] mixed nanocrystalline materials [26,27] or layered structures [28,29].

Efforts have been devoted to the preparation of BFO-BTO systems in thin film form through PLD [30-35] and sputtering [36-38]. A few studies have also been reported on the preparation of BFO-BTO composite thin films through chemical solution processes [39-41]. Recently, PLD has been also applied to the growth of multiferroic BiFeO₃–BaTiO₃ superlattices [42-44].

The BFO-BTO solid solutions yield the opportunity to create improved unexpected or superior properties beyond averaging of their end member properties. The addition of BaTiO₃ to BiFeO₃ improves the properties of BFO, playing a crucial role in reducing the conductivity of the mixture and decreasing the leakage current, potentially allowing for a better multiferroic material. In particular, due to their strongly enhanced dielectric and energy storage

properties, the BFO–BTO solid solution films represent promising candidates for energy storage applications [45-47].

In this context, application of a simple and highly versatile synthetic approach such as metal-organic chemical vapor deposition (MOCVD) to synthesize these doped systems would be highly appealing. MOCVD has been already applied to the deposition of undoped $BiFeO_3$ films [48-53] but, to our knowledge, there are very few reports on the MOCVD deposition of doped $BiFeO_3$ films. Recently, the MOCVD fabrication of $xBiCoO_3$-$(1-x)BiFeO_3$ films with various $BiCoO_3$ concentrations ($0 \leq x \leq 58$ at.%) has been reported [54,55]. In previous studies, we focused on the synthesis of single crystalline pure $BiFeO_3$ films [56,57] and $BiFeO_3$ films doped at the A or B site with Ba or Ti, respectively, [57,58] with the goal of studying the suitable processing conditions to introduce Ba or Ti within the structure.

In this chapter, the MOCVD process has been exploited as a synthetic route to produce Ba and Ti co-doped $BiFeO_3$ thin films. This study represents, to our knowledge, the first report on the MOCVD fabrication of Ba/Ti co-doped BFO solid solutions or nanocomposites on niobium doped $SrTiO_3$ (STO) (100) and yttria stabilized zirconia (YSZ) (100) substrates. Films have been grown using a facile approach based on a molten multi-component source, that consists of the $Bi(phenyl)_3$, $Fe(tmhd)_3$, $Ba(hfa)_2 \bullet tetraglyme$ and $Ti(tmhd)_2(O\text{-}iPr)_2$ (phenyl= $-C_6H_5$, H-tmhd=2,2,6,6-tetramethyl-3,5-heptandione; O-iPr= iso-propoxide; H-hfa=1,1,1,5,5,5-hexafluoro-2,4-pentanedione; tetraglyme = 2,5,8,11,14-pentaoxapentadecane) precursor mixture. A comprehensive, in depth study of both the vaporization mass-transport behavior of the multi-component source and of the structural, morphological and compositional characterizations of deposited films provides a clear correlation between composition of the multi-component source and the formation of the $Bi_{(1-x)}Ba_xFe_{(1-y)}Ti_yO_3$ solid solution films or the $Bi_{(1-x)}Ba_xFeO_3/Bi_{(1-x)}Ba_xFe_{(1-y)}Ti_yO_3$ nanocomposite films. To this aim, X-ray diffraction (XRD), transmission electron microscopy (TEM), energy dispersive X-ray analysis (EDX) and X-ray photoelectron spectroscopy (XPS) have been essential to identify the formed phases and, together with piezoresponse force microscopy (PFM) and piezoresponce force spectroscopy (PFS), to correlate film nature and piezoelectric and ferroelectric properties.

4.2. Experimental section

$Fe(tmhd)_3$, $Bi(phenyl)_3$ and $Ti(tmhd)_2(O\text{-}iPr)_2$ complexes were purchased from STREM Chemicals and used without further purification, while the $Ba(hfa)_2 \bullet tetraglyme$ has been synthesized following a slightly modified procedure (dichloromethane has been used instead of toluene) of that reported in *ref. 59*. Dynamic and isothermal thermogravimetric (TG) measurements were made using a Mettler Toledo TGA2 and the STARe software. The weight of the samples investigated was between 8-12 mg. Analyses were made under prepurified nitrogen (30 sccm, sccm = standard cubic centimeter per minute) using a 5 °C/min heating rate. Temperature was measured with an accuracy of ± 0.1 °C.

The undoped and doped $BiFeO_3$ films were deposited in a low pressure, horizontal, hot wall reactor equipped with a single sublimation zone. The precursor mixture was heated at 120-130 °C, a suitable temperature for an efficient vaporization without thermal degradation. Argon was used as a carrier gas (flow = 150 sccm), while the reactant gas (oxygen flow = 150 sccm) was introduced in the main flow in close to the reaction zone. The gas flows were controlled by mass flowmeters. Depositions were carried out for 60 min at 800 °C and 5 torr. Niobium doped (100) $SrTiO_3$ single crystals were purchased from Crystal Gmbh.

X-ray diffraction measurements (XRD) were recorded using a Smartlab Rigaku diffractometer in Bragg-Brentano mode, equipped with a rotating anode of Cu Kα radiation operating at 45 kV and 200 mA. The Cu K_β was eliminated using a Ni filter. The rocking curves were recorded after correcting ψ and ϕ angles in order to optimize the intensity of the (00l) substrate and thin film peaks.

Film surface morphology was examined by field emission scanning electron microscopy (FE-SEM) using a ZEISS VP 55 microscope. The atomic composition of the films was analyzed by energy dispersive X-ray analysis (EDX), using an INCA-Oxford windowless detector with an electron beam energy of 15 keV.

Cross-section TEM analysis have been performed using a JEOL 2010 F, equipped with the Gatan imagining filter instrument.

X-ray photoelectron spectra (XPS) were measured at 45° take-off angles relative to the surface plane with a PHI 5600 Multi Technique System (base pressure of the main chamber 3 x 10^{-10} Torr). The spectra were excited with the Al-K_α radiation. XPS peak intensities were obtained after a Shirley background removal. Spectra calibration was achieved by fixing the "adventitious" C 1s peak at 285.0 eV. A 60 s Ar^+-ion sputter etching was performed by rastering a 3 x 3 mm^2 area (3 kV, 20 mA emission, beam current 1.0 µA).

Scanning probe microscopy and spectroscopy have been performed with a Solver P47 NT-MTD instrument. For simultaneous topographic and piezoelectric properties evaluation, Atomic Force and Piezoresponce Force Microscopies (AFM and PFM) were performed adopting Au-coated silicon probe with a nominal 35 nm tip curvature radius and a typical force constant of 0.1N. AFM images were obtained in contact mode. The noise level before and after each measurement was 0.01 nm.

To evaluate the piezoelectric/ferroelectric properties simultaneously to the topological scanning in contact mode, a lock-in technique is used to measure the modulated motion of the $BiFeO_3$ films (Z_{ac}), under a modulated tip voltage, (V_{ac}), that is applied by a function generator between the tip and the STO:Nb substrate used as bottom electrode. The amplitude of the vertical displacement Z_{ac} and the phase difference between Z_{ac} and V_{ac} signal have been monitored through a lock-in amplify. Single-point Piezoresponce Force Spectroscopy has been performed measuring the piezoresponse (in terms of amplitude and phase differences) upon

applying a cyclic additional bias voltage in the ± 9V range between the AFM tip and STO:Nb substrate.

4.3.   Results

4.3.1.   Thermal behavior of the multi-component mixtures

A multicomponent source containing Bi(phenyl)$_3$, Fe(tmhd)$_3$, Ba(hfa)$_2$•tetraglyme and Ti(tmhd)$_2$(O-iPr)$_2$ with two different element ratios, namely Bi:Ba:Fe:Ti of 1:1:1:1 and 1:2:1:1, has been applied. The thermal behavior of the precursor mixtures has been characterized by dynamic and isothermal thermogravimetric (TG) analyses at atmospheric pressure under nitrogen flow. TG dynamic data of both mixtures show mainly a single step, indicating that the mixtures vaporize without decomposition with low residues. The TG curves of the 1:1:1:1 and 1:2:1:1 mixtures are reported in the Figure 1. They show a single step weight loss in the temperature range of 150-300 °C with a residue of about 12.6% and 9.5%, respectively.

Given the similar behavior of the two mixtures, as a case study we choose the 1:2:1:1 source to investigate in more detail the mass transport properties of the multicomponent mixture. In Figure 2a, the isothermal curves of the 1:2:1:1 mixture are reported, starting from when the sample reached the set temperature, i.e. after 12 min with a heating rate to reach the set temperature of 5 °C/min. The measurements show a linear behavior in the investigated temperature range of 120-150 °C. The linear trend is a clear indication that the mixture containing the four Bi:Ba:Fe:Ti precursors presents a behavior of a well performing "single-source mixture". From these data, the vaporization rate was derived, and it is reported in Figure 2b. In this case, being the mixture composed of four different precursors, the vaporization rate is reported as related to the mixture weight loss and not to the vaporized moles, so the unit are mg/min and not mol/min. The apparent vaporization energy has been derived and it is equal to 29.1 ± 1.5 kJ.mol^{-1}. The linear trend of the "single source mixture" clearly points to a proper behavior of the four-component mixtures for application in MOCVD processes of Bi-Ba-Fe-Ti based films.
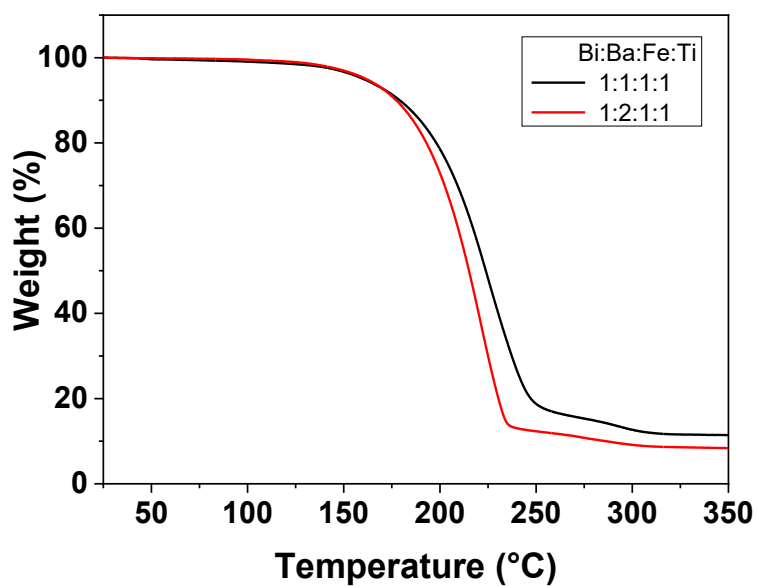
Figure 1. TG curves of the 1Bi:1Ba:1Fe:1Ti and 1Bi:2Ba:1Fe:1Ti mixtures carried out at atmospheric pressure under 30 sccm of nitrogen.
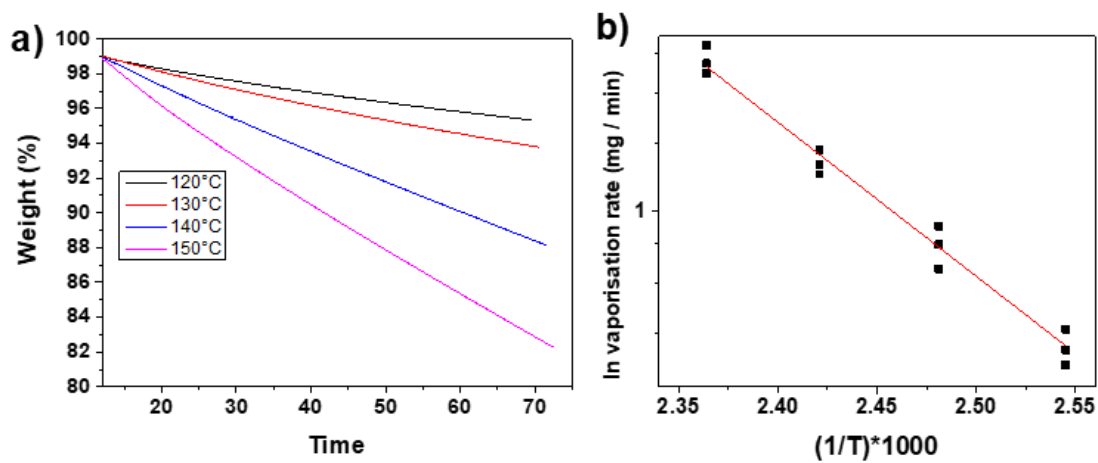
Figure 2. Isothermal curves a) and Arrenhius plot b) of the 1:2:1:1 mixture carried out at atmospheric pressure under 30 sccm of nitrogen.

4.4. Structural investigation of BiFeO₃ based films

The above described mixtures have been applied to the deposition of the Ba and Ti co-doped $BiFeO_3$ thin films on (100) $SrTiO_3$:Nb and yttria stabilized zirconia (YSZ) (100) substrates. The $SrTiO_3$:Nb substrate has been chosen because $SrTiO_3$ is the best substrate for the epitaxial growth of $BiFeO_3$ due to the excellent lattice match and, being doped with Nb, it possesses the suited electrical properties to be used as a bottom electrode for Piezo Force Microscopy (PFM) measurements. The YSZ substrate (a_Y-axis parameter of 5.139 Å) has been used to allow compositional characterization through EDX analysis (vide infra).
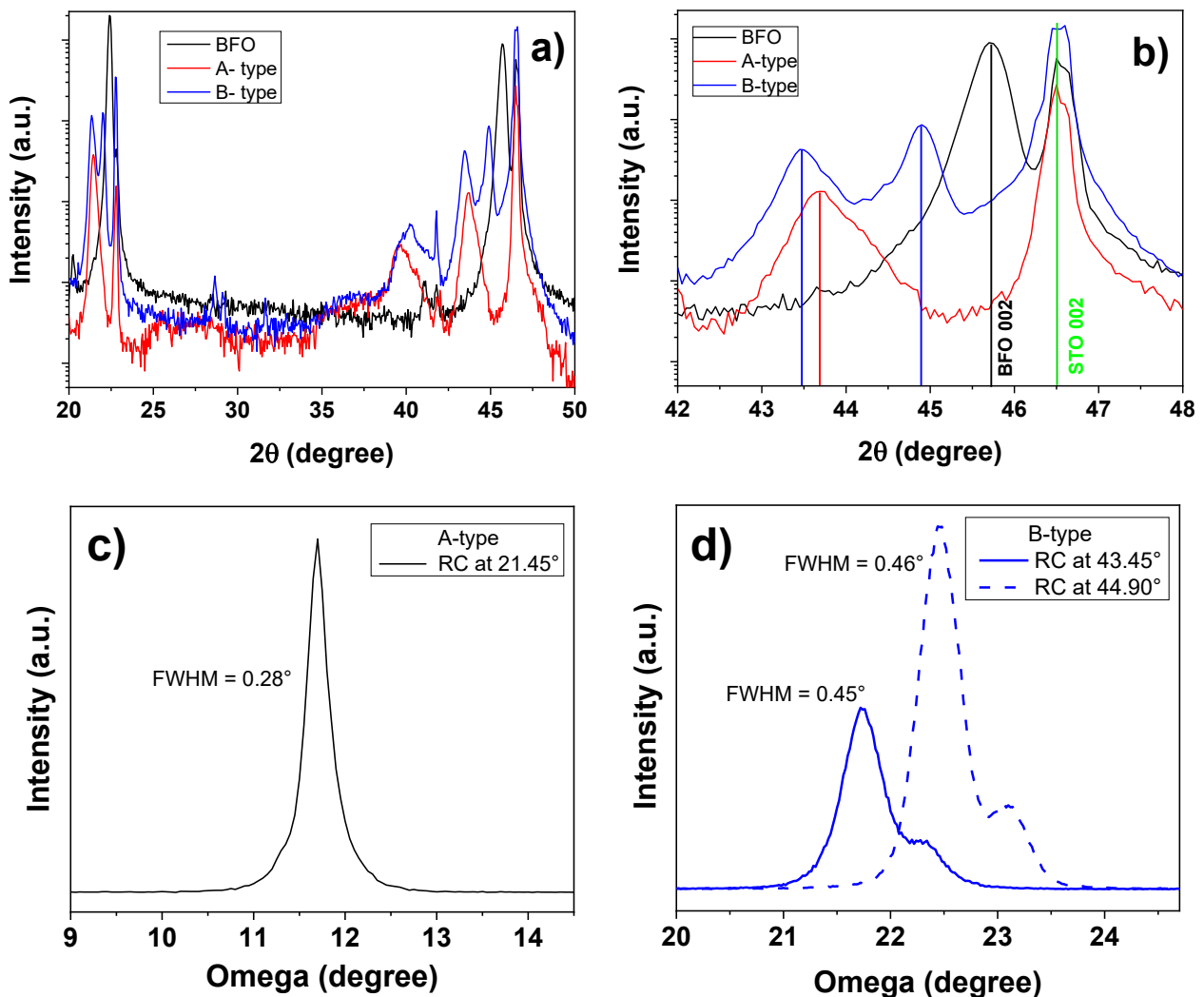
Figure 3. a) XRD patterns and b) enlarged region in the 42-48° range of an undoped BiFeO₃ (———), A-type (———) and B–type (———) films grown on SrTiO₃:Nb (100) substrates; c) Rocking curve of the A-type film at 2ϑ = 21.45°; d) Rocking curves of the B-type film for the two reflections at 2ϑ = 43.50° and 44.90°.

BiFeO$_3$ has a rhombohedral structure with a_{rh}= 3.965 Å and α_{rh}= 89.4° but given the angle of almost 90° it may be considered as a pseudocubic and the cubic notation is used throughout the manuscript. The substrate SrTiO$_3$ has a lattice parameter a_S= 3.905 Å, thus a mismatch of 1.53% is expected for a <001> growth of the BiFeO$_3$ pure phase.

Deposition temperature of 800 °C was chosen for this study since it has been previously shown that it is a suited temperature in our growth process for the deposition of pure BiFeO$_3$ [55]. The in-situ deposited films are mirrorlike, dark orange in color and have a thickness that ranges in the 400-500 nm. Thus, considering a 1h deposition duration time, an average growth rate of about 8 nm/min is obtained.

X-ray diffraction (XRD) technique has been used to characterize the film structure and crystallinity. Figure 3a and 3b report the XRD θ-2θ scans of films deposited at 800 °C using the 1:1:1:1 and the 1:2:1:1 mixtures and from now on indicated as A-type (solid solutions) and B-type (nanocomposite) films, respectively, compared with the pattern of an undoped BiFeO$_3$ phase film. In Figure 3b, the peak positions are evidenced by a green (STO substrate), black (pure BFO), red (A-type) and blue (B-type) line.

In the A-type film, in addition to the substrate peaks at 22.75° and 46.50°, only two peaks at 21.45° and 43.70°, the second of which represents the second order reflection, are observed, thus pointing to the formation of a single-phase film out-of-plane oriented. Therefore, this pattern is indicative of a high degree of texturing. In addition, the peaks are shifted toward lower angles as clearly observable in the enlarged XRD region reported in Figure 3b, thus indicating an out-of-plane parameter, as calculated from the 002 peak position, of 4.143 Å, a value larger than the one of 3.965 Å, reported for the pure BiFeO$_3$ phase. The increase in the out-of-plane parameter may be related to both the insertion of Ba^{2+} ($r_{6-coord}$ = 1.35 Å) at the Bi^{3+} ($r_{6-coord}$ = 1.03 Å) site, and of Ti^{4+} ($r_{6-coord}$ = 0.605 Å) at the Fe^{3+} ($r_{6-coord}$ = 0.55 Å) site. The choice to consider a six-fold octahedral coordination for both the A and B ions is due to the fact that to fit the structure correctly in the Goldschimdt [60] perovskite classification, ionic radii values of ions six-coordinated have to be considered.

The very good out-of-plane alignment of crystallites of the A-type films has been confirmed by the full width half maximum (FWHM) value of 0.28° for the rocking curve of the 001 reflection at 21.45° (Figure 3c).

B-type films, deposited using the 1:2:1:1 mixture, show a more complex pattern (Figure 3a). In addition to the substrate peaks, more peaks are observed at 21.35°, 22.00°, 43.45° and 44.90°, with the last two being the second order reflection of the lowest angle peaks. The very broad peak observed around 40° can be likely assigned to another orientation of the doped phases [19].
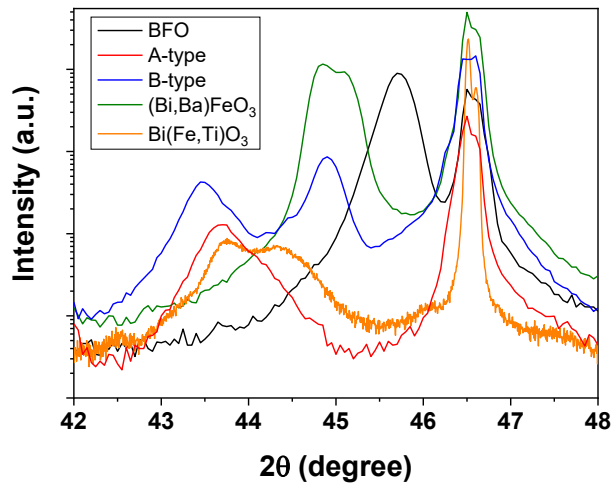
Figure 4. XRD patterns in the 42-48° range of a A-type sample (———) and B–type sample (———) compared with undoped BiFeO$_3$ (———), and singly doped Bi$_{(1-x)}$Ba$_x$FeO$_3$ (———) and BiFe$_{(1-y)}$Ti$_y$O$_3$ (———) films grown on SrTiO$_3$:Nb (100) substrates.

Based on the position of the second order reflections at 43.45° and 44.90°, the out-of-plane parameters have been calculated to be 4.165 Å and 4.037 Å, respectively for the two phases.

The film is also in this case highly aligned as confirmed by the recorded rocking curves (Figure 3b) of the 002 peaks at 43.45° and 44.90°, respectively. The FWHM of the two rocking curves are 0.45° and 0.46°, respectively. Both rocking curves show a shoulder on the higher angle side likely arising as rocking curves of the higher angle peaks.

The presence of more peaks having small FWHM of the rocking curves prompted us to assume that two different textured phases are formed in the B-type films. Matching the B-type pattern with ICDD database, the peak at 43.45° is slightly shifted with respect to the peak Bi$_6$Ti$_3$Fe$_2$O$_{18}$ (ICDD N° 21-0101), while the peak at 44.90° may be associated either with BaFeO$_3$ (*a-axis* parameter = 4.012 Å, ICDD N° 14-0180), or BaTiO$_3$ either as a cubic (*a$_c$-axis* parameter = 4.031 Å, ICDD N° 31-0174) or tetragonal (*c$_t$* = 4.038 Å, ICDD N° 05-0626) structure phases.

To shed more light on the peak attribution, the pattern was also compared with those of the singly doped Ba- or Ti-BiFeO$_3$ films synthesized through MOCVD using similar deposition conditions (Figure 4a) [58]. The peak at 44.90° resembles to the peak found in the Bi(Ba)FeO$_3$ film, [58] while the peak at 43.45° may correspond to the peak found at 43.65° of the Bi(Fe,Ti)O$_3$ film [58]. It is interesting to observe that both the singly doped films show large peaks, where two components may be seen.

This peak "splitting" may be associated with concentration gradients of the BFO doped phase film either with Ba or Ti elements.

On the other hand, the peak at 43.45° is also similar to the value (43.70°) found for the A-type sample. This comparison points to the following situation: the deposited B-type film is a nanocomposite made of two differently doped BiFeO$_3$ phases. Additional investigations are needed to unveil the nature of the B-type films.

4.4.1.   TEM characterization of BiFeO₃ based films

To have further insights on the nature of the nanocomposite films, TEM investigations have been carried out. The TEM bright image (Figure 5a) shows a 400 nm total thick film, which actually presents three main structural and morphological features: a 200 nm thick layer deposited near the substrate surface, some columns embedded inside this initial layer and a further 200 nm thick film. In addition, the TEM image shows that the film peeled off from the substrate, as clearly visible from the presence of the very light zone at the film/substrate interface (Figure 5a).
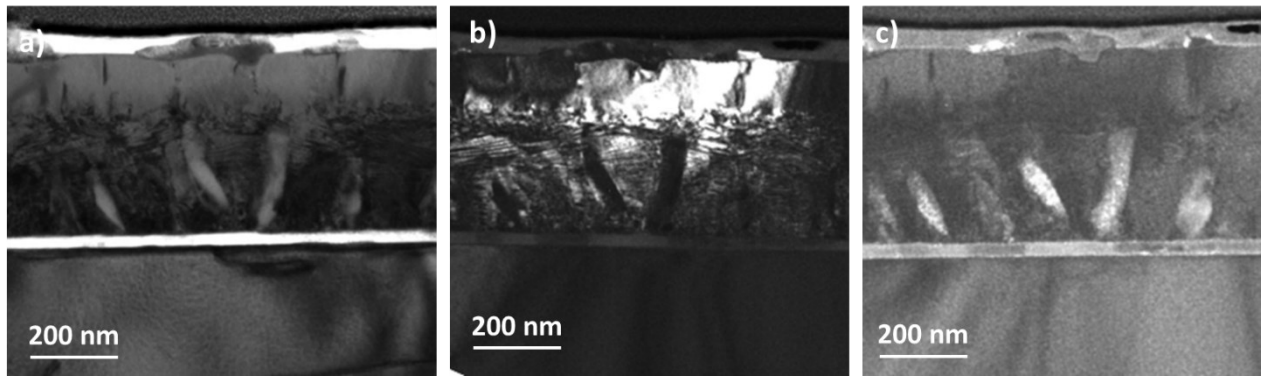
Figure 5. TEM cross-section of the B-type film: bright field image (a) and dark field images of (b) grains possessing the SAED of Figure 6b and (c) of embedded columns showing the SAED of Figure 6d.

The peel off was probably due to the mechanical stress suffered during the sample preparation for TEM analysis. The dark field images (Figure 5b,c) clearly indicate that the total deposited film belongs to the same phase, while the columns possess a different brightness, thus indicating a different crystalline structure and/or chemical composition. To confirm this observation, the selected-area electron diffraction (SAED) patterns of the different features have been observed with the incident electron beam perpendicular to the cross-section and are reported in Figure 6. Figure 6a shows the SAED pattern of the substrate indicating an a-axis parameter of 3.912 Å, very close to the theoretical STO value. Figure 6b-d reports the SAED patterns of the more external 200 nm film (point A indicated in the Figure 5a), the 200 nm layer deposited near the substrate surface and the columns embedded inside this initial layer (point B indicated in the Figure 5a). The SAED pattern of the B-type film at point A shows spots perfectly matching those of the STO substrate, supporting not only the oriented film growth, as indicated by the XRD pattern, but also pointing to the formation of a textured film. The lattice constants measured by the SAED patterns for the external layer indicate squared grains with an a-axis parameter of about 3.941 Å. This value is slightly smaller than the a-axis parameter of pure BFO.
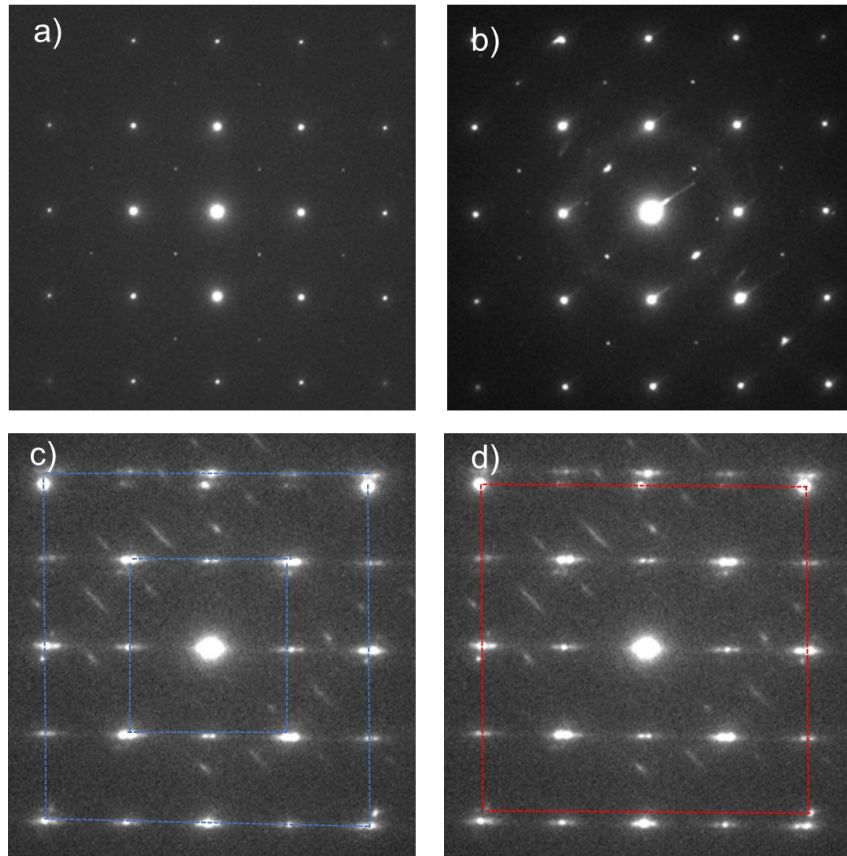
Figure 6. SAED patterns of the a) STO substrate, b) the more external 200 nm film (point A), c) the 200 nm layer deposited near the substrate surface (point B), and d) the columns embedded inside this initial layer (point B). For points A and B notation, see Figure 5a.

A closer look to SAED pattern from the lower part of the B-type film (Figure 6c,d) allows to distinguish spots from the embedded columns and broad spots due to the defective layer with defects and/or stress. In Figure 6c, two blue concentric distorted squares highlight spots from the 200 nm layer deposited near the substrate, while in Figure 6d the red square represents the SAED pattern of the embedded columns. The two different SAED patterns clearly indicate that the 200 nm layer at the interface with the substrate have in-plane and out-of-plane parameters of 3.988 Å and 4.162 Å, respectively. The columns likely possess a cubic structure, and since the first order reflection is not allowed, it should be either a body centered or a face centered cell. The observed lattice parameter is about 4.016 Å.
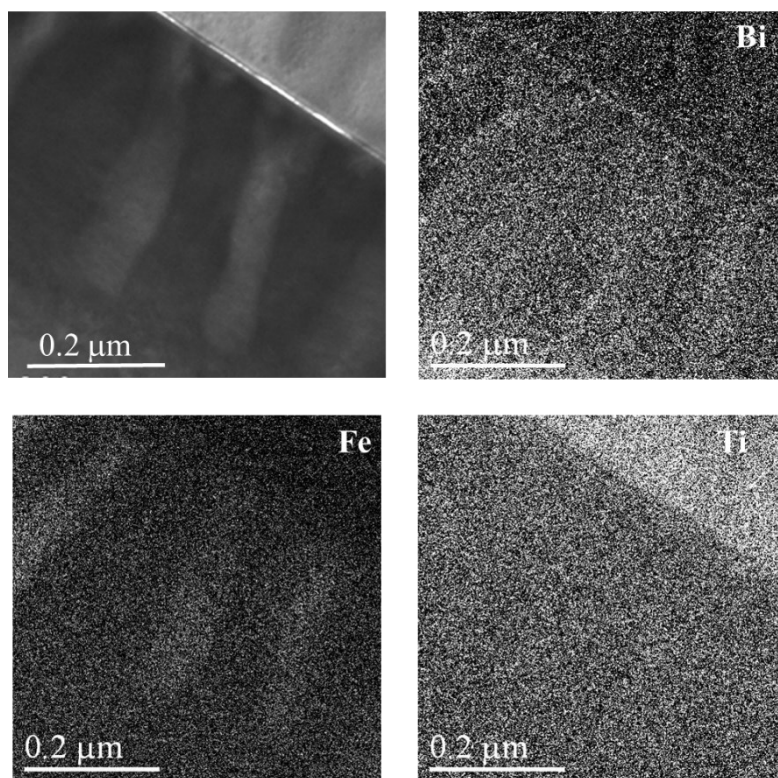
Figure 7. EF-TEM images of Bi, Fe and Ti signals of the B-type sample.

To further support identification of the different phases present in the B-type films, the Energy Filtered-TEM (EF-TEM) analysis has been performed to image the distribution of the elements within the film. In Figure 7, the Bi, Fe and Ti maps are shown, while it was not possible to record the Ba map because of the overlapping with the Bi signal. The EF-TEM analyses indicate that the Bi and Ti are uniformly distributed within the entire film, but the columns are Fe-rich. On the other hand, it is not possible to exclude that the Ti observed also for the nanocolumns may arise from the layer underneath.

4.4.2. Compositional characterization of $BiFeO_3$ based films

The elemental and chemical composition of films has been determined using EDX and XPS. To determine the elemental composition of the deposited layers using EDX is not an easy task due to the overlap of the Ba L lines and Ti K_α lines and to the presence of Ti in the substrate. To overcome this problem, EDX analyses were carried out also on singly doped systems grown on YSZ substrates to check the correlation between the nominal mixture stoichiometry and the film composition. EDX data on singly doped $Bi(Ba)FeO_3$ and $BiFe(Ti)O_3$ films are compared in Table 1 with the mixture nominal stoichiometries.

Sample	Nominal mixture stoichiometry	Film stoichiometry Bi:Ba:Fe:Ti (atomic %)	A_{cation} : B_{cation} ratio
Bi(Ba)FeO$_3$	1Bi:2Ba:1Fe	12.4:14.9:21.8	1.2:1
BiFe(Ti)O$_3$	1Bi:1Fe:1Ti	7.6 :2.5:3.3	1.3:1
A-type	1Bi:1Ba:1Fe:1Ti	9.7 :2.8:5.6:5.1	1.2:1
B-type	1Bi:2Ba:1Fe:1Ti	9.6:7.4:8.7:7.6	1:1

Table 1. EDX analyses of A-type and B-type samples compared to singly doped Bi(Ba)FeO$_3$ or BiFe(Ti)O$_3$
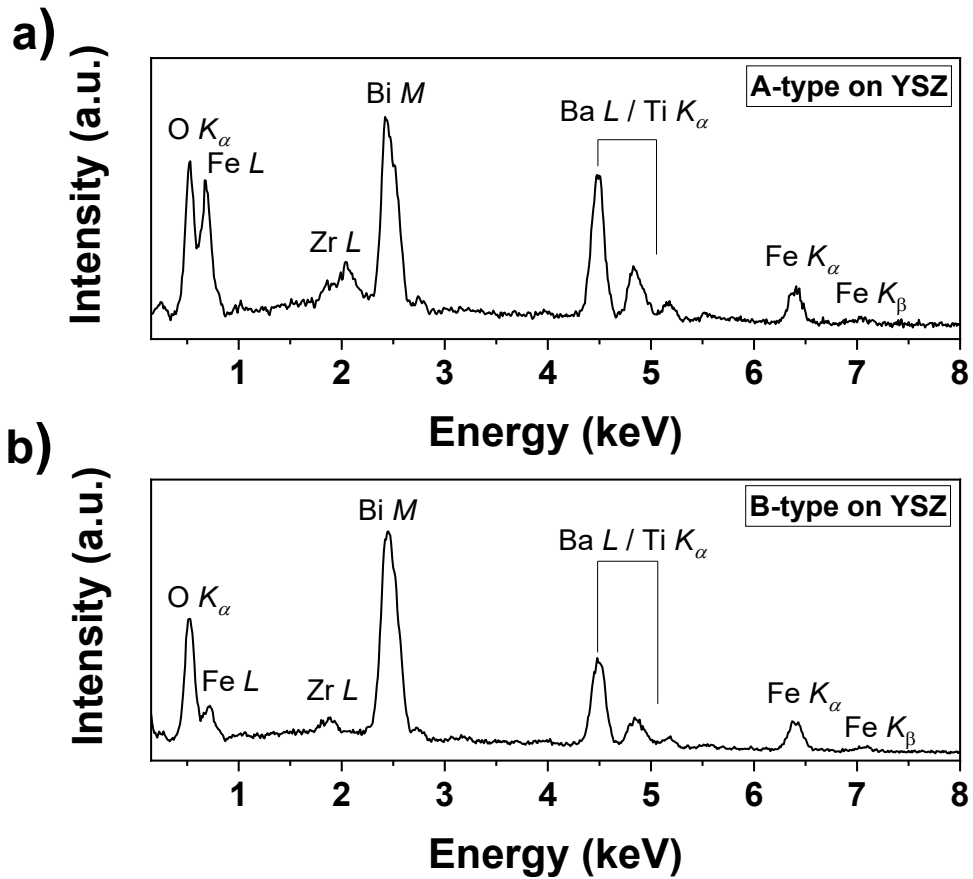
Figure 8. EDX Spectra of the a) A-type sample and b) the B-type sample on YSZ substrate.

From this data compared to the A-type and B-type EDX spectra (Figure 8) it is possible to extrapolate the compositions of the A-type and B-type samples (Table 1), yielding an average composition of $Bi_{0.8}Ba_{0.2}Fe0.5Ti_{0.5}O_3$ and a $Bi_{0.6}Ba0.4Fe_{0.6}Ti_{0.4}O_3$ compositions, respectively.

These compositions have been confirmed through XPS quantitative analyses. XPS atomic concentration was evaluated by estimating the integrated area of C 1s, O 1s, Bi 4f, Ba 3d $_{5/2}$, Ti 2p$_{3/2}$, and Fe 2p$_{3/2}$ peaks corrected for the corresponding relative atomic sensitivity factor based on empirical data reported by Wagner [61] and corrected for the transmission function of the PHI spectrometer [62]. In Table 2, the quantitative analyses of the A-type and B-type samples produce a composition of films as-deposited and after 5 min sputtering. Both samples show surface carbon contamination, which is mainly due to adventitious C. A small amount of carbonate (shoulder at about 288.5 eV) is observed only for B-type films due to the higher atomic % of Ba, which like all the alkaline-earth metal is prone to carbonate formation. After sputtering, data indicate that only negligible C contamination is present in the film bulks and the following compositions are observed $Bi_{0.9}Ba_{0.1}Fe_{0.5}Ti_{0}.5O_3$ and $Bi_{0.6}Ba_{0.4}Fe_{0.6}Ti_{0.4}O_3$ for A-type and B-type films, respectively.

In Figure 9 a, high resolution spectra region of Bi 4f of the A-type and B-type samples are compared to those observed for the pure BFO and singly-doped $(Bi,Ba)FeO_3$ and $Bi(Fe,Ti)O_3$.

The spectrum of the pure BFO shows a single component with the binding energy of the Bi 4f$_{7/2}$ observed at 158.6 eV. A similar spectrum is observed for the $(Bi,Ba)FeO_3$ film, indicating that Bi experiences the same environment of the pure BFO, thus confirming that Ba is occupying the A site of the perovskite. On the other hand, in the case of the $Bi(Fe,Ti)O_3$, the Bi 4f$_{7/2}$ is observed at 159.0 eV as a consequence of the different environment experienced by Bi in this sample, thus confirming that Ti substitutes Fe in the structure, i.e. occupies the B-site of the perovskite. The Bi 4f$_{7/2}$ binding energy of the A-type sample is found at 159.1 eV, a similar position to that observed for the $Bi(Fe,Ti)O_3$.

Different findings are observed for the B-type sample, for which the Bi 4f$_{7/2}$ peak position is at 158.9 and the FWHM of the peak (1.8 eV) is broader than the one observed in the other cases (1.4 eV), thus indicating that two different components are likely present in the structure.

		Atomic %					
		Bi	Ba	Fe	Ti	O	C
Type-A	surface	7.4	0.1	1.9	1.3	38.1	51.2
	after sputter	17.9	2.2	9.1	9.8	60.0	1.2
Type-B	surface	4.4	3.9	1.3	0.9	24.3	65.2
	after sputter	12.9	10.5	11.9	8.5	59.3	1.7

Table 2. XPS analyses of the surface and after 5 min sputtering of A-type and B-type samples.
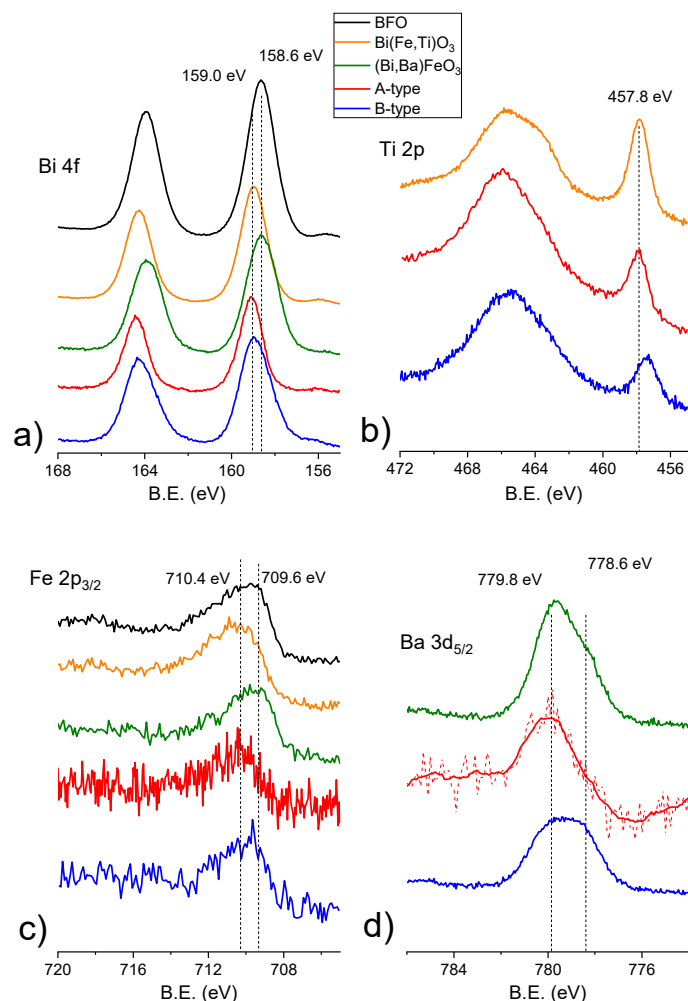
Figure 9. a) Bi 4f, b) Ti 2p, c) Fe 2p$_{3/2}$, and d) Ba 3d$_{5/2}$ XPS spectral regions of BFO (black), Bi(Fe,Ti)O$_3$ (orange), (Bi,Ba)FeO$_3$ (green), A-type (red) and B-type (blue) samples.

To assess this observation, the deconvolution of these peaks has been done and reported in Figure 10. Of the two components, one is found at 158.6 eV and can be assigned to Bi with similar environments to BFO and (Bi,Ba)FeO$_3$ samples. The second component is observed at 159.2 eV indicating a Bi environment similar to Bi(Fe,Ti)O$_3$ and A-type samples.
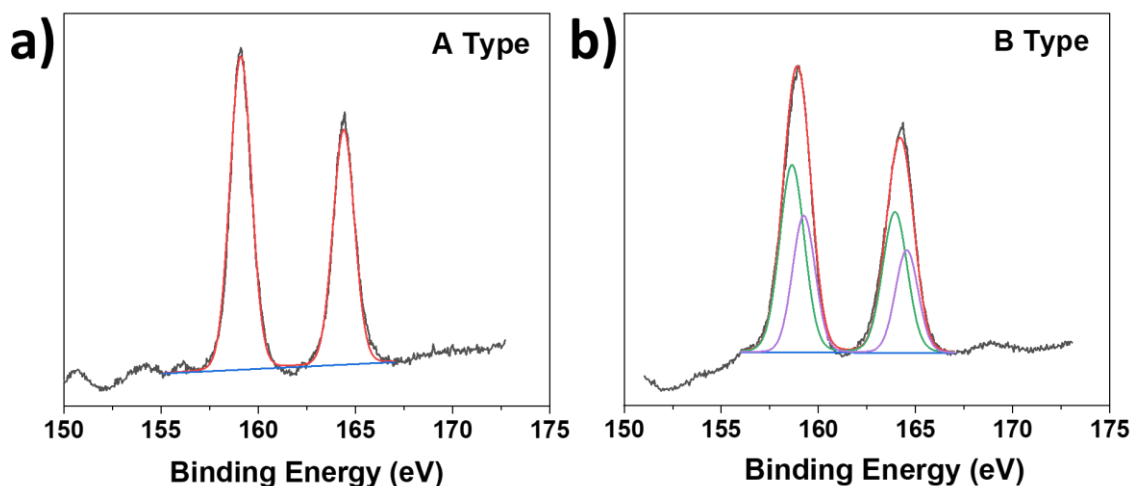
Figure 10. Deconvolution of XPS Bi 4f spectra region for the a) A-type and b) B-type samples.

Similarly to what observed for Bi, the positions of the Ti $2p_{3/2}$ peaks (Figure 9b) are similar between Bi(Fe,Ti)O_3 and A-type films (457.8 eV). On the other hand, the Ti $2p_{3/2}$ peak of B-type film is observed at lower B.E. (457.4 eV) compared to the other two, thus indicating the effect of the Ba amount within the phase. Note that the Ti $2p_{1/2}$ peak is overlapped with Bi $4d_{3/2}$.

The Fe $2p_{3/2}$ band (Figure 9c) consists for all samples of broad peaks with a maximum around 709.6 eV for BFO, (Bi,Ba)FeO$_3$ and B-type films and around 710.4 eV for Bi(Fe,Ti)O_3 and A-type sample. It is worth to note that the broad peak of Fe $2p_{3/2}$ for B-type films may be related to contribution of two different stoichiometric phases referable to the A-type or Bi(Fe,Ti)O_3 component and the (Bi,Ba)FeO$_3$ component.

Finally, the Ba $3d_{5/2}$ region of A- and B-type films and of (Bi,Ba)FeO$_3$ sample is reported in Figure 9d. The Ba signals in all cases is dominated by the contribution of surface carbonate contaminations at 779.8 eV, which are typical of alkaline-earth-containing oxides, although a shoulder at low BE (in the 778.2 – 778.6 eV range) can be observed for the three films. This low BE shoulder can be assigned to the barium ions in the BFO lattice.

4.4.3. Morphological characterization of BiFeO$_3$ based films

The FE-SEM images of the A-type films show a very uniform, homogeneous and flat morphology (Figure 11a). The cross-section indicates the formation of a very compact and dense film of about 350 nm in thickness (Figure 11b).

B-type films (Figure 12a) show a homogeneous surface with outgrowth grains of about 150-200 nm in dimensions coming out from the underneath flat surface. The electron backscattered (BSE) image (Figure 12b) indicates the presence of brighter grains, that means grains which are rich in heavier elements, likely Bi. The cross-section (Figure 12c) confirms the formation of a dense film with a rougher surface and a thickness of about 450-500 nm.

A- and B-type films topography have been investigated using atomic force microscopy (AFM) (Figure 12 d,e). AFM data confirm film morphology previously observed through FE-SEM (Figure 12a). The A-type sample (Figure 12d) presents a flat sample surface with fully coalesced grains and a root mean square (RMS) roughness of about 3.3 nm (measured on an area of 5 μm × 5 μm).

B-type film (Figure 12e) displays a much more intricate surface morphology with many high spots also corresponding to the FE-SEM investigation (Figure 11), the root mean square (RMS) roughness on a 5 μm × 5 μm area is 16.0 nm.
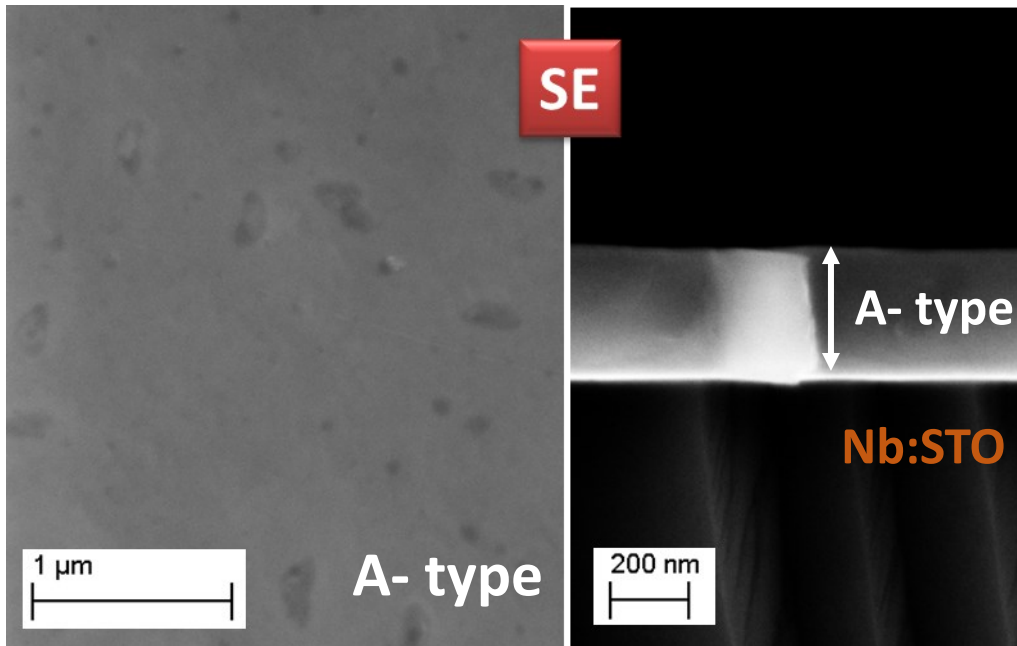
Figure 11. Secondary electron FE-SEM plan view (left) and cross-section (right) images of the A-type sample.
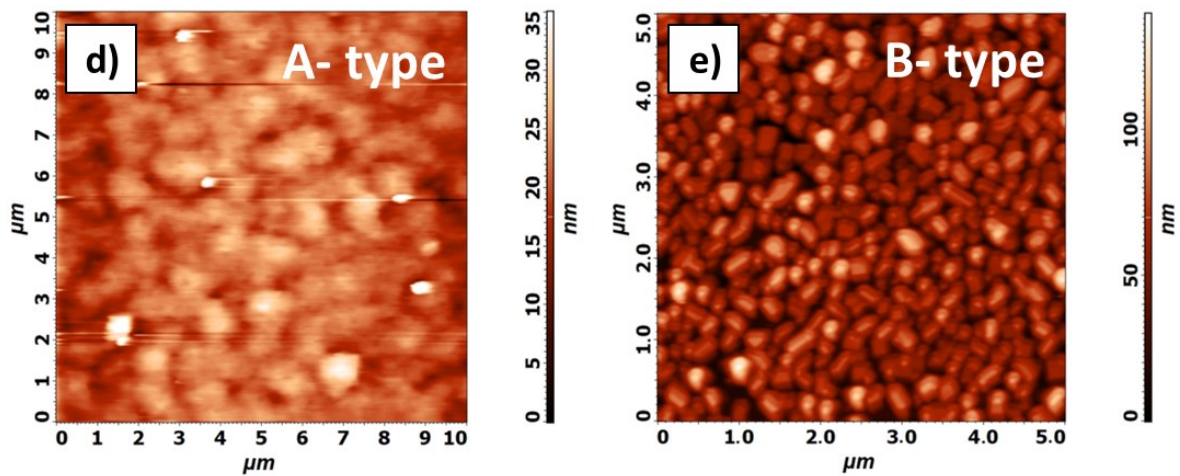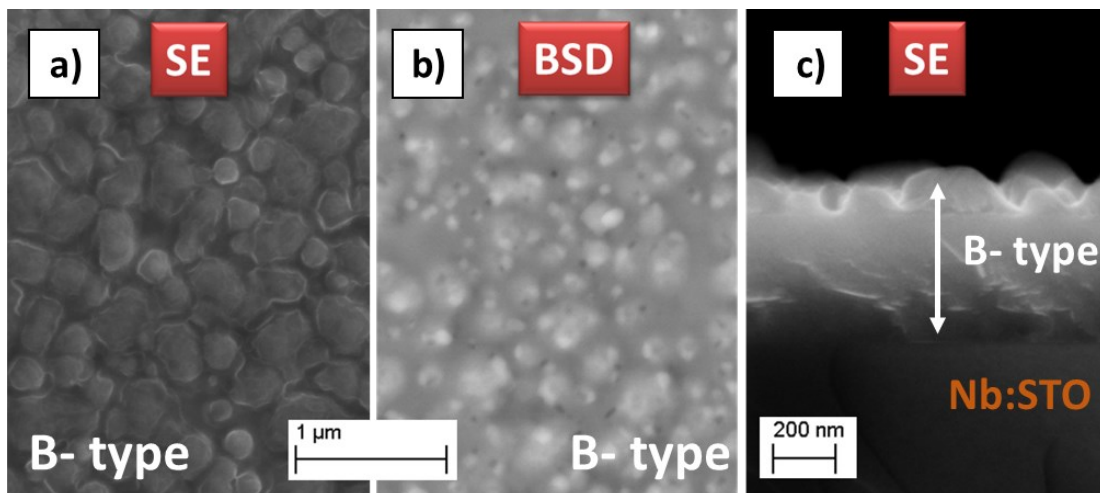
Figure 12. Secondary electron FE-SEM plan view (a), backscattered electron plan view (b) and secondary electron cross-section (c) images of the B-type sample. AFM topography images of A-type film d) and of B-type film e).

4.4.4. Piezoelectric characterization of BiFeO₃ based films

Piezoresponse Force Spectroscopy (PFS) has been used to determine if piezoelectric/ferroelectric properties are present in doped A-type and B-type films. Single-point PFS has been obtained by applying between the tip and the sample a ±9V round trip bias voltage to the oscillating voltage (V_{ac}). Piezoresponse was measured in terms of the amplitude of the out-of-plane displacement (Mag) and phase difference (Phase) between piezoresponse signal and the alternating voltage [63,64].

Figure 13a shows the dependence of amplitude and phase upon the bias voltage for Type A sample. Amplitude measurement presents the classical piezoelectric butterfly loop and the phase analysis also present the typical hysteresis loop associated with the ferroelectric switching behavior [65]. The coercitive voltage of the studied domain is about 2V. A writing experiment has been performed on A-type sample.
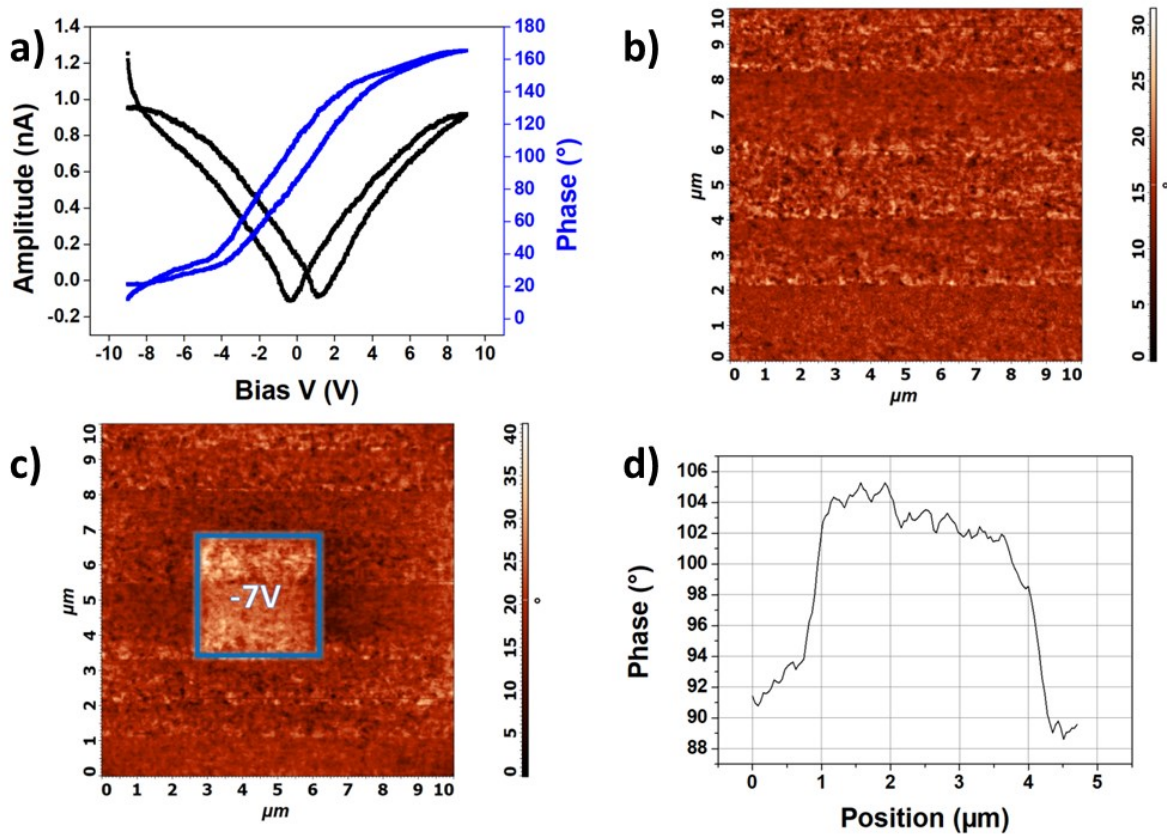
Figure 13. (a) Butterfly loop (black curve) and hysteresis ferroelectric loop (blue curve) in the −9V to +9V scan of the A-type film on STO:Nb. AFM scan (b) of a 10 μm × 10 μm area and (c) AFM image after writing with a -7 V on a 3 μm × 3 μm area. d) Phase switch of 15° observed in the 3 μm × 3 μm area after -7V bias voltage application.

The PFM images of the Phase between applied V_{ac} potential and the vertical piezoresponse of the films on a 10 μm x 10 μm area has been obtained with a 0V bias voltage between the tip and the film (Figure 13b) [56]. Then, a −7 V bias has been imposed to the tip, which has been moved along a smaller (3 μm× 3 μm) area. After the writing, the new phase image (Figure 13c) of the same area shows a clear phase switch of 15° (Figure 13d) where the -7V bias voltage has been applied.

B-type sample has shown no piezoelectric or ferroelectric properties. This finding may be related to various observations such as the cubic structure of the more external part of the film (see TEM section) and the high roughness of the layer analogously to data previously reported by Lorenz et al., [66] who found no ferroelectric response on BTO33/BFO67 composite (vide discussion section for further interpretation).

4.5.   Discussion

Nanocomposite systems of the type $(1-x)BiFeO_3-xBaTiO_3$ have, recently, attracted a great attention due to their interesting multiferroic properties. Several reports appeared in the literature for the $(1-x)BiFeO_3-xBaTiO_3$ in ceramic form and a few studies have been reported on the preparation of solid-solutions thin films and BFO-BTO multilayers. Nevertheless, to our knowledge, no reports are known on the fabrication of solid solutions BFO-BTO in thin film form through a scalable and industrially appealing technique such as MOCVD. In the last two decades, we have studied a great variety of perovskite based oxide films, going from the high Tc superconductors such as TlBaCaCuO [67] and $La_{(1-x)}Ba_xCuO_4$ [68] to the giant k $CaCu_3Ti_4O_{12}$ [69,70], from the dielectric $LaAlO_3$ [71] to the ferromagnetic $Pr_{0.7}Ca_{0.3}MnO_3$ [72].

In the present study, we exploited the possibility to apply the successful approach, standardized in the past in our group, for the deposition of perovskite films to the fabrication of even more complex systems containing four different elements in a perovskite phase.

A combination of XRD, TEM, EDX and XPS investigations has allowed a clear-cut identification of the nature of the deposited films. The presence of a few peaks in the patterns of both type films indicates the formation of highly out-of-plane oriented samples, as confirmed by the FWHM of the rocking curves of the two samples. XRD data point to the formation of two different phase films starting from different precursor mixture stoichiometries. A single phase is observed for the A-type sample. The occurrence of a higher number of peaks in the B-type films clearly indicates the presence of two different phases in the film. Nevertheless, for the thin films, it is very difficult to univocally identify the phase due to the peak broadening, merging and shift due to doping.

In the present study for the first time a combination of techniques has allowed identification of formed phases in MOCVD grown BFO-BTO films. According to the XRD data, the XPS studies confirm the formation of a single phase for the A-type film. In fact, the binding energy peaks indicate a unique component for the various elements. On the other hand, the presence of

two components in the Bi binding energy peak in B-type sample confirms the presence of two-phase components, whose nature has been unveiled through TEM investigation.

TEM investigation has been used to complete characterization in the complex B-type sample. Morphological observation, EF-TEM analysis and SAED patterns of B-type film point to the formation of nanocolumns embedded in the growing layer of a different composition. EF-TEM analysis indicates that the nanocolumns are iron rich and this finding, combined with results obtained from the XRD patterns of B-type and $(Bi,Ba)FeO_3$ films, points to the formation of $Bi_{(1-x)}Ba_xFeO_3$ nanocolumns. The possibility that the nanocolumns may be formed of $BaTiO_3$ can be ruled out. In fact, even though the $BaTiO_3$ possesses a cubic structure (a_c= 4.031 Å, ICDD N° 31-0174) or a tetragonal structure (a_t= 3.994 Å and c_t= 4.038 Å, ICDD N° 05-0626) at temperature higher than 800 °C, thus the out-of-plane parameter would fit the 4.022 Å value found for the nanocolumn, the excess of Fe in the nanocolumn clearly point to the formation of $(Bi,Ba)FeO_3$. columns. The defective phase, where the nanocolumns are embedded, has a different diffraction.

It is interesting to compare the out-of-plane parameters derived from TEM with those estimated from XRD pattern (Table 3). The good agreement between the two sets of data and the difference with the in-plane parameter point to the formation of a tetragonal doped phase for the layer at the substrate interface with a c/a ratio of 1.04.

Feature		In-plane axis (Å) (TEM)	Out-of-plane axis (Å) (TEM)	Out-of-plane axis (Å) (XRD)
Squared grains		3.941	3.936	3.928
Columns		4.016	4.022	4.037
Defective layer		3.988	4.162	4.165
STO substrate		3.912	3.915	3.905

Table 3. Comparison of cell parameter value of the B-type sample derived from TEM and XRD measurements.

On the other hand, squared grains are found in the most external layer of B-type sample, having an a-axis parameter of about 3.93 Å. The peak associated with this value is not immediately visible in the XRD pattern due to its position being hidden under the low angle side of the STO (002) peak at 2θ=46.48°. The nature of this phase is still an open issue. On the other hand, this kind of systems are very complex as recently reported by Nan et al., [73] who realized $BiFeO_3$-$BaTiO_3$-$SrTiO_3$ solid-solution films where rhombohedral and tetragonal nanodomains coexist embedded in a cubic matrix.

Another comment deserves the non-isovalent nature of doping ions at the A-site or B-site of BFO. Nevertheless, in present samples charge compensation is likely to occur due to the almost equal amount of Ba^{2+} and Ti^{4+} doping ions [74].

Morphological characterization through FE-SEM and AFM indicate the formation of a very smooth surface (R_{rms} = 3.3 nm) for the lower Ba doping, i.e. the A-type $Bi_{(1-x)}Ba_xFe_{(1-y)}Ti_yO_3$ solid solution and a rough surface (R_{rms} = 16.0 nm) for the higher doping phase, the B-type composite $Bi_{(1-x)}Ba_xFeO_3/Bi_{(1-x)}Ba_xFe_{(1-y)}Ti_yO_3$.

The high roughness of the B-type film may be responsible for the absence of piezoelectric and ferroelectric response in accordance with data previously reported for BTO33/BFO67 composite films having a R_{rms} of 8.5 nm [66]. In the present case, the absence of piezoelectric response may be also ascribed to the cubic nature of the upper part of the film. On the other hand, the A-type film shows a piezoelectric and ferroelectric behavior with a coercitive voltage of 2V.

These piezoelectric behavior findings are also in accordance with literature data, which report the occurrence of the morphotropic phase boundary for a percentage of $BaTiO_3$ between 32 and 35% [19,75].

4.6. Conclusion

The MOCVD approach proved a powerful tool for the fabrication of Ba and Ti co-doped $BiFeO_3$ films. An accurate control of processing parameters, in particular the multicomponent source mixture ratio, resulted selectively and reproducibly in the formation of two different systems: a single-phase solid solution $Bi_{0.8}Ba_{0.2}Fe_{0.5}Ti_{0.5}O_3$ for the A-type sample and a nanocomposite for the B-type sample with an average composition of $Bi_{0.6}Ba_{0.4}Fe_{0.6}Ti_{0.4}O_3$, formed by $Bi_{(1-x)}Ba_xFeO_3$ nanocolumns embedded in a $Bi_{(1-x)}Ba_xFe_{(1-y)}Ti_yO_3$ phase. To our knowledge, this study represents the first report on MOCVD of Ba and Ti co-doped $BiFeO_3$ films and the presently addressed comprehensive characterization adds a notable tile in the overall mosaic of the $BiFeO_3$-$BaTiO_3$ systems. This synthetic approach exemplifies a more cost-effective process, with respect to previously reported methodologies, and the major advantage to be easily scalable.

References

[1] G. Catalan and J. F. Scott, Physics and Applications of Bismuth Ferrite, Adv. Mater., 2009, 21, 2463.

[2] T. Choi, S. Lee, Y. J. Choi, V. Kiryukhin, S.W. Cheong, Switchable Ferroelectric Diode and Photovoltaic Effect in $BiFeO_3$ Science, 2009, 324, 63.

[3] J. Wu, Z. Fan, D. Xiao, J. Zhu, J. Wang, Prog., Multiferroic bismuth ferrite-based materials for multifunctional applications: Ceramic bulks, thin films and nanostructures, Mater. Sci., 2016, 84, 335.

[4] Q. Zhang, D. Sando, V. Nagarajan, Chemical route derived bismuth ferrite thin films and nanomaterials, J. Mater. Chem. C, 2016, 4, 4092.

[5] S. Li, R. Nechache, I. A. V. Davalos, G. Goupil, L. Nikolova, M. Nicklaus, J. Laverdiere, A. Ruediger, F. Rosei, Ultrafast Microwave Hydrothermal Synthesis of $BiFeO_3$ Nanoplates, J. Amer. Cer. Soc., 2013, 96, 3155.

[6] K. Sardar, J. Hong, G. Catalan, P. K. Biswas, M. R. Lees, R. I Walton, J. F. Scott, S. A. T. Redfern, Structural, spectroscopic, magnetic, and electrical characterization of Ca-doped polycrystalline bismuth ferrite, $Bi_{1−x}Ca_xFeO_3−x/2$ (x ≤ 0.1), J. Phys.: Condens. Matter 24 (2012) 04590.

[7] A. Chaudhuri, K.Mandal, Study of structural, ferromagnetic and ferroelectric properties of nanostructured barium doped Bismuth Ferrite, J. Magn. Magn. Mater. 353 (2014) 57-64.

[8] Y. Tian and Fei Xue, Impedance spectrum and magnetic properties of $BiFe_{0.95}Ti_{0.05}O_3$ ceramics, J. Mater. Sci.: Mater. Electr., 2019, 30, 15452.

[9] C. H. Yang, J. Seidel, S.Y. Kim, P. B. Rossen, P. Yu, M. Gajek, Y. H. Chu, L. W. Martin, M. B. Holcomb, Q. He, P. Maksymovych, N. Balke, S. V. Kalinin, A. P. Baddorf, S. R. Basu, M. L. Scullin and R. Ramesh, Electric modulation of conduction in multiferroic Ca-doped $BiFeO_3$ films Nat. Mater., 2009, 8, 485.

[10] H.S.Park, J. S, Lim, J. Suh, C.H. Yang, Real-time observation of filamentary conduction pathways in Ca-doped $BiFeO_3$, App. Phys. Lett., 2019, 115, 183901.

[11] X. L. Wen, Z. Chen, X. Lin, Structural, Ferroelectric and Ferromagnetic Properties of Single-Phase $Bi_{0.95}Ba_{0.05}FeO_3$ Thin Film Prepared by Pulsed Laser Deposition, J. Supercond. Nov. Magn., 2015, 28, 3707.

[12] L. Zhang, Y.L. Huang, G. Velarde, A. Ghosh, S. Pandya, D. Garcia, R. Ramesh, L. W. Martin, Enhanced pyroelectric properties of $Bi_{1-x}La_xFeO_3$ thin films, APL Mater., 2019, 7, 111111.

[13] T. M. W. J. Bandara, C. S. Knee, M. Furlani, I. Albinsson, B. E. Mellander, Novel photo-voltaic device based on $Bi_{1−x}La_xFeO_3$ perovskite films with higher efficiency, J. Mater. Sci.: Mater. Electr., 2019, 30, 1654.

[14] D. Chen, C. T. Nelson, X. Zhu, C. R. Serrao, J. D. Clarkson, Z. Wang, Y. Gao, S.-L.Hsu, L.R. Dedon, Z. Chen, D. Yi, H.-J. Liu, D. Zeng, Y.-H. Chu, J. Liu, D. G. Schlom, R. Ramesh, A strain-driven antiferroelectric-to-ferroelectric phase transition in La-doped BiFeO3 thin films on Si, Nano Letters 17 (2017), 5823-5829

[15] Chen, D., C.T. Nelson, X. Zhu, C.R. Serrao, J.D. Clarkson, Z. Wang, Y. Gao, S.-L. Hsu, L.R. Dedon, Z. Chen, D. Yi, H.-J. Liu, D. Zeng, Y.-H. Chu, J. F Liu, D.G. Schlom, and Ramamoorthy Ramesh. "A Strain-

Driven Antiferroelectric-to-Ferroelectric Phase Transition in La-Doped BiFeO3 Thin Films on Si." Nano Letters 17 (2017) 5823-5829..

[16] M. Kumar and K. L.Yadav, The effect of Ti substitution on magnetoelectric coupling at room temperature in the $BiFe_{1-x}Ti_xO_3$ system, J. Phys.: Condes. Matter, 18 (2006) 40

[17] A. Kumar, A. Kumar, S. Saha, H. Basumatary, R. Ranjan, Ferromagnetism in the multiferroic alloy systems $BiFeO_3$-$BaTiO_3$ and $BiFeO_3$-$SrTiO_3$: Intrinsic or extrinsic?, Appl. Phys. Lett. 114 (2019) 022902.

[18] T.-H. Wang, C.-S. Tu, H.-Y. Chen, Y. Ding, T. C. Lin, Y.-D. Yao, V. H. Schmidt, K.-T. Wu, Magnetoelectric coupling and phase transition in BiFeO3 and (BiFeO3)0.95(BaTiO3)0.05 ceramics, J. Appl. Phys., 109 (2011) 044101.

[19] A. Singh, V. Pandey, R. K. Kotnala, and D. Pandey, Direct Evidence for Multiferroic Magnetoelectric Coupling in 0.9 BiFeO3 − 0.1 BaTiO3, Phys. Rev. Lett., 101 (2008) 247602.

[20] D.V. Karpinsky, M.V. Silibin, A.V. Trukhanov, A.L. Zhaludkevich, S.I. Latushka, D.V. Zhaludkevich, V. Sikolenko, V.A. Khomchenko, Evolution of crystal structure of Ba and Ti co-doped $BiFeO_3$ ceramics at the morphotropic phase boundary, J. Alloys Comp. 803 (2019) 1136-1140.

[21] F. P. Gheorghiu, A. Ianculescu, P. Postolache, N. Lupu, M. Dobromir, D. Luca, L. Mitoseriu, Preparation and properties of $(1 − x) BiFeO_3 − x BaTiO_3$ multiferroic ceramics, J. Alloys Comp. 506 (2010) 862.

[22] S. Cheng, B.-P. Zhang, L. Zhao and K.-K. Wang, Enhanced insulating and piezoelectric properties of $0.7BiFeO_3$–$0.3BaTiO_3$ lead-free ceramics by optimizing calcination temperature: analysis of Bi^{3+} volatilization and phase structures, J. Mater. Chem. C, 2018, 6, 3982.

[23] N. Itoh, T. Shimura, W. Sakamoto, T. Yogo, Fabrication and Characterization of BiFeO3-BaTiO3 Ceramics by Solid State Reaction, Ferroelectrics 356 (2007) 19-23.

[24] I. Calisir and D. A. Hall, Chemical heterogeneity and approaches to its control in $BiFeO_3$–$BaTiO_3$ lead-free ferroelectrics, J. Mater. Chem. C, 2018, 6, 134.

[25] G. Wang, Z. Fan, S. Murakami, Z. Lu, D. A. Hall, D. C. Sinclair, A. Feteira, X. Tan, J. L. Jones, A. K. Kleppe, D. Wang, I. M. Reaneya, Origin of the large electrostrain in BiFeO3-BaTiO3 based lead-free ceramics, J. Mater. Chem. A 7 (2019) 21254-21263.

[26] A. Pakalniskis, A. Lukowiak, G. Niaura, P.Głuchowski, D.V. Karpinsky, D.O. Alikin, A.S. Abramov, A. Zhaludkevich, M. Silibin, A.L. Kholkin, R. Skaudzius, W. Strek, A. Kareiva, Nanoscale ferroelectricity in pseudo-cubic sol-gel derived barium titanate - bismuth ferrite (BaTiO3-BiFeO3) solid solutions, J. Alloys Comp. 830 (2020) 154632/1-154632/7.

[27] K. Singh, A. Gautam, K. Sen, R. K. Kotnala, M. Kumar, P. Gautam and M. Singh, Room temperature long range ferromagnetic ordering in (BiFeO3)1-x(PbTiO3)x nanocrystallites, J. Appl. Phys. 109 (2011) 123911/1- 123911/5.

[28] T.-J. Park, G. C. Papaefthymiou, A. J. Viescas, Y. Lee, H. Zhou, S. S. Wong, Composition-dependent magnetic properties of BiFeO3-BaTiO3 solid solution nanostructures, Phys. Rev. B, 82 (2010) 024431/1-024431/10.

[29] H. Toupet, V. V. Shvartsman, F. LeMarrec, P. Borisov, W. Kleemann and M. Karkut, Enhanced magnetization in BiFeO3/BaTiO3 multilayers: an interface effect?, Integrated Ferroelectrics 100 (2008) 165-176.

[30] P. Yang, K. M. Kim, J.-Y. Lee, J. Zhu and H. Y. Lee, Magnetic properties of multiferroic BiFeO3/BaTiO3 Bi-layer thin films, Integrated Ferroelectrics 113 (2009) 26-30.

[31] K. Ueda, H. Tabata, T. Kawai, Coexistence of ferroelectricity and ferromagnetism in BiFeO3-BaTiO3 thin films at room temperature, Appl. Phys.Lett. 75 (1999) 555-557.

[32] P. Murugavel, J.-H. Lee, J. Y. Jo, H. Y. Sim, J.-S. Chung, Y. Jo, M.-H Jung, Structure and ferroelectric properties of epitaxial (1−x)BiFeO3–xBaTiO3 solid solution films, J. Physics: Cond. Matter, 20 (2008) 415208/1- 415208/6.

[33] M. Park, T. Kanashima, M. Okuyama, S. Nakashima, K. M. Kim, J.-Y. Lee, H. Y. Lee, Multiferroic properties of epitaxial 0.7BiFeO3-0.3BaTiO3 solid solution thin films on La-doped SrTiO3 (001) substrate, J. Korean Phys. Soc. 58 (2011) 674-677.

[34] J. Wu, J. Wang, Multiferroic behavior of BiFeO3-RTiO3 (Mg, Sr, Ca, Ba, and Pb) thin films, J. Appl. Phys. 108 (2010) 026101/1-026101/3.

[35] T. Sasaki, Y. Hirabayashi, H. Kobayashi, Y. Sakashita, Effect of dopant on piezoelectric properties of lead-free BiFeO3-BaTiO3 film, Jpn. J. Appl. Phys., 50 (2011) 09NA08/1-09NA08/5.

[36] Y. Hu, Q. Xie, R. Liang, X. Zhao, Z. Zhou, X. Dong, F. Wang, Y. Tang, N. Liu, X. Liu, High energy storage performance in lead-free BiFeO3-BaTiO3 ferroelectric thin film fabricated by pulsed laser deposition, AIP Advances 9 (2019) 085005/1-085005/5.

[37] T. Fujii, S. Shimizu, A. Kajima, T. Miyama, Film fabrication of solid solution of the bismuth ferrite (BiFeO3)-barium titanate (BaTiO3) system by rf-reactive sputtering, J. Magn. Magn. Mater. 54-57 (1986), 1303-1304.

[38] B. Madon, H. B. Kang, M. G. Kang, D. Maurya, B. A. Magill, M. J. P. Alves, J.-E. Wegrowe, H.-J. Drouhin, S. Priya, G. A. Khodaparast, Room temperature ferromagnetic resonance in hetero-epitaxial BTO – BFO/LSMO magnetoelectric composite, AIP Advances 8 (2018) 105034/1-105034/8.

[39] Y. F. Hou, W. L. Li, T. D. Zhang, W. Wang, W. P. Cao, X. L. Liu, W. D. Fei, Large piezoelectric response of BiFeO3/BaTiO3 polycrystalline films induced by the low-symmetry phase, Phys. Chem. Chem. Phys. 17 (2015) 11593—11597.

[40] Dai, Q. Gao, C. Cui, L. Yang, C. Li, X. Li, Role of ferroelectric/ferromagnetic layers on the ferroelectric properties of magnetoelectric composite films derived by chemical solution depositio, Mater. Res. Bulletin 99 (2018) 424-428.

[41] Y. Wang, J. Li, J. Chen, Y. Deng, Ba and Ti co-doped BiFeO3 thin films via a modified chemical route with synchronous improvement in ferroelectric and magnetic behaviors, J. Appl. Phys. 113 (2013) 103904/1-103904/5.

[42] S. Sharma, M. Tomar, A. Kumar, N. K. Puri, V. Gupta, Stress induced enhanced polarization in multilayer BiFeO3/BaTiO3 structure with improved energy storage properties, AIP Advances 5 (2015), 107216/1-107216/8.

[43] S. Hohenberger, J. K. Jochum, M. J. Van Bael, K. Temst, C. Patzig, T. Höche, M. Grundmann, M. Lorenz, Enhanced Magnetoelectric Coupling in BaTiO3-BiFeO3 Multilayers—An Interface Effect, Materials 13 (2020) 197/1-194/14.

[44] M. Lorenz , V. Lazenka , P. Schwinkendorf , M. J. Van Bael, A. Vantomme, K. Temst, M. Grundmann, T. Höche, Epitaxial Coherence at Interfaces as Origin of High Magnetoelectric Coupling in Multiferroic BaTiO$_3$-BiFeO$_3$ Superlattices, Adv. Mater. Interfaces 3 (2016) 1500822/1-1500822/7.

[45] M. Lorenz, D. Hirsch, C. Patzig, T. Höche, S. Hohenberger, H. Hochmuth, V. Lazenka, K. Temst, M. Grundmann, Correlation of Interface Impurities and Chemical Gradients with High Magnetoelectric Coupling Strength in Multiferroic BiFeO3-BaTiO3 Superlattices, ACS Appl. Mater. Interfaces 9 (2017) 18956-18965.

[46] S. Cho, C. Yunb, Y. S. Kima, H. Wang, J. Jian, W. Zhang, J. Huang, X. Wang, H. Wang, J. L. MacManus-Driscoll, Strongly enhanced dielectric and energy storage properties in lead-free perovskite titanate thin films by alloying, Nano Energy 45 (2018) 398–406.

[47] R. R. H. H. Mudiyanselage, B. A. Magill, J. Burton, M. Miller, J. Spencer, K. McMillan, G. A. Khodaparast, H. B. Kang, M. G. Kang, D. Maurya, S. Priya, J. Holleman, St. McGill, C. J. Stanton, Coherent acoustic phonons and ultrafast carrier dynamics in hetero-epitaxial BaTiO3–BiFeO3 films and nanorods, J. Mater. Chem. C, 2019, 7, 14212-14222.

[48] M. K. Singh, Y. Yang, C. G. Takoudis, A. Tatarenko, G. Srinivasan, P. Kharel and G. Lawes, Multiferroic BiFeO3 thin films for multifunctional devices, J. Nanosci. Nanotech. 10 (2010) 6195.

[49] N. Deepak, P. Carolan, L. Keeney, P.F. Zhang, M.E. Pemble, R.W. Whatmore, Bismuth self-limiting growth of ultrathin BiFeO3 films, Chem. Mater. 27 (2015) 6508–6515.

[50] H. Funakubo, S. Yasui, T. Yamada, M. Ishikawa, MOCVD growth of BiFeO3-based ferroelectric films and their characterization Mater. Integration, 22(2) (2009) 25-31.

[51] M. S. Kartavtseva, O. Yu. Gorbenko, A. R. Kaul, S. Fusil, A. Barthelemy and K. Bouzehouane, Control of the Cation Stoichiometry in the Multiferroic BiFeO3 Thin Films, Ferroelectrics 374 (2008) 20-45.

[52] M. S. Kartavtseva, O. Yu. Gorbenko, A. R. Kaul, T. V. Murzina, S. A. Savinov and A. Barthelemy, BiFeO3 thin films prepared using metalorganic chemical vapor deposition, Thin Solid Films 515 (2007) 6416-6421.

[53] J. Thery, C. Dubourdieu, T. Baron, C. Ternon, H. Roussel and F. Pierre, MOCVD of BiFeO3 thin films on SrTiO3, Chem. Vap. Deposition, 13 (2007)   232-238.

[54] S. Yasui, M. Nakajima, H. Naganuma, S. Okamura, K. Nishida, T. Yamamoto, T. I., Masaki Azuma, H. Morioka, K. Saito, M. Ishikawa, T. Yamada, H. Funakubo, Composition control and thickness dependence of {100}-oriented epitaxial BiCoO3 –BiFeO3 films grown by metalorganic chemical vapor deposition, J. Appl. Phys. 105 (2009) 061620/1- 061620/5.

[55] H. Naganuma, S. Yasui, K. Nishida, T. Iijima, H. Funakubo, S. Okamura, Enhancement of magnetization at morphotropic phase boundary in epitaxial BiCoO3-BiFeO3 solid solution films grown on SrTiO3 (100) substrates, J. Appl. Phys. 109 (2011) 07D917/1-07D917/3.

[56] G. G. Condorelli, M. R. Catalano, E. Smecca, R. Lo Nigro, G. Malandrino, Piezoelectric domains in BiFeO3 films grown via MOCVD: Structure/property relationship, Surf. Coat. Technol. 230 (2013) 168–173.

[57] M. R. Catalano, G. Spedalotto, G. G. Condorelli, G. Malandrino, MOCVD Growth of Perovskite Multiferroic BiFeO3 Films: The Effect of Doping at the A and/or B Sites on the Structural, Morphological and Ferroelectric Properties, Adv. Mater. Interfaces (2017) 1601025/1-1601025/7.

[58] D. Scillato, N. Licciardello, M. R. Catalano, G. G. Condorelli, R. Lo Nigro and G. Malandrino, J. Nanosci. Nanotech., 2011, 11, 8221.

[59] G. Malandrino, F. Castelli, I. L. Fragalà, A novel route to the second-generation alkaline-earth metal precursors for metal-organic chemical vapor deposition: one-step synthesis of M(hfa)2·tetraglyme (M = Ba, Sr, Ca and Hhfa = 1,1,1,5,5,5-hexafluoro-2,4-pentanedione), Inorg. Chim. Acta 224 (1994) 203-207.

[60] M. Goldschimdt, Die Gesetze der Krystallochemie, Akad. Oslo. I. Mat. Natur. 1926, 2, 477-485..

[61] C. D. Wagner, L. E. Davis, M. V. Zeller, J. A. Taylor, R. H. Raymond, L. H. Gale, Empirical atomic sensitivity factors for quantitative analysis by electron spectroscopy for chemical analysis, Surf. Interface Anal., 1981, 3, 211.

[62] J. F. Moulder, W. F. Stickle, P. E. Sobol and K. D. Bomben Handbook of X-ray Photoelectron Spectroscopy, Ed. J. Chastain, Perkin-Elmer Corporation Physical Electronics Division, Minnesota, 55344 USA, 1992.

[63] Q. Micard, G. G. Condorelli, G. Malandrino, Piezoelectric BiFeO3 Thin Films: Optimization of MOCVD Process on Si, Nanomaterials, 10 (2020) 630/1-630/10.

[64] C. Tudisco, A. L. Pellegrino, G. Malandrino, G. G. Condorelli, Surface anchoring of bi-functional organic linkers on piezoelectric BiFeO3 films and particles: Comparison between carboxylic and phosphonic tethering groups, Surf. Coat. Technol. 343 (2018) 75–82.

[65] S.M. Lee, A. Cho, Y. S. Cho, Enhanced optical and piezoelectric characteristics of transparent Ni-doped BiFeO3 thin films on a glass substrate, RSC Adv. 6 (2016) 16602–16607.

[66] M. Lorenz, V. Lazenka, P. Schwinkendorf, F. Bern, M. Ziese, H. Modarresi, A. Volodin, M. J Van Bael, K. Temst, A. Vantomme, M. Grundmann, Multiferroic BaTiO3-BiFeO3 composite thin films and multilayers: strain engineering and magnetoelectric coupling, J. Phys. D: Appl. Phys. 47 (2014) 135303/1- 135303/10.

[67] G. Malandrino, L. M. S. Perdicaro, I. L. Fragalà, A. M. Testa, D. Fiorani, MOCVD Growth, Micro-Structural, and Superconducting Properties of a-Axis Oriented TlBaCaCuO Thin Films, Chem. Mater. 16 (2004) 608-613.

[68] G. Malandrino, L. M. S. Perdicaro, G. Condorelli, I. L. Fragalà, A. Cassinese and M. Barra, Synthesis and characterization of La2-xBaxCuO4+δ thin film through a simple MOCVD approach, J. Mater. Chem., 15 (2005) 4718-4722.

[69] R. Lo Nigro, R. G. Toro, R. Malandrino, I. L. Fragala, M. Losurdo, M. M. Giangregorio, G. Bruno, V. Raineri, P. Fiorenza, Calcium copper-titanate thin film growth: Tailoring of the operational conditions through nanocharacterization and substrate nature effects, J. Phys. Chem. C 110 (2013) 17460-17467.

[70] R. Lo Nigro, G. Malandrino, R. G Toro, M. Losurdo, G. Bruno, I. L. Fragala, Recent advances in characterization of CaCu3Ti4O12 thin films by spectroscopic ellipsometric metrology, J. Amer. Chem. Soc. 127 (2005) 13772-13773.

[71] G. Malandrino, I. L. Fragala, P. Scardi, Heteroepitaxy of LaAlO3 (100) on SrTiO3 (100): In situ growth of LaAlO3 thin films by metal-organic chemical vapor deposition from a liquid single source, Chem. Mater. 10 (1998) 3765-3768.

[72] M. R. Catalano, G. Cucinotta, E. Schilirò, M. Mannini, A. Caneschi, R. Lo Nigro, E. Smecca, G. G. Condorelli, G. Malandrino, Metal-Organic Chemical Vapor Deposition (MOCVD) Synthesis of Heteroepitaxial Pr0.7Ca0.3MnO3 Films: Effects of Processing Conditions on structural/Morphological and Functional Properties, ChemistryOpen 4 (2015) 523-532.

[73] H. Pan, F. Li, Y. Liu, Q. Zhang, M. Wang, S. Lan, Y. Zheng, J. Ma, L. Gu, Y. Shen, P. Yu, S. Zhang, L.-Q. Chen, Y.-H. Lin, C.-W. Nan, Ultrahigh–energy density lead-free dielectric films via polymorphic nanodomain design, Science 365 (2019) 578–582.

[74] G. F. Cheng, Y. J. Ruan, W.Liu, X. S. Wu, Effect of local structural distortion on magnetic and dielectric properties in BiFeO3 with Ba,Ti co-doping, Physica B 468-469 (2015) 81–84.

[75] M. H. Lee, D. J. Kim, J. S. Park, S. W. Kim, T. K. Song, M.-H. Kim, W.-J. Kim, D. Do, I.-K. Jeong, High-Performance Lead-Free Piezoceramics with High Curie Temperatures, Adv. Mater. 27 (2015) 6976–6982.

5. Cobalt doping of BiFeO$_3$ films: optimization of the synthetic procedure to selectively grow solid solutions or nanocomposites

Multiferroics are materials that combine two or more ferroic orders and have been at the center of numerous researches because of their potential used in a wide range of fields such as sensors, actuators, or electronic memory devices [1]. In the case of data storage, the information could be encoded either in the polarization or the magnetization of the material, thanks to the interactions between ferroic orders. Such material can store data written by applying an external electric field and read those data magnetically (and vice versa), giving the potential to better device integration and reduced power consumption. [2]

Magnetoelectricity (ME) is the name given to the coupling between a material magnetic and electric properties. ME makes possible the manipulation of the magnetization by applying an electric field or the control of the polarization by applying a magnetic field. The magnetoelectric coupling has been reported in single-phase or two-phases composite systems. Normally, for a single-phase material to display ME coupling, it implies that ferroelectric and ferromagnetic orders are coexisting in this material [2].

Compared with single-phase multiferroic thin films, two-phase nanocomposite ones have advantages regarding compositional flexibility, phase selections and distribution, and morphology. Two-phase systems have a strain-mediated magnetoelectric coupling resulting from close contact between magnetostrictive (or piezomagnetic) and piezoelectric materials (or electrostrictive). The larger the interfacial area between the two phase composite, the larger will be the ME coupling observed in the material [2,3].

In this context, because nanocomposite systems can provide electric control of magnetic anisotropy by exploiting the elastic strain transfer from one component to another. Perovskite-spinel nanocomposite thin films are of great interest for multiferroic devices due to ferroelectric and ferromagnetic properties' coexistence and the observation of magnetoelectric coupling between two immiscible phases. The most widely studied examples are BiFeO$_3$–CoFe$_2$O$_4$ (BFO–CFO) or BaTiO$_3$–CoFe$_2$O$_4$ (BTO-CFO) [3-6].

At room temperature, BiFeO$_3$ (BFO) is a multiferroic perovskite, in a single phase coexist ferroelectric (Curie temperature TC ~ 1103 K) and antiferromagnetic (TN ~ 643 K) properties, which can persist even at high temperature. The ferroelectric and the antiferromagnetic components lead to weak linear intrinsic magnetoelectric properties in the material [2, 7].

Among magnetic materials, spinel ferrites are of high interest because of their important magnetic response. CoFe$_2$O$_4$ (CFO) is a typical ferrimagnetic oxide with a high saturation

magnetization, high Curie temperature, and a large magnetocrystalline anisotropy. Moreover, CFO has a large magnetostriction coefficient, making it a promising candidate for its integration in nanocomposite to improve the ME coupling with the ferroelectric phase.

Depending on phase organizations, nanocomposite thin films can be divided into three different categories [3,8,9]:

- 0-3 type nanocomposite films (*nanoparticles dispersed in a continuous matrix*): their synthesis is quite straightforward, but the induced important leakage current makes it very difficult to polarize. Moreover, the particle's random distribution in the matrix is a challenge to obtain a homogeneous nanocomposite structure.
- 2-2 type nanocomposite films (*consisting of bilayer or multilayer thin films stacks*): consist of an alternating growth of an epitaxial ferroelectric (ferromagnetic) thin film on a ferromagnetic (ferroelectric) film. Such structures are easy to fabricate simply by alternating the deposited films, and they also offer a good reduction of leakage currents. The main drawback is the clamping effect between film and substrate, which may reduce or even suppress in-plane elastic deformation of the film induced by an external magnetic or electric field and so degrading the ME coupling.
- 1-3 type nanocomposite films (*aligned nanocolumns within a continuous matrix*): can be described as a ferroelectric (ferromagnetic) matrix in which ferromagnetic (ferroelectric) vertically aligned nanostructure (VAN) is grown epitaxially. Compared to 2-2 type nanocomposite, 1-3 type are more subjected to leakage current but are less impacted by substrate clamping and are expected to have a larger ME coefficient.

BFO-CFO nanocomposites have already been obtained through several synthetic routes PLD [3,4,10], sputtering [11], sol-gel [9,12], chemical solutions [13], and obtained in the form of powders [13], fibers [14], and thin films. 1-3 type films have been mostly obtained by PLD on $SrTiO_3$ (100) [4], but other examples can be found on (110) or (111) [6,10] STO, on (100) $LaAlO_3$ single crystal [15], or pre-patterned Si-based substrates [16].

MOCVD protocols have been studied to propose the one-step facile MOCVD deposition process of BFO-CFO 1-3 type nanocomposite thin films $SrTiO_3$ (100). A mixture of $Bi(phenyl)_3$, $Fe(tmhd)_3$, $Co(tta)_2TMEDA$ (Htta= 2-thenoyl-trifluoroacetone, TMEDA= N,N,N',N'-tetramethylethylendiamine) precursors has been used for all the depositions. Process investigation focused on the impact of precursor ratio and mixture vaporization temperature on the final films' quality. As it has been done in the previous parts, depositions have been carried out for one hour at 750°C in an MOCVD hot-wall reactor, with a single sublimation zone. Argon and oxygen have been used as carrier and reactant gas, respectively, with a constant 150mL/min flow rate.

Film morphologies have been controlled by field emission scanning electron microscopy (FE-SEM), and limits of the chemical quantification by energy dispersive X-ray analysis (EDS) have been commented. Finally, identification has been permitted by X-ray diffraction analysis

(XRD) analysis. Atomic force microscopy coupled with piezoresponse force microscopy (AFM/PFM) and vibrating sample magnetometry (VSM) have been used to confirm the piezoelectric and ferroelectric properties of some films and to investigate their magnetizations, respectively.

5.1.   First Approach

The first approach focused on the deposition of the $BiFeO_3$ and $CoFe_2O_4$ phases as two independent phases. Two precursor mixtures have been independently designed to deposit separately BFO or CFO.

- For the deposition of $BiFeO_3$ thin films to compensate Bi volatility, the Bi(phenyl)$_3$: Fe(thmd)$_3$ molar ratio is : (*1: 0.66*)
- For the deposition of $CoFe_2O_4$ phase, Co(tta)$_2$(tmeda) and Fe(thmd)$_3$ has been considered as a ratio of: (*1:2*)

Then after the selection of the two based mixture for the deposition, they have been mixed at different BFO:CFO molar ratio :

- 1:1 which is equivalent to a precursor mixture of Bi:Co:Fe → (*1 : 1 : 2.66*)
- 1:1.5 which is equivalent to a precursor mixture of Bi:Co:Fe → (*1 : 1.5 : 3.66*)
- 1:2 which is equivalent to a precursor mixture of Bi:Co:Fe → (*1 : 2 : 4.66*)

Considering the amount of different precursors, the vaporized mixture (total weight of 250 mg) needs to be prepared before each deposition. Making it in advance for several deposition is not advisable because this procedure could lead to a bad precursor mixing and an uncontrolled stoichiometry in the vaporized mixture and, consequently, in the deposited film.

For this first method, depositions of four different types are reported (Table 1); the focus was on the impact of the BFO:CFO ratio of the vaporized mixture on the deposited thin film morphology and structure.

Table. 1 List of the four different types of film deposited.

Samples	BFO:CFO	$T_{precursors}$ [°C]
Sample 1	1:1	130
Sample 2	1:1	120
Sample 3	1:1.5	120
Sample 4	1:2	120
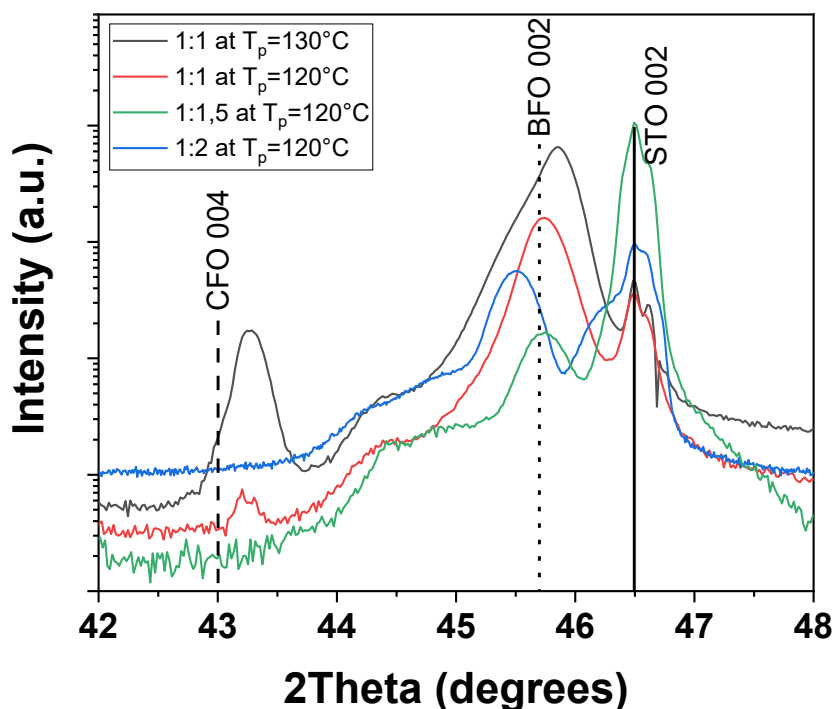
Figure 1. XRD ϑ-2ϑ diffraction pattern of the 42° to 48° of all the reported samples.

X-ray diffraction (XRD) analysis has been used to control the nature of the deposited films and to identify if the samples show the characteristics of a $BiFe_xCo_{(1-x)}O_3$ solid solution or a BFO-CFO nanocomposites. Film comparison is permitted by taking the substrate STO 002 reflection peaks ($2\theta= 46.485°$) as reference. Large θ-2θ scans acquired in Bragg-Brentano configuration from 20° to 60° indicates the presence of well out-of-plane oriented films for the four reported samples. However, for (*1:1.*5) and (*1:2*), the films present a small Bi_2O_3 parasitic phase component. For an easier understanding of the deposited systems, a zoom on the 42° to 48° region is reported in Figure 1. The threes samples deposited with the lower BFO:CFO ratio show a diffraction peak around $2\theta= 45.69°$ and have been attributed to a BFO like phase. In the case of BFO:CFO ratio (*1:2*), a shift toward lower angles has also been noted ($2\theta= 45.50°$) and is combined with the presence of a shoulder at $2\theta= 46.24°$ suggesting the presence of a supplementary peak. In this case, no CFO phase has been deposited, but this splitting in two peaks suggests the presence of two BFO-like phases in the films. The two BFO:CFO films deposited with a (*1:1*) ratio give the most promising results compared to the other samples. With a vaporization temperature of 120°C, a minimal CFO quantity is present in the film. However, by raising the vaporization temperature to 130°C, the amount of CFO detected in the film increases significantly. With a theoretical CFO (004) diffraction peak at $2\theta= 43.06°$, the peak shift at $2\theta= 43.25°$ indicates an out-off plane compression of the CFO phase. Also, the broad shoulder at 44.5° has been previously reported as a stressed BFO phase [17].
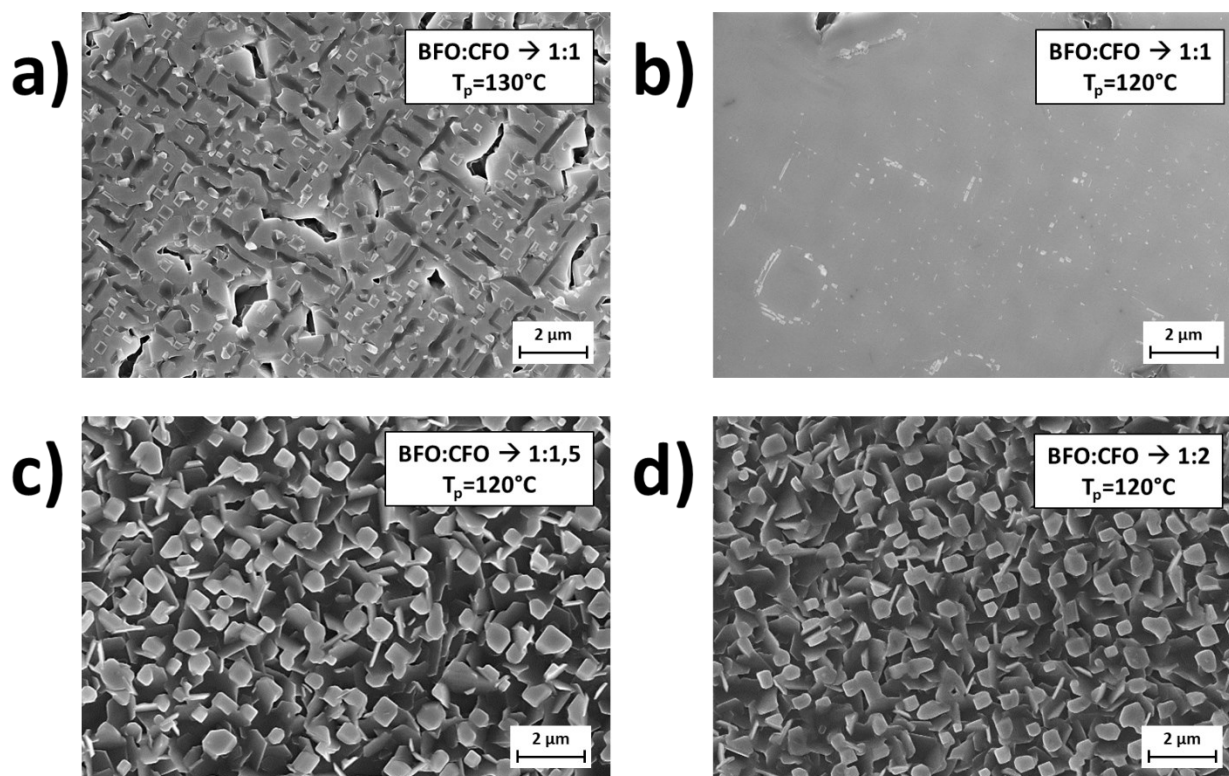
Figure 2. FE-SEM micrographs of the films deposited with the first approach a) Sample 1 b) Sample 2 c) Sample 3 and d) Sample 4.

FE-SEM observations have been used to explore the film morphologies for the different deposition conditions and initial vaporized mixture (Figure 2). From the analysis of the XRD patterns, the samples of interest, because of the presence of the CFO phase, are the ones obtained with the BFO:CFO ratio of (*1:1*). Films obtained with a vaporization temperature of 120 °C, even if few points with incomplete coalescence are visible, display a very smooth surface. At its surface, the small cubic structures diffused in the BFO matrix are attributed to CFO. The other (*1:1*) film deposited with a vaporization temperature of 130°C had a similar diffraction pattern but indicated a larger CFO component in the film. Figure 2a shows a similar view to Figure 2b: a BFO matrix in which cubic CFO nanocolumns are self-grown, but film morphology is more uneven with an increase of coalescence problem. However, columns dimension and density across the film is significantly higher with a T_p=130 °C suggesting control of CFO phase density through the precise control of the vaporization temperature. For BFO:CFO (*1:1.5*) and (*1:2*), very similar morphologies have been observed. Films growth is not homogeneous, giving poorly coalesced films with high roughness.

Coupled with FE-SEM investigation, the chemical composition of the film was attempted by EDX.. Due to the proximity of Fe K_β and L line (6.398 keV and 0.705 keV respectively) and Co K_α and L (7.059 keV and 0.776 keV), accurate quantification of the two elements is a real challenge (Figure 3) and the reported element atomic % does not correspond to the XRD and FE-SEM analysis.
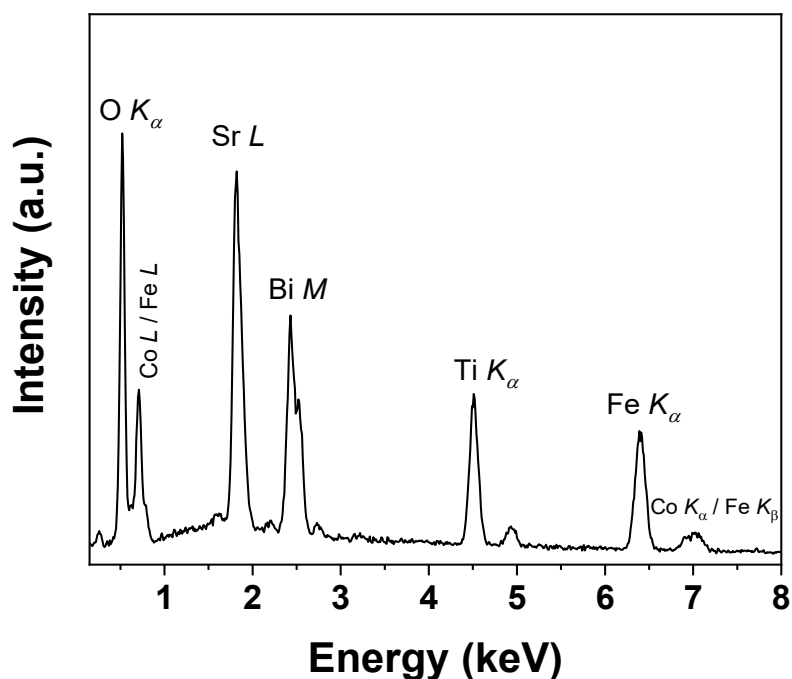
Figure 3. EDX spectra of Sample 4, illustrating the Fe and Co K lines overlap.

5.2. Second approach

The second approach is similar to what has been done in Chapter 3. for $BiFeO_3$ A-site doping with rare-earth elements with a constant vaporization temperature of 120°C. Cobalt ions can substitute Fe in the B-site of $BiFeO_3$ perovskite structure and be incorporated in a $BiFe_xCo_{(1-x)}O_3$ solid solution. While a first route investigated the vaporization of a BFO and CFO combined precursor preparations, the second method used BFO precursors mixture (Bi:Fe -->1:0.66) as the starting point for the incorporation of Co in the perovskite structure and the simultaneous deposition of $BiFeO_3$ and $CoFe_2O_4$ phase.

In this part, three different types of depositions are reported. Synthetic conditions are identical between all the reported samples, which differ only in the formulation of the vaporized mixture. As seen previously, quantification of Co-doping in the thin film is difficult because of the overlap between K and L lines of Co and Fe (Figure 3). To facilitate the results discussions, all the reported experiments have been identified by the precursors mixture they have been deposited with:

- Sample 1: Bi:Fe:Co → *1: 0.66 : 0.11*
- Sample 2 : Bi:Fe:Co → *1 : 0.66 : 0.17*
- Sample 3 : Bi:Fe:Co → *1 : 0.53 : 0.134*

The first two depositions have been done maintaining the ideal Bi:Fe ratio (*1:0.66*) needed to stabilize the BFO phase. At the third attempt, it has been decided to deviate from this ideal ratio as an attempt to go out of the ideal deposition condition of the BFO phase and see if it favors the formation of the CFO phase.

5.2.1. Structural and morphological characterization

X-ray diffraction (XRD) technique has been used to characterize the film structure and identify the different deposited phases. The XRD θ-2θ scans of films have been acquired in Bragg-Brentano mode from 20° to 60° and have been compared to study the impact of various Co-doping (Figure 4a). For better accuracy, all diffraction patterns have been aligned on the substrate STO 002 reflection peaks (2θ= 46.485°). The large scan of the films reveals good out-of-plane orientation in the [001] direction for all the deposited films., only the *(1:0.66:0.11)* contains a superficial parasitic phase of Bi_2O_3. A closer look at the 42° to 48° region reveals more information on the films (Figure 4b). All the deposited systems show one peak around pure BFO 002 reflection at 45.69°, indicating a major component of BFO related phase in the films. Co-doping increase does not provoke a significant peak shift, but a broadening of the BFO 002 reflection is clearly visible for higher doping concentration. Due to the extremely close ionic radius of Fe^{3+} ($r_{6\text{-coord spin low}}$ = 0.55 Å and $r_{6\text{-coord spin high}}$ = 0.645 Å) and Co^{3+} ($r_{6\text{-coord spin low}}$ = 0.545 Å and $r_{6\text{-coord spin high}}$ = 0.61 Å) [18] in the case of the deposition of a $BiFe_xCo_{(1-x)}O_3$ solid solution a low Co-doping would not significantly distort the BFO structure to induce a visible shift in the diffractions peaks. For the *(1:0.66:0.11)* and *(1:0.53:0.134) samples*, the peak corresponding to the 004 reflection of CFO is observed at 2θ=43.25°. The shift with respect to the theoretical value of 2θ=43.06° indicate a compressive strain along the *c*-axis. A broad shoulder at around 2θ=44.5° is present on all the samples. After in-plane measurements, a previous study attributed it to strain along the *c*-axis of the BFO related phase [17].
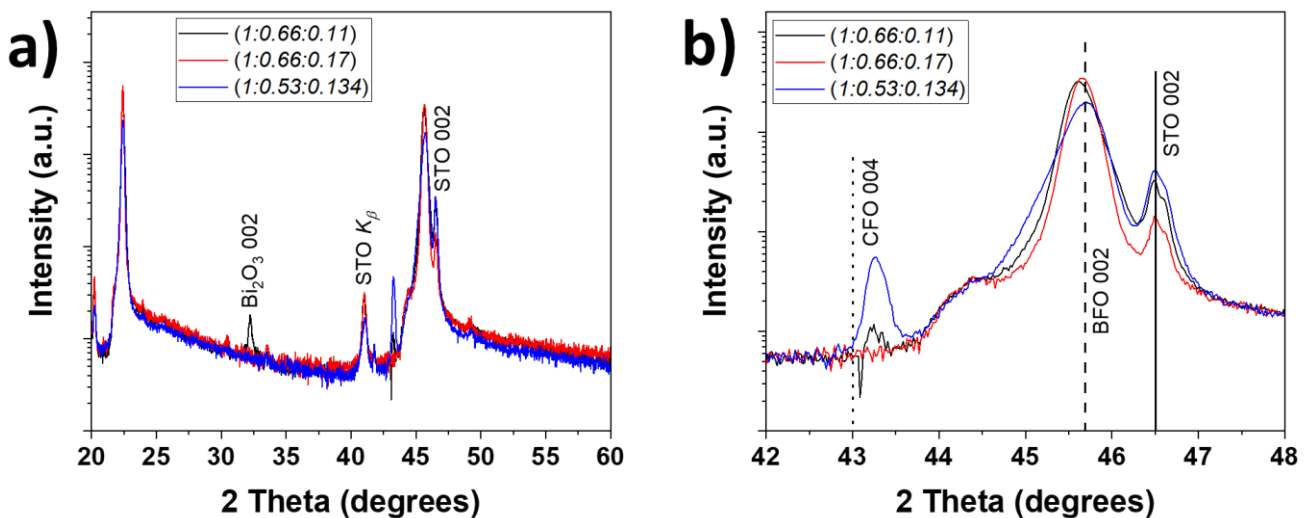
Figure 4. XRD patterns of the films obtained with the second approach: a) Large scan of samples showing high out-of-plane alignment and b) 42° to 48° patterns for phases identification.
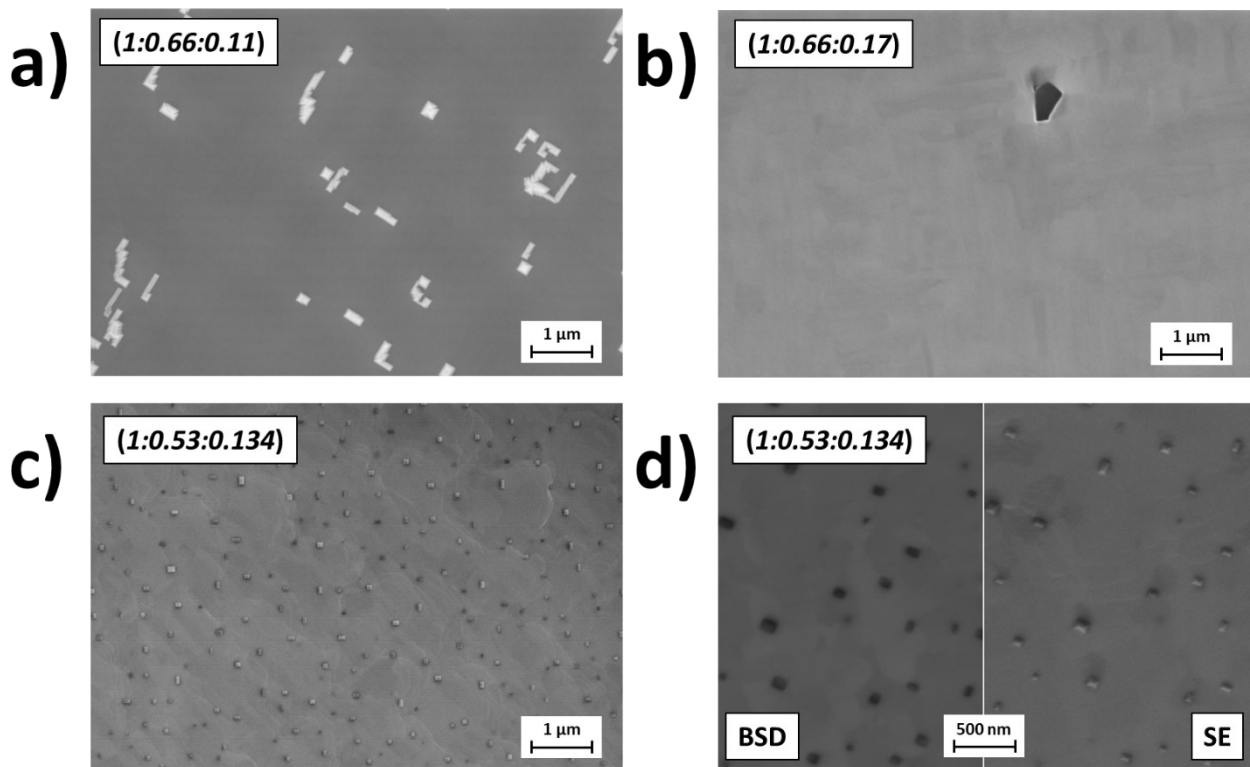
Figure 5. FE-SEM micrographs of the reported samples a) (1:0.66:0.11), b) (1:0.66:0.17), c) (1:0.53:0.134) and d) comparison between morphology (SE) and density (BSD) in the (1:0.53:0.134) film.

FE-SEM observation of sample morphologies confirmed what has been understood from the XRD analysis. For *(1:0.66:0.11)* the presence of a small number of Bi_2O_3 superficial squared grains on the sample surface is easily identified, while for *(1:0.66:0.17)* only the mirror-like surface is observed. All samples show high homogeneity in their morphology across the whole films with a very flat surface with no apparent grains of the BFO matrix. In *(1:0.53:0.134)* sample, the only systems where a clear nanocomposite system was deposited according to the XRD pattern, a similar uniform BFO-like matrix is visible, but 50 to 100 nm squared structure of vertically aligned CFO nanopillars can also be identified. To confirm their nature, electron backscattered images of the film is reported in Figure 5d. The use of the electron backscattered detector (BSD) helps visualize the film's chemical difference thanks to the different atomic composition of its different phases: the heaviest the elements, the brightest appears the region. CFO columns containing cobalt, a lighter element with respect to bismuth present in BFO, look significantly darker than the BFO matrix, confirming the CFO phase's regular distribution in the BFO homogeneous matrix.

5.2.2.   Functional characterization

Not only does BFO-CFO composites possess exciting ME coupling properties, but previous studies have demonstrated some significant increase in the magnetic properties in Co-doped BFO (solid solution) [19]. Samples of BFO-Co solid solution films and BFO-CFO nanocomposites have been sent to Ramesh Lab at University of California, Berkley for functional characterization. Following data on the ongoing work have been provided and are used with the authorization of Prof. Ramamoorthy Ramesh, Dr. Lucas M Caretta, Dr. Eric Parsonnet, and Rustem Ozgur. Studies are still ongoing and aim to characterize ferroelectric, piezoelectric, magnetic, and magnetoelectric coupling of the different systems. Preliminary results of *(1:0.66:0.17)* and *(1:0.53:0.134)* are reported below; the focus has been the confirmation of piezoelectric and ferroelectric and on the measurement of samples magnetic property. Piezoresponse force microscopy (PFM) has been used to confirm the presence of piezoelectric and ferroelectric behavior in the deposited (1:0.66:0.17) film. Out-of-plane (Figure 6a) and in-plane (Figure 6d) atomic force microscopy topographic images of large 20 µm x 20 µm areas have been recorded. The out-of-plane (Figure 6b and c) and in-plane (Figure 6e and f) piezoresponse and phase difference between the piezoresponse signal and the alternating voltage (Vac= 500mV) are also reported. As previously observed by FE-SEM, the (1:0.66:0.17) sample displays a very flat and consistent surface. A homogeneous out-of-plane piezoresponse is measured, and the phase scan shows an extremely uniform response, indicating a similar out-of-plane orientation for all the ferroelectric domains. In-plane scans reveal more information about in-plane domain distributions; two domains in-plane orientations are visible with phase differences of 135° and -135°. The in-plane piezoresponse map exhibits the same information as the phase scan, with opposites piezoresponse for the two domain in-plane directions.
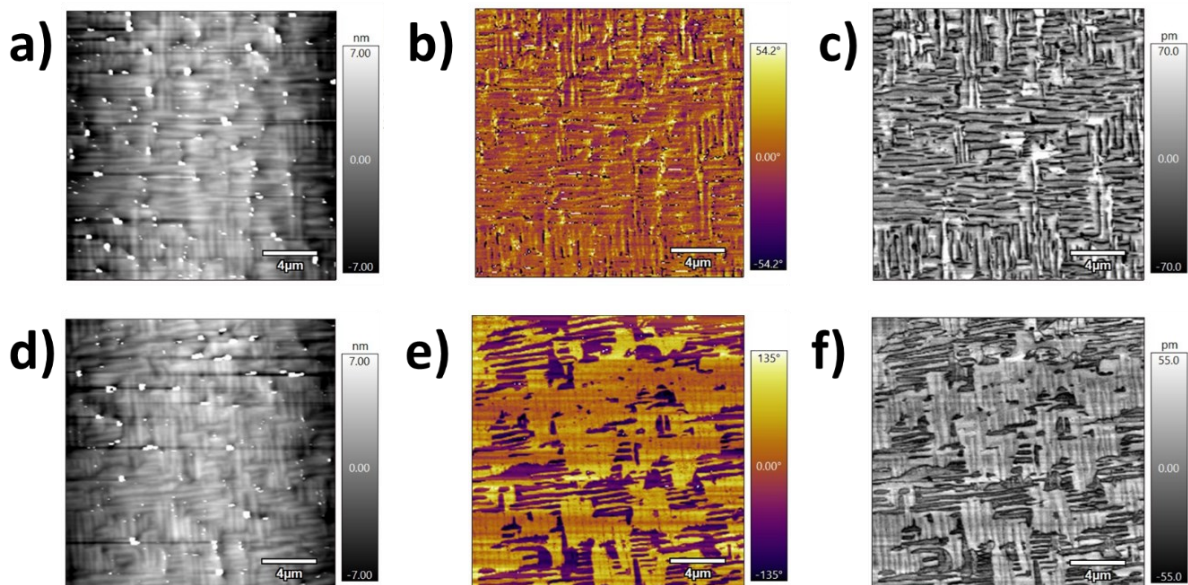
Figure 6. Out-of-plane a) AFM topography, b) Phase scan, c) Piezoresponse scan and in-plane: d) AFM topography, e) Phase scan and f) Piezoresponse scan. All images are from the (1:0.66:0.17) film.

Then, to confirm the possibility of the deposited film ferroelectric properties and visualize its domain switching, a writing experiment has been carried out on a smaller region. AFM topography scan of the 4 μm x 4 μm area of interest is reported in Figure 7a, and the written pattern in Figure 7b. The film was not subjected to any poling process, the following procedure has been performed on the "as-deposited" material. The domain switching is caused by the application of a bias voltage (between the PFM the tip and the film) of +9V (white area) or a - 9V (black area) (see Figure 7b). After applying the bias voltage, an out-of-plane of the film piezoresponse and phase maps have been registered. Piezoresponse mapping shows the clear boundaries of the areas where the bias voltages have been applied (Figure 7c). The phase scan shows that a clear switch occurred in the films between the areas poled with +9V and -9V, with a 220° phase difference (Figure 7d). The film can maintain those two different polarizations states, demonstrating the film domain switching and thus confirming its ferroelectric nature.

After assessment of piezoelectric and ferroelectric behavior of the deposited BFO-Co solid solution , investigation on the material magnetic properties has been carried out using vibrating sample magnetometry (VSM). Sample *(1:0.66:0.17)* shows an in-plane magnetization of about 30 emu/cc (Figure 8a). Previous studies on Co-doped BFO systems deposited by MOCVD on STO report a strong correlation between Co-doping amount/phase structure and sample magnetization. Co-doped BFO systems display a significant magnetization increase up to a Co-doping of 25%. Above this concentration, rhombohedral structure changes to tetragonal, and a decrease of the magnetization was reported. The morphotropic phase boundary has been estimated to be between a Co-doping of 20% to 25% [19-21]. *The nanocomposite (1:0.53:0.134) film* has also been investigated by VSM and has shown an out-of-plane magnetization, which was expected regarding CFO orientation in the material. However, the measured Ms≈27 emu/cc is lower than expected, and further investigations need to be done (Figure 8b).
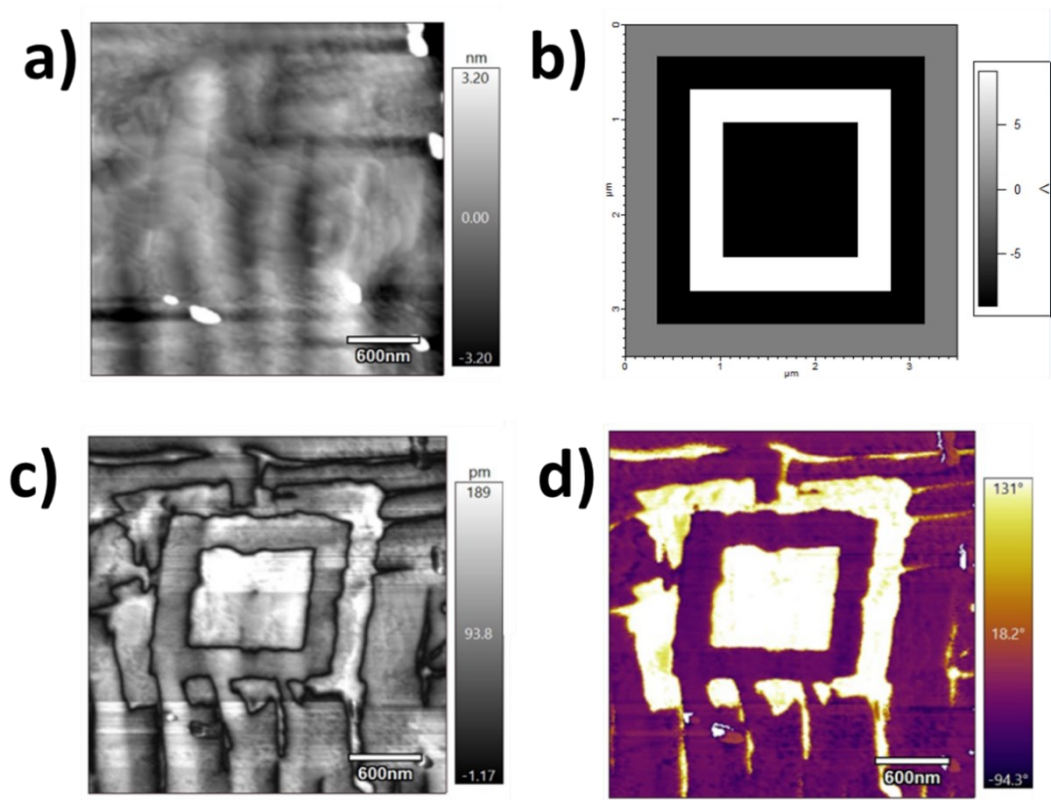
Figure 7. a) Out-of-plane AFM topography of the studied zone, b) Written pattern with a DC bias voltage of +9V (white) and -9V (black). After writing experiment: Out-of-plane c) piezoresponse scan and d) phase scan.
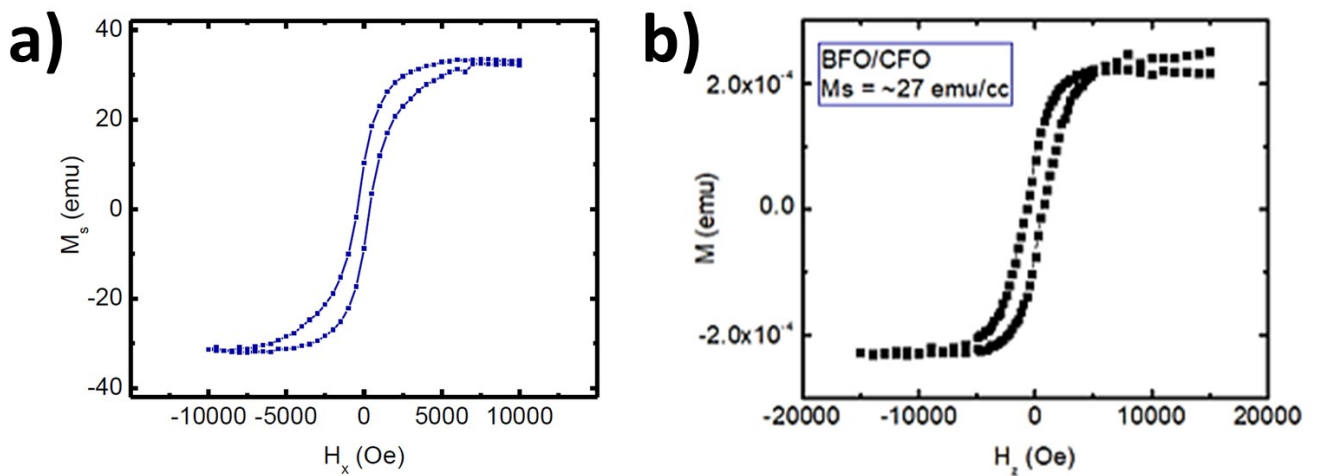
Figure 8. Magnetization hysteresis loop obtained by VSM of the a) In-plane (1:0.66:0.17) solid solution sample and b) Out-of-plane (1:0.53:0.134) nanocomposite sample.

5.3.   Conclusion

Deposition protocols of $BiFeO_3$-$CoFe_2O_4$ 1-3 type nanocomposite in a single step MOCVD process have been successfully investigated. Both reported approaches allowed the deposition of VAN of CFO in a BFO matrix. Moreover, $BiFe_xCo_{(1-x)}O_3$ solid solution has also been obtained, allowing us to understand more on the deposition mechanism.

The first approach shows that precursor vaporization plays a crucial role in tuning the CFO dimension and distribution density. However, the use of a large quantity of precursors really impacted film quality and a better balance in vaporized mixture stoichiometry is mandatory to improve film quality.

The second approach can be considered softer because it implies a reduced quantity of precursors and a lower vaporization temperature to deposit the nanocomposite. Co precursor relative concentration to BFO mixture is one of the key parameters to regulate the different phase formation. Precise control of the precursors' ratio helped in the selective growth of solid solution or nanocomposite, demonstrating its critical impact on developing high-quality films. Clear ferroelectric and piezoelectric behaviors of the solid solution have been observed. Magnetization properties of both solid solution and nanocomposite have been measured.

Further functional characterizations are ongoing in the Ramesh Lab (Prof. R. Ramesh, UC Berkley): ferroelectric, piezoelectric, magnetic, and so ME coupling are yet to be investigated. For Co-BFO solid solutions, an in-depth study of the Co concentration impact on the material properties needs to be carried out. Then, for BFO-CFO systems, properties depend on both the morphologies and the ratio of the BFO and CFO phases, further development in the deposition process is of special interest to finely tune the integration of CFO nanostructures.

References

[1] G. Catalan, J.F. Scott, Physics and Applications of Bismuth Ferrite. Adv. Mater. (2009) 21, 2463–2485.

[2] W. Eerenstein, N. D. Mathur & J. F. Scott, Multiferroic and magnetoelectric materials, Nature 442 (2006) 759–765.

[3] H. Zheng, J. Wang, S. E. Lofland, Z. Ma, L. Mohaddes-Ardabili, T. Zhao, L. Salamanca-Riba, S. R. Shinde, S. B. Ogale, F. Bai, D. Viehland, Y. Jia, D. G. Schlom, M. Wuttig, A. Roytburd, and R. Ramesh, Science 303 (2004) 661.

[4] F. Zavaliche, H. Zheng, L. Mohaddes-Ardabili, S. Y. Yang, Q. Zhan, P. Shafer, E. Reilly, R. Chopdekar, Y. Jia, P. Wright, D. G. Schlom, Y. Suzuki, R. Ramesh, Electric Field-Induced Magnetization

Switching in Ep, J. Mater. Res. 22 (2007) 8 2087 - 2095

[5] M. Rafique, A. Herklotz, K. Dörr, S. Manzoor, Giant room temperature magnetoelectric response in strain controlled nanocomposites, Appl. Phys. Lett. 110 (2017) 202902

[6] H. Zheng, F. Straub, Q. Zhan, P.-L. Yang, W.-K. Hsieh, F. Zavaliche, Y.-H. Chu, U. Dahmen, R. Ramesh (2006). Self-Assembled Growth of BiFeO3–CoFe2O4 Nanostructures, Adv. Mater. 18 (2006) 2747–2752

[7] V.A. Reddy, N.P. Pathak, R. Nath, Enhanced magnetoelectric coupling in transitionmetal-doped BiFeO3 thin films, Solid State Commun. 171 (2013) 40–45.

[8] R. Ramesh, N.A. Spaldin, Multiferroics: progress and prospects in thin films, Nature 6 (2007)

[9] Y.Q. Liu, B. Zhang, Y.H. Wu, J. Zhang, D. Li, Y. Liu, M.B. Wei, J.H. Yang, Synthesis, structure, and magnetic studies on the CoFe2O4–BiFeO3 nanocomposite films with different number of CoFe2O4 layers, Superlattices and Microstructures 61 (2013) 174–180

[10] G. Singh, M. K. Singh, A. Kumar, S. Dussan, R.S. Katiyar, Multiferroics Properties in BiFeO3/ CoFe2O4 Heterostructures Thin films Deposited on (111) SrTiO3, AIP Conf. Proc. 1731 (2016) 080043.

[11] T.C. Kim, S. Ojh, G. Tian, S.H. Lee, H.K. Jung, J.W. Choi, L. Kornblum, F.J. Walker, C.H. Ahn, C. A. Ross, D.H. Kim, Self-assembled multiferroic epitaxial BiFeO3–CoFe2O4 nanocomposite thin films grown by RF magnetron sputtering, J. Mater. Chem. C 6 (2018) 5552-5561

[12] X.M. Liu, S.Y. Fu, C.J. Huang, Synthesis and magnetic characterization of novel CoFe2O4–BiFeO3 nanocomposites, Materials Science and Engineering: B 121 (2005) 3.

[13] A. Khalid, M. Saleem, S. Naseem, S.M. Ramay, H. M. Shaikh, S. Atiq, Magneto-electric coupling and multifunctionality in BiFeO3–CoFe2O4 coreshell nano-composites, Ceram. Int. 46 (2020) 8.

[14] F. An, G. Zhong, Q. Zhu, Y. Huang, Y. Yang, S. Xie, Synthesis and mechanical properties characterization of multiferroic BiFeO3-CoFe2O4 composite nanofibers, Ceram. Int. 44 (2018) 11617–11621.

[15] M. Gao, R. Viswan, X. Tang, C. M. Leung, J. Li, D. Viehland, Magnetoelectricity of CoFe2O4 and tetragonal phase BiFeO3 nanocomposites prepared by pulsed laser deposition 8 (2018) 323

[16] D.H. Kim, S. Ning, C.A. Ross, Self-assembled multiferroic perovskite–spinel nanocomposite thin films: epitaxial growth, templating and integration on silicon, J. Mater. Chem. C 7 (2019) 9128-9148

[17] N. Dix, R. Muralidharan, J. Guyonnet, B. Warot-Fonrose, M. Varela, P. Paruch, F. Sánchez, J. Fontcuberta, On the strain coupling across vertical interfaces of switchable BiFeO3–CoFe2O4 multiferroic nanostructures, Appl. Phys. Lett. 95 (2009) 062907.

[18] L. H. Ahrens, The use of ionization potentials Part 1. Ionic radii of the elements, Geochim. Cosmochim. Acta 2 (1952) 155-169.

[19] H. Naganuma, S. Yasui, K. Nishida, T. Iijima, H. Funakubo, S. Okamura, Enhancement of magnetization at morphotropic phase boundary in epitaxial BiCoO3-BiFeO3 solid solution films grown on SrTiO3 (100) substrates, J. Appl. Phys 109 (2011) 07D917

[20] S. Yasui, K. Nishida, H. Naganuma, S. Okamura, T. IIJIMA, H. Funakubo, Crystal Structure Analysis of Epitaxial BiFeO3–BiCoO3 Solid Solution Films Grown by Metalorganic Chemical Vapor Deposition, Jpn. J. Appl. Phys. 46 (2007) 10 6948–6951

[21] M. Azuma, S. Niitaka, N. Hayashi, K. Oka, M. Takano, H. Funakubo, Y. Shimakawa, Rhombohedral-Tetragonal Phase Boundary with High Curie Temperature in (1 -x)BiCoO3–xBiFeO3 Solid Solution, Jpn. J. Appl. Phys. 47 (2008) 9 7579–7581

Conclusion

Within the MSCA-ITN ENHANCE project the present work have been focused on the optimisation of the Metal-organic chemical vapor deposition process of lead-free prevoskite thin films of multiferroic $BiFeO_3$ systems for hybrid energy harvesting. Materials ferroelectric, piezoelectric, pyroelectric and photovoltaic properties have been investigated on Si-based and $SrTiO_3$:Nb single crystal substrates. $BiFeO_3$ doping has been extensively investigated and the relationship between dopants and functional/structural properties have been exposed.

In the Chapter 2, we first focused on the deposition of $BiFeO_3$ by MOCVD on silicon substrate, with IrO_2 acting as a stable, at high-temperature, buffer layerand bottom electrode for the film functional characterization. The morphology, density, thickness, and Bi:Fe ratio in the films are homogenous on the whole sample surface of 10 mm × 10 mm. The BFO thin films show different growth orientations, but no specific relationship has been found between orientation and experimental conditions. Various experiments indicate that the optimal deposition temperature range is between 650 °C and 750 °C with a fixed argon flow of 150 mL/min and the use of high oxygen flow, 900 mL/min for 10 min., in order to induce the formation of numerous BFO nucleation sites, and 150 mL/min for 50 min. to trigger the growth of a denser film with smaller grains when compared to the other investigated conditions. Thus, the BFO films can be successfully deposited on Si at a lower temperature and in a more cost-effective process, with respect to the previously reported methodologies. Moreover, the present approach offers the major advantage of being easily scalable and the use of IrO_2, as a conductive oxide, gives the opportunity for future characterizations and device microfabrication. Finally, it can be pointed out that the material quality and production cost of lead-free perovskites, as BFO, are key points for the scaling-up development of a new generation of hybrid energy harvesting devices. The reported MOCVD approach answers to both demands and is compatible with the current technologies.

Then, to optimize the growth of $BiFeO_3$ on Si (001) and $SrTiO_3$ (100) substrates, a study devoted to the deposition of a $LaNiO_3$ buffer layer by MOCVD has been realized. The versatility of the MOCVD approach has facilitated the work on multiple precursor systems to define the most promising precursor mixture between: La(hfa)$_3$·diglyme and Ni(acac)$_2$, vaporized at 120 °C; La(hfa)$_3$ ·diglyme and Ni(hfa)$_2$·diglyme, vaporized at 115 °C; La(hfa)$_3$·diglyme and Ni(tta)$_2$·TMEDA, vaporized at 130 °C. Substrates were heated up to 750 °C and maintained on a 20° susceptor to optimize gas flow on the substrate. The carrier (argon) and reactant (oxygen) gas flows were maintained at 150 mL/min. The most promising results have been obtained with the precursor mixture of La(hfa)$_3$·diglyme and Ni(acac)$_2$, which help to stabilize the La_2NiO_4 phase. Other precursor mixture, despite their good thermal behavior, produced films with high LaOF contamination. Multiple points for the MOCVD protocol optimizations have been proposed and are still under study.

Exchange periods in Prof. Paul Muralt's Lab at EPFL and Prof. Ausrine Bartasyte's Lab at UFC/Femto-ST allowed us to look at the major steps of $BiFeO_3$(poly)/IrO_2/Si cantilevers microfabrication. Critical points regard the preparation of the vibrational harvester's fabrication and the films' growth quality. Future improvements of the process are needed to reach a functional BFO vibrational energy harvester. Film general quality is crucial and can always be pushed forward. We observed a preferential $[001]_{pc}$ growth orientation of BFO on IrO_2, and it opens a promising route for the development of highly textured BFO film on Si-based substrates by MOCVD. Finally, the main failure cause has been attributed to significant leakage current in the samples; working with doped-$BiFeO_3$ films and post-process treatment would be one of the ways to reduce them.

In Chapter 3, we focused our investigation on the A-site doping of the $BiFeO_3$ with elements from the lanthanides' series. This approach has been selected because of the simplicity with which it can be adapted and included in an MOCVD single-step methodology, with respect to other strain-controlled properties or post-process treatments to fine-tune material properties.

The first doping element of interest has been the dysprosium, with as main interest the study of $Bi_{1-x}Dy_xFeO_3$ (x = 0, 0.06, 0.08 and 0.11) thin films deposited on STO:Nb (100) through an industrially appealing MOCVD route. Our goal was to determine if dense films of undoped and Dy-doped $BiFeO_3$ may be integrated as a lead-free pyroelectric energy harvester. Thus, the ferroelectric, dielectric, and pyroelectric properties of pure $BiFeO_3$ and solid solution of Dy-doped $BiFeO_3$ thin films have been investigated. An extraordinary high pyroelectric coefficient of 188 µC/(m² K) has been found for the undoped BFO film, an indication of the possible self-poling and the high quality, of the epitaxial films grown by MOCVD. Dy^{3+} substitution has been shown to lead to a large increase of pyroelectric properties with respect to the undoped system. A giant value of the pyroelectric coefficient of 426 µC/(m² K) has been achieved for the 8% Dy^{3+} doping. Above this concentration, pyroelectric properties start to degrade. The presently found pyroelectric coefficients are significantly higher than those reported in the literature and the figure of merit values for energy harvesting are impressively promising. In fact, the obtained F_E value of 82 J/(m³ K²) for the BDFO-8% sample is a striking improvement with respect to the previously highest reported value of F_E = 17 J/(m³ K²) for a $Bi_{1-x}Sm_xFeO_3$ ceramic sample. Additionally, Dy-doping influence on material bandgap and piezoelectric response has been checked. In-depth structural characterisations by XRD and Raman spectroscopy were done to assess film quality and report structural changes caused by the Dy-doping. The very appealing and excellent properties reported in this part indicate that the presently reported, straightforward MOCVD synthetic route produces high-quality epitaxial BFO and BDFO thin films, which may be envisaged as lead-free materials of choice for pyroelectric energy harvesting.

The second and third doping elements investigated for the tuning of $BiFeO_3$ properties have been neodymium and ytterbium. Pure $BiFeO_3$ and solid solutions of $Bi_{1-x}Nd_xFeO_3$ (x = 0.07, 0.09, 0.145 and 0.245) and, $Bi_{1-x}Yb_xFeO_3$ (x = 0.09, 0.12, 0.14 and 0.30) have been prepared by

MOCVD on 1 cm x 1cm STO:Nb (100) conductive substrate. Prepared samples have been sent to Dr. David Munoz-Rojas and Abderrahime Sekkat at Laboratoire des Matériaux et du Génie Physique (LMGP) to investigate the photovoltaic properties of the deposited materials. Moreover, the impact of doping on film morphologies, structure, and bandgap have been carried out. Preliminary results show the moderate influence of Nd-doping on $BiFeO_3$ properties even though it helps reducing leakage current. According to the bandgap measurements made, Yb-doping seems to have a more defined impact on the film photovoltaic response.

The fourth and last of the lanthanides used to substitute Bi^{3+} ions in the $BiFeO_3$ perovskite structure was samarium. Interest in this doping was brought to us by Prof. R. Ramesh, University of California Berkeley. An MOCVD approach, similar to those previously described, has been used to prepare thinner 100-150 nm films of pure $BiFeO_3$ and $Bi_{1-x}Sm_xFeO_3$ (x = 0.09, 0.12, 0.14 and 0.30) solid solutions. Classic morphological and structural characterization has been reported. Ferroelectric and piezoelectric characterizations are still ongoing.

In Chapter 4, the MOCVD approach proved to be a powerful and flexible tool for the fabrication of Ba and Ti co-doped $BiFeO_3$ films. Accurate control of processing parameters, in particular the multicomponent source mixture ratio, resulted selectively and reproducibly in the formation of two different systems: a single-phase solid solution $Bi_{0.8}Ba_{0.2}Fe_{0.5}Ti_{0.5}O_3$ and a nanocomposite sample with an average composition of $Bi_{0.6}Ba_{0.4}Fe_{0.6}Ti_{0.4}O_3$, formed by $Bi_{(1-x)}Ba_xFeO_3$ nanocolumns embedded in a $Bi_{(1-x)}Ba_xFe_{(1-y)}Ti_yO_3$ phase. To our knowledge, this study represents the first report on MOCVD of Ba and Ti co-doped $BiFeO_3$ films, and the presently addressed comprehensive structural and compositional characterizations add a notable tile in the overall mosaic of the $BiFeO_3$-$BaTiO_3$ systems.

In Chapter 5, we presented the development of two single-step MOCVD deposition protocols of $BiFeO_3$-$CoFe_2O_4$ nanocomposite and $BiFe_{1-x}Co_xO_3$ solid solutions. Both approaches allowed the deposition of VAN of CFO in a BFO matrix and Co-doped BFO films. A careful investigation allowed us to identify key mechanisms in the selection of the growth phases. We saw that the large quantity of precursors impacted film quality and that precursor vaporization plays a crucial role in tuning the CFO distribution across the film. Precise control of mixture stoichiometry and more specifically Co precursors relative concentration to Bi and Fe helped in the selective growth of solid solution or high-quality nanocomposite films. Clear ferroelectric and piezoelectric behaviors of the solid solution have been observed, and magnetization properties of both solid solution and nanocomposite have been assessed. Further functional characterizations are ongoing at Ramesh Lab (UC Berkeley) with indepth studies of ferroelectric properties, piezoelectric and, magnetic properties, and ME coupling.

Appendix 1

Summary Table of photovoltaic properties of BiFeO$_3$ systems

Materials & Heterostructures	Orientation	Open circuit voltagec Voc (V)	Short circuit current Isc (pA)	Short circuit current density Jsc (mA/cm2)	Irradiation λ (nm)/intensity (mW/cm2)	PCE (%)	EQE (%)	Comments	Reference
Single crystals									
BaTiO$_3$ (AFM tip electrode)	1		22.8	36.3	405 / 100		1.11	BPVE	[1]
BaTiO$_3$ (AFM tip electrode)	1		47.6	75.8	405 / 160		1.45	BPVE	[1]
BaTiO$_3$ (AFM tip electrode)	1		69.8	111,1	405 / 275		1.24	BPVE	[1]
BaTiO$_3$ (AFM tip electrode)	1		178.7	284.4	405 / 470		1.85	BPVE	[1]
BaTiO$_3$ (AFM tip electrode)	1		12	19.1	AM1.5 G / 100	4.8		BPVE	[1]
ITO/PMN-PT doped with 0.5 mol % WO3 /ITO		~0.2			406 /260				[2]
Au/BFO/Au			0.0075		532 /				[3]
Pt/BFO /Pt	110	13		0.001	405		3x10^{-5}		[4]
Ceramics									
BaTiO$_3$ + 5wt.% CaTiO$_3$ (Au electrode)		~70		~10^{-7}	Mercury arc lamp/10				[5]
KNbO$_3$-Ba(Ni$_{1/2}$Nb$_{1/2}$)O$_3$ ceramic (ITO electrode)		~7x10^{-4}		~10^{-4}	halogen lamp/4				[6]
ITO/BFO /Au		0.58		0.005	405 /10	0.005	0.16	(p-n junction)	[7]
ITO/(Bi$_{1-x}$Sm$_x$)FeO$_3$ /Au		0.7		0.094	405 /10	0.25	3	(p-n junction)	[7]
ITO/BFO3Nd /Au (d= 0.15 mm)		0.77		0.045	405 /~10	0.08	1.4	(p-n junction)	[8]
ITO/BFO5Nd /Au (d= 0.15 mm)		0.72		0.127	405 /~10	0.24	4	(p-n junction)	[8]
ITO/BFO7Nd /Au (d= 0.15 mm)		0.73		0.139	405 /~10	0.32	4.4	(p-n junction)	[8]
ITO/BFO10Nd /Au (d= 0.15 mm)		0.71		0.067	405 /~10	0.09	2.1	(p-n junction)	[8]
Au/BFO/Au				0.0075	532 / <20				[3]
ITO/BFO3Nd/Au (d = 0.10mm)		0.87		0.098	405 / 91	0.25 mac (I=2.4mW/cm^2)	0.33		[8]
ITO/BFO3Nd/Au (d = 0.15mm)		0.86		0.076	405 / 91	0.23 (I=2.4mW/cm^2)	0.26		[8]
ITO/BFO3Nd/Au (d = 0.20mm)		0.89		0.067	405 / 91	0.23 (I=2.4mW/cm^2)	0.23		[8]
ITO/BFO5Nd/Au (d = 0.10mm)		0.78		0.388	405 / 91	0.82 (I=2.4mW/cm^2)	1.31		[8]
ITO/BFO5Nd/Au (d = 0.15mm)		0.8		0.317	405 / 91	0.7 (I=2.4mW/cm^2)	1.07		[8]
ITO/BFO5Nd/Au (d = 0.20mm)		0.76		0.296	405 / 91	0.28 (I=2.4mW/cm^2)	1		[8]

ITO/BFO7Nd/Au (d = 0.10mm)		0.9	0.344	405 / 91	0.76 (I=2.4mW/cm²)	1.16	[8]
ITO/BFO7Nd/Au (d = 0.15mm)		0.82	0.35	405 / 91	0.75	1.18	[8]
ITO/BFO7Nd/Au (d = 0.20mm)		0.87	0.186	405 / 91	0.59	0.63	[8]
Pt/(Bi$_{0.85}$;Pr$_{0.15}$)FO/ITO							[9]
Thin films							
Pt/PZT(52/48)/Ni		0.8	6×10^{-5}	300-390 /1			[10]
Pt/PZT(20/80)/Pt	Poly.		0.008	350-450/10			[11]
ITO/PZT(53/47)/ITO	Poly.	0.25	5×10^{-6}	632 / 0.45	0.22		[12]
LSMO/PLZT(3/52/48)/Nb:STO	-100	0.71	$\sim 2 \times 10^{-3}$	365 / 0.0|587	~0.05		[13]
LSMO/PLZT(3/52/48)/Nb:STO	-100	0.71	$\sim 1 \times 10^{-3}$	365 / 0.8563	~0.28		[13]
ITO/BFO/SrRuO$_3$/ SrTiO$_3$	-1	0.3	4×10^{-4}	435 / 0.75			[14]
Pt/BFO/Pt		20	0.05	375 /100			[15]
ITO/Bi$_2$FeCrO$_6$/Nb:STO		~0.6	~0.11/0.99	635 / 1.5		~0.8 /6	[16]
ITO/PZT/Cu$_2$O/Pt		0.4	4.5	AM1.5G / 100	0.57		[17]
glass/ZnO:Al/BiFeO$_3$/La$_{0.67}$Sr$_{0.33}$CoO$_3$		0.22	4	white light / 1% of normal sun light			[18]
Pt/BFO/SrRuO3	Poly.	0.08	0.063	white light / 100			[19]
0.9(BiFeO$_3$)–0.1(YCrO$_3$)/Pt/TiO$_2$/SiO$_2$/Si (bottom-up electrode)	Poly.	0.51	0.00148	white light / 100			[20]
0.9(BiFeO$_3$)–0.1(YCrO$_3$)/Pt/TiO$_2$/SiO$_2$/Si (lateral electrode)	Poly.	0.32	0.44×10^{-3}	white light / 100			[20]
Pt/BFO/STO	111	3.9	0.262×10^{-3}	100			[21]
Pt/BFO/STO (poled)	111	17.8	0.3×10^{-3}	Sun light simulator / 100			[21]
Nb:STO/BFO/Au	1	0.04	6	white light / 285	0,03		[22]
AZO = Al-doped Zn/ BiFeO$_3$/F- doped SnO$_2$ = FTO	Poly.	0,63	0,13	AM1.5G / 100	2.0810^{-2}	7 max (λ= 488nm)	[23]
Fe/BFO/LSMO/STO	1	0,21	6×10^{-4}	"light" / 20			[24]
Graphene/BFO/Pt/Ti/SiO$_2$/Si	Poly.	0.44	0.025	AM1.5G / 100			[25]
Graphene/BFO/Pt/Ti/SiO$_2$/Si (After HNO3 treatment)	Poly.	0.2	2.8	AM1.5G / 100			[25]
ITO/BFO/Pt	Poly.	0.1	0.0025	X / 0.45	0.125		[26]
Pt/BFO/Pt	1	16	0.12	white-light / 285			[27]
ITO/BFO/SRO	1	0.8	1.5	AM1.5G / 285		10 (λ = 325 nm)	[28]
Pt/BSFCO/Pt	Poly.	0.9	5×10^{-5}	white light / 100			[29]
Au /Na$_{0.5}$Bi$_{0.5}$FeO$_3$/TiO$_2$/ITO glass	Poly.	0.394	4.63×10^{-3}	AM1.5G / 100	0.0006 (maximum of 0.0075		[30]

Device							Ref.
Au /BFO /(111)Pt/TiO₂/SiO₂/Si(100) (Anneal under air and poled)	Poly.	0.45	FIG. 5.	250 to 2500 /166			[31]
Au /BFO /(111)Pt/TiO₂/SiO₂/Si(100) (Anneal under O₂ and poled)	Poly.	0.14	FIG. 5.	250 to 2500 /166			[31]
Au /BFO /(111)Pt/TiO₂/SiO₂/Si(100) (Anneal under N₂ and poled)	Poly.	0.13	FIG. 5.	250 to 2500 /166			[31]
Au /BFO /(111)Pt/TiO₂/SiO₂/Si(100) (Anneal under air and poled)	Poly.	-0.47	FIG. 5.	250 to 2500 /166			[31]
Au /BFO /(111)Pt/TiO₂/SiO₂/Si(100) (Anneal under O₂ and poled)	Poly.	-0.2	FIG. 5.	250 to 2500 /166			[31]
Au /BFO /(111)Pt/TiO₂/SiO₂/Si(100) (Anneal under N₂ and poled)	Poly.	-0.14	FIG. 5.	250 to 2500 /166			[31]
CuSCN and senstise with N719 / BFO/ZnO/FTO	Poly.	0.51	1.4	AM1.5G / 100	0.38		[32]
CNT/BFO/Pt	Poly.	0.47	$2.10E^{-3}$	AM1.5G / 100	$2.2x\ 10^{-4}$		[33]
Pt/BFO/STO	001			405 nm laser		BPVE	[34]
BFO/Pt/TiOx/SiO₂/Si	Poly.	0.24	$2.00E^{-4}$	450 / 1.0	Power density 25nW/cm2	(p-n junction)	[35]
Al-doped ZnO BFO bilayer/Pt/TiOx/SiO₂/Si	Poly.	0.45	0.15	450 / 1.0	Power density 20μW/cm2	(p-n junction)	[35]
Pt/TiO₂/BFO/ITO	Poly.		-0.46	Xe-lamp /100			[36]
Au/BFO/FTO (Anealing 450°C)	Poly.	0.09	0.96	365 / 250			[37]
Au/BFO/FTO (Anealing 500°C)	Poly.	0.7	1.11	365 / 250			[37]
Au/BFO/FTO (Anealing 550°C)	Poly.	0.15	4.58	365 / 250			[37]
Au/BFO/ITO	-1	0.2	0.06	375 / 630			[38]
Ag/BFO/FTO	Poly.	0.25	0.02	Xe lamp / 100	0,00075		[39]
Ag/BFO (Nd-Cr co-doped) / FTO	Poly.	0.8	0.16	Xe lamp / 100	0.0262		[39]
Ag/BFO/FTO	Poly.	-0.16	0.0204	405 / 200			[40]
Ag/(Bi;Ca)CFO/FTO	Poly.	-0.36	0.646	405 / 200			[40]
Ag/(Bi;Ca)CFO/FTO	Poly.	0.11	0.116	405 / 200			[40]
Au/(Bi;Nd)FO/ITO	Poly.	~0.7	0.5	405 /	0.82		[41]
Au/BFO/ITO	Poly.	~0.7	0.014	405 /			[41]
ITO/AuNPs/BFO/FTO	Poly.	0.2	0.0053				[42]

ITO/AuNPs/Bi0.85La0.15FeO3/FTO	Poly.	0.3	0.0185		[42]
Au/RGO/BFO/TiO₂/Pt/TiO₂/SiO₂/Si	Poly.	0.814	5.17	AM1.5G / 100	3.11	[43]
Nanomaterials					
Ag/ (Pr-Cr) BFO NTs/Ag	Poly.	~0.20	405 / 91		[44]
Ag/ (Pr) BFO NTs/Ag	Poly.	~0.22	AM1.5G / 10	0.5 max	[44]
Ag/ (Cr) BFO NTs/Ag	Poly.	~0.12	AM1.5G / 10	0.106 max	[44]
Ag/ BFO NTs/Ag	Poly.	~0.15	AM1.5G / 10	0.207 max	[44]

References

[1] J.E. Spanier, V.M. Fridkin, A.M. Rappe, A.R. Akbashev, A. Polemi, Y. Qi, Z. Gu, S. M. Young, C.J. Hawley, D. Imbrenda, G. Xiao, A.L. Bennett-Jackson, C.L. Johnson, Power conversion efficiency exceeding the Shockley–Queisser limit in a ferroelectric insulator, Nature Photonics 10 (2016).

[2] C.S. Tu, F.T. Wang, R.R. Chien, V.H. Schmidt, C.M. Hung, C.T. Tseng, Dielectric and photovoltaic phenomena in tungsten-doped Pb (Mg 1∕3 Nb 2∕3) 1 − x Ti x O 3 crystal, Applied Physics Letters 88 (2006) 032902.

[3] T. Choi, S. Lee, Y. J. Choi, V. Kiryukhin, S.W. Cheong, Switchable Ferroelectric Diode and Photovoltaic Effect in BiFeO3, Science 324 (2009).

[4] M. Alexe, D. Hesse, Tip-enhanced photovoltaic effects in bismuth ferrite, Nature communication (2011) 2:256.

[5] P. S. Brody, Large Polarization dependent photovoltage in ceramic BaTiO3 +5wt.% CaTiO3, Solid State Communications 12 (1973) 673—676.

[6] I. Grinberg, D.V. West, M. Torres, G. Gou, D.M. Stein, L. Wu, G. Chen, E.M. Gallo, A.R. Akbashev, P.K. Davies, J.E. Spanier, A.M. Rappe, Perovskite oxides for visible-light-absorbing ferroelectric and photovoltaic materials, Nature letter research (2013)

[7] C.S. Tu, C.S. Chen, P.Y. Chen, H.H. Wei, V.H. Schmidt, C.Y. Lin, J. Anthoniappen, J.M. Leef, Enhanced photovoltaic effects in A-site samarium doped BiFeO3ceramics: The roles of domain structure and electronic state, J. Eur. Ceram. Soc. (2015).

[8] C.S. Tu, P.Y. Chen, C.S. Chen, R.R. Chien, V. H. Schmidt, C.Y. Lin, Photovoltaic conversion and quantum efficiency in perovskite multiferroic ceramics, Acta Materialia 149 (2018) 248-255.

[9] Arti, S. Kumar, P. Kumar, R. Waliac, V. Vermaa, Improved ferroelectric, magnetic and photovoltaic properties of Pr-doped multiferroic bismuth ferrites for photovoltaic application, Results in Physics 14 (2019) 102403

[10] V.K. Yarmarkin, B.M. Gol'tsman, M.M. Kazanin, V. V. Lemanov, Barrier Photovoltaic Effects in PZT Ferroelectric Thin Films, Physics of the Solid State 42 (2000) 3 522-527.

[11] F. Zheng, J. Xu, L. Fang, M. Shen, X. Wu, Separation of the Schottky barrier and polarization effects on the photocurrent of Pt sandwiched Pb (Zr 0.20 Ti 0.80) O 3 films, Applied Physics Letters 93 (2008) 172101.

[12] B. Chen, Z. Zuo, Y. Liu, Q.F. Zhan, Y. Xie, H. Yang, G. Dai, Z. Li, G. Xu, R.W Li, Tunable photovoltaic effects in transparent Pb(Zr0.53,Ti0.47)O3 capacitors, Applied Physics Letters 100 (2012) 173903.

[13] M. Qin, K. Yao, Y.C. Liang, High efficient photovoltaics in nanoscaled ferroelectric thin films, High efficient photovoltaics in nanoscaled ferroelectric thin films, Appl. Phys. Lett. (932008) 122904.

[14] W. Ji, K. Yao, Y.C. Liang, Bulk Photovoltaic Effect at Visible Wavelength in Epitaxial Ferroelectric BiFeO3 Thin Films, Adv. Mater. 22 (2010) 1763–1766.

[15] J. Seidel, D. Fu, S.Y. Yang, E.A. Llado, J. Wu, R. Ramesh, J.W. Ager, Efficient Photovoltaic Current Generation at Ferroelectric Domain Walls, PRL 107 (2011) 126805.

[16] R. Nechache, C. Harnagea, S. Licoccia, E. Traversa, A. Ruediger, A. Pignolet, F. Rosei, Photovoltaic properties of Bi2FeCrO 6 epitaxial thin films, Applied Physics Letters 98 (2011) 202902

[17] D. Cao, C. Wang, F. Zheng, W. Dong, L. Fang, M. Shen, High-Efficiency Ferroelectric-Film Solar Cells with an n-type Cu2O Cathode Buffer Layer, Nano Lett. 12 (2012) 2803–2809.

[18] R.K. Katiyar, A. Kumar, G. Morell, J.F. Scott, R.S. Katiyar, Photovoltaic effect in a wide-area semiconductor-ferroelectric device, Applied Physics Letters 99 (2011) 092906.

[19] R.K. Katiyar, P. Misra, S. Sahoo, G. Morell, R.S. Katiyar, Enhanced photoresponse in BiFeO3/SrRuO3 heterostructure, Journal of Alloys and Compounds 609 (2014) 168–172.

[20] Y. Sharma, P. Misra, R.K. Katiyar, R.S. Katiyar, Photovoltaic effect and enhanced magnetization in 0.9(BiFeO3)–0.1(YCrO3) composite thin film fabricated using sequential pulsed laser deposition, J. Phys. D: Appl. Phys. 47 (2014) 425303.

[21] R.K. Katiyar, P. Misra, G. Morell, R.S. Katiyar, Effect of Poling on Photovoltaic Properties in Highly Oriented BiFeO3 Thin Films, Integrated Ferroelectrics, 157 (2014) 168–173.

[22] T. L. Qu, Y.G. Zhao, D. Xie2 J P. Shi1 Q P. Chen, T.L. Ren, Resistance switching and white-light photovoltaic effects in BiFeO3 /Nb–SrTiO3 heterojunctions, Appl. Phys. Lett. 98 (2011) 173507.

[23] W. Dong, Y. Guo, B. Guo, H. Liu, H. Li, H. Liu, PhotovoltaicpropertiesofBiFeO3 thin film capacitors by using Al-doped zinc oxide as top electrode, Materials Letters 91 (2013) 359–361.

[24] R. Guo, L. You, Y. Zhou, Z.S. Lim, X. Zou, L. Chen, R. Ramesh, J. Wang, Non-volatile memory based on the ferroelectric photovoltaic effect, Nature communication 4 (2013) 1990.

[25] Y. Zang, D. Xie, X. Wu, Y. Chen, Y. Lin, M. Li, H. Tian, X. Li, Z. Li, H. Zhu, T. Ren, D. Plant, Enhanced photovoltaic properties in graphene/polycrystalline BiFeO3/Pt heterojunction structure, Applied Physics Letters 99 (2011) 132904.

[26] B. Chen, M. Li, Y. Liu, Z. Zuo, F. Zhuge, Q.F. Zhan, R.W. Li, Effect of top electrodes on photovoltaic properties of polycrystalline BiFeO3 based thin film capacitors, Nanotechnology 22 (2011) 195201.

[27] S.Y. Yang, J. Seidel, S.J. Byrnes, P. Shafer, C.H. Yang, M.D. Rossell, P. Yu, Y.-H. Chu, J. F. Scott, J.W. Ager, L. W. Martin, R. Ramesh, Above-bandgap voltages from ferroelectric photovoltaic devices, Nature Technology 5 (2010)

[28] S. Y. Yang, L. W. Martin, S. J. Byrnes, T. E. Conry, S. R. Basu, D. Paran, L. Reichertz, J. Ihlefeld, C. Adamo, A. Melville, Y.-H. Chu, C.-H. Yang, J. L. Musfeldt, D. G. Schlom, J.W. Ager III, R. Ramesh, Photovoltaic effects in BiFeO3, Applied Physics Letters 95 (2009) 062909.

[29] V.S. Puli, D.K. Pradhan, R.K. Katiyar, I. Coondoo, N. Panwar, P. Misra, D.B. Chrisey, J.F. Scott, R.S. Katiyar, Photovoltaic effect in transition metal modified polycrystalline BiFeO3 thin films J. Phys. D: Appl. Phys. 47 (2014) 075502.

[30] X. Wu, Z. Wan, J. Qi, M. Wang, Ferroelectric photovoltaic properties of perovskite Na0.5Bi0.5FeO3-based solution processed solar cells, Journal of Alloys and Compounds (2018)

[31] P. P. Biswas, Ch. Thirmal, S. Pal, P. Murugavel, Dipole pinning effect on photovoltaic characteristics of ferroelectric BiFeO3 films, Journal of Applied Physics 123 (2018) 024101.

[32] L. Loh, J. Briscoe, S. Dunn, Bismuth ferrite enhanced ZnO solid state dye-sensitised solar cell, Procedia Engineering 139 (2016) 15–21.

[33] Y. Zang, D. Xie, Y. Chen, X. Wu, T. Ren, J. Wei, H. Zhu, D. Plant, Electrical and thermal properties of a carbon nanotube/polycrystalline BiFeO3/Pt photovoltaic heterojunction with CdSe quantum dots sensitization, Nanoscale 4 (2012) 2926.

[34] M.M. Yang, Z.D. Luo, D.J. Kim, M. Alexe, Bulk photovoltaic effect in monodomain BiFeO3 thin films, Applied Physics Letters 110 (2017) 183902.

[35] T. Katayama, W. Sakamoto, I. Yuitoo, T. Takeuchi, K. Hayashi, T. Yogo, Enhancement of photoinduced electrical properties of Al-doped ZnO/BiFeO3 layered thin films prepared by chemical solution deposition, Japanese Journal of Applied Physics 54 (2015) 10NA05.

[36] H. Shen, X. Zhou, W. Dong, X. Su, L. Fang, X. Wu, M. Shen, Dual role of TiO2 buffer layer in Pt catalyzed BiFeO3 photocathodes: Efficiency enhancement and surface protection, Appl. Phys. Lett. 111 (2017) 123901.

[37] J.Wang, L. Luo, C. Han, R. Yun, X. Tang, Y. Zhu, Z. Nie, W. Zhao, Z. Feng, The Microstructure, Electric, Optical and Photovoltaic Properties of BiFeO3 Thin Films Prepared by Low Temperature Sol–Gel Method, Materials 12 (2019) 1444.

[38] Y. Zhou, C. Wang, S. Tiana, X. Yao, C. Gea, E.J. Guo, M. Hea, G. Yang, K. Jina, Switchable ferroelectric diode and photovoltaic effects in polycrystalline BiFeO3 thin films grown on transparent substrates, Thin Solid Films 698 (2020) 137851.

[39] J. Zhang, P. Ma, T. Shi, X. Shao, Nd-Cr co-doped BiFeO3 thin films for photovoltaic devices with enhanced photovoltaic performance, Thin Solid Films 698 (2020) 137852.

[40] Y. Zhang, H. Zheng, X. Wang, H. Li, Y. Wu, Y. Zhang, H. Su, G. Yuan, Enhanced photovoltaic properties of gradient calcium-doped BiFeO3 films, Ceramics International 46 (2020) 10083–10088.

[41] Y.T. Peng, S.H. Chiou, C.H. Hsiao, C. Ouyang, C.S. Tu, Remarkably enhanced photovoltaic

effects and first-principles calculations in neodymium doped BiFeO3, Scientific Reports 7 (2017) 45164 .

[42] F. Li, H. zheng, M. zhu, X. zhang, G. yuan, Z. xie, X. Li, G. Yue, W. Zhang, Photovoltaic enhancement by Au surface-plasmon effect for La doped BiFeO3 films, J. Mater. Chem. C (2017).

[43] S. Xiao, H. Sun, X. Liu, H. Sui, Investigations on photovoltaic performance of sol–gel derived BiFeO3-based heterostructures via compositional modification, Materials Letters 260 (2020) 126964.

[44] G.G. Khan, R. Das, N. Mukherjee, K. Mandal, Effect of metal doping on highly efficient photovoltaics and switchable photovoltage in bismuth ferrite nanotubes, Status Solidi RRL (2012) 1–3.

Appendix 2

Summary Table of piezoelectric coefficients for BiFeO$_3$ systems

Material & Heterostructure	Orientation (pseudocubic)	Piezoelectric coefficients [pC/N]	Dielectric constant	K2	Ref.
Films					
BiFeO$_3$	Poly.		At 1MHz ε_r=107		[1]
BiFeO$_3$	(001)	d_{33}= 70	180		[2]
BiFeO$_3$	Poly.	d_{33}=50			[3]
BiFeO$_3$	Poly.	d_{33}= 90			[4]
Bi$_{1-x}$Tb$_x$FeO$_3$ (BTFO)	Poly.	At x=0.11; d33=140			[4]
BiFeO$_3$	(001) and (110)		At 100Hz ε_r=200		[5]
La-doped BiFeO$_3$	(001) and (110)		At 100Hz ε_r=300		[5]
(1-x)BiFeO$_3$–xBiCoO$_3$ (x = 0-0,30)	(001)	d_{33}=100 at x=0,1			[6]
BiFeO$_3$	(001)	d_{33}=51			[6]
BiFeO$_3$	(001) and (111)	$e_{31,f}$= -3,5 C/m² (001) $e_{31,f}$=-1,3 C/m² (111)	At 10kHz ε_r=122 for (001) and ε_r=58 (given from the ε_{33})		[7]
BiFeO$_3$	(001)	d_{33}= 50			[8]
BiFeO$_3$	(100)	d_{33} = 17 and d_{33} = 22			[9]
BiFeO$_3$	(100)	d_{33}= 58 ; $e_{31,f}$= -4 C/m²	At 100kHz = 130		[10]
BiFeO$_3$	(100)	$e_{31,f}$= -4,3 C/m²	~150		[11]
BiFeO$_3$	(100)	$e_{31,f}$= -3,6 C/m²	At 100Hz ε_r=150	K²=0,1% ; $k^2_{31,f}$ = 6,0%	[12]
Ceramics					
Na$_{0.5}$K$_{0.5}$NbO$_3$–BiFeO$_3$ (1-2% of BFO)		185		Kp=46%	[13]
(1–x–y)(Bi$_{0.5}$ Na$_{0.5}$ TiO$_3$)–x(Bi$_{0.5}$K$_{0.5}$ TiO$_3$) – y (x = 0.18; y = 0.03)		170		Kp=0,366	[14]
(1-x)BiFeO$_3$–xBaTiO$_3$ Mn doped		d_{33}=116 (x= 0,25)	At 1kHz ε_r = 557 (for x= 0,25)		[15]
(1-x)BiFeO$_3$–xBaTiO$_3$ Mn undoped		d_{33}=47 (x= 0,25)	At 1kHz ε_r = 605 (for x= 0,25)		[15]
(0.6)BiFeO$_3$–(0.4)PbTiO$_3$		d_{31}=-41.6 ; d_{33}= 49,1; d_{15}=211,4; d_h= 132,4; g_{31}=-9,65 x 10-3 Vm/N ; g_{33}=-12.3 *10-3 Vm/N ; g_{15}=40,2 *10-3 Vm/N ; e_{31}=8,7 C/m; e33=9,16 C/m ; e_{15}=6,62 C/m;	$\varepsilon_{t33}/\varepsilon_0$ = 488 ; $\varepsilon_{s33}/\varepsilon_0$ = 404,2 ; $\varepsilon_{t11}/\varepsilon_0$ = 594 ; $\varepsilon_{s11}/\varepsilon_0$ = 436	kp = -0,3 ; k$_{31}$ = -0,18; k$_{33}$=0,23 ; k$_{15}$=0,52; kt= 0,14	[16]
0.65BiFeO$_3$–0.35BaTiO$_3$		d_{33}= 104			[17]
(1-y)BiFe$_{1-x}$(Mg$_{0.5}$Ti$_{0.5}$)$_x$O$_3$ –y BaTiO$_3$ (y=0.29, x=0-0.12)		155 (x=0.03 BFMT-BT)			[18]

Material		d	dielectric	Kp	Ref
(1-x)BiFeO₃–xBaTiO₃ (x=0,3)		d_{33}= 134	860	Kp=0,29	[19]
Mn- and Cu-doped BiFeO₃–BaTiO₃		165		Kp=0,32	[20]
(0.7-x)BiFeO₃–0.3BaTiO₃-xLaFeO₃ (x = 0–0.2)		for x=0 d_{33}=80; for x=0,025 d_{33}=244 and d_{33}max=350	At 1MHz with x=0.025 ε_r=406		[21]
x Li₂CO₃-doped BiFeO₃-BaTiO₃-Bi(Zn0.5Ti0.5)O₃ (x= 0.3 mol%)		184		Kp = 0.357	[22]
BiFeO₃		151	673		[23]
BiFeO₃-PbTiO₃-BaTiO₃ (x = 0.21)		150	At 1kHz ε_r = 479		[24]
BiFeO₃-PbTiO₃-BaTiO₃ (x = 0.23)		222	At 1kHz ε_r = 545		[24]
BiFeO₃-PbTiO₃-BaTiO₃ (x = 0.25)		149	At 1kHz ε_r = 496		[24]
La-doped BiFeO₃–BaTiO₃ (1.5BaLa)		340			[25]
La-doped BiFeO₃–BaTiO₃ (1.0BaLa)		297			[25]
Bulk					
BiFeO₃		d_{15} = 27.6; d_{31} = 12.67; d_{33} = 18			[26]
Nanofibers					
BiFeO₃	Poly.	d_{33} = 11			[27]

References

[1] V. R. Palkar, J. John, R. Pinto, Observation of saturated polarization and dielectric anomaly in magnetoelectric thin films, Appl. Phys. Lett. 80 (2002) 1628.

[2] J. Wang, J. B. Neaton, H. Zheng, V. Nagarajan, S. B. Ogale, B. Liu, D. Viehland, V. Vaithyanathan, D. G. Schlom, U. V. Waghmare, N.A. Spaldin, K. M. Rabe, M. Wuttig, R. Ramesh, Epitaxial BiFeO3 Multiferroic Thin Film Heterostructures, Science 299 (2003).

[3] S.K. Singh, R. Ueno, H. Funakubo, H. Uchida, S. Koda, H. Ishiwara, Dependence of Ferroelectric Properties on Thickness of BiFeO3 Thin Films Fabricated by Chemical Solution Deposition, Jpn. J. Appl. Phys. 44 (2005) 8525.

[4] X. Chen, G.Hu, W. Wu, C. Yang, X. Wang, Large Piezoelectric Coefficient in Tb-Doped BiFeO3 Films, J. Am. Ceram. Soc., 93 (2010) 4 948–950.

[5] F. Yan, T.J. Zhu, M.O. Lai, L. Lu, Enhanced multiferroic properties and domain structure of La-doped BiFeO3 thin films, Scripta Materialia 63 (2010) 780–783.

[6] Y. Nakamura, M. Kawai, M. Azuma, M. Kubota, M. Shimada, T. Aiba, Y. Shimakawa, Enhanced Piezoelectric Constant of (1-x)BiFeO3–xBiCoO3 Thin Films Grown on LaAlO3 SubstrateJpn. J. Appl. Phys. 50 (2011) 031505.

[7] K. Ujimoto, T. Yoshimura, A. Ashida, N. Fujimura, Direct piezoelectric properties of (100) and (111) BiFeO3 epitaxial thin films, Applied Physics Letters 100 (2012) 102901.

[8] C. Daumont, W. Ren, I.C. Infante, S. Lisenkov, J. Allibe, C. Carrétéro, S. Fusil, E. Jacquet, T. Bouvet, F. Bouamrane, S. Prosandeev, G. Geneste, B. Dkhil, L. Bellaiche, A. Barthélémy, M. Bibes, Strain dependence of polarization and piezoelectric response in epitaxial BiFeO3 thin films, J. Phys.: Condens. Matter 24 (2012) 162202.

[9] J. M. Vila-Fungueiriño, A. Gomez, J. Antoja-Lleonart, J. Gazquez, C. Magén, B. Noheda and A. Carretero-Genevrier, Direct and Converse Piezoelectric Responses at the Nanoscale from Epitaxial BiFeO3 Thin Films Grown by Polymer Assisted Deposition, Nanoscale (2018).

[10] K. Kariya, T. Yoshimura, S. Murakami, N. Fujimura, Enhancement of piezoelectric properties of (100)-orientated BiFeO3 films on (100)LaNiO3/Si, Jpn. J. Appl. Phys. 53 (2014) 09PA14.

[11] T. Yoshimura, K. Kariya, N. Okamoto, M. Aramaki and N. Fujimura, Direct piezoelectric properties of BiFeO3 epitaxial films grown by combinatorial sputtering, Journal of Physics: Conf. Series 1052 (2018) 012020.

[12] M. Aramaki, T. Yoshimura, S. Murakami, K. Satoh, N. Fujimura, Demonstration of High-performance Piezoelectric MEMS Vibration Energy Harvester using BiFeO3 Film with Improved Electromechanical Coupling Factor, Sensors and amp; Actuators: A. Physical (2019).

[13] R. Zuo, C. Ye, X. Fang, Na0.5K0.5NbO3–BiFeO3 lead-free piezoelectric ceramics, Journal of Physics and Chemistry of Solids 69 (2008) 230–235.

[14] C. Zhou, X. Liua, W. Li, C. Yuana, Structure and piezoelectric properties of Bi0.5Na0.5TiO3–Bi0.5K0.5TiO3–BiFeO3 lead-free piezoelectric ceramics, Materials Chemistry and Physics 114 (2009) 832–836.

[15] S O. Leontsev, R.E. Eitel, Dielectric and Piezoelectric Properties in Mn-Modified, (1-x)BiFeO3–xBaTiO3 Ceramics, J. Am. Ceram. Soc., 92 (2009) 12 2957–2961.

[16] V.F. Freitas, I.A. Santos, Piezoelectric Characterization of (0.6)BiFeO3–(0.4)PbTiO3 Multiferroic Ceramics, J. Am. Ceram. Soc., 94 (2011) 3 754–758.

[17] Y. Wei, X. Wang, J. Jia, X. Wang, Multiferroic and piezoelectric properties of 0.65BiFeO3–0.35BaTiO3 ceramic with pseudo-cubic symmetry Ceramics International 38 (2012) 3499–3502.

[18] C. Zhou, A. Feteira, X. Shan, H. Yang, Q. Zhou, J. Cheng, W. Li, H. Wang, Remarkably high-temperature stable piezoelectric properties of Bi(Mg0.5Ti0.5)O3 modified BiFeO3–BaTiO3 ceramics, Appl. Phys. Lett. 101 (2012) 032901.

[19] Y. Wei, X. Wang, J. Zhu, X. Wang, J. Jia, Dielectric, Ferroelectric, and Piezoelectric Properties of BiFeO3–BaTiO3 Ceramics, J. Am. Ceram. Soc. (2013) 1–6.

[20] H. Yang, C. Zhoub, X. Liu, Q. Zhoub, G. Chenb, W. Li, H. Wang, Piezoelectric properties and temperature stabilities of Mn- and Cu-modified BiFeO3–BaTiO3 high temperature ceramics, Journal of the European Ceramic Society 33 (2013) 1177–1183.

[21] M. Zhang, X. Zhang, X. Qi, H. Zhu, Y. Li, Y. Gu, Enhanced ferroelectric, magnetic and magnetoelectric properties of multiferroic BiFeO3– BaTiO3–LaFeO3 ceramics, Ceramics International (2018).

[22] Y. Sun, H. Yang, S. Guan, Y. Cao, M. Jiang, X. Liu, Q. Chen, M. Li, J. Xu, Strong piezoelectricity of Li2CO3-doped BiFeO3eBaTiO3eBi(Zn0.5Ti0.5) O3 lead-free piezoelectric ceramics with high Curie temperature and high temperature stability, Journal of Alloys and Compounds 819 (2020) 153058.

[23] H. Zhao, Y. Hou, X. Yu, M. Zheng, M. Zhu, Enhanced piezoelectric property in quenched BiFeO3-based piezoceramics: role of defects and mesophase, J. Mater. Chem. C (2020).

[24] Z. Ning, Y. Jiang, J. Jian, J. Guo, J. Cheng, H. Cheng, J. Chena, Achieving both large piezoelectric constant and high Curie temperature in BiFeO3-PbTiO3-BaTiO3 solid solution, Journal of the European Ceramic Society 40 (2020) 2338–2344.

[25] M. Habib, M. H. Lee, D. J. Kim, H. I. Choi, M.H. Kim, W.J. Kim, T. K. Song, K. S. Choic, Enhanced piezoelectric performance of donor La3+-doped BiFeO3–BaTiO3 lead-free piezoceramics, Ceramics International 46 (2020) 7074–7080.

[26] G. Jian, F. Xue, Y. Guo, C. Yan, Orientation Dependence of Elastic and Piezoelectric Properties in Rhombohedral BiFeO3, Materials 11 (2018) 2441.

[27] A. Queraltó, R. Frohnhoven, S. Mathur, A. Gómez, Intrinsic piezoelectric characterization of BiFeO3 nanofibers and its implications for energy harvesting, Applied Surface Science 509 (2020) 144760.

Published or submitted papers

- Q. Micard, G.G. Condorelli, G. Malandrino, *Piezoelectric BiFeO$_3$ Thin Films: Optimization of MOCVD Process on Si*, Nanomaterials 10 (2020) 630.

- Q. Micard, A.L. Pellegrino, R. Lo Nigro, A. Bartasyte, G.G. Condorelli, G. Malandrino, *Piezoelectric Ba and Ti co-doped BiFeO$_3$ textured films: selective growth of solid solutions or nanocomposites*, J. Mater. Chem. C 8 (2020) 16168-16179.

- Q. Micard, G. Clementi, A. Bartasyte, P. Muralt, G.G. Condorelli, G. Malandrino, *Self-poled heteroepitaxial Bi$_{(1-x)}$Dy$_x$FeO$_3$ films with giant pyroelectric properties, J. Mater. Chem. A (submitted)*

Manuscripts in preparation

- Q. Micard, S. Margueron, G.G. Condorelli, G. Malandrino, *MOCVD of Dy-doped BiFeO$_3$ thin films: piezoelectric and bandgap tuning (to be submitted).*

- Q. Micard, A. Sekkat, D. Munoz-Rojas, G.G. Condorelli, G. Malandrino, *Ln-doped BiFeO$_3$ films for photovoltaic application (in preparation).*

- Q. Micard, R. Ramesh, G.G. Condorelli, G. Malandrino, *Ferroelectric and magnetic properties in Co-doped BiFeO$_3$ films, (in preparation).*

- Q. Micard, R. Ramesh, G.G. Condorelli, G. Malandrino, *Properties of self-assembled BiFeO$_3$ – CoFe$_2$O$_4$ nanocomposite thin films by MOCVD, (in preparation).*

- Q. Micard, R. Ramesh, G. Malandrino, *Morphotropic Phase Boundary in Bi$_{(1-x)}$Sm$_x$FeO$_3$ thin films, (in preparation).*

- Q. Micard, G.G. Condorelli, G. Malandrino, *MOCVD of La$_2$NiO$_4$ and LaOF, (in preparation).*

Attended schools and conferences

- ENHANCE Introductory School, Besançon (France), May 16-18, 2018. Poster: *Dy-doped BiFeO$_3$ films grown by MOCVD on single crystal substrate*

- International School of Materials for Sustainable Development and Energy 1st Course, "Materials for Energy and Sustainability – ISMES VII", Erice (Italy), July 6 – 13, 2018. Poster: *MOCVD of Dy-doped BiFeO$_3$ films on single crystal SrTiO3*

- Training School "Career Opportunities "(EPFL), Lausanne (Switzerland), September 5-6, 2018.

- 2nd International Rhine Round Table Emerging Frontiers in Ceramic Materials and Glass, Inaugural symposium of the Rhine Chapter, Cologne (Germany), September 24, 2018

- From Molecular Engineering to advanced Materials, Workshop, Cologne (Germany), 21-25 May 2019. Oral and Poster: *Multiferroic BiFeO3 films and nanostructures for hybrid energy harvesters.*

- EuroCVD 22 Baltic ALD 16 Conference, Luxembourg, June 24-28, 2019. Poster: *Perovskite Bi$_{(1-x)}$Dy$_x$FeO$_3$ thin films on Si based substrates: MOCVD growth and characterization*

- ESONN School 2019 - European School on Nanosciences & Nanotechnologies, Grenoble (France), 26th of August to 14th of September 2019. Poster: *MOCVD grown functional Dy-doped BiFeO$_3$ thin films on Si based substrates*

- IWPMA 2019, Lyon (France), 1-4 October2019. Oral and poster: *MOCVD of Bi(1-x)DyxFeO3 thin film on Si for energy harvesting*

- PowerMEMS 2019, Micro and Nanotechnology for Power Generation and Energy Conversion Applications, Kraków (Poland), 2-6 December 2019. Poster: *Functional $Bi_{(1-x)}Dy_xFeO_3$ thin films grown by MOCVD*

- KTN- Knowledge transfer, patenting & commercialisation, Online, July 13th and 16th 2020, ENHANCE Training School, Poster: *Optimization of MOCVD Process of Piezoelectric BiFeO3 Thin Films on Si*

- Cedrat Technologies - Mechatronics and Electronics for EHs, Online, September 15th to 23rd 2020, ENHANCE Training School.

- MSE 2020 – Material Science and Engineering Congress, Online, September 22nd to 25th 2020, Oral: *MOCVD of Piezoelectric Ba and Ti co-doped $BiFeO_3$: between nanocomposites and solid solutions*

- MRS Fall Meeting, Online, November 28th to December 4th 2020, Poster: *MOCVD of Functional Dy-Doped $BiFeO_3$ Film Grown on Single Crystal*

Secondments

- AIXTRON, Herzogenrath (Germany), April 2018 (1 month)
  Supervisor: Prof. Dr. Michael Heuken

- Ecole Polytechnique Fédérale de Lausanne (EPFL), Lausanne (Switzerland), From April to July 2019 (3 months)
  Supevisor: Prof. Paul Muralt

- Unviversité de Franche Compté / Femto-ST, Besançon (France), From September to November (2 months)
  Supervisors: Prof. Ausrine Bartasyte and Prof. Samuel Margueron

- ST-Microelectronics, Catania (Italy), July, September and December 2020 (3 months)

Tutoring activity

- Master thesis: *Ottimizzazione del processo di deposizione chimica da fase vapore di film di nichelato di lantanio,* Marco Patané

- Master thesis:, *Effetto del dragaggio di lantanidi sulle proprietà funzionali della Ferrite di Bismuto*, Vanessa Cutraro

- Master thesis: *Ottimizzazione del processo di deposizione chimica da fase vapore di film di Ferrite di Cobalto Besançon*, Federica Pizzorni (*ongoing*)